Modelling metastatic melanoma in zebrafish

Groenewoud, A.

Modelling metastatic melanoma in zebrafish

Arwin Groenewoud

Cover: *Tg(fli:GFP) x Casper* zebrafish larva with green fluorescent blood vessels, injected with red fluorescent (tdTomato) expressing melanoma cells

ISBN: 978-94-6423-828-0

Modelling metastatic melanoma in zebrafish

Proefschrift

ter verkrijging van
de graad van doctor aan de Universiteit Leiden,
op gezag van rector magnificus prof. dr. ir. H. Bijl,
volgens besluit van het college voor promoties
te verdedigen op dinsdag 7 juni 2022
klokke 13.45 uur

door
Arwin Groenewoud
geboren te Heerjansdam
in 1988

Promotor: Prof. dr. B. E. Snaar-Jagalska

Co-promotor: Dr. A. G. Jochemsen (LUMC)

Promotiecommissie:

Prof. dr. G. P. van Wezel

Prof. dr. H. P. Spaink

Dr. S. E. Le Dévédec

Prof. dr. P. ten Dijke (LUMC)

Prof. dr. F. B. Engel (FAU, Germany)

Contents

Chapter 1:

General introduction and thesis outline

Introduction

Cancer is one of the leading causes of disease-mediated death worldwide.[1] In almost all cases, cancer patients do not die from the primary tumor but from the metastatic form of the disease, and the subsequent perturbation of the functions of invaded tissues[2].

After the establishment of the original primary tumor, cells escape and enter into a blood or lymphatic vessel to disseminate passively through blood flow or lymphatic drainage. Cells subsequently anchor and extravasate and eventually outgrow, sometimes after years of dormancy[2,3]. Current treatment is focused either on the prevention of disease progression (in the case of primary tumors) or on the mitigation of symptoms (metastases).

Cancer, and by extension the mechanisms of metastasis, is commonly held in check through cell intrinsic (P53, cell cycle checkpoints, etc.) and extrinsic (adaptive and innate immune cells) means. Over time, the acquisition of multiple mutations (mostly preluded by a loss or inactivation of P53) leads to the escape of the cells from these safeguard mechanisms. During and after this malignant transformation, the cells continuously exchange signals with their surroundings, secreting growth factors influencing themselves and their surroundings or alternatively through direct contact-mediated interaction or indirect communication through vesicles (exosomes). Through this communication, the cancerous cells cultivate a pro-malignant environment, or cancerized field (original term coined by Slaughter et al in 1953)[4]. This environment, called the tumor microenvironment (TME), changes as the cancer progresses contributing to further tumor growth, treatment resistance, and metastatic dissemination (Figure 1).

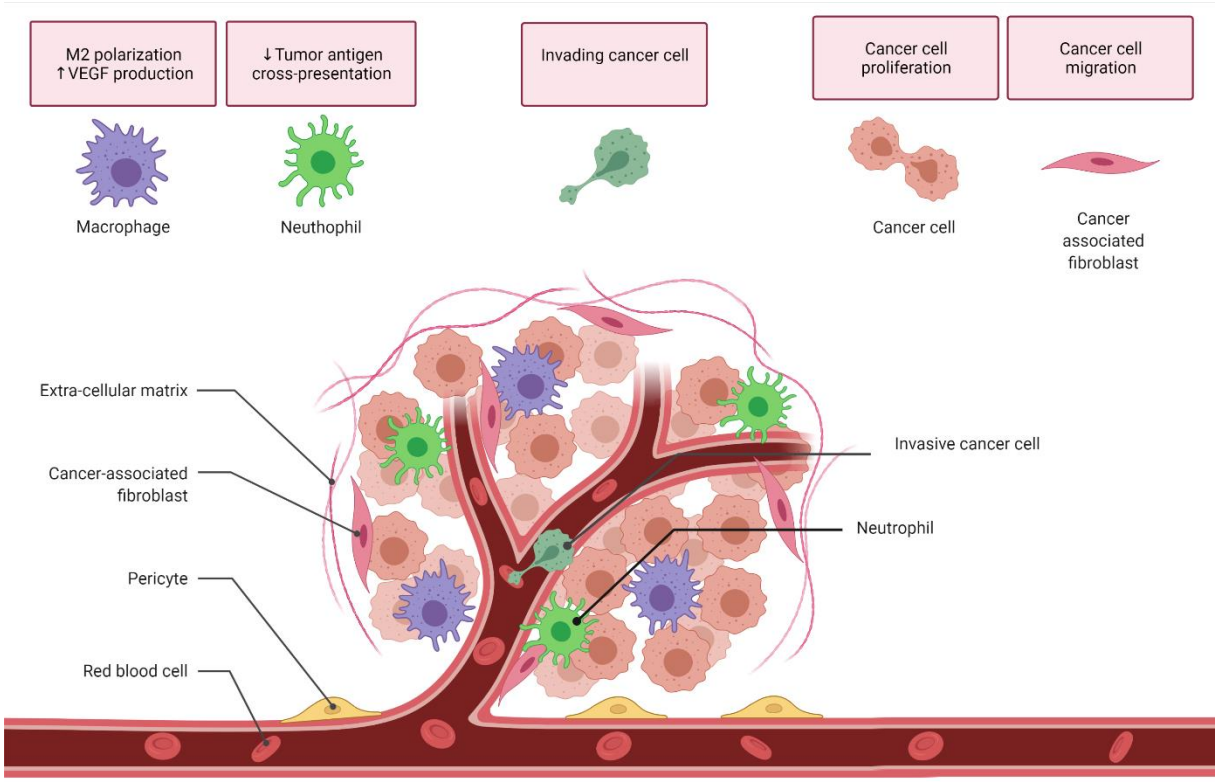

Figure 1. Cancer heterogeneity on an intertumoral level.

Primary tumors are made up of both cancer cells and "normal" non-cancer cell tissue. Intertumoral heterogeneity stems from the inclusion of these normal derived cells and extracellular matrix components, named stroma.: In many tumors a substantial percentage of the tumor volume is made up out of stroma compose of. innate and adaptive immune cells (i.e macrophages and neutrophils versus T- and NK- cells respectively), fibroblasts, extracellular matrix components and blood vessels, among others. The intertumoral heterogeneity, or the differences in clonal populations within one tumor, stems from the highly dynamic nature of the selection pressures inside the tumor. Patches of tumor subclones divide and speciate towards survival under a vast array of exogenous stimuli. Ultimately, the tumor will expand beyond the limits of its metabolic capacity, driving the recruitment of neovasculature. Cancer will then infiltrate this vasculature or invade locally into the lymphatic or vascular system and will be dispersed passively to distant sites, forming metastases. Adapted from Joyce and Pollard 2009[5].

Cancer is characterized as an uncontrolled growth of the hosts cells leading to the overgrowth and infiltration of healthy tissues, ultimately leading to metastasis to remote organs when left untreated[6,7]. During the early stages of tumorigenesis, the nascent (non-malignant, hyperplastic) cell gradually changes into a malignant (neoplastic) cell, resembling the shared etiology among malignancies[8,9]. This process is driven by the accumulation of increasing amounts of genomic mutations, thought to be preceded by a simultaneous deletion or inactivation of a tumor suppressor gene

(i.e. *P53, Rb*) and the hyperactivation of an oncogenic pathway (i.e *RAS, AKT* pathway)[10,11]. At least two mutations are needed (a loss of both alleles of a tumor suppressor gene), given that a singular instance of tumor suppressor has been shown to be insufficient for malignant transformation. This hypothesis (known as the two-hit hypothesis) explains, in part, the relative rarity of tumorigenesis on a (cellular) population basis[10]. A key part of this process is the switch of mitogenic (growth factor) dependency, to mitogenic independency, where cells shift from paracrine to autocrine mitogenic stimulation. This process further liberates the malignant cells from the control of their micro-environment.

Additional mechanisms driving tumorigenesis are acquired through sequential random somatic mutations facilitated by the cancer cell inherent genetic instability (i.e. loss of P53 or other cell cycle checkpoint proteins during tumorigenesis)[12–14]. This genetic instability greatly increases the mutational ability of cancer cells and therefore drive the microevolutionary process of cancer progression[15]. This process, combined with the increasingly hostile character of the TME, leads to the selection of mutations which allow the cell to proliferate at an increased rate, to resist cancer inhibitory immune functions, and plays an important role in the metastasis and development of resistance to treatment[5,7,16]. This gradual process enables tumor formation of high structural intricacy and heterogeneity. In the majority of tumors this increase in complexity, and concordant enhancement of stressors (nutrient deprivation, oxygen starvation etc.) within the primary tumor, some cells eventually gain metastatic capacity. This small subset of cells is not only able to disseminate but also to colonize distant organs[17].

Cancer pathogenesis and general hallmarks delineating malignant transformation

In essence, cancer cells arise from healthy cells after multiple mutations that ultimately lead to the subversion of apoptosis and the enhancement of proliferation[18]. As already mentioned, the most prominent mutations in cancer cells are mutations in tumor suppressor genes (P53, Rb etc.) and oncogenes (RAS cascade, NRAS etc.). On the one side, tumor suppressor genes mostly play a role in cell cycle progression, DNA damage repair and the integration of both processes to ensure genome stability. Inactivating mutations in such tumor suppressor genes (most commonly P53) leads to

a perturbation of the cellular safeguard mechanisms and furthers the instability of the cancer cells genome. On the other side, proto-oncogenes are genes which normally control proliferation and differentiation. These genes become oncogenic only after its mutation and subsequent enhancement of activity or effective elevation of protein levels.

In addition to the enhanced cell division capacity and a lack of programmed cell death, additional changes are required to transform a healthy cell into a cancer cell. These have been summarized as the distinct hallmarks of cancer by Hanahan and Weinberg in 2000 and updated in 2011 (Figure 2)[19]. The subsequent development of the cancer cell population is largely delineated as a small-scale evolutionary process, with selection pressure arising from the increasing hostility of the tumor micro-environment and interaction with the host immune system[20–22]. This selection pressure is thought to yield increasingly malignant cancer cells and will eventually lead to the invasion of neighboring tissues and the spreading of the cancer cells to remote organs (i.e., metastasis).

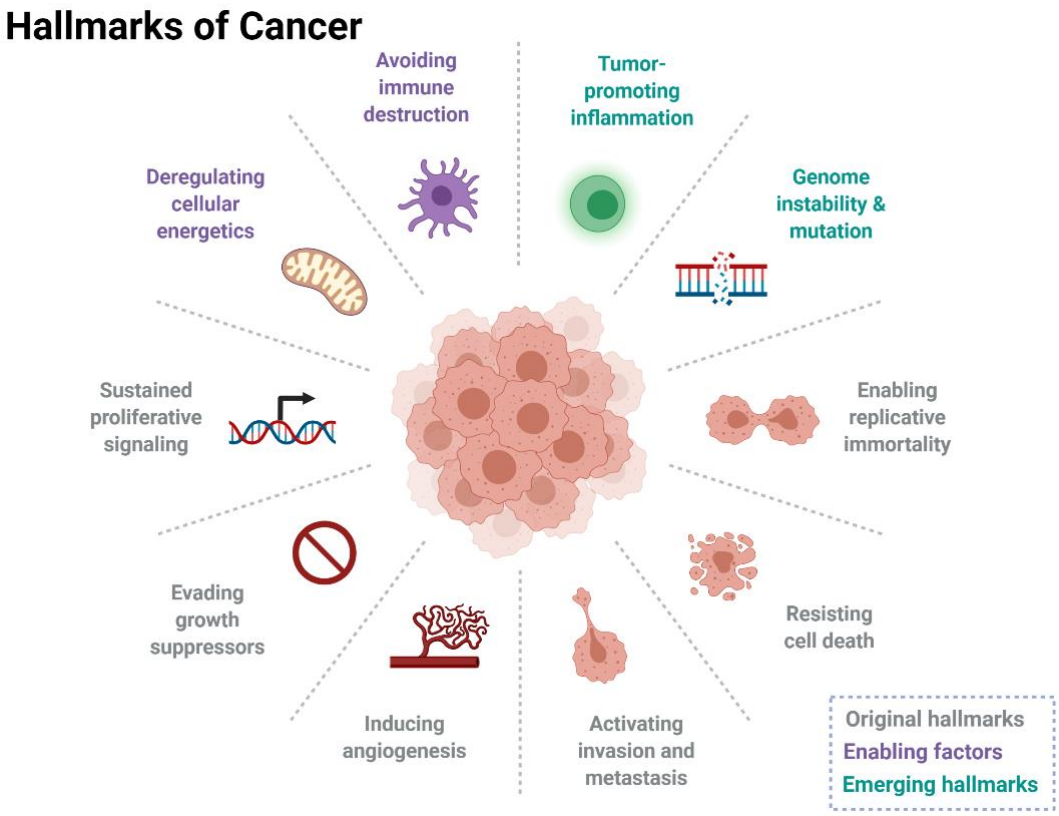

Figure 2. The canonical hallmarks of cancer.

Coined in 2000 and updated in 2011 by Hanahan and Weinberg, these features both define and drive tumorigenesis and metastasis in all cancers. Some, if not most, of these features are enhanced in tumors when compared to their wild type progenitor. Although all cancers can be seen as distinct disease entities, they have evolved mechanisms to compensate or circumvent the bodies intrinsic capacity to deal with malignant disease (evading cell death, growth suppression, immune destruction) and eventually lead to the development of metastatic capacity (inducing angiogenesis, activating invasion, migration and metastasis), which are further enhanced by cancer intrinsic mechanisms (genome instability and pro-tumorigenic inflammation). Adapted from Hannahan and Weinberg 2000&2011[18,19].

Metastasis: distant colonization, the culmination of late-stage cancer and its complications.

In 1889 Paget discovered that blood flow dictates the metastatic sites favored by metastasizing breast cancer[23]. Moreover, his findings showed that while metastatic cancer cells are found in most tissues, only in some discrete locations a metastatic colony can arise. This theory, named the “seed and soil hypothesis”, states that although cancer cells (seeds) are spread throughout the body, only in some locations where the tissue (the 'soil') is amiable to metastatic growth a metastasis will be able to sprout. Later experiments by Fiddler starting in 1970, indicated that when cells are harvested from metastatic sites they retain a certain pre-metastatic property, which can be enhanced by subsequent passages through metastatic models. These experiments hinted at a cell intrinsic mechanism that predetermines the metastatic capacity of a sub-set of cells. Moreover, the retention and amplification of these features indicated that this was presumably due to a genetic mechanism. Subsequently, Massagué and colleagues showed the existence of specific genetic drivers for metastasis in breast cancer, and that these drivers predisposed cells to grow in certain areas. With these experiments they proved that cancer cells intrinsically harbor the capacity to metastasize to all organs on a whole tumor level, but that specific sub-clones of this cancer have enhanced metastatic outgrowth capacity in common metastatic sites (brain, bone, lung and liver). Moreover, subsequent re-injection of these metastatic sub-populations demonstrated that these features can be further amplified.

To enable this passage into circulation, cancer cells have to change from their conventional stationary phenotype into a more motile and plastic phenotype, this

conversion (known as the epithelial to mesenchymal transition (EMT) in epithelial cells) allows the cells to sequentially gain cell migratory capacity while suppressing proliferation[24–27]. The signaling underlying EMT and its converse mesenchymal to epithelial transition (MET) required for the re-establishment of proliferation potential– are deemed indispensable for metastatic dissemination and outgrowth[28,29].

The canonical routes of metastasis are through the lymphatic system and the blood circulatory system, where the final steps of metastasis ultimately occur through capillary processes[30–32].Upon subsequent extravasation from circulation through either adhesion or physical entrapment in a capillary, cancer cells go through the reverse process re-establishing its epithelial phenotype and possibly generating a novel cancer cell colony, or metastasis.

Although the vast majority of all cancer patients die from the effects that the metastatic colonization has on the function of distant organs, metastasis is a highly inefficient process. This is in part explained by the previously mentioned “seed and soil hypothesis” where most of the “seeds” end up in inhospitable soil and therefore fail to grow out into a metastatic colony. This soil hostility can be seen as an oversimplification, since this context dependent tumorigenic capacity arises from both cell intrinsic mechanisms (i.e. lack of appropriate cell-cell adhesion machinery, lack of appropriate mitogen receptors) or conversely cell extrinsic (blood flow, lack of mitogen expression)[5]. Furthermore, there are a host of factors that form a functional bottleneck limiting the efficiency of metastasis (i.e. nutrient deprivation, anoikis, reactive oxygen species, immune surveillance)[7,33].

Driven by its growth and the microscale evolution underlying the developments of the primary tumor, most cancer are ultimately driven to metastasize. Metastatic dissemination can be subdivided into several different stages (Figure 3): 1) intravasation, the passage of a cancer cell form a primary tumor into a vessel (blood of lymphatic); 2) proper dissemination, the mostly passive spread of a cancer cells from a primary tumor throughout the body, a highly inefficient process thought to kill >95% of all cancer cells; 3) colonization, the adherence and survival at a distant site, eventually leading to extravasation; and 4) outgrowth, the process growing a *de novo* extravascular metastatic colony, often leading to the perturbation of organ function and ultimately host death.

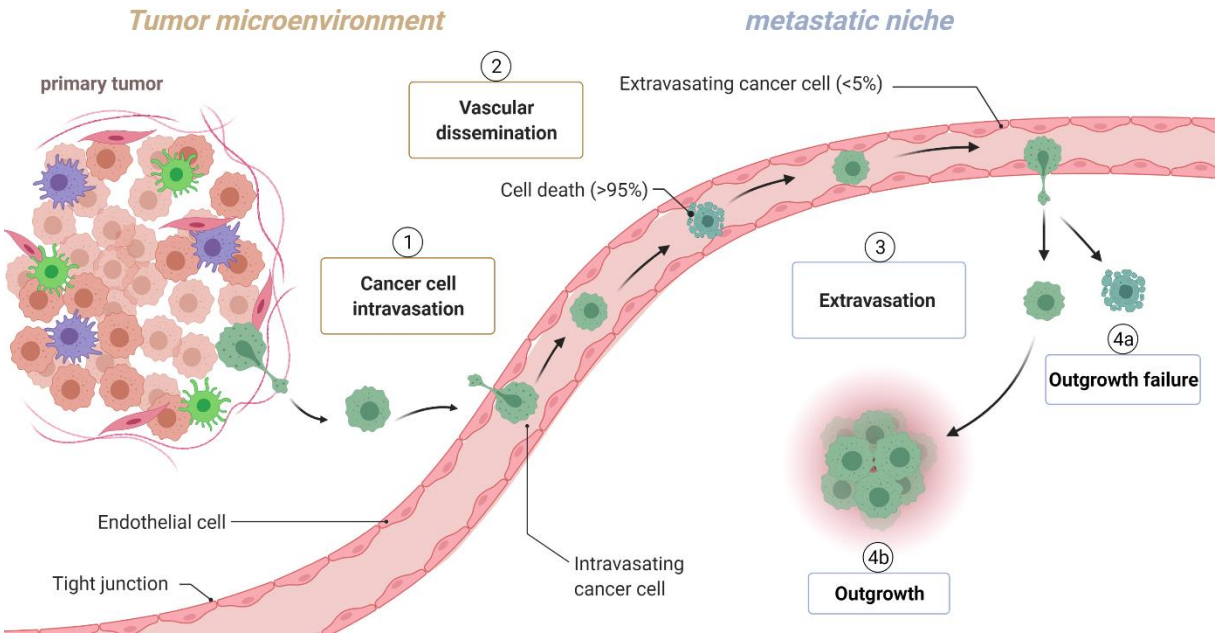

Figure 3. The process of metastasis.

Cancer cells, once intravasated, are transported through the body passively and dispersed semi-randomly following the way of least resistance, and will, in most cases, end up in either the closest lymphatic node or in the next vascularized tissue "downstream" of the tissue of origin. Next to following the physical constraint of blood flow, cancer cells will be entrapped in a capillary blood vessel and either grow out (i.e establishing a metastatic colony) or perish, either through active host interference (i.e NK-cell activation) or through a lack of viable niche (i.e., lack of required mitogens in the new environment). Despite being a highly inefficient process where 95-99% of the cancer cells do not survive, the vast majority of cancer patients (>95%) are killed by the metastatic form of the disease and not the primary tumor. Adapted from Gupta 2006 and Massague 2016[7,34].

Cutaneous, conjunctival and uveal melanoma: genetic drivers and (dis)similarities.

One of the most common types of cancer are melanomas. These cancers derive from melanocytes in the organ of origin, either in the melanocytes of the dermis, in the conjunctival melanocytes or in the melanocytes of the uvea (made up out of the iris, ciliary body and the choroid). As with all cancers, primary tumor development preludes metastatic disease formation (Figure 4).

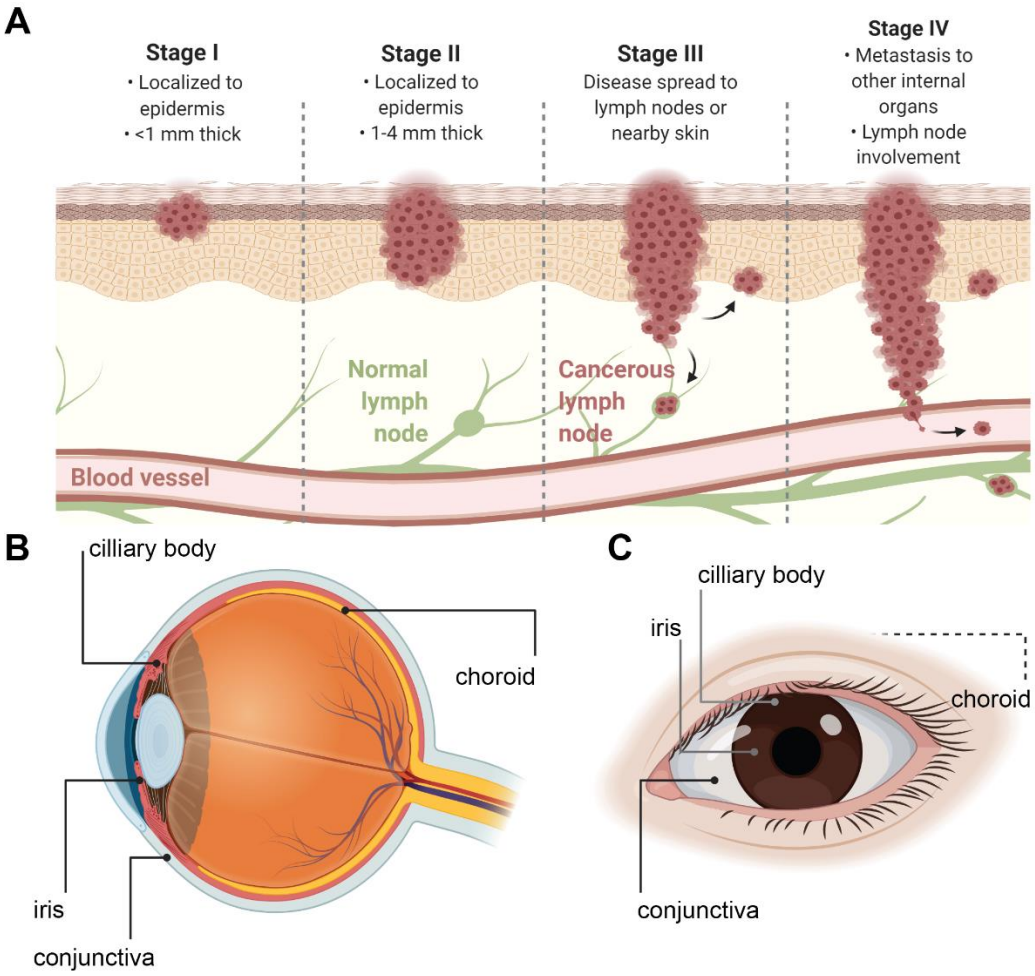

Figure 4. Melanomas and their pathological locations.

A) Cutaneous Melanoma (CM) deriving from a hyperplastic nevus (mole). As disease progresses, cells proliferate and infiltrate local tissue. Staging is largely based on size and depth of penetrance into the underlying tissue, stage I (<1 mm in thickness). Stage II, still localized to the epidermis (1-4 mm in thickness). stage III, penetration beyond the epidermis and localized micro-metastasis, cancer cells found in local lymph nodes. Stage IV (defined by lymph node involvement and metastasis to other organs). B) General location of ocular melanomas (transverse view). Uveal melanoma (UM) derives from the ciliary body, iris or choroid, whereas Conjunctival Melanoma (CoM) forms in the outer layer of the eye (conjunctiva). C) Front view of the eye, with indicated locations of UM and CoM formation. UM sites (grey lines and dotted line); note that the choroid in not visible since it is on the inside of the eye, CoM site (black line). Adapted from Damato and Coupland 2014 and Jager 2020.

Cutaneous melanoma is one of the most common malignancies in the Caucasian population, occurring in approximately 3 out of 100,000 individuals. There is high variability between populations, possibly related to the inherent skin type of the affected populations[35], moreover the overall incidence shows a steadily increasing

trend[36]. Approximately, 5 in 100,000 people are diagnosed with UM[37] and COM affects approximately 0.02 to 0.08 per 100,000 individuals per year[38].

In general, for all melanoma types**,** the prognosis for the metastatic form of the disease is grim, with an average survival of <6 months after diagnosis for metastatic CM[39], 8.1-years for metastatic CoM[38]**,** and <6 months for metastatic UM[40]. Strikingly one shared pre-disposing factor between all aforementioned melanoma is a Caucasian, light skin-type combined with blue or green eyes and an inability to tan.

Genome instability, one of the hallmarks of cancer, is one of the features that underscores the stark differences between CM, CoM and UM. Whereas CM and CoM are highly mutated, UM seems to be largely genomically stable. This genome instability subsequently drives both an enhanced risk of metastasis and an underlying basis for the development of treatment resistance. Conversely, genome instability governs the generation of neo-epitopes, used for the development of cancer immune-therapy, a highly efficient treatment option for CM, to which UM is largely refractory. Where CM and CoM cells are canonically transformed through DNA damage incurred by UV exposure, UM does not share this intrinsic UV-mediated DNA damage signature[20,41].

Ocular melanoma is relatively rare, making up approximately 3-4% of all melanomas[42,43]. Out of all ocular melanomas about 90% are uveal melanoma, with CoM making up the remaining 10%[42]. Although generally treatment of the primary tumor is effective, there is a high rate of metastasis, even as high as 50% for UM.

As previously discussed, oncogenic transformation of normal cells is conventionally driven by hyperactivation of pathways supportive of survival and proliferation, or conversely a stunting of pathways governing cell death mechanisms. One commonly implicated pathway is the MAP kinase cascade, signaling through the proteins RAS-RAF-MEK-ERK. Conjunctival melanoma share most common molecular features with CM and is, in the majority of the cases**,** driven by a hyperactivation of the RAS-RAF-MEK-ERK signaling pathway[44]**.**

Although CM, CoM and UM seem to derive from the same cell type (melanocytes), both the disease progression and therapy response is starkly different. Broadly, these cancers are grouped by their driver mutations**:** RAS/RAF for CM and CoM**,** and

GNA_q/GNA_{11} for UM (Figure 5). Oncogenic hyperactivation of these pathways or parts thereof are discussed below (Figure 5).

RAS proteins (H, K and N-RAS) are pleotropic intracellular factors that regulate pathways required for proliferation and cell survival. Dysregulation of this proto-oncogene hyperactivates these pathways and drives oncogenic transformation. RAS proteins are G-proteins possessing an intrinsic GTPase activity. The GTP-bound state is the active state and is regulated by GEFs (Guanine nucleotides exchange factors) and GAPs (GTPase activating proteins). Hyperactivating mutations in RAS proteins result in a higher fraction of the protein in the active, GTP-bound state, thereby enhancing overall RAS and downstream signaling activation. In CM, approximately 27% of all tumors carry an activating RAS mutation (HRAS (6%), KRAS (3%) and NRAS (18%)). In CoM approximately 18-19% bear a RAS mutation, with the vast majority being NRAS mutations[45]. Oncogenic mutations of RAS in UM are generally absent.[46]

In addition, activating mutations in BRAF, a signaling node immediately downstream of RAS in the MAP kinase signal transduction pathway are found in approximately 50% of CMs[47] and 30-36% of CoMs[48]. This constitutively activating mutation is generally driven by a single point mutation. Mutations of the 600th amino acid, a valine, into either glutamine (V600E) or lysine (V600K) make up the vast majority (95%) oncogenic BRAF forms[49]. As with Ras mutations, oncogenic mutations in BRAF are generally absent in UM.[50]

Signaling via PI3K-AKT-mTOR regulates cell survival through downregulation of anti-apoptotic mediators such as, for instance FOXO factors and BAD. This signal transduction pathway relies on the capacity of PI3K to phosphorylate phosphatidylinositol (4,5)-bisphosphate (PI(4,5)P2 or PIP2) generating second messenger (3,4,5)-trisphosphate (PI(3,4,5)P3 or PIP3)[51,52]. The kinases AKT and PDK1, among others, can bind to this phospholipid and are thereby recruited to the cell membrane. AKT becomes phosphorylated and activated and subsequently activate pro-survival pathways and stimulates cell growth.

Tumor suppressor gene, phosphatase and tensin homologue deleted on chromosome 10 (PTEN) works directly to revert the conversion of PIP_2 into PIP_3 and therefore serves as a negative regulator of PI3K signaling.

Direct deregulation of PI3K by mutation is relatively common in UM but is relatively rare in CM (<3%) and is not known in CoM[53]. PTEN inactivation, in contrast, is more prevalent in most melanomas, CM (19%)[54], CoM (14%)[55] whereas in UM a loss of PTEN was reported in 16% of the assessed cases (with as much as 75% UMs showing a loss of heterozygosity)[56].

Another commonly de-regulated signal transduction pathway in cancer is the hippo pathway. One part of this pathway that is commonly hyperactivated is yes associated protein (YAP). YAP and transcriptional co-activator with PDZ-binding motif (TAZ) function as transcription factors in conjunction with interplay with TEADs, driving the expression of pro-survival genes[57]. The majority of the oncogenic functions of YAP/TAZ seem to be regulated through TEADs, although the exact underlying processes are not yet well defined. YAP/TAZ signaling is mainly implicated in the progression of UM, where it is activated through upstream Gq/G11 mutations (see figure 5)[58].

Oncogenesis of UM is largely driven through an inactivating mutation in a protein of the GNA family (GNAq and GNA11), found in approximately 90% of all cases. These mutations block the intrinsic GTPase activity within this catalytic subunit of the protein, effectively locking Gq or G11 in a constitutive active, GTP-bound state, driving oncogenic hyperactivation of Gq/G11 downstream signaling. This hyperactivation leads to a subsequent increase in downstream signaling, including the protein kinase C (PKC)/MAP kinase axis.

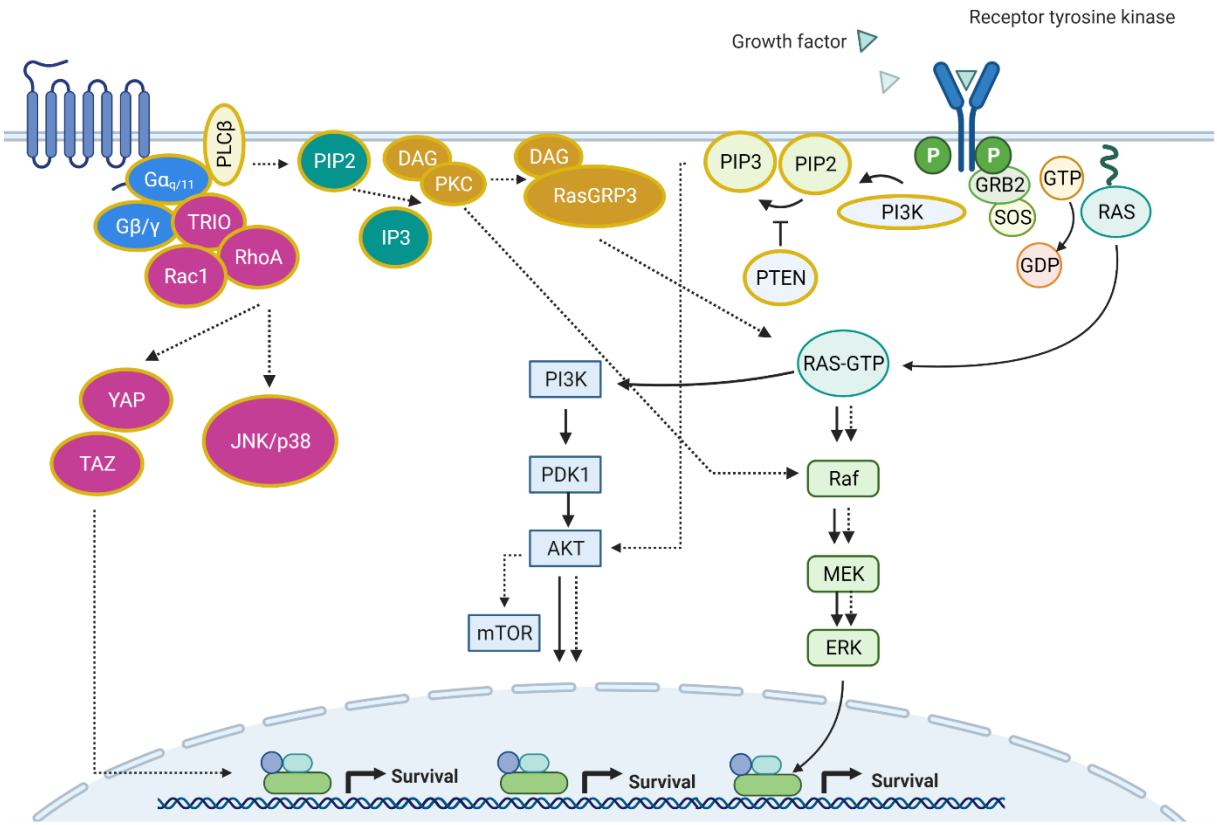

Figure 5. Similarities and differences between common driver mutations in Cutaneous Melanoma, Conjunctival Melanoma and Uveal Melanoma.

UM specific driver mutations constitutively activating $GNA_{q/11}$, upregulating phospholipase Cβ (PLCβ), protein kinase C (PKC) and GTPases RhoA and Rac. Furthermore, in UM an indirect activation of RAS along the PKC-RASGRP3-RAS axis occurs, although this non-canonical activation leads to a variegation of downstream signaling when compared to direct RAS activation. For both cutaneous melanoma (CM) and conjunctival melanoma (CoM) usually a Ras (RAS-RAF-MEK-ERK signaling axis) activation is seen as the predominant driver of oncogenesis, either through receptor tyrosine kinase hyperactivation or through direct mutational activation of RAS or downstream RAF. Either through direct or indirect activation all melanoma types (and most cancers) are dependent of downstream hyperactivation of cell survival pathways PI3K-AKT, AKT-mTOR or RAS-RAF-MEK-ERK signaling cascades. All proteins making up the signaling pathways predominantly hyperactivated in UM are bordered with orange, and the signal transduction routes are shown in dotted arrows. The proteins making up both CM and CoM are outlined in blue and signal transduction routes are shown with unbroken arrows. Adapted from Calses et al 2019, Altomare et al 2005, Chen et al 2017, Davies et al 2002 and Jager et al 2020.

Melanocyte-derived tumors, their underlying biology and melanin biosynthesis.

Cancers deriving from the melanocytes of the skin and the eye are commonly referred to as melanomas. Melanocytes are all thought to derive from a common, neuroectodermal ancestor, and after embryogenesis these cells migrate to the dermis or to the lining of the eye[59,60]. In these tissues they are believed to convey a photoprotective role through biosynthesis of melanin pigments, pheo- and eumelanin[61,62]. Generally, melanin biosynthesis is stimulated by the production of alpha melanocyte-stimulating hormone (αMSH) and its subsequent binding to the melanocortin Receptor 1 (MC1R). After ligand binding the MC1R receptor activates downstream adenyl cyclase (AC), driving up intracellular cyclic AMP (cAMP) levels. Enhanced levels of cAMP activate protein kinase alpha (PKA), which phosphorylates the transcription factor cAMP response element binding protein (CREB), which in turn enhances the transcription of the gene encoding the Microphthalmia-associated transcription factor (MITF). This transcription factor drives the expression of most melanin biosynthetic genes, and confers melanocytic identity to melanocytes (figure 6)[61,63].

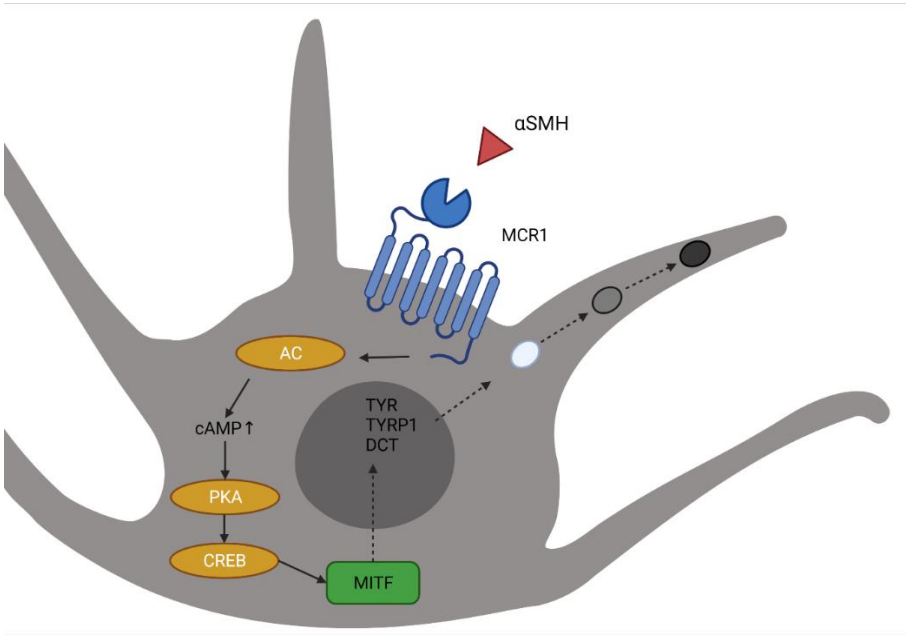

Figure 6. Melanin biosynthesis induction in melanocytes.
In untransformed melanocytes melanin biosynthesis is induced through activation of the MC1R receptor by binding of αMSH. Activation of MC1R drives intracellular activation of AC enhancing intracellular cAMP levels subsequently activation PKA and CREB, leading to MITF activation and translocation to the nucleus. MITF drives the expression of the enzymes required for melanin biosynthesis, TYR, TYRP1 and DCT. Adapted from Itoh et al 2020[64].

Melanin biosynthesis is prevalent in melanocytes as well as melanoma cells, their transformed counterpart. The widespread presence of melanin indicates a biological requirement driving the selection pressure for melanoma biosynthesis. Conversely, melanin biosynthesis is rapidly lost in *in vitro* cultures of melanoma cells. Several scientific publications attribute both anti-migratory and anti-metastatic functions to intracellular melanin[65–67].Paradoxically, within one of the previously mentioned studies, there is experimental evidence that melanin inhibits small scale migration within the primary tumor, while enhancing distant metastasis[65]. Statistical and pathological evidence indicates that higher levels of melanation result in shorter overall survival of CM patients. Taken together we conclude that the biological function of melanin in melanoma cells remains largely unknown.

Treatment options

Treatment of cancer remains highly complex, and is largely dependent on the stage of progression and the location of the specific tumor. This is further complicated by the inherent heterogeneity of tumors and the lack of highly specific markers whereupon treatment can be based[68]. Although several advances in cancer treatment have been made in the past decades, conventional treatment still largely revolves around surgical resection of the tumor, radiation- or chemotherapy, or a combination thereof[69]. With the exception of surgical resection, these treatments function through the induction of DNA damage, whereby faster dividing cells are more susceptible to damage because of its enhanced cell division. In concordance, side effects subsequently arise in untransformed, rapidly dividing tissues as the colonic mucosa or the bone marrow.

To circumvent systemic side effects newly developed drugs generally focus on the development of “personalized medicine” or “targeted chemotherapeutic” approaches as a proposed form of treatment. This approach allows focusing on the underlying molecular characterization of a tumor prior to the treatment[70,71]. For example, vemurafenib showed promising response in clinical trials for the treatment of cutaneous melanoma[72]. This therapeutic works through specific targeting of cells carrying the oncogenic, hyperactivating BRAFV600E mutation in the *BRAF* gene[73]. However, while most patients initially showed significant positive clinical response, they quickly developed vemurafenib-resistant metastases, effectively rendering this targeted therapeutic useless as a single agent treatment[74].

Given the similarities between CM and CoM on a genetic basis, and their relatively large dissimilarity with UM, we will further discuss treatment of CM and UM separately. Due to the comparatively high incidence of CM among melanomas, the largest body of experimental evidence and the most profound advances in therapeutic development have been made for CM. Generally surgical resection along with a wide margin around the affected area is employed, often combined with a sentinel lymph node biopsy to assess the possibility of system dissemination[75]. Upon diagnosis of metastatic dissemination combinations of “conventional” chemotherapeutics, targeted therapies and immunotherapies are currently used for the treatment of CM. Chemotherapeutic treatments mainly employ either DNA damage inducers dacarbazine or temozolomide. Targeted therapies against melanoma focus on RAF-MEK hyperactivation, using

either the mutation specific (BRAFV600E) inhibitor vemurafenib or possibly combined with the MEK inhibitor trametinib[47,76].

Subsequent advances in treatment of CM have come from the development of immune checkpoint inhibitors (ICI's) blocking tumor protective activities of specific T-cell ligands such as PD-1 (nivolumab and pembrolizumab) or through the blocking of CTLA-4 (ipilimumab). These antibody-based therapies focus on the activation of the host's intrinsic adaptive immune system that has been undermined during tumor development, effective re-instating host defense. These ICI's use antibodies to block the extracellular binding of either PD1 to PDL1 or CTLA4, driving the release of cytotoxic granules containing perforin and granzyme B release from the bound T-Cell, resulting in cancer cells destruction[77]. Given the overt similarities between CM and CoM many treatment options that have been proven to be clinically effective for the treatment of CM can or could be adapted for the treatment for CoM[78,79]. Strikingly, these apparent similarities in treatment response between CM and CoM do not directly translate to effective advancements in the treatment of CoM, possibly due to the low amount of clinical trials dedicated to CoM[78].

Uveal melanoma can be seen as a rare and genetically distinct subclass of melanoma and can be considered as a separate disease entity[80]. Therefore, UM is treated vastly differently from both CM and CoM. Given the discrete intra-ocular localization of this tumor the general first line treatment entails either (localized) radiation therapy or teletherapy. Alternatively complete surgical removal of the eye (enucleation), or eye-sparing treatment options are combined with radiation therapies[81–83]. Although first line treatments are generally effective, a large proportion (approximately 50%) of patients diagnosed with UM develop metastases[84]. The vast majority of UM metastasizes to the liver and there are currently no standardized treatment options for metastatic UM. Both prior treatment of primary UM and following experimental treatments of metastatic UM have not significantly enhanced patient survival[84]. All clinical trials to date that have assessed the efficacy of targeted therapies on metastatic uveal melanomas have been unsuccessful, or have been withdrawn due to intolerable side-effects[85].

Zebrafish models for metastatic melanoma and the elucidation of novel drivers of the metastatic process.

The highly complex nature of the metastatic process carries inherent difficulty to recapitulate metastasis using *in vitro* models, and in *in vivo* models the latter stages of the metastatic cascade are difficult to track. In that sense, both the semi-random nature and the difficulty to track cells during metastasis greatly limits basic research in metastatic dissemination.

The study of metastasis in murine models, generally cutaneous melanoma, has been one of the foundation stones of metastasis research. However, the use of bioluminescent imaging techniques in murine xenograft models limits spatial resolution, and yields no information of the surroundings of the metastatic colony. Both genetically engineered mouse (GEM) models and graft models (syn-, allo- and xenograft, Figure 7) have been developed for the study of metastatic spread. GEM models in general entail the overexpression and knock-down of several pro-tumorigenic factors, that eventually lead to the spontaneous formation of tumors. Although this is a highly powerful method to study the formation of primary tumors, its unpredictable nature does not make it very suitable for the study of metastatic dissemination.

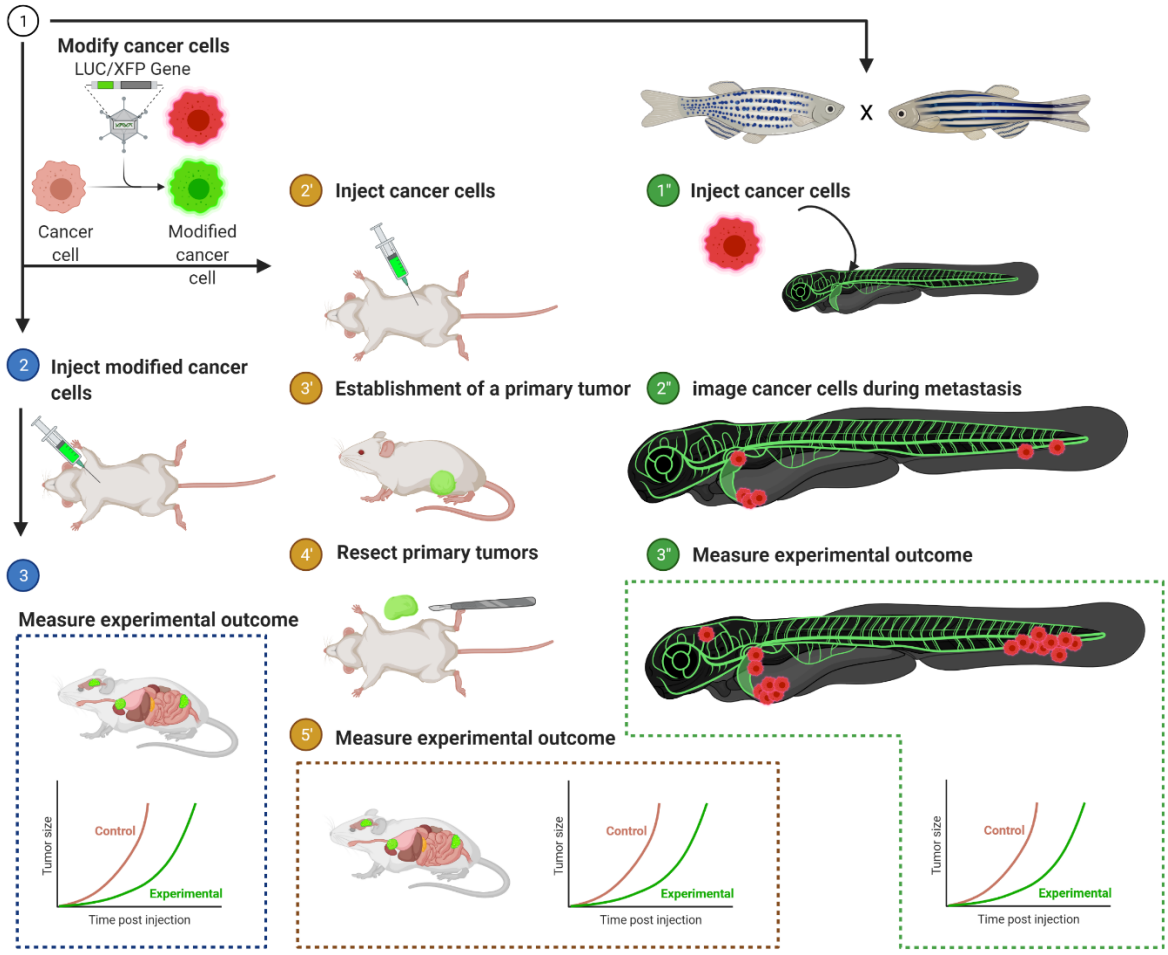

Figure 7. Schematic overview of conventional vertebrate metastasis models.

1) Modification of the engrafted cells, prior to engraftment, with either a bioluminescent reporter (Luciferase or similar proteins) and/or a fluorescent protein (XFP). Murine systemic engraftment models (delineated in blue) 1-3) intra-cardiac injection of cancer cells, allowing for quick and systemic dissemination of the engrafted cancer cells. During the time prior to the ethical endpoint of the experiment, the efficacy of cell mutations (knock-out, knock-down or overexpression) or experimental treatment efficiency can be assesed. Spontaneous metastasis models (1'-5'), utilize a similar approach but instead of directly injecting cancer cells into the blood circulation the cancer cells are first injected either sub-cutaneously, or orthotopically whenever possible. After the primary tumor reaches a pre-set diameter (before the ethical endpoint of the experiment) the primary tumor is removed surgically and the previously established spontaneous metastatic colonies are left to develop. The assessment of the effect of drugs or cell instrinsic alterations can be assessed much in a similar manner to the cardiac-injection model. Zebrafish xenografts (1"-3") allow for the injection of cells, directly into the circulation, mostly utilizing XFP based labels for the tracking of metastatic cells, in a similar manner as is commonly used for the murine cardiac-injection model.

Most of the models used for metastatic research employ fluorescent labeled cells, injected through either the tail vein or through intra-cardiac injection. This direct hematogenous injection allows for the delivery and immediate dissemination of high amounts of cancer cells, making it rapid and relatively tractable. The major downside of this method is the removal of the first stage of the metastatic cascade (intravasation) and, therefore, does not faithfully recapitulate the entire metastatic cascade. More advanced engraftment models are injected subcutaneously or orthotopically, after allowing the tumor to develop the primary growth is resected, followed by a second incubation period allowing for the establishment of distant metastatic lesions.

The zebrafish (*Danio rerio*) xenograft models as first described by Lee and colleagues in 2005 highlighted the possibility of using the zebrafish as a cancer model[86]. Since the advent of this model many variations have been proposed and rigorously assessed. Through a combination of different cancer types and injection sites we can generate discrete models for the study of primary tumor and metastasis formation. Using the zebrafish as a cancer model, we can overcome some of the challenges that hamper metastasis research. The zebrafish is hallmarked by transparent tissue architecture in its larval developmental stages. Therefore, we can use this as a model to observe the metastatic cascade from its mid- to late stages (Figure 5). Combining transgenic fluorescent zebrafish reporter lines for metastatic organs or blood vessels, we are able to closely study the complex and difficult to visualize processes of metastasis with relative ease. Moreover, the zebrafish is amenable to semi-high throughput implantation and analysis. This enables the rapid screening of compounds or the validation of the effects of genetic perturbations on the metastatic process. Taken together, the zebrafish model is an excellent platform for the study of the metastatic process and allows the tracking of metastatic cells with high spatial and temporal resolution.

In addition, the zebrafish larvae model allows for upscaling of *in vivo* analyses. Where normally a drug efficacy test *in vitro* would be performed in triplicate or quadruplicate, using zebrafish larvae we are easily capable of measuring the effect of compounds, *in vivo*, in multiples of 20 larvae per condition. In the future, development of this platform with stable, functional reporters (cell death and cell cycle reporters, etc.) integrated into the implanted cells will allow for functional readouts of the effects of drugs on implanted cells (i.e., cell cycle progression, cell death, cytoskeletal and vesicular

dynamics, etc.). Combining these models with further validation using patient derived material, generating zebrafish patient-derived xenografts (zfPDX) and experimental validation in murine models should allow cancer biologists not only to gain new insights into the biology of metastatic cancers, but also to expedite drug and therapy development through pre-screening in the zebrafish xenograft of zfPDX model.

Thesis outline

Chapter 1 provides a general introduction into cancer biology, pathogenesis and treatments, and particularly highlights cutaneous, conjunctival and uveal melanoma.

In **Chapter 2** we outline the establishment of an orthotopic zebrafish model and its use for the assessment of the efficacy of novel (targeted) cancer therapeutics. Subsequently, we give a detailed description of the methodology to generate not only metastatic tumors, but primary orthotopic eye tumors. We describe in great detail the overall methodology – starting with a novel cell line, transducing this cell line with lentiviral markers, and determining its suitability in the zebrafish xenograft model. Subsequently, we recapitulate the efficacy of a known effective inhibitor (Vemurafenib) on engrafted zebrafish, and discuss the potential pitfalls that are to be avoided while using this model.

In **Chapter 3** we use the zebrafish model for the efficacy assessment of BRAFV600E specific inhibitor Vemurafenib on conjunctival melanoma. We validate, using this novel model, the inhibitory action of Vemurafenib on conjunctival melanoma. By establishing this model, we generate a semi-high throughput screening model for the determination of drug efficacy in conjunctival melanoma, a rare cancer in dire need of an elaboration of its treatment options.

In **Chapter 4** we established patient derived spheroid cultures of uveal melanoma, the most prevalent and deadly tumor of the eye. Using the previously described zebrafish xenograft model (Chapter 2 and 3), the tumorigenic capacity of these cultures was assessed in comparison with “conventional” adherent cultures, and determined the reason underlying the loss of tumorigenic potential inherent to, most if not all, available uveal melanoma cell lines. We hypothesized that the underlying, cell autonomous, mechanism of cell death during uveal melanoma metastasis could be driven by reactive oxygen species (ROS). After analysis of patient survival databases, we

determined that high expression of ferroptosis related genes (*GPX4, SLC7A11*) significantly correlated with a decrease in disease-free survival. Subsequently we assessed the cell killing potential *in vivo* by ferroptosis induction. Ferroptosis is a recently discovered, ROS-based, iron-dependent cell death mechanism, initially shown to be effective in mutant RAS driven tumors. Experimental induction of ferroptosis was shown to be effective in reducing experimental uveal melanoma metastasis in Bap1 loss patient derived zfPDX.

In **Chapter 5** we investigate the inclusion of melanin in melanoma cells and the role that melanin plays on the negation of intracellular ROS and its effect on melanoma metastatic potential. We observed that inclusion of melanin in uveal melanoma correlates positively with engraftment rates in zebrafish xenografts. We determined, using both pathological data assigning melanin levels and transcriptional data, that the transcriptional activity of melanin biosynthesis and the overt presence of melanin significantly correlates with reduced disease-free survival in uveal melanoma patients. Subsequently we assessed the effect of melanin depletion on metastatic colonization of cutaneous melanoma in zebrafish model. We concluded that melanin depletion significantly reduces metastatic colonization, while maintaining cell migration capacity. We determined that inclusion of melanin and expression of tyrosinase related protein 1 (*TYRP1*) correlates with tumorigenic capacity in all melanocyte-derived melanomas (conjunctival, cutaneous, and uveal) in the zebrafish xenograft model. Following, we established a co-culture model to transfer melanin into non-melanated uveal melanoma and showed that re-introduction of melanin into uveal melanoma significantly enhances metastatic capacity. Finally, we showed that melanin levels increase resistance to reactive oxygen (ROS) induction both *in vitro* and *in vivo.* We showed that ferroptosis (ROS-based cell death mechanism) induction was affected *in vivo*, inversely correlating with intracellular melanin levels in conjunctival and cutaneous melanoma.

In **Chapter 6** we describe an open access, zebrafish xenograft data sharing platform for the Xenograft phenotype interactive repository (Xephir.org). This dissemination platform allows for the quick and visual determination of a xenograft suitability to a certain scientific question. Through this platform we strive to enhance visibility, accessibility, reproducibility and the overall popularity of the zebrafish xenograft model.

Finally in **Chapter 7** we summarize and discuss the preceding chapters, highlight our findings in the context of general cancer biology and provide an outlook for the implementation of our work in future research and its translation to future treatment of (uveal) melanoma patients.

References

1. Bray, F., Laversanne, M., Weiderpass, E. & Soerjomataram, I. The ever-increasing importance of cancer as a leading cause of premature death worldwide. *Cancer* **0**, 2021 (2021).

2. Chambers, A. F., Groom, A. C. & MacDonald, I. C. Dissemination and growth of cancer cells in metastatic sites. *Nat. Rev. Cancer* **2**, 563–572 (2002).

3. Luzzi, K. J. *et al.* Multistep nature of metastatic inefficiency: dormancy of solitary cells after successful extravasation and limited survival of early micrometastases. *Am. J. Pathol.* **153**, 865–73 (1998).

4. Slaughter, D. P., Southwick, H. W. & Smejkal, W. “Field cancerization” in oral stratified squamous epithelium. Clinical implications of multicentric origin. *Cancer* **6**, 963–968 (1953).

5. Joyce, J. a & Pollard, J. W. Microenvironmental regulation of metastasis. *Nat. Rev. Cancer* **9**, 239–252 (2009).

6. Fares, J., Fares, M. Y., Khachfe, H. H., Salhab, H. A. & Fares, Y. Molecular principles of metastasis: a hallmark of cancer revisited. *Signal Transduction and Targeted Therapy* vol. 5 1–17 (2020).

7. Gupta, G. P. & Massagué, J. Cancer Metastasis: Building a Framework. *Cell* vol. 127 679–695 (2006).

8. Cowell, C. F. *et al.* Progression from ductal carcinoma in situ to invasive breast cancer: Revisited. *Mol. Oncol.* (2013) doi:10.1016/j.molonc.2013.07.005.

9. Eddy, K., Shah, R. & Chen, S. Decoding Melanoma Development and Progression: Identification of Therapeutic Vulnerabilities. *Frontiers in Oncology* vol. 10 3357 (2021).

10. Knudson, A. G. Two genetic hits (more or less) to cancer. *Nat. Rev. Cancer* **1**, 157–162 (2001).

11. Chung, C. H., Bernard, P. S. & Perou, C. M. Molecular portraits and the family tree of cancer. *Nat. Genet.* **32 Suppl**, 533–540 (2002).

12. Fujiwara, T. *et al.* Cytokinesis failure generating tetraploids promotes tumorigenesis in p53-null cells. *Nature* **437**, 1043–1047 (2005).

13. Williams, B. R. *et al.* Aneuploidy affects proliferation and spontaneous immortalization in mammalian cells. *Science (80-.).* **322**, 703–709 (2008).

14. Holland, A. J. & Cleveland, D. W. Boveri revisited: Chromosomal instability, aneuploidy and tumorigenesis. *Nature Reviews Molecular Cell Biology* vol. 10 478–487 (2009).

15. Lengauer, C., Kinzler, K. W. & Vogelstein, B. Genetic instabilities in human cancers. *Nature* vol. 396 643–649 (1998).

16. Holohan, C., Van Schaeybroeck, S., Longley, D. B. & Johnston, P. G. Cancer drug resistance: an evolving paradigm. *Nat. Rev. Cancer* **13**, 714–26 (2013).

17. Meacham, C. E. & Morrison, S. J. Tumour heterogeneity and cancer cell plasticity. *Nature* vol. 501 328–337 (2013).

18. Hanahan, D. & Weinberg, R. A. The Hallmarks of Cancer. *Cell* **100**, 57–70 (2000).

19. Hanahan, D. & Weinberg, R. A. Hallmarks of cancer: the next generation. *Cell* **144**, 646–674 (2011).

20. Birkeland, E. *et al.* Patterns of genomic evolution in advanced melanoma. *Nat. Commun.* **9**, 1–12 (2018).

21. Shain, A. H. *et al.* The genetic evolution of metastatic uveal melanoma. *Nat. Genet.* **51**, 1123–1130 (2019).

22. Shain, A. H. *et al.* The Genetic Evolution of Melanoma from Precursor Lesions. *N. Engl. J. Med.* **373**, 1926–1936 (2015).

23. S, P. The distribution of secondary growths in cancer of the breast. 1889. *Cancer Metastasis Rev.* **8**, 98–101 (1989).

24. Dhasarathy, A., Phadke, D., Mav, D., Shah, R. R. & Wade, P. a. The transcription factors Snail and Slug activate the transforming growth factor-beta signaling pathway in breast cancer. *PLoS One* **6**, e26514 (2011).

25. Katsuno, Y., Lamouille, S. & Derynck, R. TGF-β signaling and epithelial-mesenchymal transition in cancer progression. *Curr. Opin. Oncol.* **25**, 76–84 (2013).

26. Thiery, J. P., Acloque, H., Huang, R. Y. J. & Nieto, M. A. Epithelial-mesenchymal transitions in development and disease. *Cell* **139**, 871–890 (2009).

27. Geiger, T. R. & Peeper, D. S. Metastasis mechanisms. *Biochim. Biophys. Acta - Rev. Cancer* **1796**, 293–308 (2009).

28. Massagué, J. TGFβ signalling in context. *Nat. Rev. Mol. Cell Biol.* **13**, 616–630 (2012).

29. Gunasinghe, N. P. A. D., Wells, A., Thompson, E. W. & Hugo, H. J. Mesenchymal-epithelial transition (MET) as a mechanism for metastatic colonisation in breast cancer. *Cancer Metastasis Rev.* **31**, 469–478 (2012).

30. Paizal, J. P., Au, S. H. & Bakal, C. Squeezing through the microcirculation: survival adaptations of circulating tumour cells to seed metastasis. *Br. J. Cancer 2020 1241* **124**, 58–65 (2020).

31. Azevedo, A. S., Follain, G., Patthabhiraman, S., Harlepp, S. & Goetz, J. G. Metastasis of circulating tumor cells: Favorable soil or suitable biomechanics, or both? *Cell Adh. Migr.* **9**, 345 (2015).

32. FL, M., FL, P., KL, van G. & CR, C. Stepping out of the flow: capillary extravasation in cancer metastasis. *Clin. Exp. Metastasis* **25**, 305–324 (2008).

33. Piskounova, E. *et al.* Oxidative stress inhibits distant metastasis by human melanoma cells. *Nature* **527**, 186–191 (2015).

34. Massagué, J. & Obenauf, A. C. Metastatic colonization by circulating tumour cells. *Nature* vol. 529 298–306 (2016).

35. Ali, Z., Yousaf, N. & Larkin, J. Melanoma epidemiology, biology and prognosis. *EJC Suppl.* **11**, 81 (2013).

36. Paulson, K. G. *et al.* Age-Specific Incidence of Melanoma in the United States. *JAMA Dermatology* **156**, 57–64 (2020).

37. Kaliki, S. & Shields, C. L. Uveal melanoma: relatively rare but deadly cancer. *Eye 2017 312* **31**, 241–257 (2016).

38. Missotten, G. S., Keijser, S., Keizer, R. J. W. De & Wolff-Rouendaal, D. De. Conjunctival Melanoma in The Netherlands: A Nationwide Study. *Invest. Ophthalmol. Vis. Sci.* **46**, 75–82 (2005).

39. Sandru, A., Voinea, S., Panaitescu, E. & Blidaru, A. Survival rates of patients with metastatic malignant melanoma. *J. Med. Life* **7**, 572 (2014).

40. Lane, A. M., Kim, I. K. & Gragoudas, E. S. Survival rates in patients after treatment formetastasis from uveal melanoma. *JAMA Ophthalmol.* **136**, 981–986 (2018).

41. Noonan, F. P. *et al.* Melanoma induction by ultraviolet A but not ultraviolet B radiation requires melanin pigment. *Nat. Commun. 2012 31* **3**, 1–10 (2012).

42. CC, M. *et al.* Incidence of noncutaneous melanomas in the U.S. *Cancer* **103**, 1000–1007 (2005).

43. AD, S., ME, T. & AK, T. Uveal melanoma: trends in incidence, treatment, and survival. *Ophthalmology* **118**, 1881–1885 (2011).

44. Cisarova, K. *et al.* Genomic and transcriptomic landscape of conjunctival melanoma. *PLoS Genet.* **16**, (2020).

45. Wong, J. R., Nanji, A. A., Galor, A. & Karp, C. L. Management of conjunctival malignant melanoma: A review and update. *Expert Review of Ophthalmology* vol. 9 185–204 (2014).

46. Chen, X. *et al.* RasGRP3 Mediates MAPK Pathway Activation in GNAQ Mutant Uveal Melanoma. *Cancer Cell* **31**, 685-696.e6 (2017).

47. Long, G. V. *et al.* Combined BRAF and MEK Inhibition versus BRAF Inhibition Alone in Melanoma. *N. Engl. J. Med.* **371**, 1877–1888 (2014).

48. Gear, H., Williams, H., Kemp, E. G. & Roberts, F. BRAF Mutations in Conjunctival Melanoma. *Invest. Ophthalmol. Vis. Sci.* **45**, 2484–2488 (2004).

49. Davies, H. *et al.* Mutations of the BRAF gene in human cancer. *Nat. 2002 4176892* **417**, 949–954 (2002).

50. Y, C. *et al.* Lack of BRAF mutation in primary uveal melanoma. *Invest. Ophthalmol. Vis. Sci.* **44**, 2876–2878 (2003).

51. Hoxhaj, G. & Manning, B. D. The PI3K–AKT network at the interface of oncogenic signalling and cancer metabolism. *Nat. Rev. Cancer 2019 202* **20**, 74–88 (2019).

52. Altomare, D. A. & Testa, J. R. Perturbations of the AKT signaling pathway in human cancer. *Oncogene 2005 2450* **24**, 7455–7464 (2005).

53. MOULIN, A., BUCHER, M., SCHALENBOURG, A. & NICOLAS, M. MAP kinase and pi3k/mTOR pathways involvement in tumor progression of conjunctival melanocytic proliferations. *Acta Ophthalmol.* **92**, 0–0 (2014).

54. Goel, V. K., Lazar, A. J. F., Warneke, C. L., Redston, M. S. & Haluska, F. G. Examination of Mutations in BRAF, NRAS, and PTEN in Primary Cutaneous Melanoma. *J. Invest. Dermatol.* **126**, 154–160 (2006).

55. Poppelen, N. M. van *et al.* Molecular Genetics of Conjunctival Melanoma and Prognostic Value of TERT Promoter Mutation Analysis. *Int. J. Mol. Sci. 2021, Vol. 22, Page 5784* **22**, 5784 (2021).

56. Abdel-Rahman, M. H. *et al.* High Frequency of Submicroscopic Hemizygous Deletion Is a Major Mechanism of Loss of Expression of PTEN in Uveal Melanoma. *J Clin Oncol* **24**, 288–295 (2006).

57. Calses, P. C., Crawford, J. J., Lill, J. R. & Dey, A. Hippo Pathway in Cancer: Aberrant Regulation and Therapeutic Opportunities. *Trends in Cancer* **5**, 297–307 (2019).

58. FX, Y. *et al.* Mutant Gq/11 promote uveal melanoma tumorigenesis by activating YAP. *Cancer Cell* **25**, 822–830 (2014).

59. Cichorek, M., Wachulska, M., Stasiewicz, A. & Tymińska, A. Skin melanocytes: biology and development. *Adv. Dermatology Allergol. Dermatologii I Alergol.* **30**, 30 (2013).

60. RL, M., IJ, J. & EE, P. The melanocyte lineage in development and disease. *Development* **142**, 620–632 (2015).

61. Maranduca, M. A. *et al.* Synthesis and physiological implications of melanic pigments. *Oncol. Lett.* **17**, 4183 (2019).

62. Brenner, M. & Hearing, V. J. The Protective Role of Melanin Against UV Damage in Human Skin. *Photochem. Photobiol.* **84**, 539 (2008).

63. D'Alba, L. & Shawkey, M. D. Melanosomes: Biogenesis, properties, and evolution of an ancient organelle. *Physiological Reviews* vol. 99 1–19 (2019).

64. Itoh, T., Fukatani, K., Nakashima, A. & Suzuki, K. MicroRNA-141-3p and microRNA-200a-3p regulate α-melanocyte stimulating hormone-stimulated melanogenesis by directly targeting microphthalmia-associated transcription factor. *Sci. Reports 2020 101* **10**, 1–11 (2020).

65. Pinner, S. *et al.* Intravital imaging reveals transient changes in pigment production and Brn2 expression during metastatic melanoma dissemination. *Cancer Res.* **69**, 7969–7977 (2009).

66. Sarna, M., Krzykawska-Serda, M., Jakubowska, M., Zadlo, A. & Urbanska, K. Melanin presence inhibits melanoma cell spread in mice in a unique mechanical fashion. *Sci. Rep.* **9**, 1–9 (2019).

67. AA, B., W, J., JA, C. & AT, S. Melanogenesis affects overall and disease-free survival in patients with stage III and IV melanoma. *Hum. Pathol.* **44**, 2071–2074 (2013).

68. Dagogo-Jack, I. & Shaw, A. T. Tumour heterogeneity and resistance to cancer therapies. *Nature Reviews Clinical Oncology* vol. 15 81–94 (2018).

69. DeVita, V. T. & Chu, E. A history of cancer chemotherapy. *Cancer Research* vol. 68 8643–8653 (2008).

70. Sawyers, C. Targeted cancer therapy. *Nature* vol. 432 294–297 (2004).

71. Gray-Schopfer, V., Wellbrock, C. & Marais, R. Melanoma biology and new targeted therapy. *Nature* vol. 445 851–857 (2007).

72. Chapman, P. B. *et al.* Improved Survival with Vemurafenib in Melanoma with BRAF V600E Mutation. *N. Engl. J. Med.* **364**, 2507–2516 (2011).

73. Tsai, J. *et al.* Discovery of a selective inhibitor of oncogenic B-Raf kinase with potent antimelanoma activity. *Proc. Natl. Acad. Sci. U. S. A.* **105**, 3041–3046 (2008).

74. Wilson, T. R. *et al.* Widespread potential for growth-factor-driven resistance to anticancer kinase inhibitors. *Nature* **487**, 505–509 (2012).

75. Michielin, O. *et al.* ESMO consensus conference recommendations on the management of locoregional melanoma: under the auspices of the ESMO Guidelines Committee. *Ann. Oncol.* **31**, 1449–1461 (2020).

76. Robert, C. *et al.* Improved Overall Survival in Melanoma with Combined Dabrafenib and Trametinib. *N. Engl. J. Med.* **372**, 30–39 (2015).

77. Seidel, U. J. E., Schlegel, P. & Lang, P. Natural killer cell mediated antibody-dependent cellular cytotoxicity in tumor immunotherapy with therapeutic antibodies. *Frontiers in Immunology* vol. 4 76 (2013).

78. Grimes, J. M., Shah, N. V., Samie, F. H., Carvajal, R. D. & Marr, B. P. Conjunctival Melanoma: Current Treatments and Future Options. *Am. J. Clin. Dermatology 2020 213* **21**, 371–381 (2020).

79. Damato, B. & Coupland, S. E. Management of conjunctival melanoma. *http://dx.doi.org/10.1586/era.09.85* **9**, 1227–1239 (2014).

80. Kooij, M. K. van der, Speetjens, F. M., Burg, S. H. van der & Kapiteijn, E. Uveal Versus Cutaneous Melanoma; Same Origin, Very Distinct Tumor Types. *Cancers (Basel).* **11**, (2019).

81. Dogrusöz, M., Jager, M. J. & Damato, B. Uveal melanoma treatment and prognostication. *Asia-Pacific Journal of Ophthalmology* vol. 6 186–196 (2017).

82. Yang, J., Manson, D. K., Marr, B. P. & Carvajal, R. D. Treatment of uveal melanoma: where are we now? *Therapeutic Advances in Medical Oncology* vol. 10 (2018).

83. Damato, B. & Coupland, S. E. Translating uveal melanoma cytogenetics into clinical care. *Arch. Ophthalmol.* **127**, 423–429 (2009).

84. Rantala, E. S., Hernberg, M. & Kivelä, T. T. Overall survival after treatment for metastatic uveal melanoma: a systematic review and meta-analysis. *Melanoma Res.* **29**, 561–568 (2019).

85. Croce, M., Ferrini, S., Pfeffer, U. & Gangemi, R. Targeted Therapy of Uveal Melanoma: Recent Failures and New Perspectives. *Cancers 2019, Vol. 11, Page 846* **11**, 846 (2019).

86. Lee, L. M. J., Seftor, E. A., Bonde, G., Cornell, R. A. & Hendrix, M. J. C. The fate of human malignant melanoma cells transplanted into zebrafish embryos: Assessment of migration and cell division in the absence of tumor formation. *Dev. Dyn.* **233**, 1560–1570 (2005).

Chapter 2:

Ortho- and ectopic zebrafish xeno-engraftment of ocular melanoma to recapitulate primary tumor and experimental metastasis development.

Chapter 2: Ortho- and ectopic zebrafish xeno-engraftment of ocular melanoma to recapitulate primary tumor and experimental metastasis development.

Arwin Groenewoud[1], Jie Yin[1], B.E Snaar-Jagalska[*]

1) Institute of Biology, Leiden University, Leiden, The Netherlands

* Corresponding author: Prof Dr B.E. Snaar-Jagalska, Institute of Biology, PO Box 9502, Leiden University, Leiden, The Netherlands

E Mail: b.e.snaar-jagalska@biology.leidenuniv.nl

Published as: *Groenewoud, A., Yin, J., Snaar-Jagalska, B.E.*
Ortho- and Ectopic Zebrafish Xeno-Engraftment of Ocular Melanoma to Recapitulate Primary Tumor and Experimental Metastasis Development. J. Vis. Exp. (175), e62356DOI: 10.3791/62356

Summary:

Here, we present a protocol to establish versatile orthotopic and ectopic zebrafish xenograft models for ocular melanoma to assess the growth kinetics of the primary tumor, dissemination, extravasation and distant, peri-vascular metastasis formation and the effect of chemical inhibition thereon.

Abstract:

There are currently no animal models for metastatic ocular melanoma. The lack of metastatic disease models has greatly hampered the research and development of novel strategies for the treatment of metastatic ocular melanoma. In this protocol we delineate a quick and efficient way to generate embryonic zebrafish models for both the primary and disseminated stage of ocular melanoma, using retro-orbital orthotopic and intravascular ectopic cell engraftment, respectively. Combining these two different engraftment strategies we can recapitulate the etiology of cancer in its totality, progressing from primary, localized tumor growth under the eye to a peri-vascular metastasis formation in the tail. These models allow us to quickly and easily modify the cancer cells prior to implantation with specific labeling, genetic or chemical interference; and to treat the engrafted hosts with (small molecular) inhibitors to attenuate tumor development.

Here we describe the generation and quantification of both orthotopic and ectopic engraftment of ocular melanomas (conjunctival and uveal melanoma) using fluorescently labelled stable cell lines. This protocol is also applicable for engraftment of primary cells derived from patient biopsy and patient/PDX derived material (manuscript in preparation). Within hours post engraftment cell migration and proliferation can be visualized and quantified. Both tumor foci are readily available for imaging with both epifluorescence microscopy and confocal microscopy. Using these models, we can confirm or refute the activity of either chemical or genetic inhibition strategies within as little as 8 days after the onset of the experiment, allowing not only highly efficient screening on stable cell lines, but also enables patient directed screening for precision medicine approaches.

Introduction:

Metastatic dissemination is considered the main cause of death of ocular melanoma, currently there is no viable treatment regime for disseminated ocular melanoma[1,2]. Furthermore, there are no animal models available for ocular melanoma that reflects the metastatic disease. To bridge this gap, we generated two distinct zebrafish models that recapitulate either primary tumor formation or the early stages of metastatic dissemination, thus readily allowing the study of these normally difficult to study processes [3]. The micro-metastasis models allow the analysis of the last phases of metastatic spread, including homing, colonization and extravasation. Genetic or chemical interventions at this stage and beyond could potentially provide a powerful handhold in the treatment of metastatic ocular melanoma.

The use of the zebrafish larvae as a recipient of xeno- and allografts is supported by the intrinsic strengths of this species, such as its optical transparency at the early stages of development (or its entire life-cycle for *casper* mutants[4]), high fecundity and *ex utero* fertilization[5]. High transcriptional homology in vertebrates ensures the retention of core signaling mechanisms between the zebrafish and humans and therefore high potential translatability of results [6], although genetic approaches are sometimes marred or complicated due to the teleost genome duplication [7]. Recent developments have underscored the importance of zebrafish xenograft models as pre-clinical “avatars” of human disease[8], effectively yielding a multitude of personalized cancer therapy models for the pre-clinical evaluation of treatment strategies from a single zebrafish experiment [9].

Considering the lack of animal models and the concordant lack of treatment options for metastatic ocular melanoma, our models provide a quick and easy translational platform to screen both genetic alterations (cancer cell intrinsic) or develop chemical intervention strategies in a pre-clinical setting. Within the same model we can visualize and measure cancer cell growth kinetics, engraftment rate/metastatic potential, and cell homing on a whole animal level using low level magnification in a stereo fluorescent microscope, and make similar measurements using medium or high magnification confocal microscopic analysis to dissect different steps of ocular melanoma progression at subcellular resolution[10].

Here, we describe comprehensive and detailed protocols for: the generation of fluorescently labeled cancer cells using highly optimized lentiviral transduction.[11]

Subsequent intravenous and retro-orbital (RO) engraftments of these cells into 2 days post fertilization (dpf) zebrafish larvae to generate ectopic and orthotopic models respectively. Followed by data acquisition and analysis. These methods although comprehensive for the applications described herein can be modified to engraft cells in the hind brain cavity, liver and perivitellin space when required (solely by changing the injection site, or time of injection)[12,13].

As a proof-of-concept we elaborated upon the findings of Pontes et al 2018, where we showed a dose and cell intrinsic mutation specific response of conjunctival melanoma cell lines in the zebrafish model [14]. We elaborated upon these findings by showing the efficacy of BRAF V600E mutation-specific inhibitor vemurafenib in both metastatic and primary conjunctival melanoma models.

Ethics statement:

All animal experiments were approved by Animal Experiments Committee (Dier Experimenten Commissie, D.E.C.) under license AVD1060020172410. All animal were maintained in accordance with local guidelines using standard protocols (www.ZFIN.org)

Protocol:

Preparation:

1.1. **Agarose Dish**

Note: When using dishes that have been stored for a long time make sure to add a small volume of egg water to the dishes before starting injection (this will prevent the fish from drying out too fast).

1.1.1. Prepare 1.5% (w/v) agarose coated dishes (agarose dissolved in egg water).

1.1.2. Use immediately, or store at 4°C in inverted position.

2. **Needles:**

Note: Make sure that the capillaries have been calibrated on the filament you are using, when you switch either filament or capillary you should determine the ramp value of the capillaries on the filament you are using (see needle puller manual).

2.1.1. One glass capillary will yield two micro injection needles. Before making needles check the structural integrity of the filament (2,5mm box filament, Science product, Hofheim, Germany) of the needle puller (P97 or P1000 Micropipette puller, Sutter, Novato, U.S.A).

2.1.2. Make sure that both filament and capillary are calibrated to get the corresponding ramp value. When the filaments structural integrity is compromised i.e. (uneven, holes, molten etc.) change the filament.

2.1.3. Use the following program (Needle #99, Heat=ramp+15, pull=95, velocity=60, time=90). Store the needles in a designated Petri dish (containing either clay or tape to stick the needles to)

3. **Generation of lentiviral particles**

Note: To prevent a waste of time and resources a quick tumorigenicity check can be performed prior to lentiviral transduction. This is done to ensure that the cell line to be used is sufficiently tumorigenic in the zebrafish model, to this end the cells can be stained with a CMdiI (or

analogous tracer) as described in Liverani et al 2017 [15]

3.1. Plate HEK 293t (ATCC, USA) cells one day prior transfection to achieve a confluency of approximately 70% (routinely done by splitting a full flask to the same volume culture flask at a dilution 1:3 one day prior).

3.2. At the day of transfection the required packaging plasmids psPAX2 and pMD2.G viral envelope expressing plasmid (both psPAX2 and pMD2.G were gifted by Didier Trono (Addgene plasmid #12260 and #12259 respectively) are co-transfected along with either a GFP (Plasmid #106172) or tdTomato (Plasmid #106173) encoding transfer plasmid, exact amount of plasmid used is specified in table 1.

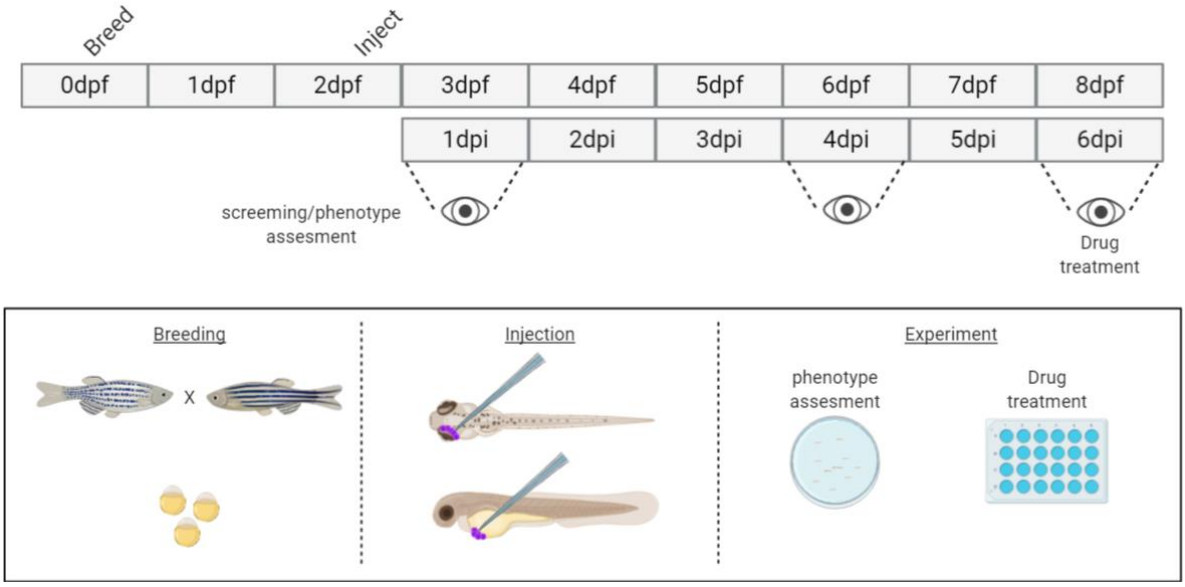

Figure 1. Schematic representation of the described zebrafish engraftment system. A) The timeline of the approach, with breeding the zebrafish at day 0 (B1), here the fish are harvested in the morning after crossing the fish (day 1). After 48-54 hours the fish have largely hatched (shedding their chorion) and the fish are injected (retro-orbitally or systemically, B2) after cleaning the water of the chorion debris (day 2), the larvae are subsequently screened using a stereo fluorescent microscope and all larvae displaying unwanted phenotypes are discarded (day 3). Depending on the goal of the experiment either the larvae are imaged over time (B3, engraftment kinetics, imaged at 1-, 4- and 6-days post injection (dpi)) or the fish are randomized and entered into experimental groups, treated with drugs and compared to vehicle control (drug screening, imaged at 6dpi).

3.3. Mix all plasmids together in 500 µL serum free medium, to allow complete mixing of all plasmids. Add 32 µL LipoD293 reagent to 500 µL serum-free DMEM, vortex to mix completely. Mix both volumes together thoroughly. Allow the plasmids and the lipoD293 to complex for 20 minutes.

3.4. Add dropwise to a 75 cm^2 cell culture flask containing 70% confluent HEK293T cells containing 9 mL of complete culture medium, add the transfection mixture directly to the cell layer using a serological pipette (flask in horizontal orientation).

3.5. Replace medium with 20 mL fresh complete DMEM 16 hours post-transfection. Harvest supernatant after 72 hours post transfection. Aliquot viral supernatant in 1 mL aliquots and store at -80°C. Lentiviral supernatant is stable at -80°C for at least 1 year.

4. **Lentiviral transduction:**

4.1. Before lentiviral transduction a kill curve has to be established when using a selectable lentiviral construct.

4.2. For the kill curve, plate the cell line to be transduced in a 12 well plate (confluence approximately 10-20 %), add a dose curve of the selectant (approximate concentrations for kill curves: puromycine 0,5-10 µg/mL, blasticidin 1-20 µg/mL, geneticin (G418) 100-2000 µg/mL, hygromycin 100-2000 µg/mL (all Gibco, Thermo-scientific, Bleiswijk, the Netherlands)).

4.3. Medium should be changed every three days to assure a stable concentration of the chosen selectant.

4.4. 1 mL of lentiviral supernatant is added to 9 mL culture medium, containing a final concentration of 8 µg/mL polybrene (Sigma) on 20-40 % confluent cells, after changing the medium (volumes can be scaled down, while maintaining this ratio of supernatant/medium).

4.5. 16-24 hours post transduction the medium is exchanged and when required the former step can be repeated to enhance phenotype penetrance (check fluorescence to decide if another transduction is required).

4.6. 48 hours post transduction the cells can be selected using the antibiotic corresponding to the resistance marker incorporated into the lentiviral cassette. The concentration to use for the selection of your transduced cell population should kill the wild type population within 7 days after application of

the selectant (i.e. allowing the transduced cells to outgrow the wildtype population).

4.7. Viral supernatant should be applied in different multiplicities of infection (MOI's) to ensure that the transduction and the genetic lesions incurred by the cellular genome does not negatively affect cell viability or tumorigenicity.

5. **Breeding zebrafish:**

5.1. On day 0, 2 days prior to engraftment of cancer cells, adult zebrafish are mated in "family cross" fashion at room temperature (as shown in Figure 1).

5.2. The tank of zebrafish is removed from the housing system (maintained at 28.5°C). The fish are separated into small breeding clusters at a 1:1 ratio male: female, with 10 fish per cluster. The fish are placed in small breeding tanks, in water drawn from the housing system, above a slanted grate (slanted, to mimic the shallows wherein zebrafish would naturally spawn).

5.3. Induced by the decline in temperature from 28.5°C to room temperature (25°C) and the entrance into the next light phase of the dark/light cycle the fish will spawn. Subsequently the adults are removed and transferred into their housing tank.

5.4. Eggs are subsequently collected and washed with egg water using a strainer, eggs divided to approximately 75-100 per dish and are maintained at 28.5°C. Approximately 6 hours post collection the dishes are cleaned of dead or malformed embryos. The next morning the egg water is exchanged and the dishes are again cleaned of dead embryos.

6. **Harvesting cells:**

Note: proper cell preparation is key to the implantation procedure, using a superfluous number of cells allows for easier downstream processing. The third centrifugation step is critical, as this will leave you with only the cell pellet, the remaining PBS stuck on the sides of the centrifuge tube greatly exceeds the final resuspension volume.

6.1. All media and solutions used in cell culture are pre-warmed in a 37°C water bath before use.

6.2. Add 2 mL TryplE/ 75 cm^2 culture flask or 1 mL 25 cm^2 flask and incubate until all cells are rounded, for most cell lines 2-5 minutes should be sufficient. For highly epithelial cells or fibroblastic cells 5-10 minutes should allow for proper detachment (insufficient trypsinization will hinder downstream processes, and facilitates cell aggregation during implantation). Gently tap the side of the flask to dislodge remaining cells.

6.3. Add up to the original culture volume of complete medium. Pipette up and down gently but thoroughly with a serological pipette to shear cell clumps into single cell suspension (do not generate foam during this process as foam is indicative of mechanical shearing of the cells).

6.4. Transfer into a sterile 15 mL tube and centrifuge for 5 minutes at 200 x g at room temperature. Aspirate supernatant and add 1 mL sterile PBS. Carefully and thoroughly resuspend the cells using a sterile 1000 µL pipette.

6.5. Remove 20 µL cell suspension for counting and transfer the remaining cell suspension to the centrifuge. Centrifuge for 4 minutes at 200 x g at room temperature.

6.6. **CRITICAL STEP: Remove all PBS, Centrifuge for 30 sec at 200 x g at room temperature, remove the remaining PBS.**

6.7. Dilute the cells to 250 cells /nL in 2% polyvinylpyrrolidon 40 (PVP_{40}, 2% (w/v) in DPBS) as follows:

$$\frac{Cell\ number\ (\times 10^6)}{250\ (cells/\mu L)} \times 1000 = volume\ PVP_{40}\ (in\ \mu L)$$

(for example, $\frac{5\ (\times 10^6)}{250\ (cells/\mu L)} \times 1000 = 20\ \mu L$)

Thoroughly resuspend the cells, while preventing the formation of air bubbles (cells can be kept for at least 2 hours in 2% PVP_{40} without loss of tumorigenic potential).

7.**Xenograft modeling**

All experiments should be performed in compliance with local animal welfare regulations.

Depending on the application two main variations in experimental design are classified as a phenotype assessment (7.1 the pre-screening stage) and secondly 7.2 a screen where either the cells have been modified prior to engraftment or 7.3 where the embryos are treated with a chemical inhibitor.

7.1.Pre-screening and determination of tumorigenic potential. Zebrafish larvae of interest (WT, transgenic or reporter line) are engrafted at 2 dpf with a varying number of fluorescent cells (i.e 200, 400, 600 ±100).

7.1.1. Larvae are screened 16-24 hours after injection to remove outliers (extremely high or low cell numbers in circulation for the ectopic model, or cells inside the head for the orthotopic model) and wrongly engrafted fish are removed. Indicate nr of larvae per experimental group for group analysis vs kinetic analysis of the same larvae.

7.1.2. The zebrafish larvae are monitored at regular intervals (1,2,4,6 days post injection (dpi)) and 20 individuals imaged (as described in paragraphs 9 and 10), out of a pool of ±50 larvae.

7.1.3. General phenotype and disease progressions is monitored and subsequently quantified with ImageJ (measuring integrated density of the fluorophore signal in the cancer cells).

7.1.4. This data is subsequently plotted to visualize the cancer cell growth kinetics within the zebrafish (Figure 3).

7.2.Cells are modified a priori (knock down or knock out of a gene of interest) and engrafted into zebrafish.

7.2.1. Fish are engrafted, all unwanted phenotypes are removed (per condition).

7.2.2. The individuals are imaged at 1dpi (20 larvae per group).

7.2.3. Individuals can be imaged at set intervals (1,2,4 and 6 dpi).

7.2.4. At 6dpi after imaging the fish are euthanized by overdosing with tricaine (10-fold over dosing at 0.4 mg/mL) and are discarded on absorbent paper lining a funnel.

7.3. Fish are treated with drugs after engraftment.

7.3.1. Prior to drug application on engrafted zebrafish, determine the maximum tolerated dose (MTD) on zebrafish (titrate down from 10 µM- 0.150 nM, using the highest volume of solvent as a negative control) we have set the MTD as the concentration where >80% of individuals survive the entire treatment.

7.3.2. One day post injection the unwanted phenotypes are removed.

7.3.3. Fish are randomly divided into groups (36-48 individuals/ condition) and maintained in a 24 wells plate with 6 larvae per well in 1 mL of egg water.

7.3.4. Drugs are applied 24 hours after engraftment, as a control use the same amount of solvent (DMSO, EtOH etc.) at the highest volume applied for an experimental group.

7.3.5. Start drug treatment at the maximum tolerated dose, change the egg water containing drug every other day. Removing egg water and dead larvae as completely as possible during every change.

8.**Injection:**

Note: Use a pneumatic pulse controller (Pico pump, World Precision Instruments) coupled to a compressed air line, supplying pressure in surplus of 100Psi, this allows for enough pressure to both inject (≈20Psi) and to eject possible cell aggregates (≈100Psi), starting pressure and time should be approximately 200ms at 20 Psi, if either has to be decreased more than 50% at the start of the injection either the cell suspension is too fluid (cell or PVP_{40} concentration too low) or needle opening is too large.

8.1. Carefully remove a capillary needle from its container. Break the needle to form an opening of app. ø20µm, using a fine watchmakers' forceps.

8.2. Carefully and thoroughly resuspend the cells using a 20µL pipette tip. Pipette cell suspension into the open glass capillary needle using a long (microloader) tip. Load the needle into the micro manipulator.

8.3. Place app. 20-40 larvae anesthetized in 0,04 mg/mL tricaine on an agarose dish using a transfer pipette. Remove excess moisture to immobilize the larvae using a

transfer pipette. The larvae will mostly be oriented in a lateral fashion due to the presence of a still relatively large yolk sac.

8.4. Inject the larvae with approximately 200, 400 and 600 cells via the Duct of Cuvier (doC) for ectopic model. Similarly, the larvae are injected retro-orbitally (RO), to yield the orthotopic model (injecting 100 ±50 cells) modifying pneumatic pulse length on the picopump (Start at app. 20Psi, 200ms and adjust accordingly). During injection ensure that the larvae do not dry out, make sure that all (or most) larvae are injected.

8.5. Injected larvae are flushed off with fresh egg water and transferred to a labelled clean Petri dish (pooling up to 150 individuals per dish). This process is repeated until sufficient larvae are injected.

8.6. After engraftment the fish are maintained at 34°C in a humidified incubator, where 34°C is the highest temperature readily tolerated by zebrafish and allows for efficient engraftment of mammalian cancer cells.

8.7. In general, with injection of single cell lines in both doC and RO we have observed an approximate death due to mechanical damage of <5% (mechanical damage kills the larvae between 1-16 hours post injection).

9.**Screening**

9.1. Using a stereo-fluorescence microscope the fish are screened for the appropriate phenotype 1 hour post implantation when comparing cells modified a priori (or 1 day post implantation, when screening drugs, before the random assignment into treatment groups).

9.2. Larvae implanted through the doC should have cells in the tail between 1 hour and 16 hours post implantation, all other fish, including fish that display abnormality are removed from the injected pool.

9.3. Larvae implanted retro-orbitally should have cells only in the interstitium behind the eye, larvae that have cells spread throughout the head or body are removed from the pool.

9.4. Positively screened larvae are cleaned and randomly assigned to experimental groups.

9.5. After engraftment the fish are maintained at 34°C in a humidified incubator and monitored daily. Hematogenous dissemination of cells implanted through the doC is almost instantaneous, whereas metastatic spread of cells implanted in the RO cavity will spread after 2-4 days.

10.**Epifluorescent imaging of zebrafish larvae:**

10.1. Zebrafish larvae are anaesthetized with 0,2 mg/mL tricaine, either by adding tricaine to the water of the fish or by moving a sub-population of fish from the maintenance dish to a dish containing 0,2 mg/mL tricaine. Zebrafish are kept in a dish with tricaine until they remain stationary, until stimulation of the lateral line does not induce flight behavior.

10.2. Fish are transferred to an agarose covered Petri dish. Approximately 10 per dish. The majority of the water is removed though gently raising one end of the dish (allowing the water to gently pool in the lower end of the Petri dish). If done carefully all fish will align, tails facing downwards. All fish are imaged from the top of the dish to the bottom, after which the fish are washed off with egg water into a dish without tricaine.

10.3. This method is repeated until enough individuals are imaged. The larvae are either transferred back to the 34°C or culled (at 6 dpi) through overdosing with tricaine (i.e 0.5 mg/mL, incubating for 10 min, prior to discarding on absorbent paper lining a funnel).

11.**Confocal imaging of (engrafted) zebrafish larvae:**

11.1. Zebrafish are anaesthetized with 0.2 mg/mL tricaine as described previously. Place a glass bottom confocal dish under a stereo microscope, and focus on the bottom of the dish. Transfer 5-10 larvae to a glass bottom confocal dish. Remove as much water as possible.

11.2. Cover the larvae with 42°C, 1% low melting agarose dissolved in egg water (important: make sure that the agarose has cooled down to at least 42°C before use, higher temperatures might harm or kill the larvae). Using the stereo microscope, quickly but gently orient the larvae pushing it down, using a trimmed down micro loader tip. If a ventral orientation is required the larvae can be held in place with the tongs of a watchmaker's forceps (without touching the embryo).

11.3. While the agarose sets make fine adjustments to the orientation of the larvae. Allow the larvae to set completely before transferring to the confocal microscope.

12. **Setting the confocal microscope:**

12.1. Switch on the green (488nm) and red (564nm) excitation laser lines. Place the confocal dish in the holder of the confocal microscope. Using the epifluorescence, move the light bundle to coalesce with the first fish (setting *x* and *y*). Through the ocular set the focus to coincide with the center of the larvae (setting *z*).

12.2. Set 700 gain on both fluorescent channels, 1-5% laser power. Increase laser power and decrease offset to approximate full dynamic range. Do not over saturate the signal, but enhance the signal to merely show a few saturated pixels.

12.3. When capturing a stitch, set the start and end of the larvae along one axis (either *x* or *y*), if set along one axis a whole embryo can be imaged in 1 x 4 segments and can be post processed into one image using ImageJ.

12.4. After imaging the larvae can be removed from the agarose by gently tearing it around the embedded larvae using watchmaker's forceps. Otherwise, the larvae can be euthanized with overdosing with undiluted tricaine, covering the agarose with a layer of tricaine and incubating 10 minutes.

13.**Data analysis:**

13.1. Open the individual data sets in ImageJ/Fiji (i.e., control, drug A, drug B, drug A+B) separately, starting with vehicle control.

13.2. Open the analysis macro (annotated script available) (http://doi.org/10.5281/zenodo.4290225).

13.3. In brief the macro analysis does the following:

13.3.1. Concatenates all open images (one condition).

13.3.2. Splits the images into the separate channels comprising the image.

13.3.3. Closes all accessory channels, (leaving the cancer cell channel).

13.3.4. Runs a thresholding algorithm, on the entire concatenated sequence.

13.3.5. Measures integrated density of each individual image.

13.3.6. Saves the measures as an excel sheet in the root folder.

13.4. The macro analysis is run on all conditions.

13.5. Measurements are combined (in general at least n=2*20), outliers are removed (Q-test in Graph pad Prism v8).

13.6. Measurements are normalized either to solvent control or to day 1 (dependent on the type of experiment, the former for a drug inhibition experiment and the latter

for a growth kinetics experiment), measurements are expressed as normalized cancer cell burden (*y* axis) over time or condition (*x* axis) as shown in figure 3 and 4 respectively.

Reagents:

- Egg water: 0.6 mg/L final concentration sea salt (Instant ocean, Blacksburg, U.S.A).
- Tricaine 25x stock, 5mg/mL: 5g tricaine (Ethyl 3-aminobenzoate methanesulfonate or MS-222) powder, 900 mL demineralized water add 21 mL 1 M Tris (pH 9) and adjust to pH=7 and fill up to 1L. Tricaine can be stored at 4°C for short term (up to six months), or can be stored at room temperature for a month at room temperature when protected from sunlight. (Sigma, Zwijndrecht, the Netherlands)
- Agarose: 1,5% (w/v) in eggwater. 1.5 g in 100 mL DPBS, microwave to dissolve.
- Low-melting agarose: 1% (w/v) in eggwater 1.5 g in 100 mL DPBS, microwave to dissolve.
- PVP40 stock: PVP40 2% (w/v) in DPBS, 1 g PVP40 in 50 mL DPBS. Vortex and incubate at 37°C to facilitate dissolving. Store at room temperature.
- DMSO: Often used as solvent in drug treatments, should be stored at 2-8°C the dark.
- TryplE: Synthetic trypsine replacement, less damaging to the cells and allows for the gentle dispersion of strongly adherent cells. (Thermo-fischer scientific, Bleiswijk
  Netherlands)
  DPBS: Dulbecco's phosphate buffered saline, without Mg^{2+} and Ca^{2+} for washing the cells, lack of Ca^{2+} impairs cell-cell adhesion through cadherins.
  Lentiviral plasmids: psPAX2 (plasmid #12260) and pMD2.G (plasmid #12259) gifted by Didier Trono and either a GFP (Plasmid #106172) or tdTomato (Plasmid #106173) encoding transfer plasmid (Addgene)
  lipodD293: Highly efficient HEK293T optimized transfection reagent (Signagen)

Representative results:

We have provided step by step instructions for a fast and easy approach to progress from a novel cell line to its analysis. Starting with the over expression of a fluorescent tracer using a lentiviral overexpression cassette (paragraphs 3 and 4). Followed by cell preparation to ensure the least possible dead volume while injecting, allowing to inject high cell numbers into both doC and retro-orbital space (paragraph 6s and 7). Subsequent semi-high throughput data acquisition using stereo-fluorescent microscopy and higher magnification confocal microscopy for qualitative analysis of whole-body cancer cell dissemination (figure 2 and paragraph 10, 11 and 12). Care has to be taken when acquiring data, as to ensure the reproducibility for both stereo and confocal microscopic imaging, the generic settings and standardization are delineated (paragraph 11 and 12). Data analysis is discussed (using imageJ/Fiji) [16], along with standardization using imageJ macros (paragraph 13).

In paragraph 3 we mentioned the transient labelling of (cancer) cells to perform a quick pre-screening to assess the tumorigenic potential of a new cancer cell line, one important caveat is that although easy to use and long living, the transient stain described herein has the possibility to form artefacts e.g. care has to be taken to ensure that cell fragments can be distinguished from whole cells as was performed extensively by Fior and colleagues [9]. In our experience the formation of these artefacts is directly linked to the extreme stability of the stain and the brightness (even after cell death), where cell fragments are dispersed and taken up by immune cells, which could subsequently be falsely concluded to derive from active metastasis.

In both described models, the systemic engraftment through the doC and the localized engraftment in the retro-orbital space, thorough screening of the larvae one day after injection is of paramount importance. As shown in figure 2B all larvae that display mechanical displacement of the engrafted cells into the head area (beyond the retro-orbital site) in the retro-orbital model and cells in the yolk sac, or displaying an edema in the doC injected pool should be removed. All negatively selected phenotypes are displayed as high-resolution confocal stitches in figure 2, but can be readily seen and removed through stereo microscopical observation.

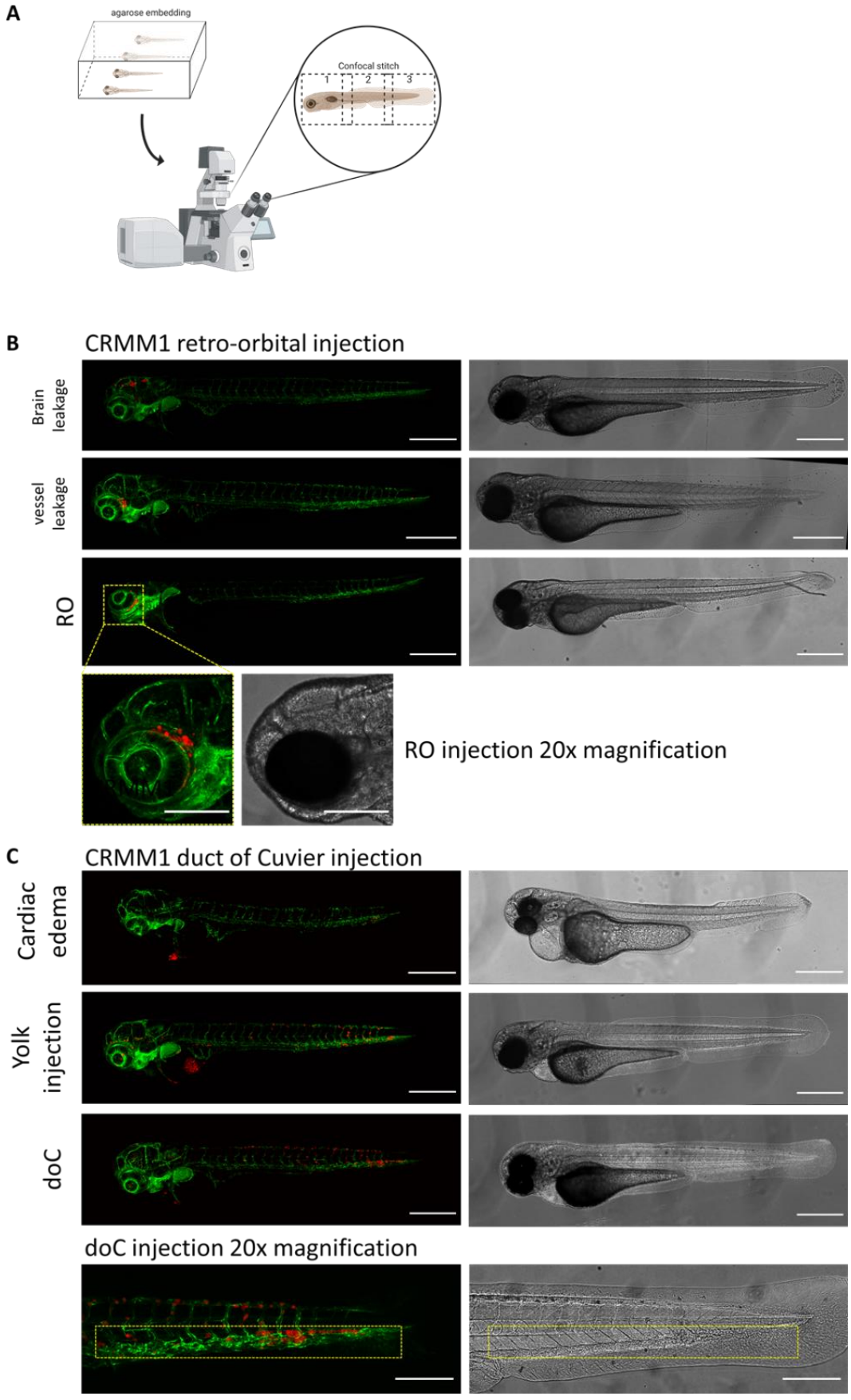
A
agarose embedding
Confocal stitch
1
2
3
B
CRMM1 retro-orbital injection
Brain leakage
vessel leakage
RO
RO injection 20x magnification
C
CRMM1 duct of Cuvier injection
Cardiac edema
Yolk injection
doC
doC injection 20x magnification

Figure 2 (Left). Phenotypic assessment and screening after injection.
A) Schematic depiction of zebrafish xenograft confocal stitch generation, yielding seamless, high-resolution images after integration of subsequent confocal projection. Here zebrafish xenografts are embedded in 1% low melting agarose and mounted on a glass bottom confocal dish (as described in paragraph 11.3). B) all possible outcomes of retro-orbital and duct of Cuvier engraftment are displayed injected in green fluorescent blood vessel reporter zebrafish Tg(*fli1*:EGFP), with cells stained through lentiviral over expression of tdTomato), here denote the correct engraftment at 1dpi (RO panel) and the unwanted phenotypes (both brain leakage and blood vessel leakage), the latter two population have to be removed to ensure they do not confound downstream experimental findings. C) The unwanted phenotypes for the hematogenous engraftment through the duct of Cuvier (doC) are outlines where cardiac edematous larvae (Cardiac edema) and larvae with cells leaking into the yolk sac (Yolk injection) have to be removed to prevent interference with downstream measurements. The correctly injected larvae are entered into experimental groups as described in paragraph 7.1. (all images acquired at 1dpi, using a Leica sp8 confocal, scale bars 200µm, yellow boxes indicate metastatic sites for both RO and doC engraftments, head region and caudal hematopoietic tissue respectively).

Over time cells will both migrate and proliferate, for the retro-orbital model we observed infiltration into neighboring tissues for CRMM1 and for CRMM2 we observed less proliferation. We strikingly did observe distant metastasis arising between 2-4 dpi in some individuals (20%), where we measured a significant difference at 6dpi, as shown in figure 4. For both cell lines we tested the proliferative potential when injected in both sites, for CRMM1 there was a significant ($p<0.0001$) increase in cancer cell number for or at the injection sites, when displayed as normalized tumor cell burden, normalizing to day one for each model (7.8-fold increase, ±3.2 for the RO model and an increase of 15-fold ±8,8 for the doC model). CRMM2 did not display significant growth when normalized to day one for each individual model (2.4-fold increase, ±1.9- and 2.3-fold increase, ±1.14 for the RO and doC). CRMM1 was found to readily proliferate in both retro-orbital tissue and the caudal hematopoietic tissue after engraftment. Cell line CRMM2 was less proliferative in both models, but interestingly was found to be capable of distant metastasis when injected in the retro-orbital space as shown in figure 3B and C.

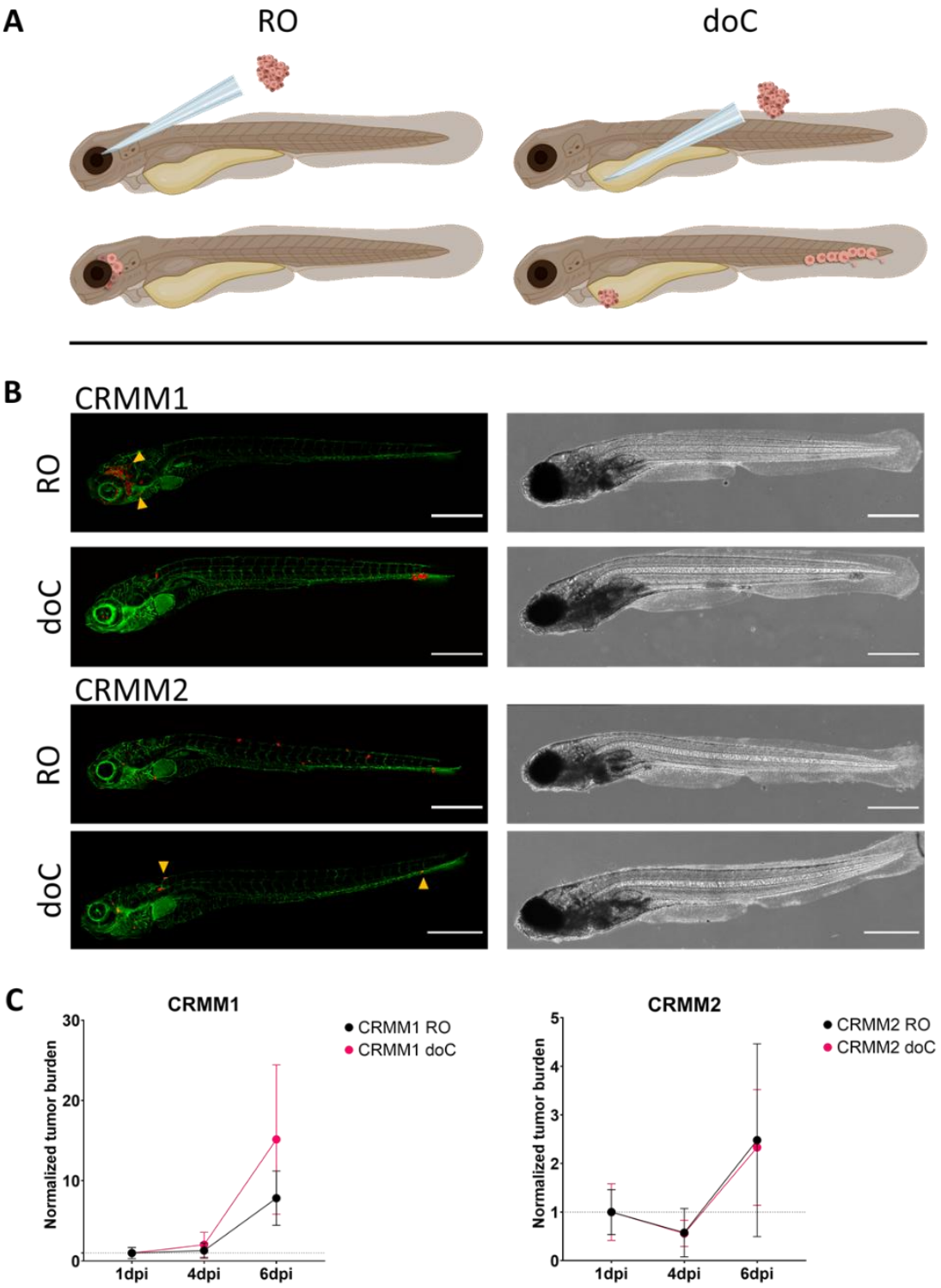

Figure 3. Comparative analysis of conjunctival melanoma cell lines CRMM1 and CRMM2 show differential metastatic and growth capacity. 3A) Schematic representation of injection models, retro-orbital model (RO) and hematogenous engraftment model (doC) the fish used are Tg(*fli1*:GFP) green blood vessel reporters, with cells over expressing tdTomato shown in red. 3B) Representative phenotypes of fish engrafted with CRMM1 and CRMM2, CRMM1 displays efficient engraftment (both RO and doC) and small scale invasion into the tissue surrounding the RO engraftment site (RO, yellow

arrowheads). CRMM2 exhibits a remarkably lower engraftment efficiency for both engraftment models, but shows distant metastasis when injected retro-orbitally (as shown in RO, denoted by the arrowheads) (all images acquired at 6dpi, using a Leica sp8 confocal, scale bars 200µm, yellow arrowheads indicate metastatic sites for both RO and doC engraftments, head region and caudal hematopoietic tissue respectively). 3C Kinetic engraftment plots for both CRMM1 and CRMM2, comparing both engraftment models to day 1 (normalizing to day 1), there is a significant ($p<0,0001$) increase in normalized tumor burden for cell line CRMM1(between 1dpi and 6dpi) where there is a (non-significant) upward trend for CRMM2. CRMM1 reveals a significant difference between RO and doC growth, where the doC model shows a higher tumor expansion rate (approximately 2-fold higher for the doC engrafted larvae). Graphs display the mean and standard error of the mean (SEM), All groups were normalized to 1dpi for each individual condition.

After screening the injected larvae at 1dpi and randomly assigning the individuals to either treatment or control groups the fish were treated for 6 days, changing the water containing Vemurafenib (this inhibitor can readily be interchanged for any other titrated antitumor compound). We chose to elaborate upon the previously published hematogenous conjunctival melanoma dissemination model engrafting CRMM1[14], by testing Vemurafenib's efficacy on orthotopically engrafted CRMM1. CRMM1 showed a strong significant reduction of the Vemurafenib treated ectopically engrafted group ($P<0.0001$) and a stunted yet significant response for the orthotopically engrafted model ($p<0.05$) as shown in figure 4.

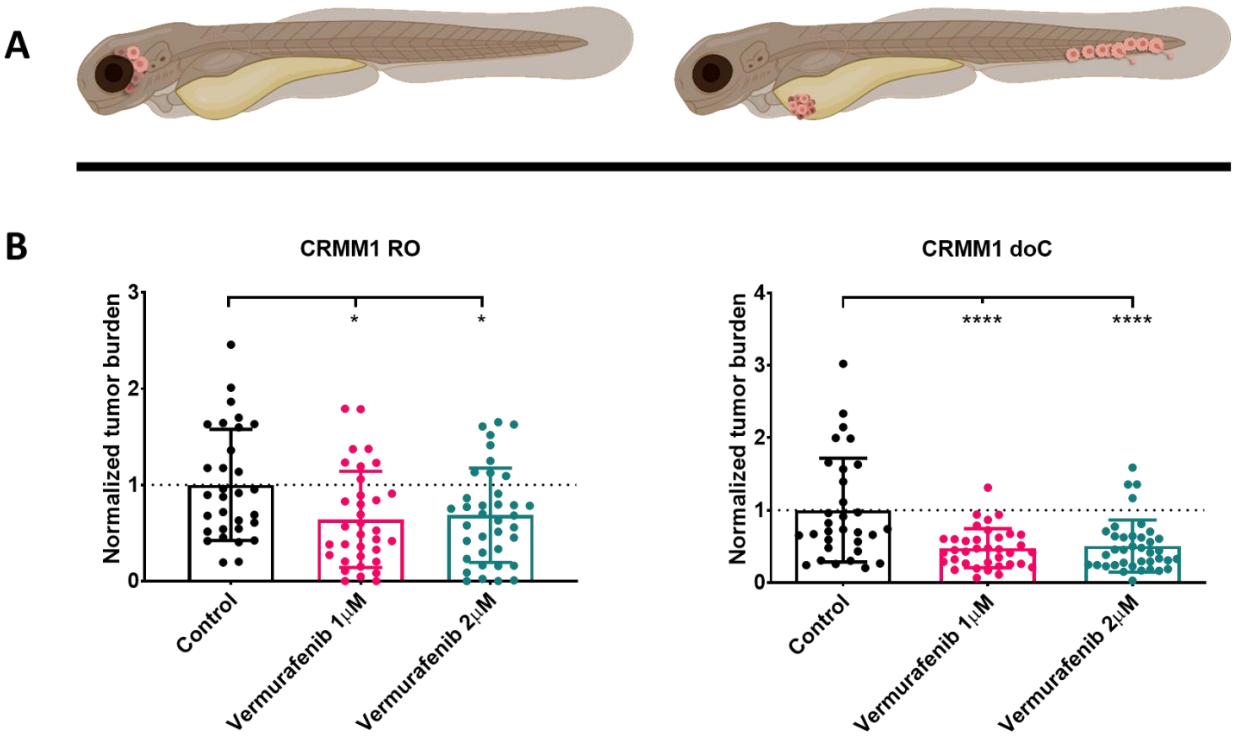

Figure 4. BRAF V600E inhibitor Vemurafenib significantly inhibits both RO and doC conjunctival melanoma engrafted zebrafish larvae. A) Schematic representation of zebrafish phenotypes, RO and doC models. B) Both RO and doC engrafted larvae, injected with conjunctival melanoma cell line CRMM1 display a significant reduction of normalized tumor burden ($p<0.05$ and $P<0.001$ respectively). The doC engrafted zebrafish models indicate an enhanced drug response and a dose independent relationship to drug inhibition, indicating a possible saturation of inhibition). Graphs show the mean and standard error of the mean (SEM), All groups were normalized to control for each individual cell line.

Discussion

Here we have defined a meticulous approach to model primary and metastatic ocular melanoma in zebrafish xenografts. By combining both a localized, orthotopic injection and a systemic, ectopic injection model we have recapitulated the etiology of carcinogenesis for a cancer where no animal models were previously available. The inherent transparency of the early zebrafish larva allows the tracking of fluorescently labelled cancer cells on a whole animal level, ensuring the easy visualization of potential metastatic sites [17]. Moreover high magnification confocal microscopical analysis allows us to track cells at a subcellular resolution [10].

We have provided step by step instructions for a fast and easy approach to progress from a novel cell line to establishment of the xenograft and its analysis. Starting with the over expression of a fluorescent tracer using a lentiviral overexpression cassette (paragraph 3 and 4). Followed by cell preparation to ensure the least possible dead volume while injecting, enabling to inject high cell numbers into both doC and retro-orbital space (paragraph 7 and 8). Subsequent semi-high throughput data acquisition using stereo-fluorescent microscopy and higher magnification confocal microscopy for qualitative analysis of whole-body cancer cell dissemination (Figure 2 and paragraph 9 and 10). Care has to be taken when acquiring data, as to ensure the reproducibility for both stereo and confocal microscopic imaging, the generic settings and standardization are delineated (paragraph 11 and 12). Data analysis is discussed (using imageJ/Fiji) [16], along with standardization using imageJ macros (paragraph 13).

In paragraph 3 we mention the transient labelling of (cancer) cells to perform a quick pre-screen to assess the tumorigenic potential of a new cancer cell line, one important caveat is that although easy to use and long living, the transient stain described herein has the possibility to form artefacts e.g. care has to be taken to ensure that cell fragments can be distinguished from whole cells as was performed extensively by Fior and colleagues [9]. In our experience the formation of these artefacts is directly linked to the extreme stability of the stain and the brightness (even after cell death), where cell fragments are dispersed and taken up by immune cells, which could subsequently be falsely concluded to derive from active metastasis.

Using these models, we simulated primary tumor development by physically confining the engrafted cells within the retro-orbital interstice. Subsequent thorough screening at 1 day post engraftment ensures that cells found at distant site later in the experiment

have actively metastasized (intravasated and disseminated, ultimately to extravasate at the metastatic niche). Engraftment through the doC, the embryonic common cardinal vein, allows for easy and highly reproducible implantation of large quantities for cells (at a surplus of 600 cells when properly concentrated) effectively circumventing the primary stages of the metastatic cascade (intravasation) and allowing us to focus on the later stages of the metastatic cascade (adhesion, extravasation and outgrowth). Although powerful tools when used properly, both models should be monitored extensively during the first day post engraftment to ensure that no false positive conclusions are drawn during the later stages of the experiment.

In line with previous publications we have shown that conjunctival melanoma lines readily form metastatic colonies after dissemination throughout the zebrafish blood circulation system[14]. Here we report the expanding of the engraftment repertoire with the retro-orbital injection as an orthotopic model, and the subsequent active metastasis to the caudal hematopoietic tissue of the cell line CRMM2. Subsequently we report the efficacy of BRAF V600E specific inhibitor Vemurafenib also on the primary form of conjunctival melanoma when modelled in zebrafish larvae.

Using the aforementioned methods, a skilled researcher is capable of generating in excess of hundreds of engrafted larvae per day (approximately 200 per hour) of either model proposed. In a timescale of two weeks a drug can be both titrated for maximum tolerated dose, and screened on established xenograft model. From start to finish, using a non-transduced cell line, to having a drug sensitivity profile in the zebrafish model can be achieved within a month (given that the injected cell line is tumorigenic within the zebrafish model). In our hands as little as 20 larvae per experiments and two biological repeats have reproducibly yielded robust drug inhibition, when two individual experiments conflict (or do not yield statistically significant growth inhibition) a third biological repeat can be conducted.

Through minor adjustments, these models have allowed us to quickly adapt these implantation strategies for glioblastoma (hind brain cavity injection), breast cancer (doC injection) and osteo sarcoma (doC) among others [18–21]. These models can subsequently be utilized for both basic research and pre-clinical screening of both

single drugs and combinatorial drug strategies. Recently, we described different administration regimes of drugs and their photo activation using these models [13]

Acknowledgements:

This work was supported by funding from the European Union's Horizon 2020 research and innovation program under grant agreement No 667787 (UM Cure 2020 project, www.umcure2020.org). The Chinese Scholarship Council is kindly acknowledged for a PhD grant to J.Y.

Disclosures:

No authors declare a conflict of interest

References:

1. Yang, J., Manson, D. K., Marr, B. P. & Carvajal, R. D. Treatment of uveal melanoma: where are we now? *Therapeutic Advances in Medical Oncology* vol. 10 (2018).

2. Wong, J. R., Nanji, A. A., Galor, A. & Karp, C. L. Management of conjunctival malignant melanoma: A review and update. *Expert Review of Ophthalmology* vol. 9 185–204 (2014).

3. Nguyen, D. X., Bos, P. D. & Massagué, J. Metastasis: from dissemination to organ-specific colonization. *Nature reviews. Cancer* **9**, 274–284 (2009).

4. White, R. M. *et al.* Transparent Adult Zebrafish as a Tool for *In vivo* Transplantation Analysis. *Cell Stem Cell* **2**, 183–189 (2008).

5. Zon, L. I. & Peterson, R. T. *In vivo* drug discovery in the zebrafish. *Nature reviews. Drug discovery* **4**, 35–44 (2005).

6. Howe, K. *et al.* The zebrafish reference genome sequence and its relationship to the human genome. *Nature* **496**, 498–503 (2013).

7. Palmblad, M. *et al.* Parallel deep transcriptome and proteome analysis of zebrafish larvae. *BMC research notes* **6**, 428 (2013).

8. Yan, C. *et al.* Visualizing Engrafted Human Cancer and Therapy Responses in Immunodeficient Zebrafish. *Cell* **177**, 1903-1914.e14 (2019).

9. Fior, R. *et al.* Single-cell functional and chemosensitive profiling of combinatorial colorectal therapy in zebrafish xenografts. *Proceedings of the National Academy of Sciences of the United States of America* **114**, E8234–E8243 (2017).

10. Campbell, P. D., Chao, J. A., Singer, R. H. & Marlow, F. L. Dynamic visualization of transcription and RNA subcellular localization in zebrafish. *Development (Cambridge)* **142**, 1368–1374 (2015).

11. Campeau, E. *et al.* A Versatile Viral System for Expression and Depletion of Proteins in Mammalian Cells. *PLoS ONE* **4**, e6529 (2009).

12. van der Helm, D. *et al.* Mesenchymal stromal cells prevent progression of liver fibrosis in a novel zebrafish embryo model. *Scientific Reports* **8**, 16005 (2018).

13. Chen, Q. *et al.* TLD1433 photosensitizer inhibits conjunctival melanoma cells in zebrafish ectopic and orthotopic tumour models. *Cancers* **12**, (2020).

14. Pontes, K. C. de S. *et al.* Evaluation of (*fli:GFP*) *Casper* Zebrafish Embryos as a Model for Human Conjunctival Melanoma. *Investigative Opthalmology & Visual Science* **58**, 6065 (2017).

15. Liverani, C. *et al.* Innovative approaches to establish and characterize primary cultures: an ex vivo 3D system and the zebrafish model. *Biology open* **6**, 133–140 (2017).

16. Schindelin, J. *et al.* Fiji: an open-source platform for biological-image analysis. *Nature Methods* **9**, 676–682 (2012).

17. White, R. M. *et al.* Transparent Adult Zebrafish as a Tool for *In vivo* Transplantation Analysis. *Cell Stem Cell* **2**, 183–189 (2008).

18. Mercatali, L. *et al.* Development of a patient-derived xenograft (PDX) of breast cancer bone metastasis in a Zebrafish model. *International Journal of Molecular Sciences* **17**, (2016).

19. Tulotta, C. *et al.* Imaging cancer angiogenesis and metastasis in a zebrafish embryo model. in *Advances in Experimental Medicine and Biology* vol. 916 239–263 (Springer New York LLC, 2016).

20. Paauwe, M. *et al.* Endoglin expression on cancer-associated fibroblasts regulates invasion and stimulates colorectal cancer metastasis. *Clinical Cancer Research* **24**, 6331–6344 (2018).

21. Cao, J. *et al.* Overexpression of EZH2 in conjunctival melanoma offers a new therapeutic target. *Journal of Pathology* **245**, (2018).

Chapter 3:

Evaluation of (*fli:GFP*) x *Casper* Zebrafish Embryos as a Model for Human Conjunctival Melanoma

Chapter 3: Evaluation of (fli:GFP) Casper Zebrafish Embryos as a Model for Human Conjunctival Melanoma

Kelly Cristine de Sousa Pontes[*]; Arwin Groenewoud[†]; Jinfeng Cao[*]; Livia Maria Silva Ataide[+]; Ewa Snaar-Jagalska[†±]; Martine J. Jager*[±]

Author Affiliations & Notes

*Department of Ophthalmology, Leiden University Medical Center, Leiden, The Netherlands

[†]Institute of Biology, Leiden University, Leiden, The Netherlands

[+]Department of Population Biology, Institute for Biodiversity and Ecosystem Dynamics, University of Amsterdam, Amsterdam, The Netherlands

†Institute of Biology, Leiden University, Leiden, The Netherlands

*Martine J. Jager

Correspondence: Martine J. Jager, Department of Ophthalmology, Leiden University Medical Center, P.O. Box 9600, 2300 RC Leiden, The Netherlands; m.j.jager@lumc.nl.

Footnotes: [±] ES-J and MJJ contributed equally to the work presented here and should therefore be regarded as equivalent authors.

Published as: *Kelly Cristine de Sousa Pontes*; Arwin Groenewoud†; Jinfeng Cao*; Livia Maria Silva Ataide+; Ewa Snaar-Jagalska†±; Martine J. Jager*±*
Evaluation of (fli:GFP) Casper Zebrafish Embryos as a Model for Human Conjunctival Melanoma
Investigative Ophthalmology & Visual Science December 2017, Vol.58, 6065-6071. doi:https://doi.org/10.1167/iovs.17-22023

Abstract

Purpose: Conjunctival melanoma (CM) is a rare malignant disease that can lead to recurrences and metastases. There is a lack of effective treatments for the metastases, and we set out to develop a new animal model to test potential therapies. Zebrafish are being used as a model for many diseases, and our goal was to test whether this animal could be used to study CM.

Methods: Three human CM cell lines (CRMM-1 and CM2005.1, which both harbor a *B-RAF* mutation, and CRMM-2, which has an *N-RAS* mutation) were injected into the yolk sac, around the eye, and into the duct of Cuvier of transgenic (*fli:GFP*) *Casper* zebrafish embryos. Fluorescent and confocal images were taken to assess the phenotype and the behavior of engrafted cells and to test the effect of Vemurafenib as a treatment against CM.

Results: While the cells that had been injected inside the yolk sac died and those injected around the eye sporadically went into the circulation, the cells that had been injected into the duct of Cuvier colonized the zebrafish: cells from all three cell lines proliferated and disseminated to the eyes, where they formed clusters, and to the tail, where we noticed extravasation and micro-metastases. Vemurafenib, a potent agent for treatment of B-RAF V600E–positive melanoma, inhibited outgrowth of CRMM-1 and CM2005.1 cells in a mutation-dependent way.

Conclusions: The (*fli:GFP*) *Casper* zebrafish embryo can be used as an efficient animal model to study metastatic behavior of human CM cells and warrants further testing of drug efficacy to aid care of CM patients.

Introduction

Conjunctival melanoma (CM) is a rare malignant ocular disease, accounting for 5% to 10% of all human ocular melanoma[1]. Over the past decades, its incidence has increased worldwide[2–4]. The current treatment of choice for primary CM is wide surgical excision, combined with brachytherapy, cryotherapy, and topical chemotherapy (e.g., mitomycin C). However, effective targeted therapies have not yet been developed to treat this malignancy[5]; CM's high recurrence rate is associated with metastasis and poor prognosis[6–8]. Furthermore, the mortality rate is high, ranging from 13% to 38% after 10 years[9–11].

In this malignancy, essential mutations occur in the *B-RAF* and *N-RAS* genes[5,12–14]. *B-RAF* mutations constitutively activate the mitogen-activated protein kinase (MAPK) pathway and its downstream kinases MEK1/2-ERK1/2, promoting tumor proliferation[15,16].

Mice have previously been used as a model to study human CM,[17,18] but there are some limitations. The major disadvantages are a slow growth and spread of the tumor, which can take weeks to months, and the high cost for reproduction and housing. The cost increases further when immunosuppressive drugs are needed to prevent tumor rejection[19]. Therefore, there is a need to find a new animal model.

The zebrafish model has been used widely in research because of its advantages, such as (1) the fish's high fecundity and short time between generations, (2) the high interspecies conservation of molecular pathways between zebrafish and mammals,[20–22] (3) their transparency, allowing direct imaging of development, organogenesis, and cancer progression,[23] which enables tracking of transplanted cells,[24] (4) the possibility of xenotransplantation, and (5) their permeability to small molecular weight compounds from water, enabling easy delivery and efficient screening of large numbers of anticancer compounds[19].Furthermore, the fact that their adaptive immune system does not reach maturity until 4-weeks postfertilization allows them to be used without the need for immunosuppression in the embryonic stages[20].

There are no studies showing whether zebrafish embryos can be used as an animal model for human CM, and our goal was to determine if this animal can be used as a screening platform based on the xenotransplantation of three human CM cell lines. Our group has shown that two of three available CM cell lines, CRMM1[25] and CM2005.1,[26] harbor a *B-RAF V600E* mutation, while the third, CRMM2, contains an *N-RAS Q61L* mutation[17,27]. We injected stable red fluorescently labeled (lentiviral

tdTomato-blas) CM cells via different routes into the embryonic zebrafish. Thus, we determined the most effective engraftment strategy for the establishment of CM xenograft tumors in zebrafish and we observed distinct phenotypes after implantation of the three CM cell lines. We subsequently validated the model through the use of the well-known B-RAF inhibitor, vemurafenib.

Material and Methods

Cell Culture

We used three CM cell lines, CRMM-1, CRMM-2, and CM2005.1, all generated from recurrent primary CM. The CRMM-1 and CRMM-2 cell lines, isolated by Nareyeck et al.,[25] were cultured in F-12K nutrient mixture, Kaighn's modification (Gibco, Life Technologies, Bleiswijk, The Netherlands), supplemented with 10% heat-inactivated fetal bovine serum (FBS; Greiner Bio-one, Alphen aan den Rijn, The Netherlands) and 1% Penicillin/Streptomycin (Gibco). CM2005.1, established in 2007 by Keijser et al.,[26] was cultured in RPMI 1640 Dutch modified medium (Gibco), supplemented with 10% FBS (Greiner Bio-one), 1% GlutaMAX, and 1% Penicillin/Streptomycin (Gibco). To generate CM cells with red fluorescence, cells were stably transduced with lentivirus expressing both tandem dimer (td)Tomato and Blasticidin-S, as previously described[28]. Virus-containing medium was replaced with fresh medium containing Blasticidin-S (2 µg/mL) to select transduced cells. Transduction of the cells with the tdTomato-expressing virus did not alter the growth pattern of parental cells. After transduction, cells were incubated with multiplicity of infection (MOI) of 2.0 in medium with 8.0-µg/mL polybrene for 16 hours. For cultivation of stable transgenic tdTomato-expressing cells, Blasticidin-S (2 µg/mL) was added to the complete medium.

Growth Kinetics of Tomato-Red Cells *In Vitro*

Transgenic tdTomato-expressing cell lines were seeded in triplicate in 96-well plates at a density of 600, 1200, and 2400 for CRMM-1 and CRMM-2 cell lines in a total volume of 100 µL of medium. Because the CM2005.1 cell line is smaller than the others, it was seeded in triplicate in 96-well plates at a density of 1000, 2000, and 4000 cells per well, in a total volume of 100 µL of medium. For testing vemurafenib, cells were seeded at a density of 2000 (CRMM-1 and CRMM-2) or 3500 (CM2005.1) cells per well, in a total volume of 100-µL medium. Cell proliferation was analyzed at 1, 3, and 5 days of incubation by an In-Cell Western assay (Odyssey Infrared Imaging

System, LI-COR, Leusden, The Netherlands): after removing the medium, cells were fixed for 1 hour in 4% formaldehyde and incubated with DRAQ5, a far-red fluorescent DNA dye (1:8000, DR50050; Biostatus Ltd., Loughborough, UK). After washing with 0.1% Tween-PBS buffer, plates were scanned with an Odyssey Infrared Imaging System (LI-COR). Odyssey 3.0 software was used to quantify signal intensity.

Animals and Injection Sites

The (*fli:GFP*) *Casper* transgenic zebrafish[29] were maintained according to standard protocols (http://ZFIN.org, in the public domain) and in compliance with Dutch animal welfare regulations and European Union Animal Protection Directive 2010/63/EU. Our research followed the ARVO Statement for the Use of Animals in Ophthalmic and Vision Research.

When the cells reached 75% to 90% confluency, they were trypsinized (0.05% trypsin-EDTA; Gibco), centrifuged for 4 minutes at 200*g*, washed with Dulbecco's phosphate-buffered saline (DPBS; Invitrogen), and diluted to 250 cells/nL in 2% polyvinylpyrrolidone-40 (PVP-40; Calbiochem, San Diego, CA, USA).

At 2-days postfertilization (dpf), dechorionated zebrafish embryos were injected with this CM cell suspension using glass capillary needles with an opening of approximately 20 to 30 µm. Embryos were anesthetized with 2% tricaine (Sigma-Aldrich Corp., Zwijndrecht, The Netherlands) and positioned in a Petri dish covered with 1% agarose. Using a pneumatic picopump and a manipulator (World Precision Instruments, Sarasota, FL, USA), 200 to 400 cells were injected inside the yolk sac in one group of embryos, or inside the duct of Cuvier in a second group, and 50 to 100 cells were injected around the right eye in a third group of zebrafish. The embryos were each placed individually in a well of a 48-well plate, with 1 mL of egg water (60-µg/mL OceanSalt in demi water) in each well and maintained at 34°C, which was the optimal temperatures for cell growth and zebrafish embryo development[30]. The egg water was refreshed daily and the injected embryos were evaluated at 2-, 4-, and 6-days postinjection (dpi), using a fluorescence stereo microscope (Leica M205FA; Leica Microsystems, Inc., Buffalo Grove, IL, USA).

Kaplan-Meier Survival Analysis of Injected Embryos

After establishing the optimal injection site for CM cells in zebrafish, we determined how injection of cancer cells influenced embryo survival, shown in a Kaplan-Meier survival analysis (cumulative survival curve). Tumor cells were injected into the Duct of Cuvier at 2 dpf. One group (*n* = 90) was injected with CRMM-1, a second group (*n* = 201) with CRMM-2, and the third group (*n* = 221) received an injection with CM2005.1. A fourth group (*n* = 121) received an injection with PVP-40 and the last group (*n* = 96) was not injected. The number of injected cells was between 200 and 400 per embryo. After injection, the embryos were maintained at 34°C, and scored daily for survival, without changing the egg water, until 6 dpi.

Phenotype of CM Cell Lines in Zebrafish and Cell Migration

The embryos were injected with CRMM-1, CRMM-2, or CM2005.1 cells and screened at 1 dpi under the same conditions as described above. Embryos were anaesthetized with 2% tricaine at 1, 4, and 6 dpi to perform image analysis using a fluorescence stereo microscope and a confocal microscope (Leica TCS SPEl; Leica Microsystems, Inc.). For cell growth quantification, the pixel numbers that represent the amount of cells were counted at 1 and 6 dpi, using ImageJ software.[31]

Statistical analysis was performed using R version 2.15.1.[32] The difference in growth among the three cell lines in the embryos was analyzed using a generalized linear model (GLM) with normal distribution after square-root transformation of the data.

Immunohistochemistry (IHC)

After 6 dpi, injected whole embryos were fixed in 4% paraformaldehyde and stored in 100% methanol at −20°C. To perform IHC, embryos were rehydrated, washed with PBS-TX, and permeabilized with 10 µg/mL of protease K in PBS-TX at 37°C (in a water bath) for 10 minutes. Then, they were washed three times using PBS-TX for 10 minutes and put in blocking buffer at room temperature (RT) for 1 hour. Following this, whole embryos were incubated with Ki67 rabbit antibody at a dilution of 1:200 (Abcam, Cambridge, UK), at RT for 2 hours and stored overnight at 4°C. After that, the embryos were washed and incubated with the second antibody, Alexa fluor 633 anti-rabbit at a 1:200 dilution (Invitrogen) at RT for 2 hours and stored overnight at 4°C. The immune-

stained whole embryos were arranged on a microplate and covered with 1% low melting agar to take pictures with a confocal microscope.

Toxicity Test and *in vivo* inhibitor treatment.

For the *in vivo* toxicity test, 1mL of drug-containing egg water was put into the wells of a 24-well plate. Six noninjected 3-dpf zebrafish embryos were placed in each well, maintained at 34°C and observed daily until 8 dpf. The drugs were refreshed every 2 days and all experiments were performed in triplicate. A drug concentration was considered nontoxic when survival was equal or higher than 80%.

At 2 dpf, embryos were injected with CRMM-1, CRMM-2, or CM2005.1 cells and treatment with Vemurafenib was started at 1 dpi. They were treated for 5 days with the inhibitor, changing the egg water and inhibitor twice, and photographed at 1 and 6 dpi using the fluorescence stereo microscope. Using ImageJ software,[31] pixel numbers were determined.

Results

Growth Kinetics of Tomato-Red Cells *In Vitro*

Our goal was to establish a CM xenograft model allowing the *in vivo* screening of drugs. We used tdTomato-red expressing cells to track the proliferation and migration of tumor cells *in vivo*. To verify the possible adverse effect of tdTomato expression on cellular growth kinetics, we used an In-Cell Western proliferation assay. No effect was observed until 5 days of incubation (Supplementary Fig. S1), indicating that we could use the tdTomato overexpressing cells in the zebrafish.

Injection Sites

To establish the model, we tested three different injection sites: engraftment around the eye, in the yolk sack, or in the duct of Cuvier. The duct of Cuvier is the common cardinal vein formed by the left and right posterior cardinal veins joining up with the anterior cardinal vein. The duct of Cuvier functions as an embryonic vein structure collecting all venous blood and leads directly to the heart's sinus venosus; it carries the blood ventrally across the yolk sac.[33] Using this site of injection ensures a rapid and a near complete dissemination of injected cancer cells throughout the blood circulation.[34]

Injecting tumor cells around the eye was technically challenging because of the small size of the eye, limiting throughput and increasing lethality. After injecting tumor cells around the eye, the cells disseminated to the head, inside the eye, and inside the circulation (Figs. 1A, 1B). Injecting cells inside the yolk sac was easy to perform, but after 6 dpi, many cells had died (Figs. 1C, 1D). Injections into the duct of Cuvier were relatively easy to perform and cells survived and proliferated (Figs. 1E, 1F).

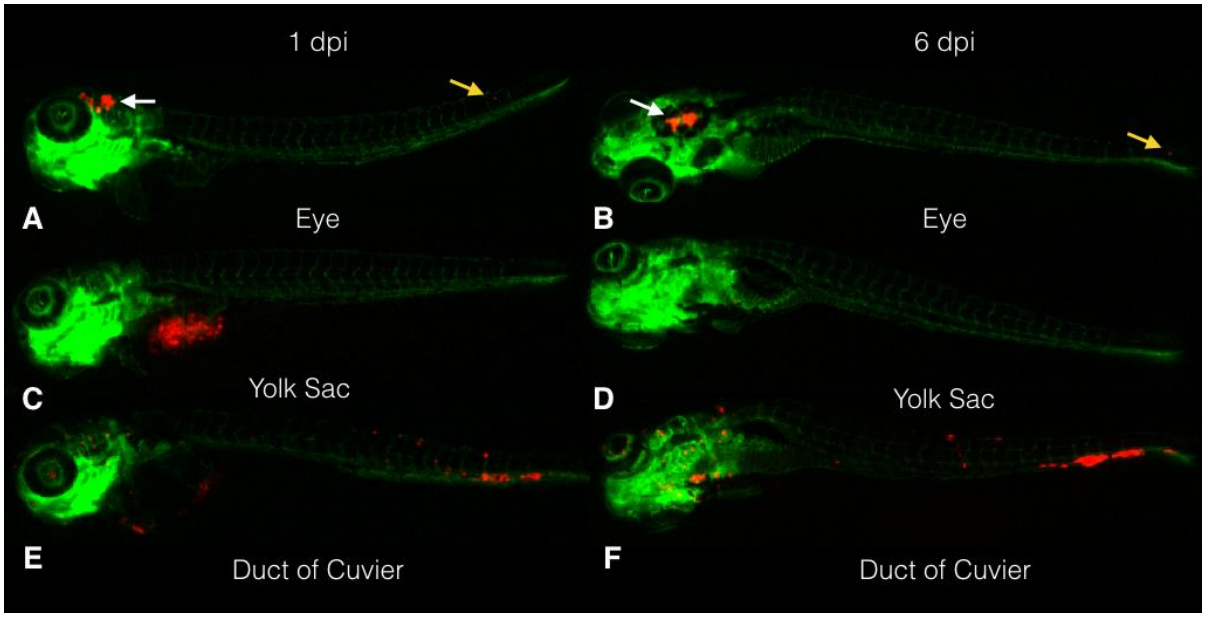

Figure 1. Stereo fluorescence image of zebrafish embryos engrafted with CM cells (vasculature in *green* and CM cells in *red*). The embryos were injected at 2 dpf with CRMM-1 CM cells labeled with tomato-red (*red*). Photographs taken of the same embryo that had been injected with CM cells around the eye at 1 (**A**) and 6 dpi (**B**), showing cells inside the head (*white arrows*) and in the tail (*yellow arrow*). Following injection in the yolk sac, an embryo shows the cells in the yolk sac at 1 (**C**), but not 6 dpi (**D**). After injection of cells into the duct of Cuvier, cells are seen inside the circulation at 1 dpi (**E**), mainly in the tail and inside the eye. The same embryo shows a cluster in the tail and cells inside the eye at 6 dpi (**F**). The stereo fluorescent images (original magnification: ×20) are representative of >10 independent experiments.

The injection into the duct of Cuvier ensures that the cells have access to the endothelium and their intrinsic adhesion molecules and nutrients and helps to disseminate the cells throughout the body. As the duct of Cuvier is the most reliable and biologically relevant injection site, we used this site in all subsequent experiments. The cumulative survival curves of all groups were above 80% (Fig. 2).

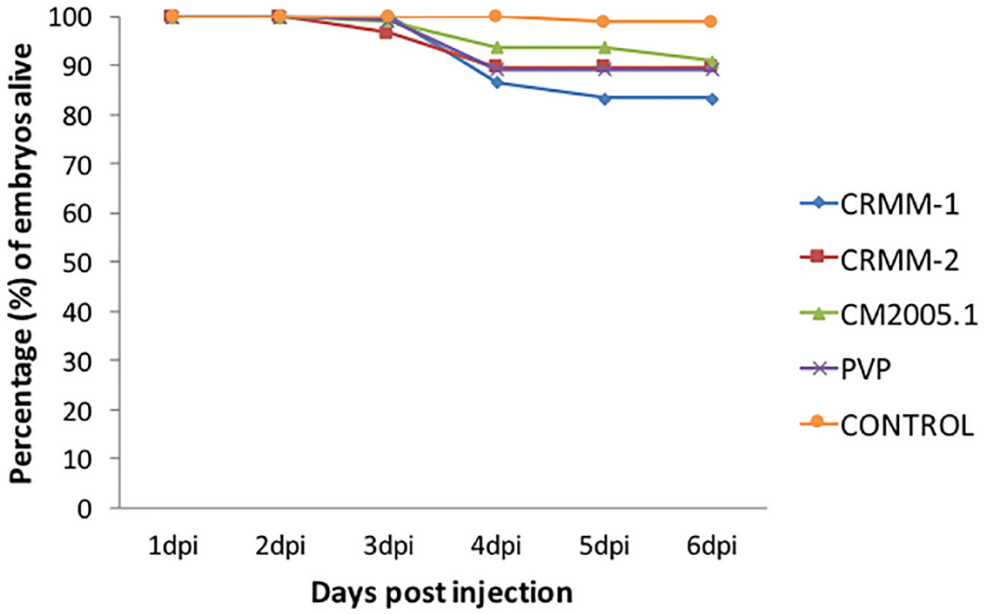

Figure 2. Survival of (*fli:GFP*) *Casper* embryos injected with different types of CM cells, after injection of 200 to 400 cells in the duct of Cuvier on 2 dpf. The number of embryos were: *n*CRMM-1 = 90, *n*CRMM-2 = 201, *n*CM2005.1 = 221, *n*PVP = 121, and *n*Control = 96.

Phenotype of CM Cells in Zebrafish

After cells had been injected inside the duct of Cuvier, migration was assessed. With all three cell lines, 10% to 30% of the embryos had cells inside the eye and between 58% and 64% of embryos showed cells in the tail (Fig. 3). At 1 dpi, cells from all three cell lines had disseminated to the eye and to the tail, forming clusters at 4 and 6 dpi, with more prominent clusters occurring when we used cell line CM2005.1 (Fig. 4). Cells from all three cell lines grew inside, outside, and around vessels during the 6 days of observation (Fig. 4). More tumor cells were observed at 6 dpi than at 1 dpi ($P < 0.001$ for CRMM-1, $P = 0.04$ for CRMM-2, and $P = 0.001$ for CM2005.1) (Fig. 5).

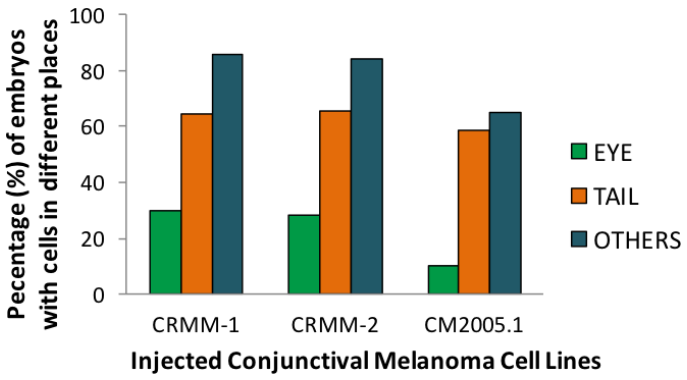

Figure 3. Location of tumor cells at 6 dpi in (*fli:GFP*) *Casper* zebrafish embryos after injection of 200 to 400 cells of the different CM cell lines into the duct of Cuvier at 2 dpf. Tumor cell locations were scored using a stereo fluorescence microscope. The same embryo could harbor cells in more than one place at the same time. "Others" indicates cancer cell retention/outgrowth at the base of the heart or in the head region. The number of embryos used was $n_{CRMM-1} = 70$, $n_{CRMM-2} = 81$, and $n_{CM2005.1} = 77$.

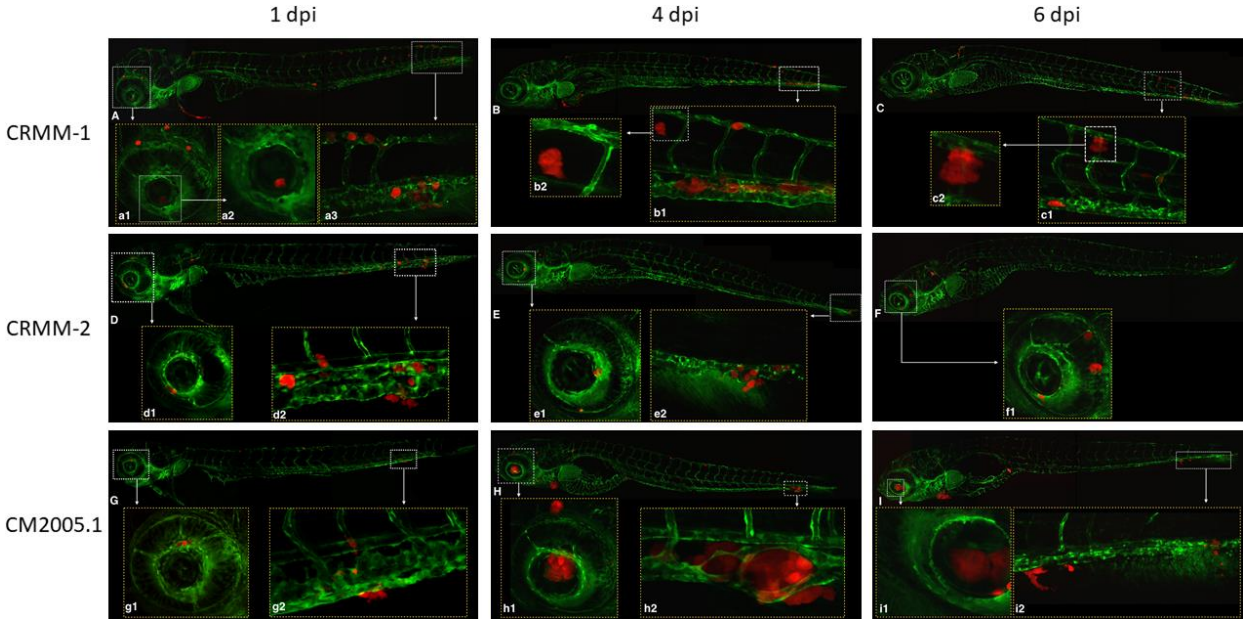

Figure 4 Confocal micrographs of the observed phenotypes at 1, 4, and 6 dpi after engraftment of three CM cell lines via the duct of Cuvier in (*fli:GFP*) *Casper* zebrafish embryos. At 1 dpi, CRMM-1 (A), CRMM-2 (D), and CM2005.1 (G) cells were already inside the eye (a1, a2, d1, g1) and in the tail (a3, d2, g2). At 4 (B, E, H), and 6 dpi (C, F, I), cells formed clusters in the tail and in the eye in all three cell lines (data not shown). The clusters were more evident in the tail (h2) and in the eye (h1, i1) after injection of cell line CM2005.1. The three cell lines (data not show) grew inside (a3, b1, d2, e2, g2, h2, i2), outside (b2), and around (c2) the vessels and the cells could be found inside the eye (f1, i1) until 6 dpi. The images were acquired using a Leica TCS SPE confocal microscope and managed in ImageJ software. Images (A–I) ×10 dry objective. All the other images: ×20 dry objective. *Red*: cells labeled with tdTomato; *green*: GFP-endothelial cells of the (*fli:GFP*) *Casper* lines.

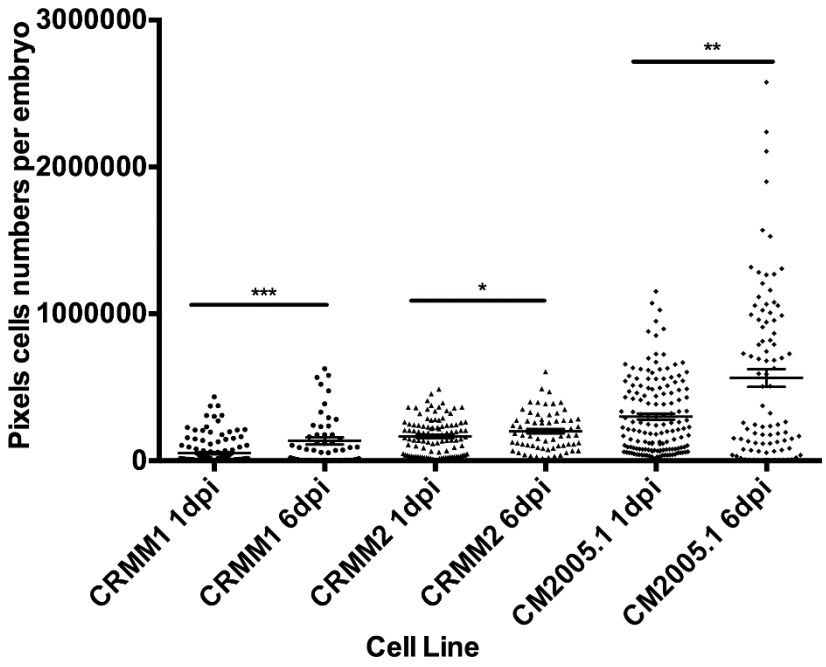

Figure 5. Outgrowth of CM cells *in vivo* in (*fli:GFP*) *Casper* zebrafish embryos engrafted with 200 to 400 cells of CM cell lines at 2 dpf via the duct of Cuvier. Images were taken at 1 and 6 dpi. Each point means one embryo and the pixel number indicates the amount of fluorescence cells counted using ImageJ software. Statistical significances were calculated by general linear model (ANOVA) and *P* values were as follows: **P* < 0.05, ***P* < 0.01, ****P* < 0.001. For all groups: *n* ≥ 51.

Immunohistochemistry (IHC)

As the image analysis suggested that the cells had divided inside the zebrafish, we tested this using IHC with the Ki67 antibody at 6 dpi. Some cells from all three CM cell lines stained positive for Ki67 at 6 dpi and in some cases, mitotic figures in tumor cells were observed (Fig. 6). These findings show that the CM cells proliferated 6 days after injection inside the duct of Cuvier.

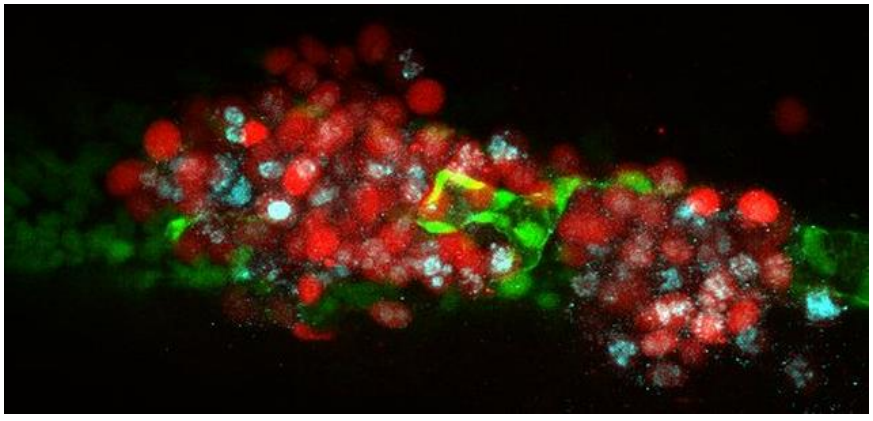

Figure 6. Confocal image of immunohistochemistry with Ki67 in a whole 6 dpi (*fli:GFP*) *Casper* zebrafish embryo. There were 200 to 400 CRMM-1 td-Tomato CM cells injected into the duct of Cuvier. We see tumor cell (*red*) migration outside the vessels (*green*); cell proliferation is indicated by Ki67 staining (*blue*). This image of the tail of a live embryo was acquired by confocal microscope (×20 dry objective). Similar images were obtained from all three CM cell lines in >10 independent experiments.

Toxicity test and treatment with vemurafenib *in vivo*

Vemurafenib inhibits the proliferation of the CM cell lines *in vitro* in a mutation-dependent way (Supplementary Fig. S2) and was, therefore, used to test the *in vivo* model. The toxicity test resulted in 94% survival at 7 and 8 dpf at a concentration of 0.25 μM, and 94% at 8 dpf when the 0.5-μM concentration was used (Supplementary Fig. S3). For all the other tested concentrations, survival of the embryos was 100%. As the drug concentration was considered nontoxic when survival was equal or higher than 80%, we concluded that vemurafenib was nontoxic to the zebrafish at the evaluated concentrations.

Considering that the highest concentrations of vemurafenib that had been evaluated *in vitro* were 3.2 μM (CRMM-1 and CRMM-2) and 0.32 μM (CM2005.1), and that this compound was nontoxic to the embryos up to a concentration of 4.0 μM, we chose a final concentration 4.0 μM/mL to treat engrafted embryos up to 5 dpi because the compound was added in egg water.

At 5-days post treatment with 4 μM of vemurafenib, we noticed inhibition of CRMM-1 (Fig. 7A) and CM2005.1 (Fig. 7C) cell growth when compared with control groups; proliferation of CRMM-2 was not affected by vemurafenib (Fig. 7B; vemurafenib treatment versus control $P = 0.013$ for CRMM-1, $P = 0.007$ for CM2005.1, and $P = 0.33$ for CRMM-2).

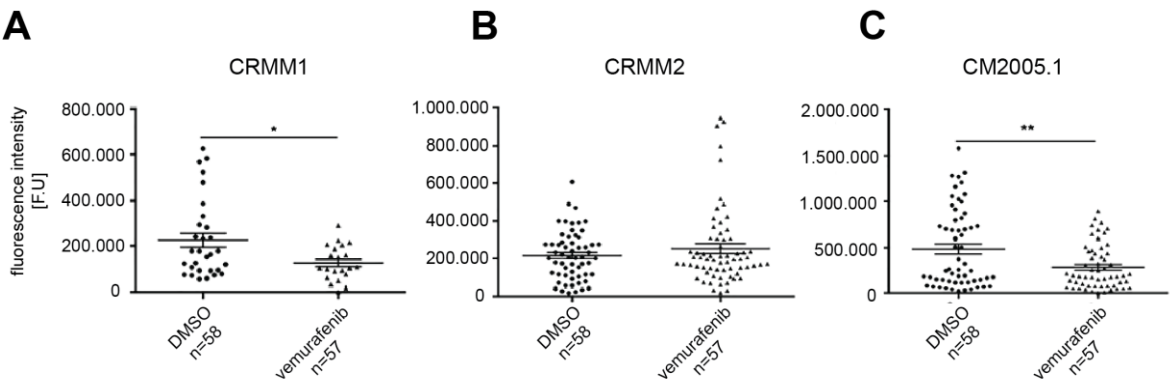

Figure 7. *In vivo* effect of 4-μM Vemurafenib on cell behavior in (*fli:GFP*) *Casper* zebrafish embryos engrafted via the duct of Cuvier with three CM cell lines, determined after 5 days. The images show a decrease in pixel numbers of cell lines CRMM-1 (A) and CM2005.1 (C), but not of CRMM-2 (B). Each point means one embryo and the pixel numbers are the fluorescent pixels counted using ImageJ software. Statistical significances were calculated by general linear model (ANOVA) and *P* values were indicated as follows: **P* < 0.05, ***P* < 0.01.

Discussion

Our results showed that when CM cells were injected around the eye (at 2 dpf), they accidentally passed into the circulation and frequently ended up in the tail, head, and ocular vessels. This is because there is a complex system of retinal blood vessels in the zebrafish's eye and intraocular vessels are already detected at 60-hours postfertilization[35].The vasculature develops quickly and, at 5 dpf, reaches from the optic disk to the intraocular lens. This site of injection is so rich in vessels that it has been used to inject cells into the circulation in adult zebrafish[36].

We believe that the injection in the yolk sac leads to cell death of the many engrafted cells because the yolk sac is a lipid-rich environment devoid of blood circulation and sparse in nutrient and adhesion molecules. Furthermore, some cells that had been injected in the yolk sac passively migrated to the embryo's body (e.g., the tail, the head or inside the eye, directly after engraftment). This may have occurred because the cells were inadvertently introduced inside the circulation, as the duct of Cuvier, the common cardinal vein, crosses the yolk sac and leads directly to the heart's venous sinus[33]. In contrast to Haldi et al.,[30] who recommended that injections can be made anywhere in the yolk sac, we believe that the injections can be done in the yolk sac while avoiding the duct of Cuvier, but we did not use this approach: our experiments show that injecting into the Duct of Cuvier led to the most reproducible results. The model that we used represents a metastatic disease model, as human CM cells were injected into the circulation of the zebrafish embryos[37].

Using Ki67 staining, we showed that CM cells survived and proliferated inside the fish until at least 6 dpi. We furthermore observed that 58% to 64% of all engrafted embryos showed dissemination of the cells to the tail at 6 dpi, demonstrating a preference of all three cell lines for this site. We believe that the reason why these cells ended up in the tail was mainly because of the presence of the caudal hematopoietic tissue (CHT) in this site. Myeloid cells have been detected at the posterior end of the CHT and are

involved in the process of both tumor vascularization and invasion, which are critical steps toward localized tumor growth and micro-metastasis formation[38]. Once the cells have reached the CHT, we believe that they are arrested there through physical entrapment and due to a slower blood flow. The CHT harbors numerous stem cell components driving metastasis formation and proliferation. The zebrafish embryo can be used to study the interaction between the innate immune system (neutrophils and macrophages) and tumor cell behavior: this is one of the reasons why we set out to develop this CM model[37,38].

The mutations involved in CM are more similar to cutaneous melanoma than uveal melanoma. Cutaneous melanoma and CM harbor a *B-RAF* mutation, while in most uveal melanoma, *GNAQ/GNA11* mutations occur[39,40]. While all three cell lines were derived from primary tumors and not from metastases, all of them migrated into the eyes in a considerable proportion of engrafted zebrafish embryos (30% of CRMM-1, 28% of CRMM-2, 10% of CM2005.1). However, metastatic cutaneous human melanoma did not migrate to the eyes when injected into zebrafish embryos[30,41]. In a recent study,[42] primary and metastatic uveal melanoma cells were seen to migrate to the eye in 10% of the embryos. This suggests that the migration of eye cancer cells to the eye is not mutation dependent, but controlled by others factors, which should be evaluated in the future.

We determined whether the CM zebrafish model can be used to test drugs: vemurafenib inhibited the growth of cell lines CRMM-1 and CM2005.1 *in vivo* and *in vitro*, and not of cell line CRMM-2. The results *in vitro* were expected as CRMM-1 and CM2005.1 harbor a *B-RAF V600E* mutation, while the CRMM-2 cell line contains an *N-RAS Q61L* mutation[17,27]. Vemurafenib was approved in 2011 by the Food and Drug Administration for treatment of unresectable melanoma harboring *B-RAF V600E* mutations[43] and is a potent agent for treatment of *B-RAF V600E*-positive melanoma[44]. It has been used to target metastases and a primary CM[45]. Vemurafenib was previously shown to have a selective effect on CM cell lines *in vitro*[46] and we used that information to validate the usability of the zebrafish CM model. In our experiments, the effects of the vemurafenib in the treatment of engrafted embryos were the same as those observed *in vitro* showing that the zebrafish embryo model can be used in drug screens against human CM.

Conclusions

The zebrafish model that we describe here allows migration and proliferation of three human CM cell lines. These cells induced a phenotype that was highly reproducible when injected via the duct of Cuvier. The engrafted embryos tolerated the treatment with vemurafenib well, while this inhibitor affected the cell proliferation *in vivo* in a mutation-dependent manner. Thus, we conclude that the (*fli:GFP*) *Casper* zebrafish embryos can be used as an efficient animal model to study metastatic behavior of CM cells and for preclinical testing of new treatments against human CM.

Acknowledgments

The authors thank Aart G. Jochemsen for transducing the cells with tomato-red.

Supported by grants from the National Council of Technological and Scientific Development CNPq (200746/2015-4; Brasilia, DF, Brazil), and the China Scholarship Council (Beijing, China).

Disclosure: K.C.S. Pontes, None; **A. Groenewoud**, None; **J. Cao**, None; **L.M.S. Ataide**, None; **E. Snaar-Jagalska**, None; **M.J. Jager**, None

References

1. Harooni H, Schoenfield LR, Singh AD. Current appraisal of conjunctival melanocytic tumors: classification and treatment. *Future Oncol*. 2011; 7: 435–446.
2. Tuomaala S, Eskelin S, Tarkkanen A, Kivela T. Population-based assessment of clinical characteristics predicting outcome of conjunctival melanoma in whites. *Invest Ophthalmol Vis Sci*. 2002; 43: 3399–3408.
3. Yu GP, Hu DN, McCormick S, Finger PT. Conjunctival melanoma: is it increasing in the United States? *Am J Ophthalmol*. 2003; 135: 800–806.
4. Triay E, Bergman L, Nilsson B, All-Ericsson C, Seregard S. Time trends in the incidence of conjunctival melanoma in Sweden. *Br J Ophthalmol*. 2009; 93: 1524–1528.
5. Riechardt AI, Maier AB, Nonnenmacher A, et al. B-Raf inhibition in conjunctival melanoma cell lines with PLX 4720. *Br J Ophthalmol*. 2015; 99: 1739–1745.
6. Shields CL, Markowitz JS, Belinsky I, et al. Conjunctival melanoma: outcomes based on tumor origin in 382 consecutive cases. *Ophthalmology*. 2011; 118: 389–395.
7. Errington JA, Conway RM, Walsh-Conway N, et al. Expression of cancer-testis antigens (MAGE-A1, MAGE-A3/6, MAGE-A4, MAGE-C1 and NY-ESO-1) in primary human uveal and conjunctival melanoma. *Br J Ophthalmol*. 2012; 96: 451–458.
8. Jovanovic P, Mihajlovic M, Djordjevic-Jocic J, et al. Ocular melanoma: an overview of the current status. *Int J Clin Exp Pathol*. 2013; 6: 1230–1244.
9. Werschnik C, Lommatzsch PK. Long-term follow-up of patients with conjunctival melanoma. *Am J Clin Oncol*. 2002; 25: 248–55.
10. Missotten GS, Keijser S, De Keizer RJ, De Wolff-Rouendaal D. Conjunctival melanoma in the Netherlands: a nationwide study. *Invest Ophthalmol Vis Sci*. 2005; 46: 75–82.
11. Shildkrot Y, Wilson MW. Conjunctival melanoma: pitfalls and dilemmas in management. *Curr Opin Ophthalmol*. 2010; 21: 380–386.
12. Gear H, Williams H, Kemp EG, et al. B-Raf mutations in conjunctival melanoma. *Invest Ophthalmol Vis Sci*. 2004; 45: 2484–2488.
13. Goldenberg-Cohen N, Cohen Y, Rosenbaum E, et al. T1799 B-Raf mutations in conjunctival melanocytic lesions. *Invest Ophthalmol Vis Sci*. 2005; 46: 3027–3030.
14. Griewank KG, Westekemper H, Schilling B, et al. Conjunctival melanoma harbor BRAF and NRAS mutations-response. *Clin Cancer Res*. 2013; 19: 6331–6332.
15. Satyamoorthy K, Li G, Guerrero MR, Brose MS, et al. Constitutive mitogen-activated protein kinase activation in melanoma is mediated by both BRAF mutations and autocrine growth factor stimulation. *Cancer Res*. 2003; 63: 756–759.
16. Banerji U, Affolter A, Judson I, Marais R, Workman P. BRAF and NRAS mutations in melanoma: potential relationships to clinical response to HSP90 inhibitors. *Mol Cancer Ther*. 2008; 7: 737–739.
17. De Waard NE, Cao J, McGuire SP, et al. A murine model for metastatic conjunctival melanoma. *Invest Ophthalmol Vis Sci*. 2015; 56: 2325–2333.
18. Schlereth SL, Iden S, Mescher M, et al. A novel model of metastatic conjunctival melanoma in immune-competent mice. *Invest Ophthalmol Vis Sci*. 2015; 56: 5965–5973.

19. Konantz M, Balci TB, Hartwig UF, et al. Zebrafish xenografts as a tool for *in vivo* studies on human cancer. *Ann N Y Acad Sci*. 2012; 1266: 124–137.

20. Granato M, Nusslein-Volhard C. Fishing for genes controlling development. *Curr Opin Genet Dev*. 1996; 6: 461–468.

21. Chen JN, Fishman MC. Zebrafish tinman homolog demarcates the heart field and initiates myocardial differentiation. *Development*. 1996; 122: 3809–3816.

22. Tulotta C, Stefanescu C, Beletkaia E, et al. Inhibition of signaling between human CXCR4 and zebrafish ligands by the small molecule IT1t impairs the formation of triple-negative breast cancer early metastases in a zebrafish xenograft model. *Dis Model Mech*. 2016; 9: 141–153.

23. Stoletov K, Montel V, Lester RD, Gonias SL, Klemke R. High-resolution imaging of the dynamic tumor cell vascular interface in transparent zebrafish. *Proc Natl Acad Sci U S A*. 2007; 104: 17406–17411.

24. White RM, Sessa A, Burke C, et al. Transparent adult zebrafish as a tool for *in vivo* transplantation analysis. *Cell Stem Cell*. 2008; 2: 183–189.

25. Nareyeck G, Wuestemeyer H, von der Haar D, Anastassiou G. Establishment of two cell lines derived from conjunctival melanomas. *Exp Eye Res*. 2005; 81: 361–362.

26. Keijser S, Maat W, Missotten GS, De Keizer RJ. A new cell line from a recurrent conjunctival melanoma. *Br J Ophthalmol*. 2007; 91: 1566–1567.

27. De Waard NE, Kolovou PE, McGuire SP, et al. Expression of multidrug resistance transporter ABCB5 in a murine model of human conjunctival melanoma. *Ocul Oncol Pathol*. 2015; 1: 182–189.

28. Carlotti F, Bazuine M, Kekarainen T, et al. Lentiviral vectors efficiently transduce quiescent mature 3T3-L1 adipocytes. *Mol Ther*. 2004; 9: 209–17.

29. Lawson ND, Weinstein BM. *In vivo* imaging of embryonic vascular development using transgenic zebrafish. *Dev Biol*. 2002; 248: 307–318.

30. Haldi M, Ton C, Seng WL, McGrath P. Human melanoma cells transplanted into zebrafish proliferate, migrate, produce melanin, form masses and stimulate angiogenesis in zebrafish. *Angiogenesis*. 2006; 9: 139–151.

31. Schindelin J, Arganda-Carreras I, Frise E, et al. Fiji: an open-source platform for biological-image analysis. *Nat Methods*. 2012; 9: 676–682.

32. R Development Core Team. *R: A Language and Environment for Statistical Computing*. Vienna: R Foundation for Statistical Computing; 2012.

33. Kimmel CB, Ballard WW, Kimmel SR, Ullmann B, Schilling TF. Stages of embryonic development of the zebrafish. *Dev Dyn*. 1995; 203: 253–310.

34. Helker CSM, Schuermann A, Karpanen T, et al. The zebrafish common cardinal veins develop by a novel mechanism: lumen ensheathment. *Development*. 2013; 140: 2776–2786.

35. Alvarez Y, Cederlund M, Cottell D, et al. Genetic determinants of hyaloid and retinal vasculature in zebrafish. *BMC Dev Biol*. 2007; 7: 114.

36. Pugach EK, Li P, White R, Zon L. Retro-orbital injection in adult zebrafish. *J Vis Exp*. 2009; (34): e1645.

37. Feng Y, Martin P. Imaging innate immune responses at tumour initiation: new insights from fish and flies. *Nature Rev Cancer*. 2015; 15: 556–562.

38. He S, Lamers GEM, Beenakker JM, et al. Neutrophil-mediated experimental metastasis is enhanced by VEGFR inhibition in a zebrafish xenograft model. *J Pathol*. 2012; 227: 431–445.

39. Sendlove HE, Damato BE, Humphreys J, Barker KT, Hiscott PS, Houlston RS. BRAF mutations are detectable in conjunctival but not uveal melanomas. *Melanoma Res*. 2004; 14: 449–452.

40. Van Raamsdonk CD, Griewank KG, Crosby MB, et al. Mutations in GNA11 in uveal melanoma. *N Engl J Med*. 2010; 363: 2191–2199.

41. Lee LMJ, Seftor EA, Bonde G, Cornell RA, Hendrix MJ. The fate of human malignant melanoma cells transplanted into zebrafish embryos: Assessment of migration and cell division in the absence of tumor formation. *Dev Dyn*. 2005; 233: 1560–1570.

42. Van Der Ent W, Burrello C, Lange MJ, et al. Embryonic zebrafish: different phenotypes after injection of human uveal melanoma cells. *Ocul Oncol Pathol*. 2015; 1: 170–181.

43. Bollag G, Tsai J, Zhang J, et al. Vemurafenib: the first drug approved for BRAF-mutant cancer. *Nat Rev Drug Discov*. 2012; 11: 873–886.

44. Flaherty KT, Puzanov I, Kim KB, et al. Inhibition of mutated, activated BRAF in metastatic melanoma. *N Engl J Med*. 2010; 363: 809–819.

45. Pahlitzsch M, Bertelmann E, Mai C. Conjunctival melanoma and BRAF inhibitor therapy. *J Clin Exp Ophthalmol*. 2014; 5: 322.

46. Cao J, Renier C, Aart G, et al. Targeting of the MAPK and AKT pathways in conjunctival melanoma shows potential synergy. *Oncotarget*. 2016; 8: 58021–58036.

Chapter 4:

Patient-derived zebrafish xenograft models reveal ferroptosis as a fatal and druggable weakness in metastatic uveal melanoma

Chapter 4: Patient-derived zebrafish xenograft models reveal ferroptosis as a fatal and druggable weakness in metastatic uveal melanoma

Arwin Groenewoud[1], Jie Yin[1], Maria Chiara Gelmi[2], Samar Alsafadi[3], Fariba Nemati[3], Didier Decaudin[3,4], Sergio Roman-Roman[3], Helen Kalirai[4], Sarah E. Coupland[4], Aart G. Jochemsen[5], Martine J. Jager[2], Ewa Snaar-Jagalska[1]

1) Institute of Biology, Leiden University, Leiden, The Netherlands

2) Department of Ophthalmology, Leiden University Medical Center, Leiden, The Netherlands

3) Laboratory of Preclinical Investigation, Translational Research Department, Institut Curie, University of Paris Saclay, Paris, France

4) Department of Medical Oncology, Institut Curie, Paris, France

4) Liverpool Ocular Oncology Research Centre, Department of Molecular and Clinical Cancer Medicine, University of Liverpool

5) Department of Cell and Chemical Biology, Leiden University Medical Center, Leiden, The Netherlands

Submitted

Abstract

Uveal melanoma (UM) is the most common intraocular melanoma, derived from transformed melanocytes of the uvea. Although treatment of primary UM is usually successful, there is a high risk (up to 50%) of liver metastasis with negligible long-term survival. There are currently no patient-derived animal models that faithfully recapitulate the latter stages of metastatic dissemination of UM, hindering the discovery of curative treatments. To overcome this problem and to accelerate the development of new metastatic UM treatments, we developed a patient-derived zebrafish xenograft (zf-PDX) model, using spheroid cultures generated from metastatic and primary UM tissues. Engrafted UM cells derived from these spheroid cultures give rise to metastatic lesions and recapitulate the molecular features of UMs and their potential drug sensitivity. Importantly, harnessing this versatile model, we reveal a high sensitivity of circulating UM cells to ferroptosis induction *in vivo* by Erastin and RSL3. Our findings are further corroborated by supportive analysis of patient data implicating ferroptosis as a new, and druggable, target for the treatment of metastatic UM patients, specifically in those with BAP1 loss in the tumor.

Introduction

Uveal melanoma (UM) is an aggressive and deadly ocular cancer, derived from melanocytic cells of the uvea (made up of the iris, choroid, and ciliary body). UM usually carry a low mutational burden when compared to other melanomas. Strikingly, UM almost obligately bear an inactivating *GNA* family mutation (mainly in *GNAQ* and *GNA11*), blocking GTPase activity within this catalytic subunit of the protein, effectively driving oncogenic hyperactivation of G_q or G_{11}[1]. This hyperactivation leads to a subsequent increase in downstream signaling, including the protein kinase C (PKC)/ MAP kinase/ ERK axis[2,3]. UM is characterized by strong prognosticators such as monosomy 3[4–8] and the loss of expression of the *BRCA*-associated-protein 1 (*BAP1*) gene located on chromosome 3, which is usually accompanied by the loss of chromosome 3[9]. Between 7-33% of all primary UM patients develop deadly metastatic disease within 10 years, and this is strongly linked to mutations in the *BAP1* gene. Primary UM is commonly treated by radiotherapy or by enucleation (surgical removal of the eye)[10]. Although this generally leads to effective local control, the prognosis of metastatic UM patients is grim, with a median survival of 3.9 months after detection of

metastases[11]. Metastatic UM responds poorly to conventional and targeted chemotherapy[12]. In contrast to cutaneous melanomas, UM is largely refractory to immunotherapy, probably due to its low mutational burden[13,14].

Although metastatic spread of cancer kills the vast majority of cancer patients, the process in itself is vastly inefficient, with between 90-99% of all circulating cancer cells dying before finding a suitable metastatic niche[15–17]. This fatal weakness of UM cells limits dissemination and has hampered successful generation of animal models for therapy development. Conversely, this does highlight an exploitable opportunity for the development of novel treatments. Recent discoveries have uncovered the role of ferroptosis in the suppression of metastasis development, contributing to the attrition of circulating tumor cells[18,19].

Ferroptosis is a non-apoptotic form of regulated cell death that is caused by cystine depletion and overproduction of lipid-based reactive oxygen species (ROS), particularly lipid hydroperoxide, in an iron-dependent manner. SLC7A11, the catalytic subunit of the cystine/glutamate antiporter (system X_c^-), is the major transporter of extracellular cystine. Intracellular cystine is rapidly converted to cysteine and serves as the precursor for glutathione synthesis. Glutathione peroxidase 4 (GPX4) protects cells against membrane lipid peroxidation and inhibits ferroptosis. In brief, *GPX4* enzymatically reduces oxidized phospholipids, under the presence of intracellular glutathione. Broadly speaking, either inhibition of *GPX4*, or lowering of the amount of available glutathione, would enhance the levels of ROS, thereby inducing ferroptosis [19]. Cells that exhibit oncogenic hyperactivation of the RAS-signaling cascade are sensitized to this type of cell death due to a purported de-regulation of iron homeostatic mechanisms concurrently affected[20]. The fact that over 90% of UM carry somatic *GNAQ*/11 mutations[21] which are known to activate the RAS-MAP kinase pathway, and SLC7A11 being reported as a key downstream target of BAP1[22], prompted us to consider ferroptosis as a druggable pathway in UM. Paradoxically, in contrast to the lethal nature of metastatic UM, no reproducible metastatic xenograft models have been established that are suitable for drug screening. Recently generated, patient-derived murine xenograft (PDX) models have been used to screen new drug combinations[23–25]; however, the PDXs are commonly grown subcutaneously and do not resemble dissemination of metastatic disease. Concordantly, this lack of metastatic UM models limits the assessment of new treatment strategies. We have sought to mitigate this

shortcoming through the establishment of a versatile, UM patient-derived zebrafish xenograft model (UM zf-PDX), combined with a novel 3D spheroid culture method for UM to ensure that metastatic properties are maintained, in order to recapitulate the final stages of the metastatic cascade.

Here we report the generation of a spheroid-derived UM zfPDX model, and its use for the screening of ferroptosis inducers on metastatic UM. We assess that circulating UM cells are extremely sensitive to ferroptosis induction *in vivo*. We have used this druggable weakness and determined that conventional ferroptosis activators are potent inducers of ferroptotic cell death in a *BAP1*-dependent manner. This new insight opens the way for possible clinical treatment with ferroptosis inducers, after *BAP1* stratification of UM patients.

Materials and methods

Adherent cell culture of UM cells

UM cell lines MP46, MM28, and Xmm66 were provided by Dr. Samar Alsafadi (Institute Curie)[24] and cell lines Omm1[26], Mel285[27], and Omm2.3[27] from Dr. Aart G. Jochemsen (Leiden University Medical Center), respectively. All lines were cultured in Dulbecco's modified eagle's medium (DMEM) containing 10% fetal bovine serum (FBS, Gibco, Thermo Fisher Scientific, Waltham, MA USA), supplemented with Glutamax (Gibco). Cell lines were kept in culture up to 20 passages and intermittently checked for the presence of mycoplasma, using the PCR-based mycoplasma detection kit from American type cell culture (ATCC, Mycoplasma detection kit), following the manufacturer's prescriptions.

Lentiviral transduction of UM spheroid cultures

Both adherent cell culture and spheroid cultures were lentivirally transduced as described in Heitzer *et al.,* 2019[28]. In brief, the adherent cell cultures were cultured in the presence of lentiviral particles containing ΔLTR flanked CMV:tdTomato-blasticidin (Addgene#106173) and 8µg/mL polybrene (Sigma, Zwijndrecht, the Netherlands), whereafter the medium was exchanged for standard culture medium. Transduced adherent UM lines were selected with 2µg/mL blasticidin (Gibco) for approximately 3 passages (approximately 10 days) until all cells were positive for the transduced tdTomato construct. For obtaining a cultured spheroid, the procedure was the same,

except of the generation of a single cell suspension prior to the addition of the viral particles and the omission of the selection.

Establishment of stable PDX-derived spheroid cultures

Metastatic PDX tissues that had been frozen down in either FBS containing 10% dimethyl sulfoxide (DMSO) or primary PDX tissues that were frozen in neuronal stem cell medium (NSC medium, Stemcell technologies, Köln, Germany) containing 10% DMSO were thawed by brief incubation at 37°C and were transferred to basal NSC medium. Subsequently, the medium was exchanged for 10 mL DMSO-free medium containing 5 mg/mL Primocin (Invivogen, Toulouse, France), the tissue was minced in 10mL basal NSC in a cell culture petri dish using a sterile scalpel blade. The material was collected in a 50mL centrifuge tube and supplemented with 0.01 mg/mL Liberase TL (Roche, Woerden, the Netherlands); the suspended tumor tissue was incubated at 37°C for 3-5 hours while shaking at 250 rpm, and the tubes were subsequently vortexed intermittently during this incubation to break up any tissue aggregates. The disaggregation process was monitored macroscopically; at the end of the procedure a small sample was observed under an inverted microscope to ensure completion of dissociation, otherwise the dissociation was prolonged. After the cell suspension was passed through a sterile 30 µm cell strainer to remove all cell and extra-cellular matrix aggregates, cells were pelleted and suspended in complete NSC medium (supplemented with both 1x B27 (Gibco) and 1x N2 (Gibco), 20 ng/mL bFGF (Peprotech, Hamburg, Germany), 20 ng/mL EGFP (Peprotech), 5 U/mL heparin and 1x primocin (Invivogen), containing 5% FCS and 200mM Glutamax). The cell suspension was diluted and plated in a 24-well ultra-low attachment plate (Corning, Wiesbaden, Germany), in approximately 8-12 wells with a 0.25 cm^3 tumor volume at the start of the dissociation. After several days of culture, the cells coalesced into larger cell aggregates to be disrupted prior to labelling and engraftment.

Staining of UM spheroid culture derived cells prior to implantation into embryonic zebrafish hosts

Spheroids were collected and concentrated through centrifugation (200 x g, 5 min). The cells were resuspended in 3mL TrypLE (Gibco), and after a 10-minute incubation at 37°C, combined with intermittent agitation with a 1000µL pipette cells, aggregates were broken up by pipetting up and down. TrypLE was subsequently inactivated by addition of 7mL complete NC medium, followed by centrifugation.

The red intra lipid dye CM-DiL (Sigma) was used to stain the cells to visualize cancer cell proliferation and metastatic initiation. In brief, the disaggregated cell suspension was concentrated to 2 mL in NC complete medium in a 15mL tube and supplemented with 2.5 µM CM-DiL followed by 30 min incubation at 37°C in the dark. The unbound labelling reagent was removed through centrifugation after addition of 8 mL complete NC medium.

Establishment of maximum tolerated drug dose in zebrafish

Prior to either single or combinatorial drug treatment on engrafted zebrafish larvae, we established a maximum tolerated dose (MTD), where we have at least 80% survival of the treated un-injected larvae. To achieve this, we crossed Casper mutant zebrafish, raised the larvae up to 2 days post fertilization (dpf) and placed 6 larvae per well in a cell-culture grade 24-well plate (Corning). We subjected the larvae to a concentration range of 10µM-156 nM of all tested compounds, in a two-fold dilution series. All compounds were changed every other day to ensure optimal stability of drug levels throughout the duration of the treatment. At 8dpf (corresponding to 6dpi for injected larvae), we scored survival and plotted the survival using Graphpad Pro 8 (Graphpad software LLC, San Diego, CA). The highest concentration at which over 80% of the treated larvae survived was chosen as the MTD for the treatment of the engrafted larvae. For combinatorial treatments to determine synergism, we followed the titrated MTD of compound A (the purported sensitizer) with a similar dilution series of compound B (the purported synergistic compound). We titrated from MTD A combined with 10µM-156 nM compound B to attain a suitable treatment concentration where >80% of all treated larvae survived up to 8dpf for a 6-day treatment (starting at 2dpf).

Preparation of cells for implantation into embryonic zebrafish host.

Cells were prepared for engraftment in accordance with the protocol published by Groenewoud *et al.,* 2021[29]. To facilitate the engraftment of single cells, cells were disaggregated immediately prior to implantation, concentrated by centrifugation at 200 x g for 5 minutes, after which the supernatant was removed and the pellet resuspended in 3 mL TrypLE (Gibco). This was followed by a 10-minute incubation with intermittent agitation (gentle vortexing every 2 minutes). The proteolytic activity of TrypLE was negated through the addition of 7 mL spheroid culture medium after which the cell suspension was pelleted at 200 x g. The cells were washed with Dulbecco's PBS without Ca^{2+} and Mg^{2+} (DPBS, Gibco). PBS was removed after 5 minutes of

centrifugation at 200 x g and subsequently after 30 seconds at 200 x g to ensure that all remaining DPBS is removed and can completely be replaced with sterile 2% PVP_{40} in DPBS. Cells were injected at a concentration of 250 x 10^6 cells/mL. The cells were transferred into a glass capillary needle (needle preparation as described in Groenewoud *et al.* 2021[29]), using a micro loader tip (Eppendorf, Nijmegen, the Netherlands).

Injection of cancer cells into zebrafish

Either *tg(fli:GFPx casper)*[30,31] or *tg(casper)*[32] fish were crossed prior to the start of the experiment, and larvae were cleaned every day after harvesting up to 2dpf. The larvae were collected after they had hatched from the chorion, and the water was removed along with the chorion debris, together with all unhatched larvae (unhatched larvae were removed with the same strainer as was used to collect the eggs at harvesting).

Approximately 300-400 cells were injected into the duct of Cuvier (doC, the embryonic common cardinal vein) of 2dpf zebrafish larvae. After injection, dead larvae were removed and the residual larvae were placed in clean eggwater. The larvae were screened using a fluorescent stereo microscope, selecting all individuals that displayed no bodily malformation and that had clearly visible cell accumulation in the caudal vein and caudal hematopoietic tissue. When using Casper transgenic zebrafish, solely the presence of cells in the tail and lack of malformations was used as a screening criterion. All positively-selected individuals were moved to a clean petri dish, and after completing the screening, the positively-selected pool of individuals was screened once again to ensure that no un-injected or otherwise aberrant individuals were placed in the treatment pool.

Confocal imaging of zebrafish xenografts

Zebrafish were anaesthetized with 0.002% tricaine (MS222, Sigma) in eggwater and embedded in 1% low melting temperature agarose dissolved in eggwater. The larvae were positioned with a trimmed down microloader tip (Eppendorf) as to be laterally oriented, gently pressing the larvae down to ensure close proximity to the lens of the confocal microscope and a level orientation of the larvae. Images were captured of both green (GFP) and red tdTomato/CMDiI channels and were recorded as approximately 1 x 4 stitches at 10x magnification using a Leica sp8 confocal

microscope (Leica, Wetzlar, Germany). Consecutive stitch sequences were processed into a single image using Fiji [33] using the plugin by Preibisch et al., 2009 [34].

IHC analysis of engrafted zebrafish larvae

Engrafted zebrafish were euthanized with tricaine and fixed for 16 hours in ice cold 4% paraformaldehyde in PBS. After fixation, larvae were washed with PBS containing 0.05% tween 20 (v/v) and 200mM Glycine. Larvae were stored in the dark at 4 °C until further processing. Fixed zebrafish larvae were arrayed in a grid and embedded in agarose (sphereoQ, Hispanagar, Burgos, Spain). Care was taken to ensure equal localization in the *x, y*, and *z* axes. Larvae were sectioned along the ventral axis, taking care to section through the tailfin and caudal hematopoietic tissue.

Sections were cut at 4 µm from formalin-fixed paraffin embedded (FFPE) blocks of UM cells-containing zebrafish as detailed above, and placed onto X-tra adhesive slides (Leica Biosystems, Milton Keynes, UK). Immunohistochemical (IHC) staining was performed using the Bond RXm Automated Stainer with high pH antigen retrieval and the Bond polymer-refine detection systems in either red or brown chromogen, according to the manufacturers' recommendations (Leica Biosystems). Primary antibodies included mouse anti-melanA (Dako, Agilent, Cheshire UK) and mouse anti-BAP1 (Santa Cruz Biotechnology, USA), both at a concentration of 1 µg/mL. Slides were counterstained with haematoxylin and mounted with a resin-based mountant. Human UM tissue was used as a positive control for each of the primary antibodies. Mouse IgG1 isotype control at a concentration of 1 µg/mL was also included in each assay.

Drug treatment of engrafted UM zf-PDX

All drugs were acquired from Cayman chemical (Ann Arbor, Michigan, USA) and were dissolved in dimethyl sulfoxide (DMSO) unless otherwise stated. All drugs were added at the beginning of the experiment, right after screening of the larvae (in the morning after injection at 1dpi). The drug-containing eggwater was exchanged every other day.

After careful screening of the engrafted zebrafish, larvae were randomly subdivided into a 24-well plate, with 6 individuals per well and 6 wells per condition. After plating, the eggwater was gently removed, without disturbing the larvae. Subsequently, the compounds were added, dissolved in eggwater. The volume of vehicle control used was the same as the highest volume of drug added to the plate. Subdividing the larvae

in this manner allowed for the screening of 3 mono treatments combined with one vehicle control or one set of drug combinations, with vehicle control, compound A, compound B and compound A+B.

At 6dpi, the larvae were pooled per condition into a 6-well plate (Corning) and as much as possible of the drug-laced eggwater was removed; after this, the larvae were washed 3 times with 5 mL eggwater to remove all traces on non-internalized drug. From this pool of larvae, 20 random individuals were selected and imaged using a MZ16FA fluorescence microscope equipped with a DFC420C camera (Leica, Wetzlar, Germany). The microscope was set (exposure time and gain) on the control group of each experiment to ensure that there was no signal saturation in the control group and that all larvae with reduced tumor burden would fall within the set margins; focus was adjusted per larva when required. All remaining groups were imaged using the same settings.

Clinical data analysis

The LUMC cohort includes clinical, histopathological, and genetic information on 64 UM cases enucleated between 1999 and 2008 at the Leiden University Medical Centre (LUMC). Clinical information was collected from the Integral Cancer Center West patient records and updated in 2019. For each sample, part of the tumor was snap frozen with 2-methyl butane and used for mRNA and DNA isolation, while the remainder was embedded in paraffin after 48 hours of fixation in 4% neutral-buffered formalin and was sent for histological analysis. Chromosome status was determined with the Affymetrix 250K_NSP-chip and Affymetrix Cytoscan HD chip (Affymetrix, Santa Clara, California, United States of America). RNA was isolated with the RNeasy mini kit (Qiagen, Venlo, The Netherlands) and mRNA expression was determined with the HT-12 v4 chip (Illumina, San Diego, California, United States of America).

Statistical analyses of the LUMC cohort were carried out in SPSS, version 25 (IBM Corp). For survival analysis, Kaplan-Meier and log-rank test were performed with death due to metastases as endpoint. Cases that died of another or unknown cause were censored. The two subpopulations that were compared in each analysis were determined by splitting the total cohort along the median value of mRNA expression for each analyzed gene.

Zebrafish data acquisition and statistical analysis

All zebrafish larval engraftments were performed in a biological duplicate, unless otherwise stated, with >20 individuals per group per biological repeat. All larvae were randomized and entered into either control or experimental groups. For imaging, larvae were randomly selected and imaged using the same exposure setting with a fluorescent stereo microscope. Outliers were removed from all data sets using Graphpad Prism 8.0, (Q5) prior to normalization and combination of all biological replicates. Data were normalized to either control (drug treatment) or to day one (in growth kinetic experiments). Statistical significance was tested with an ANOVA for normally distributed data sets, while otherwise a Kruskal-Wallis test was used. Error bars depict ±SEM. Data are presented as mean ±SEM or mean ±SD. P-values ≤0.05 are considered to be statistically significant (*p ≤ 0.05, **p < 0.01, ***p < 0.001, ****p < 0.0001).

***In vitro* growth assay**

To investigate the effect(s) of inducers (Erastin and RSL3) and inhibitors of ferroptosis (Ferrostatin-1 and Liproxstatin) on cell survival *in vitro,* cell lines were seeded in triplicate or quadruplicate in 96-well plates. The next day, cells were treated with the different compounds. Survival was determined after 5 days of incubation using the Cell Titre-Blue assay (Promega). All cell lines were treated with 4 and 8 µM Erastin and 3 and 6 µM RSL3, with the exception of Mel285 which was treated with 0.05 and 0.2 µM Erastin or RSL3.

qPCR analysis

Spheroid cells were harvested ($1x10^6$) by centrifugation (200 x g for 5 min at 25°C), or in case of adherent cells, after prior trypsinization. Whole RNA was isolated using the Qiagen RNeasy kit (Qiagen) according to the manufacturer's description, reducing sample viscosity by passing the cell lysate 5 times through a sterile 20-gauge needle and treating the isolate on-column with RNase free DNAse (provided by the manufacturer) for 15 minutes at room temperature. Total RNA yield was quantified using Nanodrop 2000 measurement (Thermo Scientific, Wilmington, USA) and cDNA was synthesized using the iSCRIPT cDNA kit (Biorad, Hercules, USA) according the manufacturer's description, to a total of 1 µg for each cell line.

Detection was performed using the iQ5 QPCR apparatus (Biorad), using IQ green super mix (Biorad), for 35 cycles, followed by a high-resolution melting curve. All

primers (supplementary table ST2, with the exception of OCT3/4 and Nanog which were taken from Chen et al 2017[35]) were diluted in PCR grade nuclease-free water (Gibco) at a concentration of 100 µM. All primers passed an efficiency test prior to use at a final concentration of 10 pmol.

Glyceraldehyde-3-phosphate dehydrogenase (GAPDH) and Calpain Small Subunit 1 (CSPN1) levels were used as an internal reference for each experimental primer set. Transcript levels were determined using the ΔCT method (when determining transcription levels without second internal normalizer, i.e., GPX4 levels in correlation with *BAP1* status) or ΔΔCT when using an internal reference (i.e., comparison of adherent and suspended cells).

Protein lysates and Western blot

To determine protein expression, cells were seeded into 6-well plates. After two days, when cells were ~70-80% confluent, they were rinsed twice with ice-cold PBS on ice and subsequently lysed in Giordano buffer (50 mM Tris-HCl at pH 7.4, 250 mM NaCl, 0.1% Triton X-100, and 5 mM EDTA; supplemented with protease- and phosphatase inhibitors) for 10 minutes on ice. After scraping and transferring lysates to tubes, lysates were centrifuged for 15 minutes at 15,000 rpm. Supernatant was transferred to a clean tube.

Lysates of primary UM samples were also made in Giordano buffer, after crushing nitrogen-frozen pieces of tumor to powder, and further processed as described for the cell lines. Subsequently, protein concentrations were determined with Bradford reagent (Bio-Rad). Equal amounts of proteins were separated on SDS-polyacrylamide gels, and proteins were transferred onto PVDF membranes (Millipore). After blocking in 10% non-fat dry milk in TBST (10 mM Tris-HCl, pH 8.0, 150 mM NaCl, 0.2% Tween-20), the blots were incubated overnight with appropriate antibodies diluted in TBST, 5% BSA. After washing with TBST and incubation with appropriate secondary antibodies coupled to HRP for 30 minutes, blots were washed thoroughly and imaged using a Chemidoc (Bio-Rad). The following antibodies were used: anti-*GPX4* (B12) and anti-BAP1 (C4) (Santa Cruz Biotechnology), anti-SLC7A11 and anti-ERK1/2 (Cell Signaling Technology), anti-di-phospho-ERK and anti-Vinculin (Sigma-Aldrich).

Results

The metastatic capacity of Xmm66 spheroid-derived cells is maintained by non-adherent culture.

During development of a zebrafish metastatic UM xenograft model for drug screening, we observed a low engraftment rate of adherent UM cell lines (Figure 1A) which hindered use of this model for robust drug screening. To address this issue, we compared the *in vivo* behavior of cells generated from spXmm66 spheroids with the adherent Xmm66 cell line derived from the same metastatic tumor tissue, and with another adherent UM cell line, Omm2.3[24,27]. After intravenous injection into zebrafish embryos, we indeed observed a significant ($p<0.001$) enhancement of the tumor cell burden induced by engraftment of cells derived from spXmm66 spheroids (Figure 1A) when compared to both adherent cell lines.

Next, we asked whether this difference could be due to an overall loss of tumorigenic capacity, or a loss of stem cell-like features under adherent conditions, which is retained in spheroid cultures. Therefore, we compared the transcriptional activity of two spheroid cultures (spXmm26 and spXmm66) with the adherent cell line Xmm66. We found clear, yet statistically insignificant enhancements in the spheroid cultures, for melanocyte differentiation markers microphtalmia-associated transcription factor (MITF), SRY-related homology box (SOX10), dopachrome tautomerase (DCT) and tyrosinase (TYR). Furthermore, we observed an overall enhancement of “Yamanaka factors” OCT3/4 and Nanog specifically in the spXmm66 spheroid culture and not in spXmm26 or adherent Xmm66 (Figure 1B),[36] indicating an overall enhancement of both differentiated melanocyte markers as well as stem-like markers, indicative of the presence of several discrete differentiation states, or a heterogeneous cell population within our spheroid cultures.

To test whether an inherent loss of metastatic potential of UM cells occurs upon adherent cultivation, we derived *de novo* adherent cell lines (spXmm66-Adherent) from spheroid culture spXmm66 using different growth conditions. These novel adherent lines were generated by seeding spheroid cultured cells in the neuronal stem cell (NSC) medium in conventional cell culture flasks and transducing them with the same lentiviral construct, CMV:tdTomato-blasticidin. We controlled for the effect of the NCS medium by generating one line in the presence of basal NCS medium. Subsequently, we grew two other lines in NCS medium, with or without 10% FCS. After the

establishment of these *de novo* adherent cell lines, cells were implanted into the doC of 48hpf zebrafish larvae and imaged at 1, 4, and 6dpi. We observed that cells derived from spXmm66 lost their metastatic potential after the shift to the 2D substrate through adhesion. We subsequently noted that the strong negative correlation between the adhesion of cells and the metastatic potential in zebrafish could be further intensified by the addition of serum, possibly due to the pro-differentiating function of the soluble factors commonly found in FCS (Figure 1C). We subsequently assayed the effect of ROCK inhibitor Y27632 to assess the effect of ROCK-dependent signaling on the loss of metastatic potential as this inhibitor is commonly used in the organoid culture to prevent differentiation of human induced pluripotent stem cells, presumably via perturbing biomechanical signal transduction through the actin cytoskeleton[37] (Figure 1C and D). Addition of ROCK inhibitor Y27632 to the *de novo* derived adherent cell lines inhibited the reduction of metastatic potential when compared to the suspension culture ($p= 0.43$), while addition of serum to the ROCK inhibitor-treated cells reduced their metastatic capacity, though not significantly ($p=0.18$). These findings lead us to conclude that, in UM, tumorigenic capacity is lost when cells are cultured in adherent conditions, while spheroid cultures retain the tumorigenic capacity.

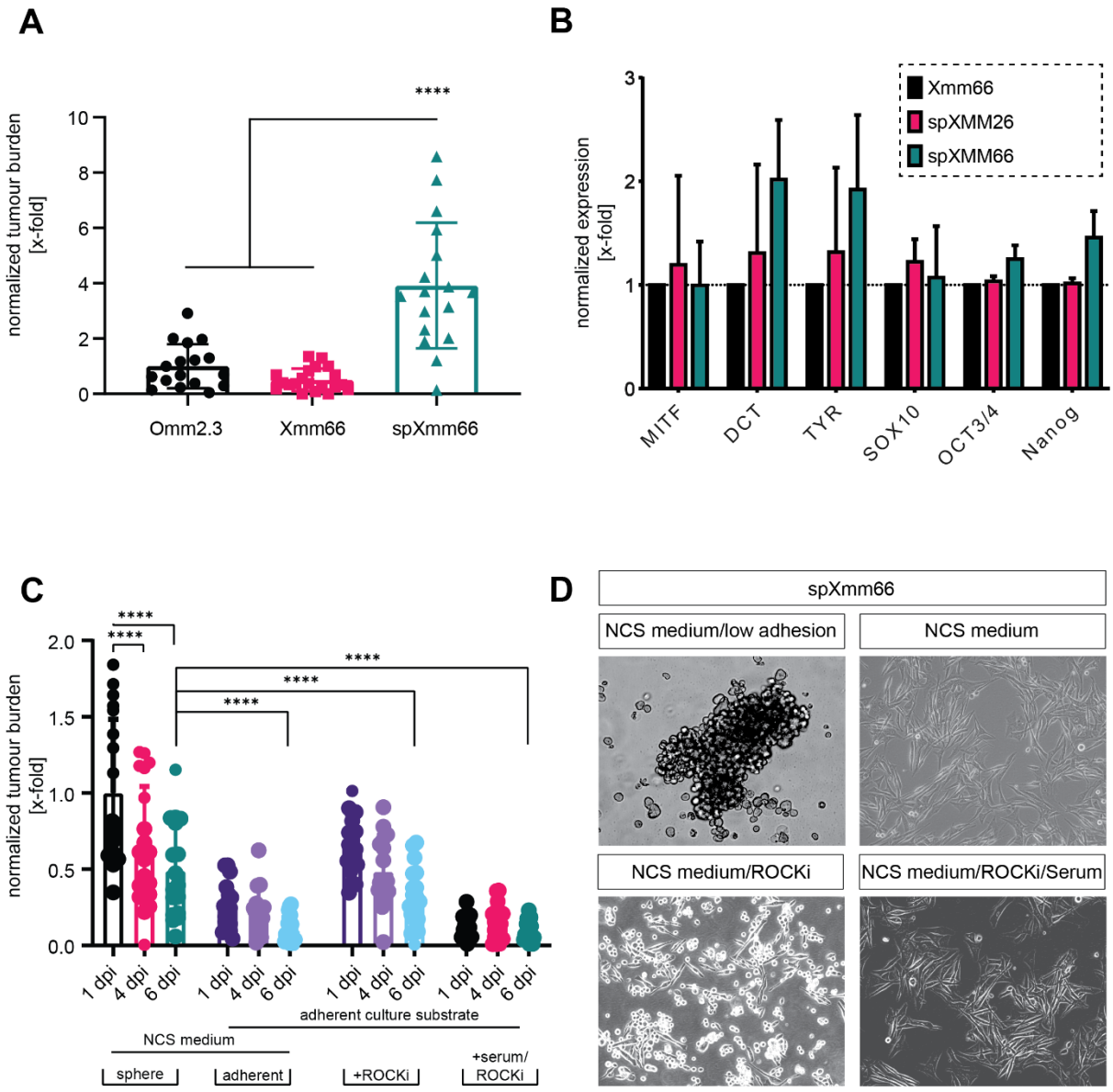

Figure 1. Loss of metastatic capacity of Xmm66-derived cancer cells upon shift to adherent culture. A) Metastatic capacity of adherent uveal melanoma cells and UM-derived spheroid line spXmm66 in zebrafish, n=20, error bar represents ±SEM. B) Transcriptional analysis of spheroidal uveal melanoma cell lines compared to adherent uveal melanoma cell line Xmm66, expression levels normalized to Xmm66. C) Comparison of zebrafish tumor burden after injection of near patient spheroid line spXmm66, compared to *de novo* adherent cultures, derived from spXmm66, cultured as a conventional cell culture on plastic (7 days), with the addition of Rock inhibitor Y276321 or the addition of both Rock inhibitor and fetal calf serum; each group n=20, error bars represent ±SEM. D) Microscopic images of the spXmm66 spheroid line when in suspension (on ultra-low adhesion plastic, in neuronal stem cell medium), in NSC medium on conventional cell culture plastic, in NSC medium containing ROCK inhibitor Y27632 and in NSC medium containing ROCK inhibitor Y27632 with 10% FCS.

Generation of spheroid cultures derived from primary and metastatic UM.

To overcome the loss of metastatic capacity of UM cells upon adherent culturing we developed a spheroid culture protocol to stabilize fresh patient-derived UM material prior to further examination of drug susceptibility in the zebrafish xenograft model.

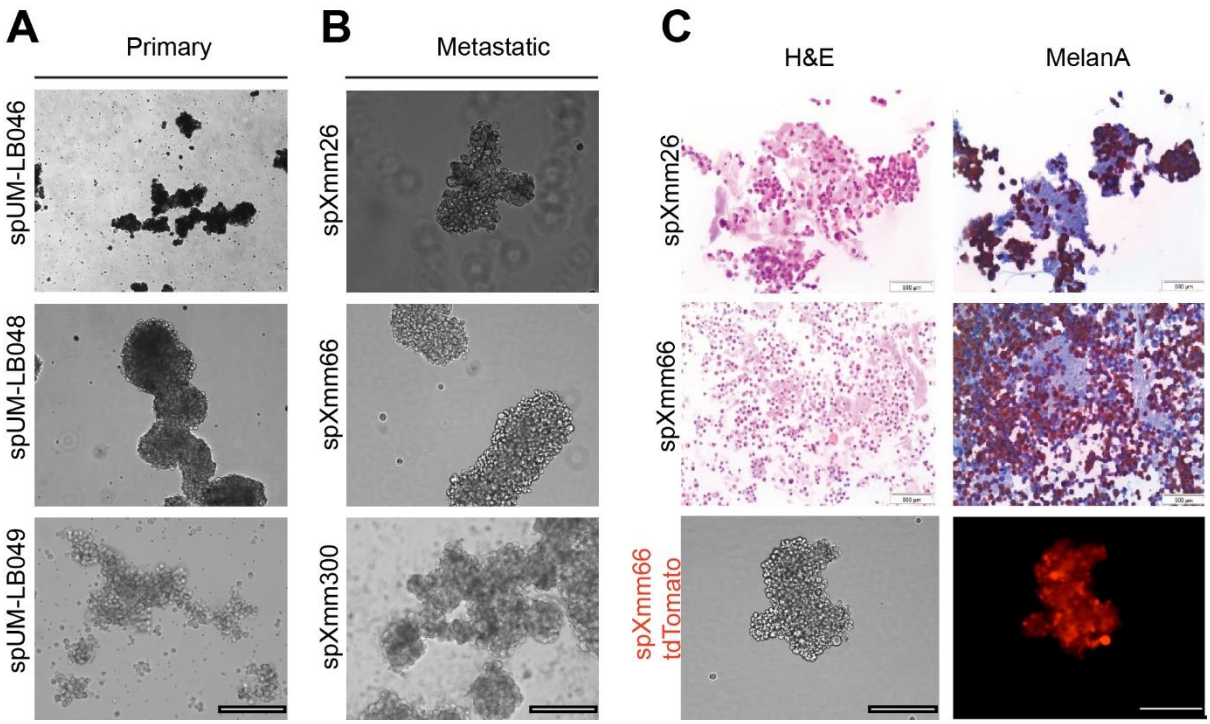

Figure 2. Spheroid cultures can readily be established from both primary uveal melanoma tumor and metastatic uveal melanoma PDX tissues. Representative images of the established spheroid cultures, derived from A) primary UM (spUM-LB046, spUM-LB048, spUM-LB049) and B) from metastatic murine PDX (spXmm26, spXmm66, spXmm300) (10x magnification brightfield, scalebar depicts 250 µm). C) H&E-stained metastatic spheroid cultures (pink) and spheroid cultures stained with melanocyte-specific antibody anti-melanA (magenta). Lentiviral transduced spXmm66, driving tdTomato expression in the spheroid culture derived from murine metastatic PDX material.

All primary tumor-derived tissue samples (n=10, representative images show samples spUM-LB046, spUM-LB048, spUM-LB049) readily formed spheroids in culture (100% success rate) within 24 hours and were cultured for 3-7 days (Figure 2A). In addition, 14 metastatic PDXs tissues were tested. One stable spheroid line (spXmm66) was generated out of 14 PDX samples (7% success rate) (Table ST1). The other 13 PDXs-derived spheroid cultures were successfully maintained as short-lived spheroid cultures for the duration of the experimental procedure (at least 7 days, 100% success). Samples derived from metastatic UM PDXs (spXmm26, 33, 66, 300) were

cultured for approximately 2 months (Figure 2B). Although all primary (n=10) and metastatic (n=13) samples effortlessly formed spheroids, there was little proliferation in these samples (Table ST1), with the exception of spXmm66. The short and long-lived culture spXmm66 stained positively for melanocyte-specific antigen melanA at passages 4 and 20, indicating the retention of its melanocytic background (Figure 2C).

Importantly, we determined that the short-lived spheroid cultures could be successfully used for *in vitro* drug treatment (Supplementary Figure S1). All tested primary tissues (between 2.5-5 mm^3 sample size during enucleation) yielded enough material after short-lived spheroid culture for at least two zebrafish engraftments within 7-14 days after establishment. Only the long-lived spXmm66 culture propagated sufficient material for repeated zebrafish engraftments, allowing single and combinatorial drug testing. Collectively, we have established a successful platform to isolate, preserve and recover viable tissue and spheroid cultures generated from UM patient material, either murine PDX or primary-tumor derived, for subsequent engraftment and validation.

Spheroid-derived metastatic xenografts yield a reproducible metastatic phenotype and recapitulate molecular features of UM cells in zebrafish.

There are currently no animal models for metastatic uveal melanoma suitable for drug screening. To address this issue, we established a zebrafish xenograft model by intravenous injection of fluorescent UM cells derived from a short-lived primary spheroid and long-lived metastatic spXmm66 spheroid cultures. Considering the limitless availability of spXmm66 cells and our interest in developing drug screening platform for metastatic UM we continued our investigation using the spXmm66 model. Engrafted fluorescent spXmm66 cells disseminated hematogenously and formed metastatic foci (Figure 3A, B). To verify the presence of viable UM cells, zebrafish engrafted with spXmm66-derived cells were selected using a fluorescent stereo microscope and subsequently fixed at 6 days post implantation, and imaged using a confocal microscope, generating 10 x whole body stitches. Representative confocal stiches indicate primary UM zf-PDX models spUM-LB048 and spUM-LB048 (Figure 3B). Paraffin-embedded zebrafish were sectioned and stained for the melanocyte-specific marker melanA and for the presence of BAP1. All engrafted larvae showed melanA and BAP1-positive cells (Figure 3C) proving that engrafted cells maintain

expression of UM histological markers after injection (additional IHC's of zf-PDX in supplementary Figure S5).

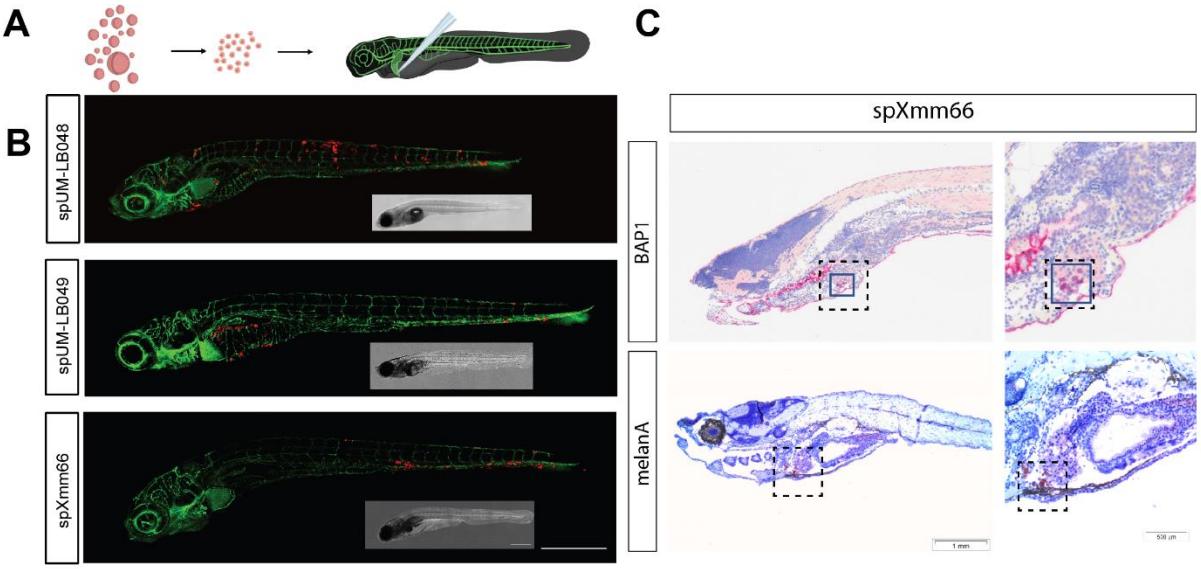

Figure 3. Establishment of a UM zf-PDX model through duct of Cuvier (doC) injection yields a reproducible metastatic phenotype. A) Schematic representation of the engraftment procedure; spheroid cultures are reduced to single cell suspensions by enzymatic dissociation, and single cells are injected into the blood circulation of 48 hpf Tg(fli:GFP) zebrafish larvae through the doC. B) Representative confocal micrographs of 6 days post injection, showing GFP (green) blood vessels in zebrafish, engrafted with cancer cells marked in red (either CM-DiL for spUM-LB048, 049 or tdTomato lentiviral over-expression for spXmm66); scale bar represents 250 µm. Disseminated cancer cells are present up to 6 days post engraftment and settle in both the hematopoietic tissue and the liver. C) Hematoxylin and eosin staining and BAP1 IHC (dark purple, boxed area), and melanA (dark purple, boxed area), staining on spXmm66 engrafted zebrafish larvae. Scale bar equals 1 mm and 500 µm for the magnification.

The long-lived spXmm66 spheroid culture, derived from the same metastatic tissue-derived PDX as the adherent UM cell line Xmm66 [24], proved to be highly proliferative and metastatic in the zebrafish xenograft model. Cancer cells were present up to 6 days post engraftment, the ethical endpoint of the experiment, with distinct cancer cell colonies arising in the liver and the caudal hematopoietic tissue of the zebrafish (Figure 3B, C).

Combinatorial small molecule inhibitor screening validates the UM zf-PDX model as a versatile tool for anti-UM drug discovery.

To confirm the validity of our metastatic UM zf-PDX spXmm66 derived model as a potential drug screening tool, we tested several known small molecule inhibitors. These therapeutics or combinatorial therapies were originally selected through a combination of genomic analysis, *in vitro* pre-screening and an efficacy study in a murine subcutaneous UM PDX model, derived from the same metastatic UM patient (Xmm66 tissue)[23]. We used spXmm66-derived cells engrafted in zebrafish and tested three combinatorial sets of small molecule inhibitors, previously published, as a means of chemical validation of the zf-PDX model[25,38,39]. The spXmm66 engrafted zebrafish were exposed to: mTORC1 inhibitor-everolimus (RAD001) together with PKC inhibitor-sotrastaurin (AEB071), BCL-2/BCL-xl inhibitor- navitoclax (ABT263) combined with RAD001 and HDAC inhibitor-quisinostat, and with CDK inhibitor-flavopiridol (Figure 4). Prior to treatment, we first established the maximum tolerated doses (MTD) of selected drugs by treating un-injected zebrafish larvae, from 72hpf for 5 days, changing the drug-laced zebrafish medium every other day, in a similar fashion as the final drug treatment (Figure S2). The MTD of everolimus was 2.5 µM and of sotrastaurin 2.5 µM (Figure S1). The combinations were made as previously mentioned, after subsequent titration: everolimus at 1.25 µM combined with sotrastaurin at 2.5 µM; everolimus at 1.25 µM combined with navitoclax (ABT263) at 5.0 µM; quisinostat at 500 nM with flavopiridol at 1.0 µM. We analyzed the decrease of tumor burden as described by Groenewoud *et al.* 2021[29]: all groups, either by mono treatment or combination treatment, were compared to vehicle control (Figure 4). For the combination of flavopiridol and quisinostat, we measured a significant reduction of tumor burden ($p < 0.001$) but not when using a single compound. For the combination of everolimus and navitoclax we saw a significant inhibition with the mono treatment of navitoclax ($p<0.05$), that was further enhanced by the addition of everolimus ($p<0.001$). After this preliminary chemical validation, we concluded that this zf-PDX model recapitulates drug sensitivity similar to corresponding murine PDX and therefore could be applied for the development of new, pre-clinical experimental treatments[24,25,38,39].

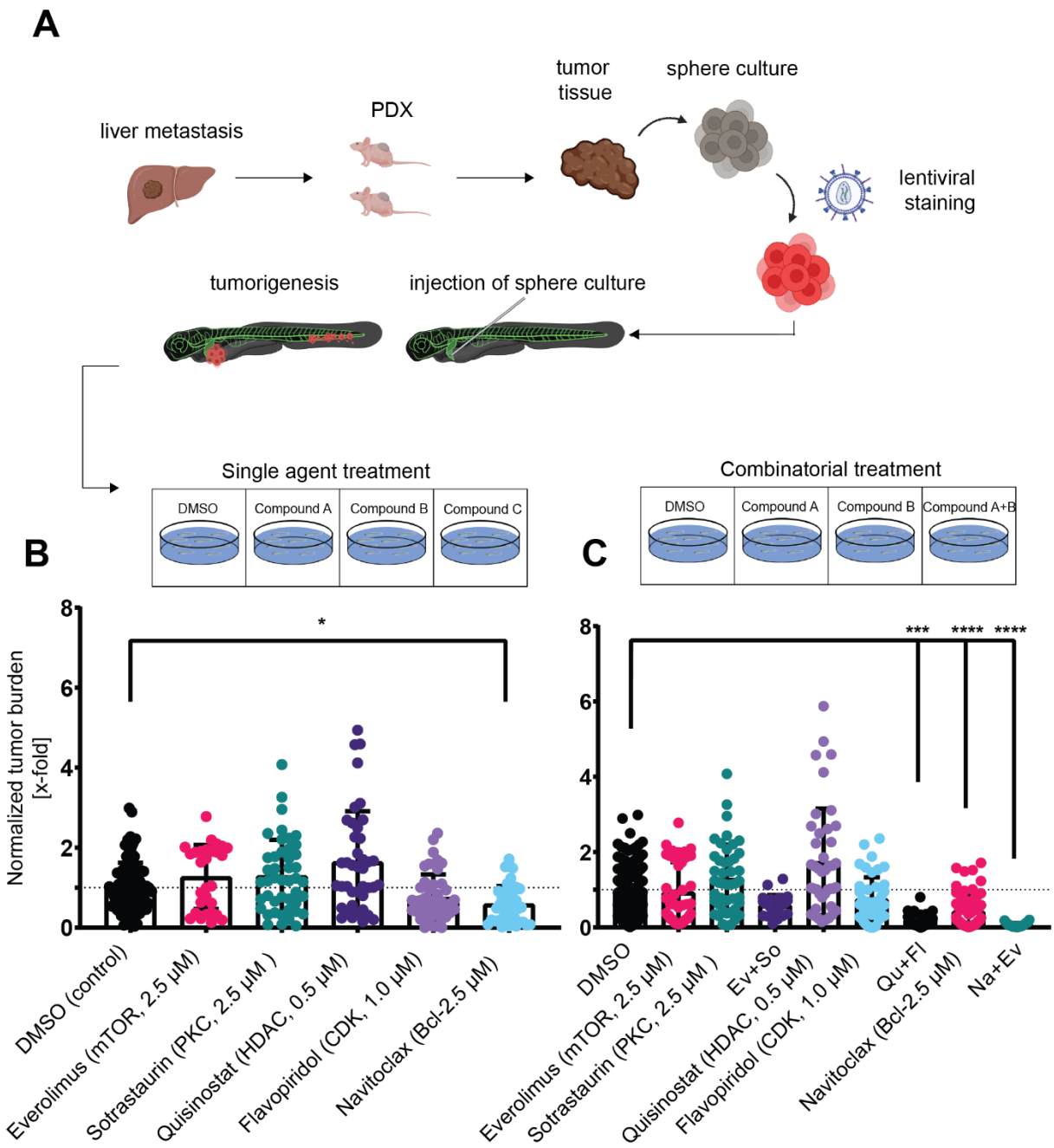

Figure 4. Chemical validation of the established metastatic uveal melanoma model. A) Engrafted zebrafish with UM cells derived from the spheroid cultures were treated with the maximum tolerated dose of the compounds, determined as previously described (shown in Figure S1). B, C) Tumor burden, normalized to DMSO control (normalized tumor burden); measurements are combined from at least 2 experiments and 20 individuals (n>20*2), error bar depicts ±SEM**.**

Uveal melanoma cells are highly sensitive to the induction of ferroptosis *in vivo,* enabling novel anti-UM therapeutic strategies.

Next, we addressed why the development of metastatic animal UM models has proven to be such a difficult challenge. During the establishment of our UM drug screening platform, we have concluded that there is a clear discrepancy between adherent cultured UM cell lines and UM cells capable of metastasis.

We hypothesized that circulating UM cells are hyper sensitive to cell extrinsic stress factors during metastatic dissemination therefore establishment of reproducible metastatic models is very inefficient process. We came to this hypothesis due to the fast and complete clearance of the engrafted adherent cells from the zebrafish host after injection (Figure 1A). We reasoned that the cells were destroyed by a cell intrinsic mechanism during metastatic dissemination. We propose that understanding of this mechanism will give us an insight into how UM cells resist clearance in circulation and induce metastasis in patient.

Recent discoveries in cutaneous melanoma metastasis and the inhibitory effects of ROS on metastasis, led us to assess the effect of some of the key regulatory proteins on UM metastasis[18,40,41]. Moreover, due to the fast and complete clearance of the adhered UM cells from the zebrafish host after injection (Figure 1A), we reasoned that these cells were destroyed by a cell intrinsic mechanism.

Recent developments in ferroptosis biology [43] and the inhibitory effects of ferroptosis on disseminating cutaneous melanoma [22] prompted us to ask if ferroptosis could be the underlying, cell intrinsic mechanism, causal to the low tumorigenic capacity and rapid clearance of UM cells. Combining these recent findings with the parallel between the rapid and complete clearance of UM cells from the engrafted zebrafish host, we hypothesized that the high metastatic potential of UM cells in patients might be explained through an upregulation of ferroptosis detoxifying mechanisms. To test this, we investigated the expression of known ferroptosis regulators and whether expression levels affect the survival of UM patients (Figure 5).

A

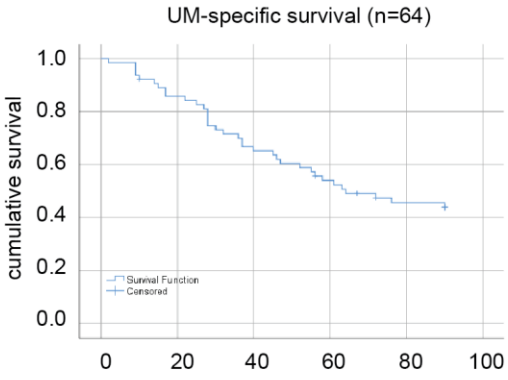

Time	0	20	40	60	80
At risk	64	54	42	32	14

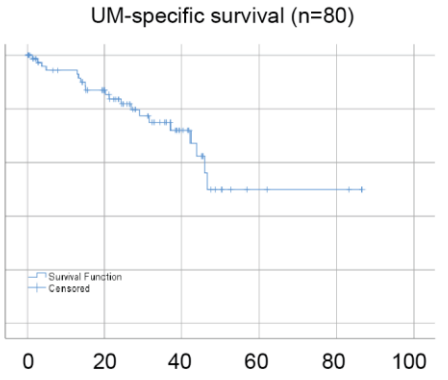

Time	0	20	40	60	80
At risk	80	40	13	3	1

B

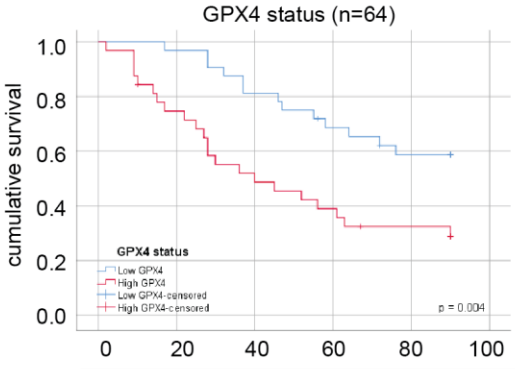

Time	0	20	40	60	80
Low GPX4	32	31	26	21	9
High GPX4	32	23	16	12	5

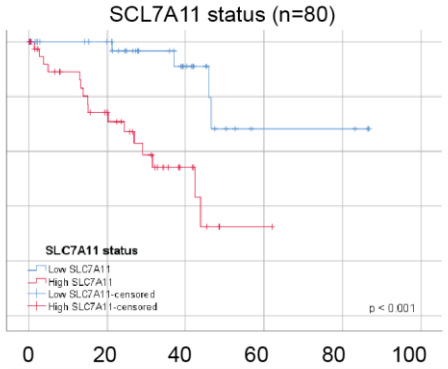

Time	0	20	40	60	80
Low SLC7A11	40	23	9	2	1
High SLC7A11	40	17	5	1	-

C

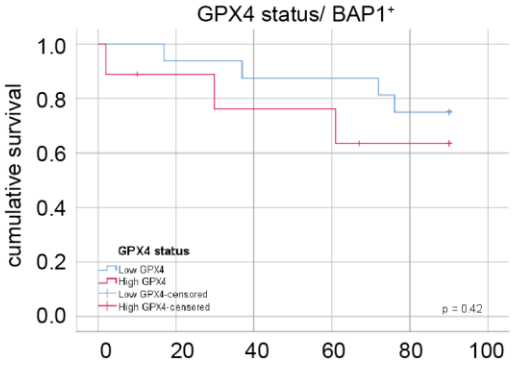

Time	0	20	40	60	80
Low GPX4	16	15	14	14	6
High GPX4	9	7	6	6	2

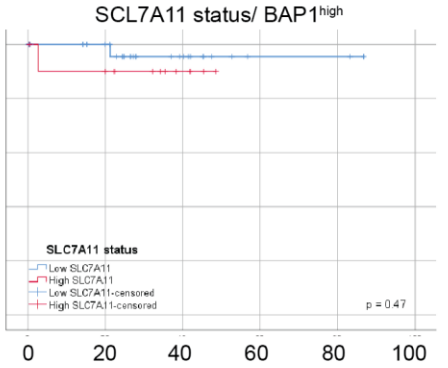

Time	0	20	40	60	80
Low SLC7A11	29	17	6	2	1
High SLC7A11	11	6	2	-	-

D

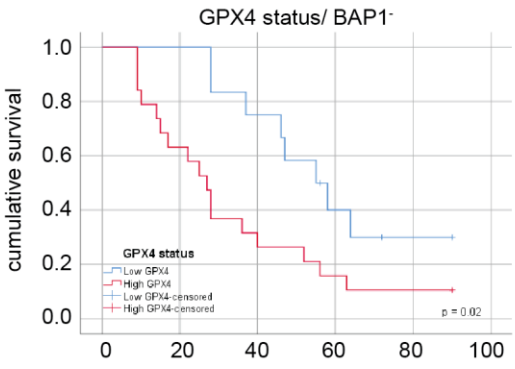

Time	0	20	40	60	80
Low GPX4	12	12	9	4	1
High GPX4	19	12	6	3	1

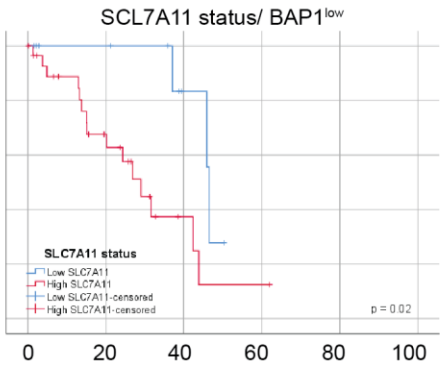

Time	0	20	40	60	80
Low SLC7A11	11	6	3	-	-
High SLC7A11	29	11	3	1	-

Figure 5. Ferroptosis detoxification mechanisms negatively correlate with UM patient survival in the Leiden cohort and with melanoma specific survival in the TCGA cohort. A) Analysis of the UM-specific survival in both LUMC UM and TCGA patient cohorts. B) UM-specific survival of GPX4 (LUMC cohort, n=64) and SCL7A11 (TCGA, n=80), expression divided over the median, shows a negative correlation of both *GPX4* (p = 0.004) and system Xc- (p = 0.0014) on patient survival C) Comparative analysis of the relation between *GPX4* and *SCL7A11* and survival in BAP1+ (LUMC, IHC, n=25) and BAP1 high (TCGA, RNAseq, n=40) UM samples and in D) BAP1 – (LUMC, IHC, n=31) and BAP1 low (TCGA, RNAseq, n=40) The expression levels of *GPX4*, *SCL7A11* and *BAP1* were split at the median, and curves were plotted using SPSS. BAP1 levels were determined via pathological analysis (IHC) in the LUMC UM cohort and divided based on transcription levels along the median in the TCGA.

Prior to assessment of the efficacy of ferroptosis induction *in vivo*, we analyzed the relation between the three major eukaryotic ROS detoxifying enzymes, catalase (*CAT*), superoxide dismutase 2 (*SOD2*), and glutathione peroxidase 4 (*GPX4*) on metastasis development and survival in two cohorts of UM. We found that out of *CAT*, p=0.25, *SOD2,* p=0.83 and *GPX4* p=0.041, only *GPX4* expression negatively correlated with UM-specific survival in the TCGA cohort (80 cases (Figure S3). Analysis of *GPX4* expression levels and the relation between *GPX4* and overall survival in primary UM patients in the TCGA were analyzed using Gene Expression Profiling Interactive Analysis (GEPIA2)[44,45]. We noted a significant reduction in melanoma-related death in patients expressing high levels of *GPX4* in a cohort of 64 UM from the LUMC as assessed by micro-array, and in the development of metastases in The Cancer Genome Atlas cohort (TCGA, p<0.04, n=78) analyzed through GEPIA2 as shown in supplementary Figure S2[45].

We focused on ferroptosis and some of the known key mechanisms that play a role in either *GPX4* function or intracellular iron metabolism because expression of both *GPX4* and glutamate/cysteine antiporter (system Xc- SCL7a11, p<0.001) showed a strong negative correlation with patient survival (Figure 5A, B). Moreover, both GPX4 and SCL7A11 showed an enhanced negative correlation with survival in patients with a loss of BAP1 (BAP1-) (GPX4 in BAP1-IHC negative cases (p<0.02) and SLC7A11 in BAP1 low TCGA cases (Fig. 5B) (p<0.02)). These findings suggest that levels of ferroptosis detoxicating enzymes correlate with worse prognosis and that the UM prognostic marker BAP1 loss is predictive of the role of ferroptosis related genes (GPX4 and SCL7A11) in UM progression.

We subsequently tested the dose-dependent ferroptosis-mediated killing of a selection of primary (MP46, MEL285) and metastatic (Omm1, MM28, and Xmm66) UM cell lines by well-established ferroptosis inducers 1S,3R-RSL3 (RSL3) and Erastin[19,20,42]. Strikingly, all tested cell lines responded to the induction of ferroptosis in a dose-dependent manner, but their overall response rate *in vitro* was weak (Figure S4C). The strongest response was noted in UM cell line MEL285, an atypical UM cell line not carrying any of the hallmark UM driver mutations but expressing a high level of pERK, which is indicative of upstream RAS-RAF-MEK hyperactivation found in cutaneous melanomas[45]. This cell line expressed low levels of *GPX4*, high levels of SCL7A11 and was killed completely by 200 nM Erastin, while it showed approximately 80% growth reduction with 200 nM RSL3. Both effects could be almost completely rescued by addition of ferroptosis inhibitors ferrostatin or liproxstatin (Figure S4C), indicating that oncogenic RAS activation in UM cells pre-disposes these cells to high ferroptosis susceptibility. Both ferrostatin and liproxstatin are thought to act through trapping free radicals, causal to the peroxidation of cell membranes[46]. Activation of pro-ferroptotic signaling in cell line MEL285 was completely blocked by the addition of ferroptosis inhibitors, ferrostatin and liproxstatin, indicating a canonical pERK dependent ferroptosis activation in this cell line. All other tested cell lines showed a dose-dependent response to the induction of ferroptosis, although these cell lines could be rescued only marginally by the addition of either liproxstatin or ferrostatin. These *in vitro* data suggest that while UM cells are broadly susceptible to ferroptosis induction, there is a pre-disposition to ferroptosis induction in pERK positive cells. Most UM samples which could only be rescued by ferrostatin or liproxstatin treatment showed strong ERK activation (suggestive of upstream oncogenic RAS hyperactivation), indicating a canonical ferroptosis susceptibility profile. Moreover, *GPX4* protein levels (Figure S4B) seem to be indicative of ferroptosis resistance *in vivo*, further enhanced by the pro-ferroptotic upstream activation of RAS-RAF-MEK-ERK, either through via GNAq/GNA$_{11}$ PKC or indirectly through RASGPR3, as reported by Moore *et al*., 2018[47].

To test the converse of this hypothesis, namely if the *a priori* inhibition of ferroptosis before engraftment could prevent the injected cells from dying in circulation. To this end, we treated Xmm66 and Omm2.3 with the ferroptosis inhibitors ferrostatin and liproxstatin prior to zebrafish engraftment (Figure 6B). Both inhibitors significantly

enhanced UM cell survival in the circulation for Xmm66 (P<0.001 for both Liproxstatin and ferrostatin), up to 24 hours after systemic implantation into zebrafish larvae. Cell line Omm2.3 showed a marked, yet statistically insignificant, increase in cancer cell burden. These results indicate that ferroptosis plays a key role in the curbing of metastatic dissemination of UM.

To test the long-term influence of ferroptosis *in vivo*, we first established the MTD for both Erastin and RSL3 on un-injected zebrafish larvae: these were 5 µM and 10 µM, respectively (Supplementary Figure 2C). We subjected 36 engrafted zebrafish larvae to either compound, alongside DMSO as vehicle control, changing the compound-containing water or vehicle every other day (Schematically represented in Figure 6A). After 5 days of treatment, we imaged 20-40 whole zebrafish larvae per condition using a fluorescent stereo microscope, and quantified the red fluorescent integrated density, as a measure of cancer cell survival, normalizing to DMSO control (as described by Groenewoud *et al.* 2021)[29].

In addition, we examined a panel of 8 primary UM patient samples, UM08002-UM08038 for the presence of *GPX4*, SCL7A11, and the BAP1 protein, to determine if there was a correlation between BAP1 expression and the ferroptosis-related proteins *GPX4* and *SCL7A11*. These samples were compared to established metastatic UM cell lines MM66 (*BAP1* positive) and MP46 (*BAP1* negative) (Figure 6C). We found that the two cell lines showed highly-elevated levels of SCL7A11 when compared to the patient-derived samples, in the case of MM66 in the absence of BAP1 mutation. The primary patient samples showed a positive correlation between *GPX4* levels and *BAP1* loss (UM08002 and UM08038 showed BAP1 expression and a low expression of *GPX4*). In parallel, we determined the dependence of GPX4 expression on BAP1 presence or absence. To this end, we performed a confirmatory qPCR-based analysis of GPX4 expression for two primary UM patient cohorts ($BAP1^{+}$=8, $BAP1^{-}$=9) and detected that GPX4 high and low populations could be segregated based on BAP1 status (p=0.035, Figure 6D, E). None of the primary samples exhibited detectable levels of SCL7A11 and hence no correlation with BAP1 levels could be determined. We examined the susceptibility of metastatic (spXmm66) and primary UM (spUM-LB046, spUM-LB049, spUM-LB007 were all $BAP1^{-}$ and spUM-LB004 was $BAP1^{+}$) to the induction of ferroptosis *in vivo,* monitored as reduction of relative tumor growth in zebrafish xenograft model (Figure 6G). Upon *in vivo* treatment, all but one primary UM

samples (with the exception of BAP1 proficient sample spUM-LB004), as well as the metastasis-derived spXmm66 sample, displayed ferroptosis when challenged with RSL3 and Erastin (spUM-LB046 $p<0.0001$ both; spUM-LB049 ns and $p=0.03$; spUM-LB004, ns; spUM-LB007, $p=0.03$ and ns). Strikingly, although spXmm66 is derived from a $BAP1^{wt}$ tumor it has high *GPX4* protein levels (data not shown), explaining its strong response to RSL3 and to a lesser extent Erastin (reduction of tumor burden, $p<0.001$ and <0.001, respectively).

In conclusion, using this zebrafish model, we have been able to demonstrate that both metastatic and primary UM cells were susceptible to pharmacological ferroptosis induction, manifesting stronger inhibition *in vivo* compared to *in vitro* (Figure 6G). Moreover, we have shown a possible predictor for ferroptosis treatment response in both clinically relevant and routinely detected UM markers BAP1 and monosomy 3, indicating that these patients could benefit from pro-ferroptotic therapy.

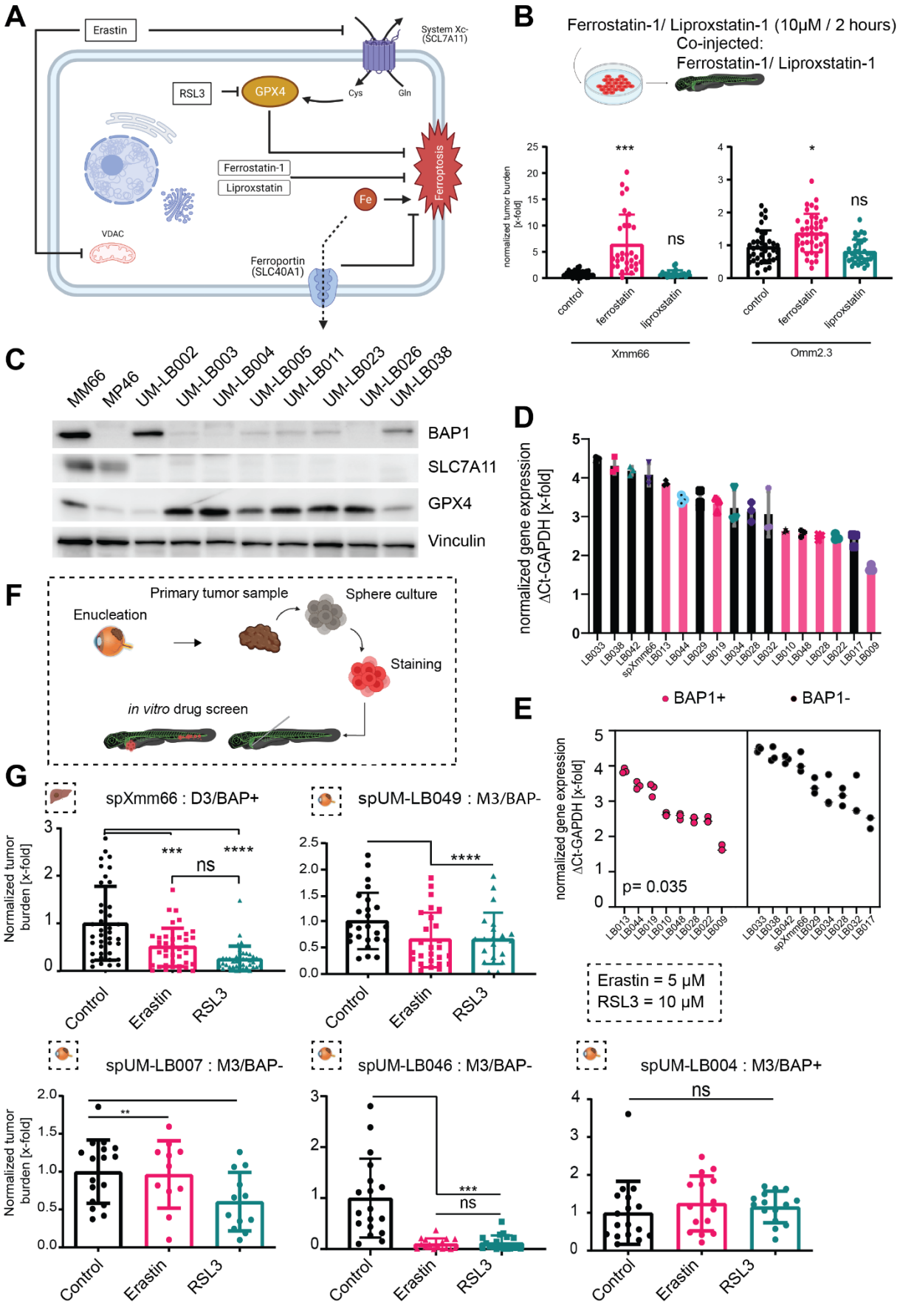
A
Erastin
System Xc-
(SCL7A11)
RSL3
GPX4
Cys
Gln
Ferroptosis
Ferrostatin-1
Liproxstatin
Fe
VDAC
Ferroportin
(SLC40A1)
B
Ferrostatin-1/ Liproxstatin-1 (10µM / 2 hours)
Co-injected:
Ferrostatin-1/ Liproxstatin-1
normalized tumor burden [x-fold]
***
ns
*
ns
control
ferrostatin
liproxstatin
Xmm66
Omm2.3
C
MM66
MP46
UM-LB002
UM-LB003
UM-LB004
UM-LB005
UM-LB011
UM-LB023
UM-LB026
UM-LB038
BAP1
SLC7A11
GPX4
Vinculin
D
normalized gene expression
ΔCt-GAPDH [x-fold]
LB033
LB038
LB042
spXmm66
LB013
LB044
LB029
LB019
LB034
LB028
LB032
LB010
LB048
LB028
LB022
LB017
LB009
E
BAP1+
BAP1-
normalized gene expression
ΔCt-GAPDH [x-fold]
p= 0.035
F
Primary tumor sample
Sphere culture
Enucleation
Staining
in vitro drug screen
G
spXmm66 : D3/BAP+
spUM-LB049 : M3/BAP-
Normalized tumor burden [x-fold]
***
****
ns
****
Control
Erastin
RSL3
Erastin = 5 µM
RSL3 = 10 µM
spUM-LB007 : M3/BAP-
spUM-LB046 : M3/BAP-
spUM-LB004 : M3/BAP+
**
***
ns
ns

Figure 6. Treatment of UM patient-derived zXenografts shows strong inhibitory potential of ferroptosis inducing compounds *in vivo*. A) Schematic representation of ferroptosis signaling. B) Pre-treatment of engrafted, adherent UM cell lines with anti-ferroptotic ROS traps ferrostatin-1 and Liproxstatin-1 prior to and its effect on UM cell survival *in vivo*. Whole body zebrafish measurements at 24 hours post injection, n=20, normalized to DMSO treated control, pre-treatment with ferrostatin-1 significantly enhances cell survival in cell line Xmm66 $p<0.0003$ and for Omm2.3 $p<0.04$ where in the liproxstatin pre-treated groups a slight enhancement of cell survival was measured (ns). Error bars represent SEM. C) Western blot staining for *GPX4*, *SCL7A11* and BAP1, with vinculin as a loading control, showing high levels of SCL7A11 on both cell line samples MM66 and MP46 and undetectable levels on patient samples (UM-LB02-38), *GPX4* levels are elevated in patient samples in a BAP1-dependent manner. UM08003-26 are $BAP1^{-/-}$ patient samples, low levels of BAP1 are detected in samples UM-LB003-26 most likely due to inclusion of stromal cells. D) qPCR analysis of GPX4 mRNA expression in primary UM tissues, with known BAP1 status, all samples measured in triplicate and normalized to GAPDH reference (ΔCT). E) Comparative analysis of GPX4 expression between BAP1+ and BAP1- patient samples indicating a significant enhancement in GPX4 levels in BAP1- patient samples. F) Schematical approach of zebrafish xenografts treatment of both primary and metastatic melanomas treated for 6 days with Erastin (5μM) or RSL3 (10μM) indicates a strong inhibition of normalized tumor burden. G) Zebrafish xenografts treatment of both primary and metastatic melanomas treated for 6 days with Erastin (5μM) or RSL3 (10μM), responding in a chromosome 3 monosomy/ Bap 1 dependent manner, with the exception of spXmm66 ($D3/Bap\ 1^{+}$). Normalized tumor burden shown, n=40 (spXmm66) and n=20 (spUM-LB046, spUM-LB049), error bars show ±SEM.

Discussion

We have been able to establish a robust protocol for the generation of metastatic UM spheroid cultures. Using this method, we generated one continuous UM culture of metastatic origin and several short-lived primary and metastatic spheroid cultures. In concordance with the general disease progression of UM and the lack of available metastatic UM material, we chose to focus on primary UM samples. In choosing these, we reasoned that our screening efforts could possibly be translated to assumed metastatic patients, providing data for adjuvant treatment. We combined our model with the knowledge of the strong prognostic value of monosomy 3/BAP1 loss to pre-screen patients with a high risk of developing metastatic UM. We developed our near patient zf-PDX model using the highly proliferative spheroid culture spXmm66, seeing as it is the only biological UM entity that readily yields perivascular metastatic colonies (Figure 3B). In concordance with these findings, we were incapable of robustly generating metastatic colonies after injection of stable adherent cell lines Omm1, Omm2.3, Omm2.5 and Xmm66 (data for Omm1, Omm2.5 not shown). Furthermore, our data indicate that the metastatic capacity of spheroid line spXmm66 is dependent on an absence of ROCK signaling. When spXmm66 was cultured in adherent culture for one week, this completely abrogated this cell line's intrinsic metastatic capacity. Inclusion of ROCK inhibitor Y267632 during the adherent culture of spXmm66 significantly reduced the loss of metastatic capacity, whereas inclusion of serum enhanced the loss of metastatic capacity. This leads us to conclude that for spXmm66, its metastatic potential is linked to its spheroidal low RhoA signaling nature; we assume that there is a mechanical force-dependent mechanism responsible for the loss of metastatic potential, which is further potentiated by the addition of serum to the medium. To exclude a direct effect of the stem cell medium, we cultured Xmm66 and Omm2.3 in complete NSC medium, but observed no enhancement of metastatic potential, neither in the adherent nor the spheroidal culture.

Subsequently we validated the zf-PDX model through single agent and combinatorial drug treatments, using experimental treatments developed to inhibit both cell line Xmm66 and murine localized tumor model. Metastatic UM PDX model spXmm66 largely recapitulated the findings in murine models, indicating that it could be used to assess drug efficacies *in vivo.*

Taking together the overall lack of tumorigenic capacity of adherent UM cells and the rapid clearance of UM cells after hematogenous engraftment we reasoned that there was a cell intrinsic mechanism responsible for the obvious disconnect between the high metastatic capacity of patient derived cells and *in vitro* propagated UM cells. Reactive oxygen and more specifically ferroptosis has recently been linked to the curbing of metastatic spread of cancer cells, specifically acting on circulating cancer cells.

To assess the efficacy of ferroptosis induction on UM cells *in vivo,* we selected two distinct ferroptosis inducers, Erastin and 1S, 3R-RSL3 (RSL3), which are, respectively, class I and class II ferroptosis inducers (FINs). Erastin inhibits the glutathione/cysteine antiporter function of system Xc- (encoded by SLC7a11 and SLC3a2), undermining GPX4's capacity to catalyze phospholipid peroxidation by depriving it of its substrate[48]. The pro-ferroptotic effect of Erastin is further enhanced by its action upon mitochondrial voltage-dependent anion channel 2 (VDAC2). VDAC2 inhibition leads to a massive increase in intracellular ROS levels through a disruption of the mitochondrial membrane potential, followed by permeation of ROS into the cytosol proper[40]. Interestingly, we found that induction of ferroptosis is highly effective against spreading of primary UM cells *in vivo* (Figure 6G), and shows a strong inhibitory tendency for all BAP1- samples tested. Furthermore, the recent publication of Luo & Ma, 2021 underscores the presence of a ferroptosis-related gene signature among UM tumors [49]. This finding, taken together with the TCGA and LUMC patient cohort-derived data, confirms the presence of a strong negative correlation of the ferroptosis-related genes *GPX4* and system Xc- (*SCL7A11*) with and (metastasis-free) survival. Furthermore, our zf-PDX based near-patient *in vivo* drug screen indicates the translational value and validity of ferroptosis inducers for the treatment of UM.

Subsequent *in vitro* data showed that most cultured UM cells are largely refractory towards ferroptosis induction at similar concentrations (Erastin 5 µM and RSL3 10 µM *in vivo*) as used during successful *in vivo* ferroptosis induction. Taken together, our findings underscore the validity of using the zebrafish model for the discovery of novel cancer therapeutics, in this instance for a malignancy where until now there was no available metastatic animal model. Ultimately, our findings add to the building body of evidence supporting the value of ferroptosis induction as a potential treatment in metastatic uveal melanoma[50].

Author's contribution

A.G. designed, performed and analyzed all *in vivo* experiments, performed GEPIA analysis, wrote the manuscript and designed the graphics. J.Y. performed additional zebrafish engraftments, Western blots and qPCR. M.C.G. provided information on the patients and performed the statistical analysis on patient information, S.A., F.N. and D.D. supplied the metastatic UM material, H.K. and S.C. performed the immuno-stains and the analysis thereof, A.G.J. performed the *in vitro* proliferation assays and Western blots and provided assessment of this manuscript. M.J. provided primary UM tissue samples, patient data and assessment of this manuscript, E.S.J. provided funding and supervised the project.

Acknowledgements

We kindly thank Emilie Vinolo for the managerial assistance provided during this UMcure2020 project.

We further thank Amina Teunisse for technical assistance.

This work has received funding from the European Union's Horizon 2020 research and innovation program under grant agreement No 667787 (UM Cure 2020 project, www.umcure2020.org

All graphics (excluding scientific data) were generated using Biorender.com

The results shown here are in whole or part based upon data generated by the TCGA Research Network: https://www.cancer.gov/tcga

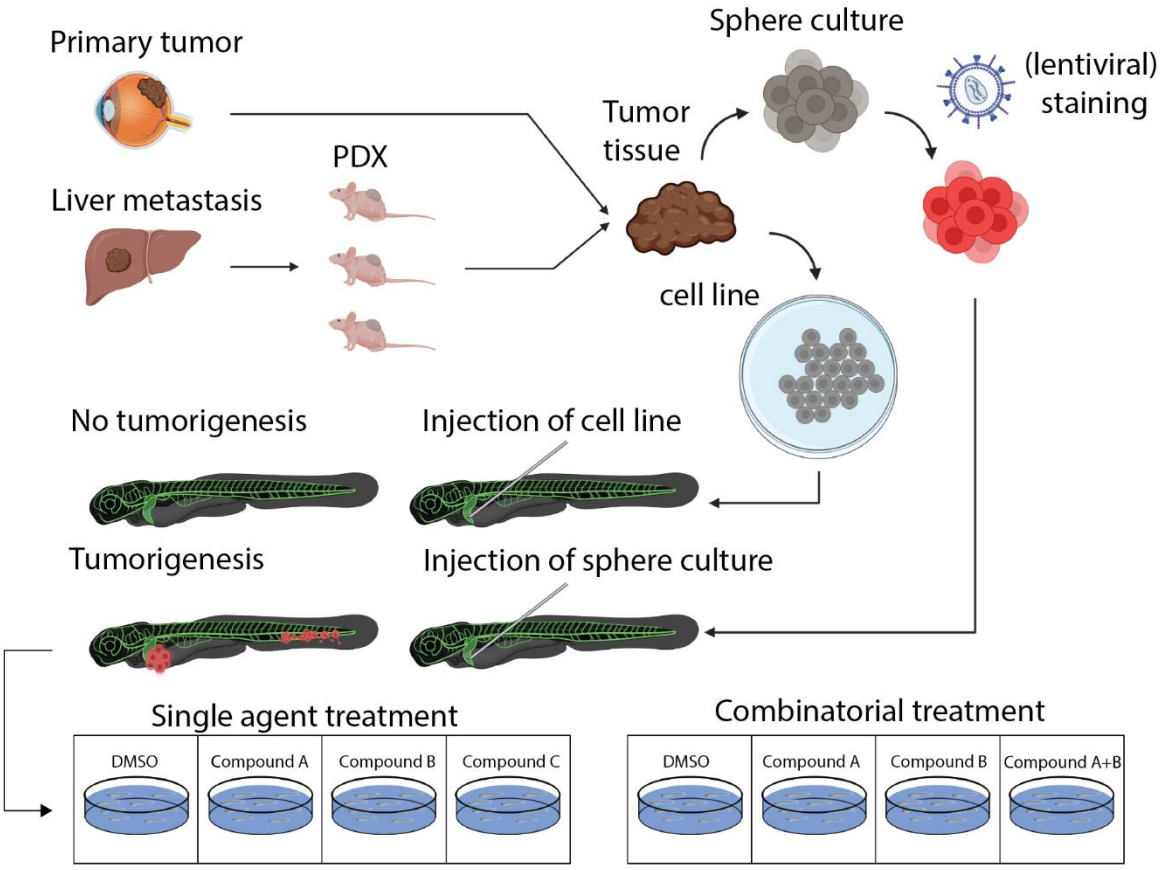

Figure 7. Establishment of a zebrafish uveal melanoma PDX model. A) Metastatic (or primary) UM are collected and are used to establish mouse xenografts and effectively propagated in NOD-SCID mice (via sub-cutaneious engraftment) or are directly used to establish a non-adherent near-patient spheroid culture (as shown under B). C) The establishment of these spheroid cultures allows for the *in vitro* (lentiviral) modification of patient material (addition of molecular tracers, reporters, etc.) prior to engraftment, allowing the separation of one biological sample over two individual experiments. In some cases, the establishment of spheroid culture allows for the generation of long-lived (p>20) metastatic UM lines, allowing the in-depth analysis of metastatic UM and drug screening. Spheroids are dissociated prior to engraftment (either physically or enzymatically) and the single cell suspension derived thereof is engrafted through the Duct of Cuvier (the embryonic common cardinal vein) of 2dpf zebrafish larvae, approximately 250-350 cells per larva. Zebrafish are screened 1 dpi, where all the selected, positively engrafted larvae, are randomly divided into groups treated with either vehicle, compound A, compound B or a combination of both compound A and B (all at the respective maximum tolerated dose of the combination of compound A and B). Anti-tumor efficacy of all groups is determined through an integrated density measure using FIJI, based on standardized fluorescent micrographs. All measures are subsequently normalized to vehicle control and shown as normalized tumor burden.

Supplementary Table ST1 Overview of tissues used for spheroid culture derivation

	Name	Recovered from freezing	Sphere culture established	Lentiviral transduction	zebrafish xenograft	Validation	Growth speed	Maximum passage number	Reference(s)
Metastatic	MM26	✓	✓	-	✓	S, IHC, C	-/±	4	Nemati, Laurent
	MM28	+/-	+/-	-	IM	N/A	-	4	Nemati, Amirouchene
	MM33	✓	✓	-	IM	S	-/±	4	Nemati, Laurent, Carita
	MM52	✓	✓	-	IM	N/A	--	4	Nemati, Laurent, Carita
	MM66	✓	✓	✓	✓	S, IHC, C, D	+	20+	Nemati, Laurent, Amirouchene
	MM252	N/A	✓	-	IM	S	N/A	N/A	N/A
	MM257	N/A	✓	-	IM	S	N/A	N/A	N/A
	MM267	✓	✓	✓	IM	S	N/A	N/A	N/A
	MM278	N/A	✓	-	IM	S	N/A	N/A	N/A
	MM293	✓	✓	✓	IM	S	N/A	N/A	N/A
	MM299	N/A	✓	-	IM	S	N/A	N/A	N/A
	MM300	N/A	✓	±	IM	S	N/A	N/A	N/A
	MM309	✓	✓	✓	IM	S	N/A	N/A	N/A
	MM325	✓	✓	✓	IM	S	N/A	N/A	N/A
Primary	UM 17-045	✓	✓	N/A	-	S	N/A	N/A	N/A
	UM 17-046	✓	✓	✓	✓	S, D	N/A	N/A	N/A
	UM 17-047	✓	✓	N/A	✓	S, C	N/A	N/A	N/A
	UM 17-048	✓	✓	N/A	✓	S, C, D	N/A	N/A	N/A
	UM 17-049	✓	✓	N/A	-	S	N/A	N/A	N/A
	UM 18-004	✓	✓	N/A	✓	S, D	N/A	N/A	N/A
	UM 18-005	✓	✓	N/A	-	S	N/A	N/A	N/A
	UM 18-007	✓	✓	N/A	✓	S, D	N/A	N/A	N/A
	UM 18-008	✓	✓	N/A	-	S	N/A	N/A	N/A
	UM 18-010	✓	✓	N/A	-	S	N/A	N/A	N/A

S=Sphere culture, IHC=Immunohistohemistry, C=confocal imaging, D=Drug screen
IM= insufficient material

Supplementary table ST2 qPCR primer sequences

	FW			RV		
MITF	5'-	AACAGAGAGTGCCCGTGAGT	-3'	5'-	GACATGGCAAGCTCAGGACT	-3'
TYR	5'-	TACGGCGTAATCCTGGAAAC	-3'	5'-	ATTGTGCATGCTGCTTTGAG	-3'
DCT	5'-	GGGAGGAACGAGTGTGATGT	-3'	5'-	TGGCAATTTCATGCTGTTTC	-3'
TYRP1	5'-	CTGGAATTTTGCAACGGGGA	-3'	5'-	CCATCCTCGGTGCTGTTACA	-3'
SOX10	5'-	CTTCATGGTGTGGGCTCAG	-3'	5'-	TGTAGTCCGGGTGGTCTTTC	-3'
GPX4	5'-	TGGACAAGTACCGGGGCTTC	-3'	5'-	CGAACTGGTTACACGGGAAG	-3'
SCL7A11	5'-	TGCTGTGATATCCCTGGCAT	-3'	5'-	AGCTGCATAACTCCAGGGAC	-3'

Supplementary figures

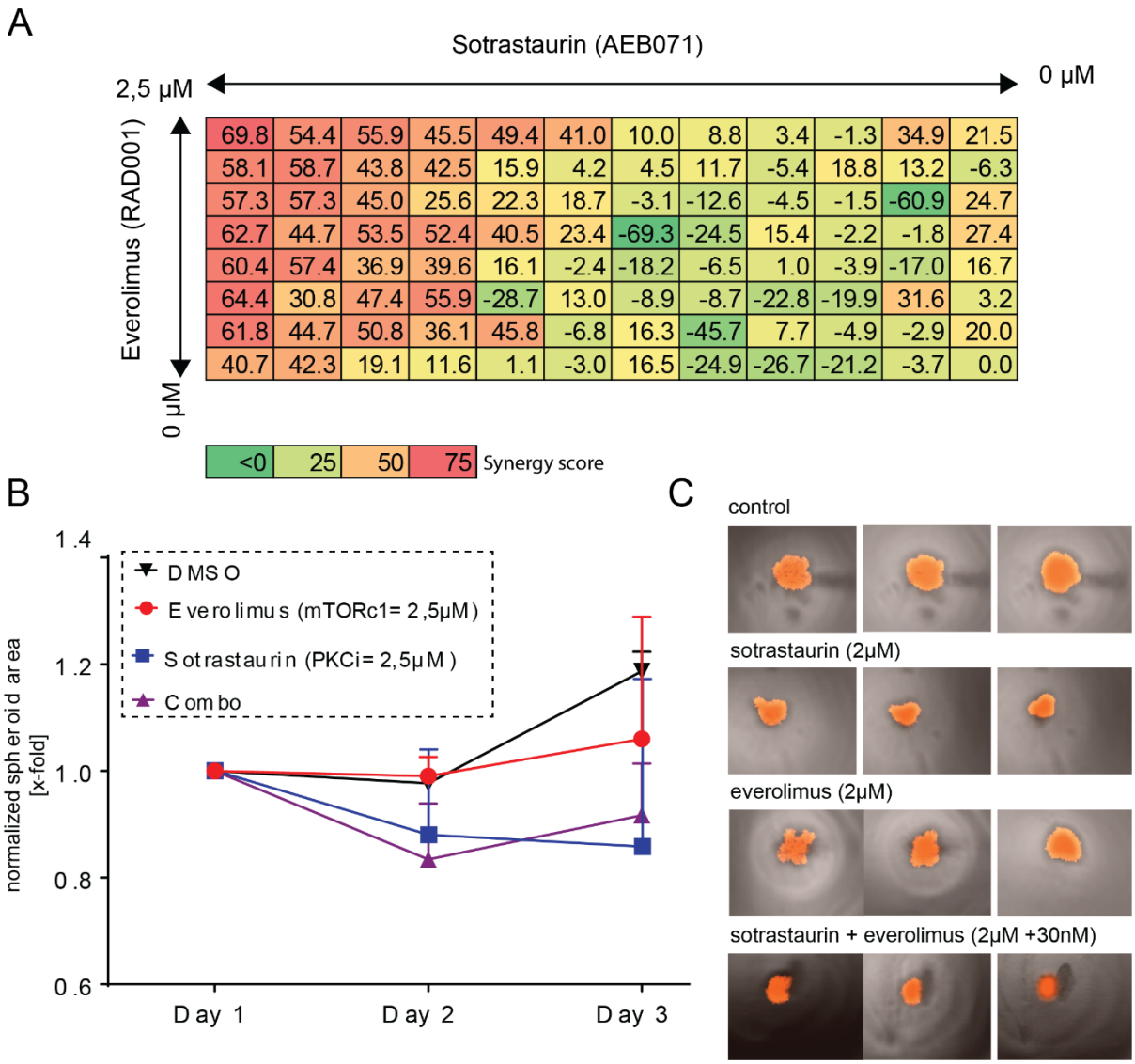

Supplementary Figure 1. Spheroid culture-based drug screening method for pre-clinical evaluation of combinatorial drug treatment. A) Heatmap of drug synergy between PKC inhibitor sotrastaurin and mTORC1 inhibitor everolimus, tested on spheroid culture line spXmm66, inhibition indicated in percentages and shown graphically as a heat-map (green to red, antagonistic to synergistic, respectively) made as an end point measurement after 3 days of treatment, using cell CellTiter Glo 2.0 as per the manufacturer's prescription. B) cell growth kinetics measured over time (based on spheroid surface area), measured on 1-,2- and 3-days post seeding in ultra-low adhesion 96-wells plates. C) Fluorescent micrographs of spXmm66 spheroids after 3 days of treatment with either sotrastaurin 2 µM, everolimus 2 µM the combination of both (sotrastaurin 2 µM and everolimus at 30 nM) compared to vehicle control (DMSO).

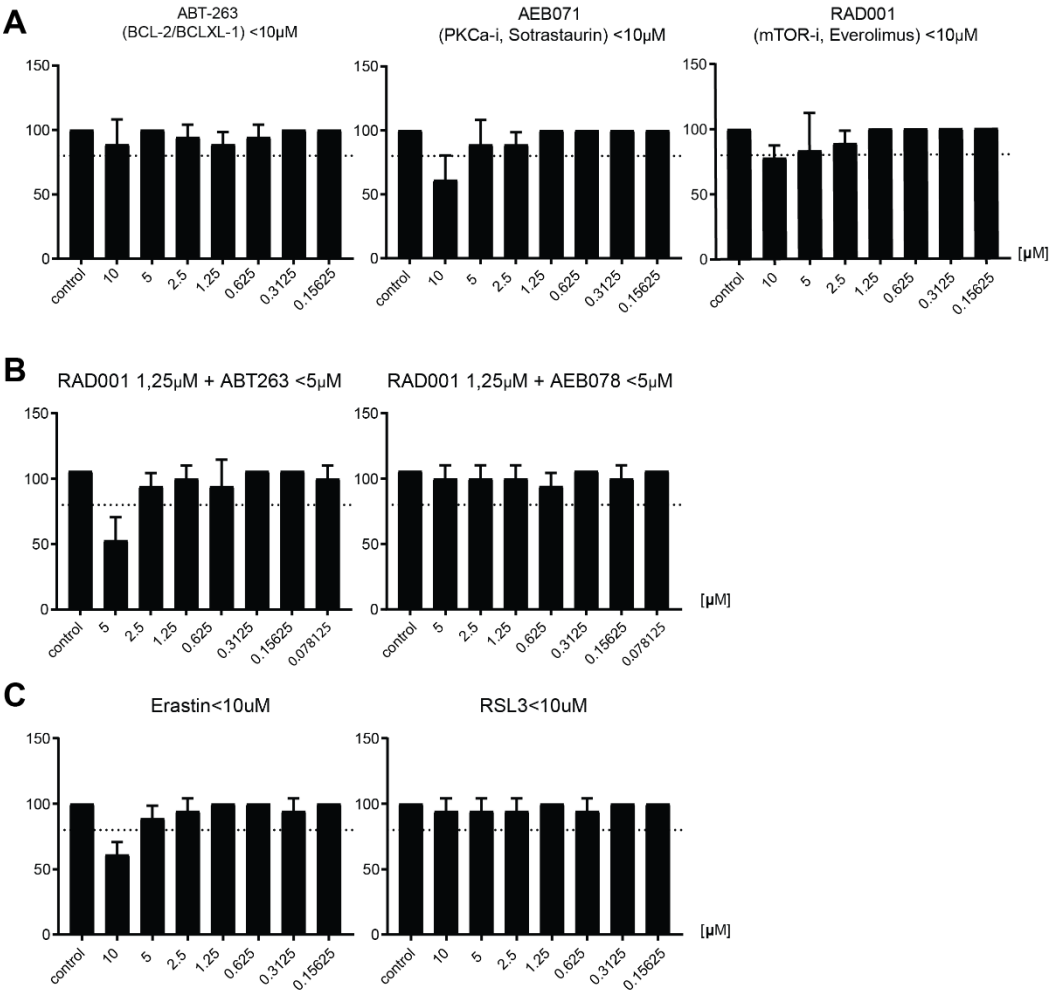

Supplementary Figure 2. Establishment of maximum tolerated dosage of tested putative anti-UM therapeutics. Dose response graphs on treated, uninjected zebrafish. Treatment concentration were deemed to be viable when at least 80% of the treated, uninjected, embryos survived for the duration of the treatment. A) First mono treatments were established (ABT-263, AB071 and RAD001) B) whereafter the combinatorial treatments were established (RAD001+ABT-263 and RAD001+AEB071). C) Ferroptosis inducing compounds.

All treatments were refreshed every other day, for 5 days post injection, up to the final day of the experiment (8 days post fertilization).

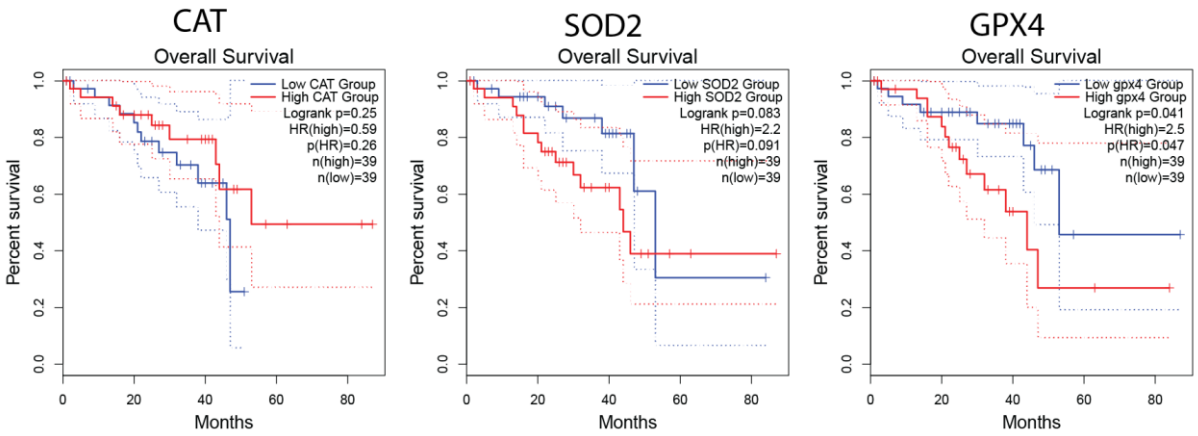

Supplementary Figure 3. In silico analysis of general ROS detoxifying enzymes in UM indicates that ferroptosis-related genes are strongly associated with a bad prognosis in UM. Analysis of the cancer genome atlas (TCGA) revealed that of the three major ROS detoxifying enzymes catalase (CAT), superoxide dismutase2 (SOD2) and glutathione peroxide 4 (*GPX4*), *GPX4* is the only one that correlates significantly with a bad prognosis.

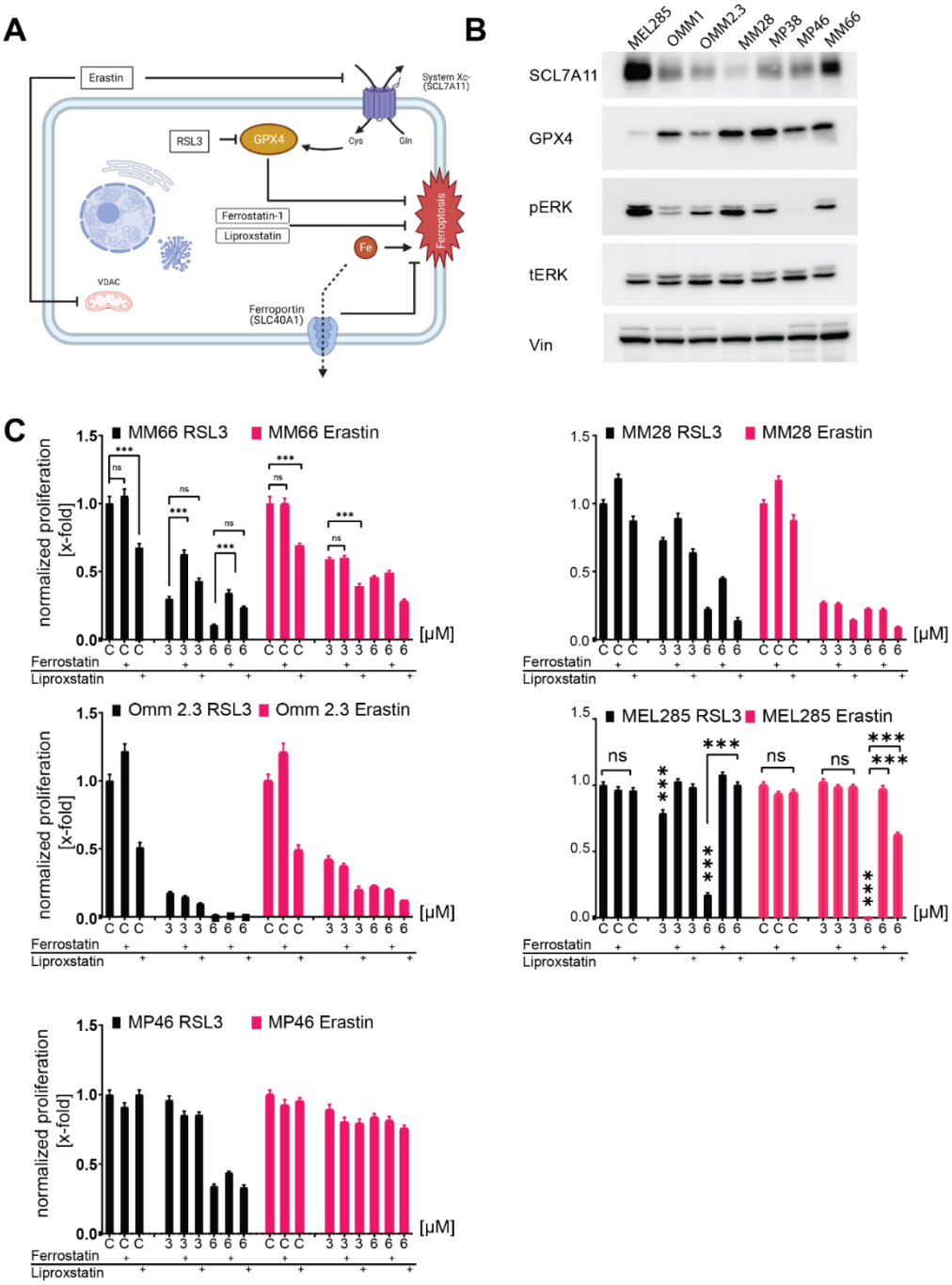

Supplementary Figure S4. Induction of ferroptosis significantly reduces cell survival *in vitro*. A) Induction of ferroptosis through inhibition of system X_c (Erastin, ER) or through inhibition of glutathione peroxidase 4 (*GPX4*) with RSL3 shows effective reduction of viability of both primary and metastatic uveal melanoma cells *in vitro* A) *in vitro* treatment of primary (MP46) and metastatic (Omm1, mm28 and Xmm66) uveal melanoma. B) Western blots detecting GPX4 and System Xc- (SCL7A11) and concordant expression of total ERK (tERK) and phosphorylated ERK (pERK) indicative of upstream RAS activation. C) Rescue experiment, All cell lines were treated with 8 and 4 µM Erastin and 6 and 3 µM RSL3, with the exception of MEL285 which was treated with 0.2 and 0.05 µM Erastin or RSL3 and subsequent rescue was attempted with ferroptosis inhibitors ferrostatin and Liproxstatin.

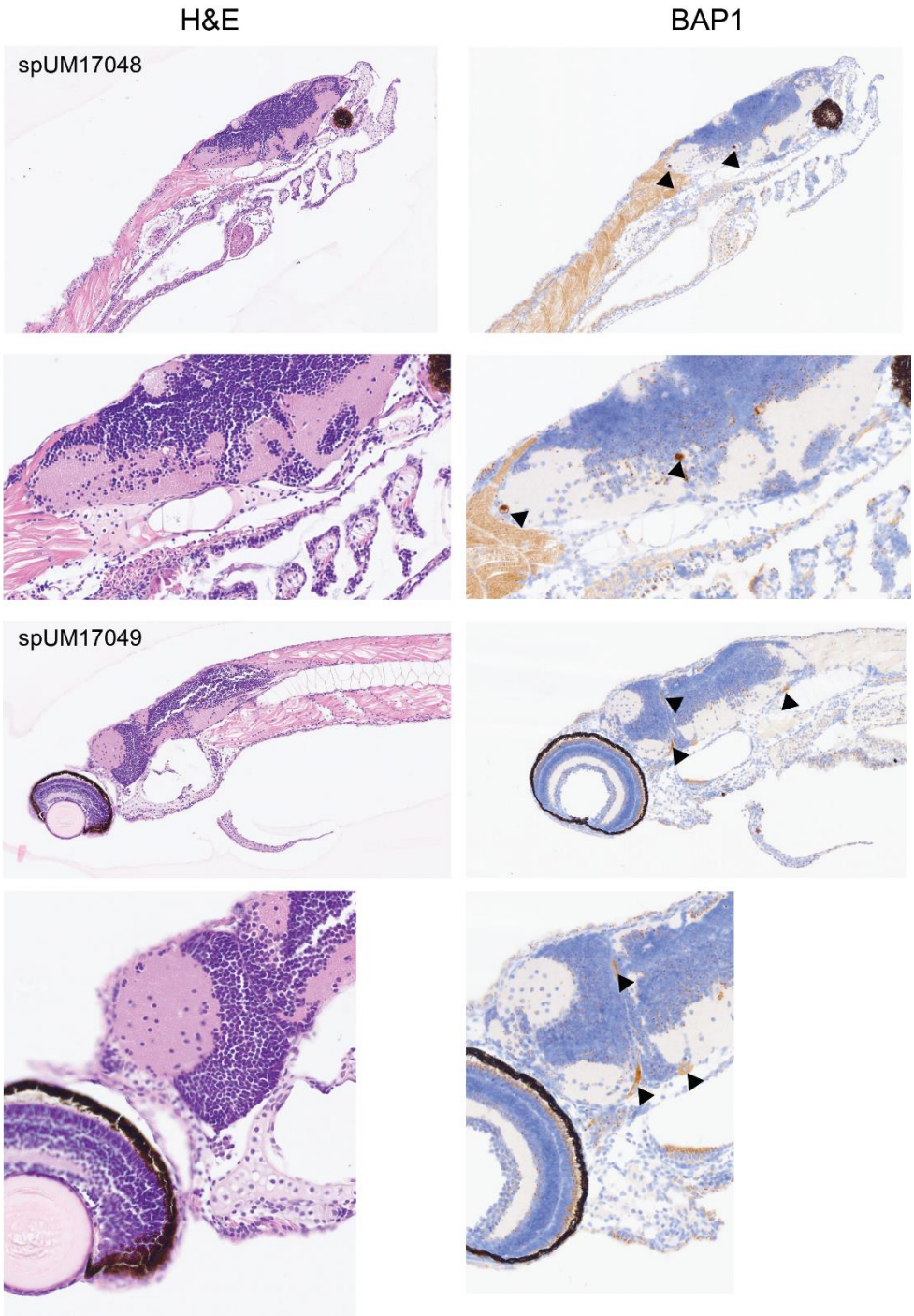

Supplementary Figure S5. Additional IHC staining of engrafted primary UM samples. Zebrafish larvae injected at 48 hpf, fixed at 6 dpi, fixed and oriented in a low melting temperature agarose block. Presence of BAP1 was assessed as previously described.

References

1. Van Raamsdonk CD, Bezrookove V, Green G, et al. Frequent somatic mutations of GNAQ in uveal melanoma and blue naevi. *Nature*. 2009;457(7229):599-602. doi:10.1038/nature07586

2. Zuidervaart W, Van Nieuwpoort F, Stark M, et al. Activation of the MAPK pathway is a common event in uveal melanomas although it rarely occurs through mutation of BRAF or RAS. *Br J Cancer*. 2005;92(11):2032-2038. doi:10.1038/sj.bjc.6602598

3. Chen X, Wu Q, Depeille P, et al. RasGRP3 Mediates MAPK Pathway Activation in GNAQ Mutant Uveal Melanoma. *Cancer Cell*. 2017;31(5):685-696.e6. doi:10.1016/j.ccell.2017.04.002

4. Prescher G, Bornfeld N, Hirche H, Horsthemke B, Jöckel KH, Becher R. Prognostic implications of monosomy 3 in uveal melanoma. *Lancet*. 1996;347(9010):1222-1225. doi:10.1016/S0140-6736(96)90736-9

5. Scholes AGM, Damato BE, Nunn J, Hiscott P, Grierson I, Field JK. Monosomy 3 in uveal melanoma: Correlation with clinical and histologic predictors of survival. *Investig Ophthalmol Vis Sci*. 2003;44(3):1008-1011. doi:10.1167/iovs.02-0159

6. Dogrusöz M, Jager MJ. Genetic prognostication in uveal melanoma. *Acta Ophthalmol*. 2018;96(4):331-347. doi:10.1111/aos.13580

7. Kilic E, Naus NC, Van Gils W, et al. Concurrent loss of chromosome arm 1p and chromosome 3 predicts a decreased disease-free survival in uveal melanoma patients. *Investig Ophthalmol Vis Sci*. 2005;46(7):2253-2257. doi:10.1167/iovs.04-1460

8. Damato B, Coupland SE. Translating uveal melanoma cytogenetics into clinical care. *Arch Ophthalmol*. 2009;127(4):423-429. doi:10.1001/archophthalmol.2009.40

9. Harbour JW, Onken MD, Roberson EDO, et al. Frequent mutation of BAP1 in metastasizing uveal melanomas. *Science (80-)*. 2010;330(6009):1410-1413. doi:10.1126/science.1194472

10. Dogrusöz M, Jager MJ, Damato B. Uveal melanoma treatment and prognostication. *Asia-Pacific J Ophthalmol*. 2017;6(2):186-196. doi:10.22608/APO.201734

11. Lane AM, Kim IK, Gragoudas ES. Survival rates in patients after treatment formetastasis from uveal melanoma. *JAMA Ophthalmol*. 2018;136(9):981-986. doi:10.1001/jamaophthalmol.2018.2466

12. Zimmerman LE, McLean IW, Foster WD. Does enucleation of the eye containing a malignant melanoma prevent or accelerate the dissemination of tumour cells? *Br J Ophthalmol*. 1978;62(6):420-425. doi:10.1136/bjo.62.6.420

13. Rossi E, Pagliara MM, Orteschi D, et al. Pembrolizumab as first-line treatment for metastatic uveal melanoma. *Cancer Immunol Immunother*. 2019;68(7):1179-1185. doi:10.1007/s00262-019-02352-6

14. Johansson PA, Stark A, Palmer JM, et al. Prolonged stable disease in a uveal melanoma patient with germline MBD4 nonsense mutation treated with pembrolizumab and ipilimumab. *Immunogenetics*. 2019;71(5-6):433-436. doi:10.1007/s00251-019-01108-x

15. Sugarbaker PH. Metastatic inefficiency: The scientific basis for resection of liver metastases from colorectal cancer. *J Surg Oncol*. 1993;53(3 S):158-160. doi:10.1002/jso.2930530541

16. Luzzi KJ, MacDonald IC, Schmidt EE, et al. Multistep nature of metastatic inefficiency: dormancy of solitary cells after successful extravasation and limited survival of early micrometastases. *Am J Pathol*. 1998;153(3):865-873. doi:10.1016/S0002-9440(10)65628-3

17. Mehlen P, Puisieux A. Metastasis: A question of life or death. *Nat Rev Cancer*. 2006;6(6):449-458. doi:10.1038/nrc1886

18. Piskounova E, Agathocleous M, Murphy MM, et al. Oxidative stress inhibits distant metastasis by human melanoma cells. *Nature*. 2015;527(7577):186-191. doi:10.1038/nature15726

19. Yagoda N, Von Rechenberg M, Zaganjor E, et al. RAS-RAF-MEK-dependent oxidative cell death involving voltage-dependent anion channels. *Nature*. 2007;447(7146):864-868. doi:10.1038/nature05859

20. Yang WS, Stockwell BR. Synthetic Lethal Screening Identifies Compounds Activating Iron-Dependent, Nonapoptotic Cell Death in Oncogenic-RAS-Harboring Cancer Cells. *Chem Biol*. 2008;15(3):234-245. doi:10.1016/j.chembiol.2008.02.010

21. Robertson AG, Shih J, Yau C, et al. Integrative Analysis Identifies Four Molecular and Clinical Subsets in Uveal Melanoma. *Cancer Cell*. 2017;32(2):204-220.e15. doi:10.1016/j.ccell.2017.07.003

22. Zhang Y, Shi J, Liu X, et al. BAP1 links metabolic regulation of ferroptosis to tumour suppression. *Nat Cell Biol*. 2018;20(10):1181-1192. doi:10.1038/s41556-018-0178-0

23. Némati F, Sastre-Garau X, Laurent C, et al. Establishment and characterization of a panel of human uveal melanoma xenografts derived from primary and/or metastatic tumors. *Clin Cancer Res*. 2010;16(8):2352-2362. doi:10.1158/1078-0432.CCR-09-3066

24. Amirouchene-Angelozzi N, Nemati F, Gentien D, et al. Establishment of novel cell lines recapitulating the genetic landscape of uveal melanoma and preclinical validation of mTOR as a therapeutic target. *Mol Oncol*. 2014;8(8):1508-1520. doi:10.1016/j.molonc.2014.06.004

25. Decaudin D, Frisch Dit Leitz E, Nemati F, et al. Preclinical evaluation of drug combinations identifies co-inhibition of Bcl-2/XL/W and MDM2 as a potential therapy in uveal melanoma. *Eur J Cancer*. 2020;126:93-103. doi:10.1016/j.ejca.2019.12.012

26. Luyten' GPM~, De Jon^ TVM, Luider TM. *ESTABLISHMENT AND CHARACTERIZATION OF PRIMARY AND METASTATIC UVEAL MELANOMA CELL LINES*. Vol 66. Wiley-Liss, Inc; 1996. doi:10.1002/(SICI)1097-0215(19960503)66:3

27. Chen PW, Murray TG, Uno T, Salgaller ML, Reddy R, Ksander BR. Expression of MAGE genes in ocular melanoma during progression from primary to metastatic disease. *Clin Exp Metastasis*. 1997;15(5):509-518. doi:10.1023/A:1018479011340

28. Heitzer E, Groenewoud A, Meditz K, et al. Human melanoma brain metastases cell line MUG-Mel1, isolated clones and their detailed characterization. *Sci Rep*. 2019;9(1):4096. doi:10.1038/s41598-019-40570-1

29. Groenewoud A, Yin J, Snaar-Jagalska BE. Ortho- and Ectopic Zebrafish Xeno-Engraftment of Ocular Melanoma to Recapitulate Primary Tumor and Experimental Metastasis Development. *JoVE (Journal Vis Exp*. 2021;(175):e62356. doi:10.3791/62356

30. Pontes KC de S, Groenewoud A, Cao J, Ataide LMS, Snaar-Jagalska E, Jager MJ. Evaluation of (*fli:GFP*) *Casper* Zebrafish Embryos as a Model for Human Conjunctival Melanoma. *Investig Opthalmology Vis Sci*. 2017;58(14):6065. doi:10.1167/iovs.17-22023

31. Lawson ND, Weinstein BM. *In vivo* imaging of embryonic vascular development using transgenic zebrafish. *Dev Biol*. 2002;248(2):307-318. http://www.ncbi.nlm.nih.gov/pubmed/12167406. Accessed June 15, 2014.

32. White RM, Sessa A, Burke C, et al. Transparent Adult Zebrafish as a Tool for *In vivo* Transplantation Analysis. *Cell Stem Cell*. 2008;2(2):183-189. doi:10.1016/j.stem.2007.11.002

33. Schindelin J, Arganda-Carreras I, Frise E, et al. Fiji: an open-source platform for biological-image analysis. *Nat Methods*. 2012;9(7):676-682. doi:10.1038/nmeth.2019

34. Preibisch S, Saalfeld S, Tomancak P. Globally optimal stitching of tiled 3D microscopic image acquisitions. *Bioinformatics*. 2009;25(11):1463-1465. doi:10.1093/bioinformatics/btp184

35. Chen L, De Menna M, Groenewoud A, Thalmann GN, Kruithof-de Julio M, Snaar-Jagalska BE. A NF-κB-Activin A signaling axis enhances prostate cancer metastasis. *Oncogene*. 2020;39(8):1634-1651. doi:10.1038/s41388-019-1103-0

36. Takahashi K, Yamanaka S. Induction of Pluripotent Stem Cells from Mouse Embryonic and Adult Fibroblast Cultures by Defined Factors. *Cell*. 2006;126(4):663-676. doi:10.1016/j.cell.2006.07.024

37. Maekawa M, Ishizaki T, Boku S, et al. Signaling from Rho to the actin cytoskeleton through protein kinases ROCK and LIM-kinase. *Science (80-)*. 1999;285(5429):895-898. doi:10.1126/science.285.5429.895

38. Carita G, Frisch-Dit-Leitz E, Dahmani A, et al. Dual inhibition of protein kinase C and p53-MDM2 or PKC and mTORC1 are novel efficient therapeutic approaches for uveal melanoma. *Oncotarget*. 2016;7(23):33542-33556. doi:10.18632/oncotarget.9552

39. Heijkants R, Willekens K, Schoonderwoerd M, et al. Combined inhibition of CDK and HDAC as a promising therapeutic strategy for both cutaneous and uveal metastatic melanoma. *Oncotarget*. 2018;9(5):6174-6187. doi:10.18632/oncotarget.23485

40. Yang WS, Sriramaratnam R, Welsch ME, et al. Regulation of ferroptotic cancer cell death by GPX4. *Cell*. 2014;156(1-2):317-331. doi:10.1016/j.cell.2013.12.010

41. JM U, A T, V R, et al. Lymph protects metastasizing melanoma cells from ferroptosis. *Nature*. 2020;585(7823):113-118. doi:10.1038/S41586-020-2623-Z

42. Dixon SJ, Patel D, Welsch M, et al. Pharmacological inhibition of cystine-glutamate exchange induces endoplasmic reticulum stress and ferroptosis. *Elife*. 2014;2014(3):2523. doi:10.7554/eLife.02523

43. Weinstein JN, Collisson EA, Mills GB, et al. The cancer genome atlas pan-cancer analysis project. *Nat Genet*. 2013;45(10):1113-1120. doi:10.1038/ng.2764

44. Tang Z, Li C, Kang B, Gao G, Li C, Zhang Z. GEPIA: A web server for cancer and normal gene expression profiling and interactive analyses. *Nucleic Acids Res*. 2017;45(W1):W98-W102. doi:10.1093/nar/gkx247

45. PT W, MJ G, SM R, et al. Mechanism of activation of the RAF-ERK signaling pathway by oncogenic mutations of B-RAF. *Cell*. 2004;116(6):855-867. doi:10.1016/S0092-8674(04)00215-6

46. Zilka O, Shah R, Li B, et al. On the Mechanism of Cytoprotection by Ferrostatin-1 and Liproxstatin-1 and the Role of Lipid Peroxidation in Ferroptotic Cell Death. *ACS Cent Sci*. 2017;3(3):232-243. doi:10.1021/acscentsci.7b00028

47. Moore AR, Ran L, Guan Y, et al. GNA11 Q209L Mouse Model Reveals RasGRP3 as an Essential Signaling Node in Uveal Melanoma. *Cell Rep*. 2018;22(9):2455-2468. doi:10.1016/j.celrep.2018.01.081

48. Xie Y, Hou W, Song X, et al. Ferroptosis: Process and function. *Cell Death Differ*. 2016;23(3):369-379. doi:10.1038/cdd.2015.158

49. Luo H, Ma C. A Novel Ferroptosis-Associated Gene Signature to Predict Prognosis in Patients with Uveal Melanoma. *Diagnostics*. 2021;11(2):219. doi:10.3390/diagnostics11020219

50. Chen X, Kang R, Kroemer G, Tang D. Broadening horizons: the role of ferroptosis in cancer. *Nat Rev Clin Oncol*. January 2021:1-17. doi:10.1038/s41571-020-00462-0

Chapter 5:

Melanin promotes melanoma metastasis by inhibiting ferroptosis

Chapter 5: Melanin promotes melanoma metastasis by inhibiting ferroptosis

Arwin Groenewoud[1, *], Maria Chiara Gelmi[2, *], Jie Yin[1], Gerda E. M. Lamers[1], Martine J. Jager[2], B.E Snaar-Jagalska[*]

1) Institute of Biology, Leiden University, Leiden, The Netherlands

2) Department of Ophthalmology, Leiden University Medical Center, Leiden, The Netherlands

*) These authors contributed equally

*Corresponding author: Prof Dr B.E. Snaar-Jagalska, Institute of Biology, PO Box 9502, Leiden University, Leiden, The Netherlands

E Mail: b.e.snaar-jagalska@biology.leidenuniv.nl

Manuscript in preparation

Abstract

Death in melanoma patients is mainly caused by metastasis. Increased melanin levels in cutaneous melanoma are associated with decreased patient survival. However, the role of melanin in this process remains poorly understood. Here, we show that melanin protects circulating melanoma cells from ferroptosis increasing their metastatic potential. We describe a strong association of high expression of the melanin biosynthesis gene *TYRP1,* the lipid peroxide reducer GPX4 and ferroptosis related mitochondrial voltage dependent anion channel 1 (VDAC1) with reduced melanoma specific survival. Furthermore, melanin levels in primary uveal melanoma patient cells positively correlate with their metastatic potential in zebrafish. Modulation of melanin levels in uveal, cutaneous and conjunctival melanoma cells results in enhanced or reduced metastatic potential upon increased or decreased melanin levels, respectively. Finally, melanin depletion sensitizes melanoma cells to ferroptosis inducers in zebrafish leading to a decreased metastatic burden. Collectively, our data identify melanin biosynthetic enzymes as potential future target to treat melanoma.

Introduction

Melanoma is one of the most common malignancies, and arises from melanocytes following malignant transformation. Subsequent metastatic spread, and not the growth of the primary tumor, kills up to 90% of cancer patients[1,2,3]. For intra-ocular melanoma, it is assumed that only a small fraction of cells that escape from the primary tumor successfully establish a metastatic colony, indicating a strong selective pressure on disseminating cancer cells within the circulation[4–6]. Among the key factors in curbing metastatic dissemination in the circulation are reactive oxygen species (ROS)[7,8]. These ROS are derived from either intracellular or extracellular stressors[9–12]. In healthy skin, melanin functions to protect against Ultraviolet (UV) radiation by preventing direct DNA damage (UV-B) and ROS-mediated genotoxicity (UV-A)[13–15]. We propose that melanin protects transformed melanocytes in a similar manner, thus enhancing cell survival during dissemination and the metastatic potential of melanoma cells.

Melanomas are derived from neuroectodermal progenitor cells during embryonic development, giving rise to different populations of melanocytic precursors[16,17]. All melanocytes harbor intrinsic melanogenic potential, which is normally induced in the skin in a UV-dependent manner through the αMSH-MITF-TYR axis[16,18]. In ocular melanocytes, melanin biosynthesis is induced through a largely unknown mechanism[18–20].

In contrast, most melanoma cell lines derived from melanated lesions lose their capacity to synthesize melanin *in vitro*. Conversely, patient-derived xenograft models retain their melanogenic potential, underscoring the apparent selective pressure *in vivo*. Interestingly, studies suggest an inverse correlation between pigmentation and migratory capacity[21,22]. Strikingly, the *in vivo* cutaneous melanoma model described by Pinner et al shows an enhancement of distant metastasis in the presence of heightened melanin levels[22].

One of the possible mechanisms of ROS-mediated cell death is thought to be ferroptosis, a lipid peroxidation-based, iron-dependent mechanism of cell death[23–26]. Ferroptosis seems to be more strongly induced in cutaneous melanoma (CM) cells expressing oncogenic RAS variants, possibly due to an increase in cellular iron levels[23,26,27].

During ferroptosis, either induction of mitochondrial stress, endoplasmic reticulum stress through inhibition of voltage-gated anion channel, or inhibition of the cysteine/glutamate antiporter system (System Xc-) cause a dramatic increase of intracellular ROS. This sharp increase in ROS catalyzes lipid peroxidation and is presumed to lead to subsequent cell membrane permeation and cell death, while maintaining nuclear integrity[28,29].

Glutathione peroxidase 4 (*GPX4*) functions as a lipid peroxide reducer, effectively reverting the damage done by ferroptosis[24,25]. Intracellular glutathione is used as a reservoir of ROS reduction and can effectively curb ferroptotic cell death. Common inducers of ferroptosis either interfere with mitochondrial or electron transport chain functions, the cellular system Xc- (erastin), or inhibit GPX4[30].

We observed a positive correlation between melanin inclusion in primary UM tissues and their respective engraftment capacity in a zebrafish model. We propose that the retained melanin protects melanoma cells in the circulation, by alleviating ferroptosis and its related intracellular ROS-mediated damage, thereby enhancing the metastatic potential of melanoma cells.

To address this hypothesis, we have tested a set of different melanoma cell lines from CM and conjunctival melanoma (CoM) origin with melanated and non-melanated phenotypes. We used a melanin depletion strategy for CM and CoM cell lines. Conversely, we developed a biological melanin transfer system, allowing us to re-introduce melanin from a melanated CM donor cell line to non-melanated uveal melanoma (UM) cell lines.

We correlated melanin inclusion within UM, CM, and CoM with an enhanced metastatic potential and proved that depletion of melanin in melanated melanoma cells decreases their metastatic potential. Furthermore, we showed that transfer of extraneous melanin into UM cells confers protection to stress during hematogenous dissemination. Finally, we demonstrated that melanin depletion significantly enhances cellular susceptibility to ferroptotic insult during dissemination *in vivo*. In conclusion, we confirmed that melanin can act as a pro-metastatic factor protecting cells from ROS and demonstrated the importance of melanin in blocking ferroptosis during metastatic dissemination.

Materials and methods:

Uveal melanoma

UM tissue was obtained from patients from the Leiden University Medical Center (LUMC) in Leiden, The Netherlands. Part of the tumor was snap frozen with 2-methyl butane and used for DNA and RNA isolation, while the remaining tumor tissue was fixed in 4% neutral-buffered formalin and embedded in paraffin.

For a gene expression array, material was obtained from 64 patients who underwent an enucleation for UM between 1999 and 2008, of which 51% were male and 49% female. The mean age at the time of enucleation was 61 years. The mean follow-up time (defined as the time period between enucleation and death) was 83 months (range 2 to 229 months). Follow-up was updated in 2020. At the end of follow up, 17 (27%) patients were alive, 37 (58%) patients had died because of metastasis, four (6%) had died because of other causes and six (9%) had died but the cause of death was unknown. Gene expression was determined with the Illumina HT12v4 array (Illumina, Inc., San Diego, CA, US). As published by de Lange et al 2015[39].

Fresh tumor material was obtained directly after enucleation to establish spheroids.

We also assessed mRNA levels of tumors included in the TCGA database (n=80) as published by Robertson et al 2017[40–42].

Institutional Review Board Statement

The analysis was approved by the METC of the LUMC (B14.003/SH/sh Approval Biobank OOG-2 “Oogtumoren (of een verdenking hierop)”, protocol Uveamelanoom-lab B20.026, approval June 2020). Fresh material was used for spheroids under METC protocol UM CURE 2020: Prospective collection: new treatment options for metastatic uveal melanoma (NL57166.058.16). The research adhered to Dutch law and the tenets of the Declaration of Helsinki (World Medical Association of Declaration 2013; ethical principles for medical research involving human subjects). Each patient had signed an informed consent.

Stable cell culture

Cell line SK-Mel28 was acquired from ATCC, while other cell lines were kindly provided by Dr. B Rinner (Mugmel2)[31], Prof. Dr. M.J. Jager (CRMM1 and CRMM2)[43], Dr. A.G Jochemsen (OMM2.3)[44] and Dr S. Alsafadi (XMM66)[45]. Human CM PDX derived cell lines PDX11917 (alternatively named, M011-5.X1.CL) was kindly provided by Prof. D. Peeper[34].

We routinely imaged or assessed the cells used in this project using an inverted automated EVOS microscope (Thermo scientific, Waltham, USA) using eGPF and RFP filters to ensure retention of normal phenotypes and to verify fluorescent tracer expression

Cells were cultured in a humidified incubator, 5% CO_2 at 37°C, all cells were intermittently tested for the absence of mycoplasma using the universal mycoplasma detection Kit (American type cell culture (ATCC), LGC Standards GmbH, Wesel, Germany) according to the manufacturer's prescriptions. All cells, with the exception of primary UM cells, were cultured in Dulbecco's modified eagles' medium (DMEM), enhancing melanin biosynthesis due to its high tyrosine levels (3,5-fold higher than RPMI1640). DMEM was supplemented with 10% fetal bovine serum and glutamax (GIBCO, Thermo scientific). Cells were propagated through subsequent medium removal, washing with Dulbecco's phosphate buffered saline (DPBS) and incubation with 2mL tryplE (GIBCO). Cells were carefully dispersed after the addition of DMEM up to the original culture volume.

Chemical melanin depletion

Commonly phenylthiourea (PTU, Sigma) is used, dissolved in water, for the inhibition of melanation of zebrafish larvae. We reasoned that PTU could also be used to block the biosynthesis of melanin *in vitro*. To this end, we treated mugmel2 cells with a concentration range of 1 - 0.0625 mM, dissolved in dimethylsulfoxide (DMSO, Sigma).

Ethics statements

All animal experiments were approved by Animal Experiments Committee (Dier Experimenten Commissie, D.E.C.) under license AVD1060020172410. All animal were maintained in accordance with local guidelines using standard protocols (www.ZFIN.org)

Zebrafish engraftment

Primary cells were dispersed as described previously by Groenewoud et al[46]. In brief, cells were harvested from adherent cultures through tryplE addition, and subsequently concentrated by centrifugation. Cells were transferred to a 15 mL centrifuge tube and centrifuged for 5 minutes at 200 x g, followed by complete removal of all DPBS. The cell pellet was resuspended in 1 mL DPBS and subsequently counted. The cells were pelleted again at 200 x g whereafter the DPBS was removed after centrifugation. To completely remove all DPBS the cells were centrifuged for another minute at 200 x g, the cell pellet was resuspended to a final concentration of $250 \times 10^6 \cdot mL^{-1}$ in 2% polyvinylpyrrolidone 40 (PVP_{40}) in DPBS.

In brief, cells were injected into zebrafish larvae of either *casper* or *Tg(fli:eGFP x casper)* zebrafish larvae at 48hpf into the duct of Cuvier (doC) also known as the embryonic common cardinal vein using a capillary glass needle.

Chemical compounds and drugs

Erastin, RSL3 and mitomycin-C were purchased from Cayman chemical (Ann Arbor, Michigan, USA). PTU was purchased from Sigma (Sigma, Zwijndrecht, the Netherlands)

Drug treatment of engrafted zebrafish

Fish were bred and maintained until 48hpf, whereafter they were injected with approximately 300-400 cells per individual, through the doC allowing the cells to disseminate hematogenously within several hours after injection. One hour post injection possible dead larvae were removed from the injected pool and the injected individuals were divided over clean Petri dishes, with approximately 100-150 individuals per dish. Approximately 16hpi the injected larvae were screened using a stereo epi-fluorescent microscope, all the unwanted phenotypes (uninjected, malformed) were discarded. All larvae were randomly assigned to experimental groups in a 24 wells plate, with at least 6 wells containing 6 fish per well per condition. After plating the fish, approximately 16-18hpi the fish were treated with the appropriate level of inhibitor dissolved in DMSO and diluted to the final concentration in eggwater.

Data acquisition and analysis

For kinetic measurements of tumorigenicity engrafted individuals were imaged at 1,4- and 6-days post implantation using an epifluorescent stereo microscope. At the first time point the microscope settings (exposure time and gain) were set on the control group of each sample population, taking care that signal saturation was not attained to allow for signal increase due to cell growth. Each sample set was imaged using the same settings throughout the duration of the experiment. All images were analyze using a custom imageJ MACRO (Zenodo DOI: 10.5281/zenodo.4290225). Data was normalized to the vehicle control group of each experimental population; two biological replicates were combined with at least 20 individuals per biological replicates.

Transmission electron microscopy sample preparation

Cells were cultured on thermanox (Thermo scientific/Nunc) coverslips, fixation was performed with a mixture of 2% glutaraldehyde and 2% formaldehyde in 0,1M Na-cacodylate buffer pH=7.2

Post-fixation was performed with 1% OsO_4 +$K_4Fe(CN)_6$ (15µg/ml) in demineralized water for 1 hour at room temperature, after dehydration through a graded series of ethanol, all specimens were kept for 16 hours in epoxy resin (Agar Scientific,) before embedding. Ultrathin sections were collected on formvar-coated one hole copper grids. Electron microscopy images were obtained with a JEOL 1400Plus Transmission Electron Microscope (Tokyo, Japan) at 80KV.

WST1 proliferation assay

Mugmel2 cells (7,5 × 10^4) were seeded in 100 µL in flat bottom 96 wells plates (Corning), combining both cells with prior chemical inhibition of melanin biosynthesis and vehicle control (DMSO) treated cells in the same plate, in triplicate. Cell were left to attach overnight and were subjected to ferroptosis induction using erastin and RSL3, compared to DMSO control for 3 days. Proliferation was measured based on WST1 conversion, following the manufacturers description. Values were normalized to vehicle treated control, 100% survival, and plotted.

qPCR analysis

Cells were harvested ($1x10^6$) by centrifugation (200 x g for 5 min at 25°C. Whole RNA was isolated using the Qiagen RNeasy kit (Qiagen) according to the manufacturer's description, treating the isolate on-column with RNase free DNAse for 15 minutes at room temperature. Total RNA yield was quantified using Nanodrop 2000 (Thermo scientific, Wilmington, USA) and 1 µg RNA was used to synthesize cDNA using the iSCRIPT cDNA kit (Biorad, Hercules, USA) according the manufacturers description.

Detection was performed using the iQ5 QPCR apparatus (Biorad), using IQ green super mix (Biorad), for 35 cycles. Primers were diluted in PCR grade nuclease free water (Gibco) at a concentration of 100 µM. All primers were tested for, and passed an efficiency test prior to use and were used at a final concentration of 10 pmol.

Glyceraldehyde-3-phosphate dehydrogenase (GAPDH) expression level was used as an internal reference for each experimental primer set. Transcript levels were corrected for loading to GAPDH expression and normalized using the ΔCT method. All samples were measured in at least 3 biological triplicates.

Cellular ROS Assay reactive oxygen measurement

To measure overall intracellular ROS concentrations, and the influence of intracellular melanin on ROS induction on mugmel2(-eGFP cells), we seeded $7,5 \times 10^4$ cells in 100µL per well, in black skirted glass bottom 96 wells plates (Corning). The cells were allowed to adhere for 16 hours prior to analysis. In the same plate we seeded mugmel2 cells with and without prior melanin depletion, in triplicate, in DMEM, without phenol red. ROS inducers were added, diluted in phenol red free culture medium, to a final concentration of 500, 100, 500 µM Paraquat, Menadione and hydrogen peroxide (H_2O_2) in 50 µL, respectively. After addition of ROS inducers, the cells were incubated for 30 minutes. Subsequently, red fluorescent Cellular ROS reagent (Abcam, Cambridge, United Kingdom) was added, 50 µL diluted in phenol red free DMEM to a 2x concentration. Cells were treated for 30 minus followed with 2 washes with PBS and subsequent fixation with 4% PFA at room temperature for 10 minutes. Cells were washed with PBS containing 200 mM glycine, 0.1 µg/mL and 4',6-Diamidine-2'-phenylindole dihydrochloride (DAPI) for 1 hour at 4 °C. Plates were imaged using an EVOS M7000 microscope (Thermo Fischer Scientific, Darmstadt, Germany), imaging DAPI stained nuclei, green cells outline, red ROS reagent and brightfield at 20x

magnification. Data was analyzed using ImageJ, measuring ROS reagent signal intensity in GFP positive area, while normalizing for the number of cells (DAPI positive nuclei counts).

Melanin measurement

Melanin was measured spectrophotometrically, after solubilization in 1M NaOH, containing 10% DMSO (v/v) as described by Friedman et al.[18] In brief, cell pellets were collected of 2 × 10^6 cells by tryplE incubation, inactivation and subsequent centrifugation. Cells were frozen at -20°C prior to measurement. A standard curve of chemical eumelanin (Sigma, Zwijndrecht, the Netherlands) was made ranging from 1 mg/mL to 7,8125 µg/mL (2-fold dilution series) in triplicate. Standards and samples were solubilized by addition of 1M NaOH, 10% DMSO and incubation at 80°C for 30min. melanin negative samples (MDA-mb231 cells expressing the same reporter gene were used as a negative control) were taken along and were used to subtract backgrounds after measurement. Absorbance was measured at 420nm and plotted; concentration was inferred from the standard curve.

Co-culture experiments

For the melanin transfer co-culture experiments we cultured highly melanotic cell line mugmel2[31] expressing eGFP in the absence and presence of phenylthiourea (PTU) a generic inhibitor of melanin biosynthesis.[20,47] After two passages the PTU treated cells were considered melanin depleted, where depletion was validated through the spectrophotometric measurement previously described. The cells were treated with 100 µg/mL mitomycin-C (Sigma) in culture medium, under normal culture conditions, for three hours. The cells were washed with sterile PBS and DMEM subsequently prior to harvesting. UM cells were harvested as previously described. For both UM-tdTOM lines 1 × 10^6 cells were seeded in a 75 cm^2 culture flask mixed together with melanin depleted cells (mel^-) and with highly melanated cells (mel^+), the cells were cultured for 4 days at normal culture conditions. Prior to harvesting the cells were checked for presence of remnant eGFP signal (donor cells) and tdTOM (acceptor cells) and for presumptive melanin transfer. The cells were washed extensively, prior to harvesting as previously described.

Lentiviral over expression and shRNA construct generation

Lentiviral overexpression and shRNA constructs from the Sigma TRC mission library were kindly provided to us by Dr. M. Rabelink from the department of department of molecular cell biology, from the Leiden university medical center (Constructs detailed in supplementary table ST1). Lentiviral particles were generated as described previously by Heitzer er al 2019[33]. In brief Hek293T cells were grown to 80-90% confluency and transfected after a medium change with psPAX2, pMD2.G and the transfer plasmid of choice at a respective molar ratio of 1.3 pmol, 0.72 pmol, 1.64 pmol using 30uL lipoD293 on a 75cm2 culture flask. Cell culture medium was exchanged for 20mL complete DMEM 24 hours post transfection. Viral particles were harvested 72h after the original transfection.

Patient data analysis

LUMC cohort: Genetic information on TYR, TYRP1 and DCT and information on the chromosome 3 status and BAP1 status was obtained from a database of 64 UMs in eyes enucleated at the Leiden University Medical Center between 1999 and 2008.

TCGA cohort: Information for both uveal and cutaneous melanoma patients were gathered from The Cancer Genome Atlas (TCGA), which is a publicly available database available at https://www.cancer.gov/tcga. The TCGA database for UM contains 80 patients and the TCGA database for cutaneous melanoma contains 458 patients. Data was accessed and analysed through GEPIA2[42].

Zebrafish data acquisition and statistical analysis

All zebrafish larval engraftments were performed in biological duplicate, unless otherwise stated. All groups were >20 individuals per biological repeat, unless otherwise stated. All individuals were randomized and entered into either control or experimental groups, all individuals were randomly selected and imaged using the same exposure setting using a stereo fluorescent microscope. Outliers were removed from all data sets using GraphPad Prism 8.0, (Q5) prior to normalization and combination of all biological replicates. Data was normalized to either control (drug treatment) or to day one (in the case of growth kinetics experiments). Statistical significance was tested with an ANOVA, for normally distributed data sets, otherwise a Kruskal-Wallis test was used. Error bars depict ±SEM.

Patient data and statistical analysis

The statistical analyses were carried out with SPSS version 25 (IBM corp).

Correlation between melanin-related genes and chromosome 3 status and BAP1 status were calculated with Mann-Whitney U test. The survival analysis was carried out using Kaplan Meier survival curves and splitting the gene expression data in the middle and comparing the 32 patients with lower TYR, lower TYRP1 and lower DCT with the 32 patients with higher TYR, higher TYRP1 and higher DCT respectively. In the LUMC cohort, survival was calculated with melanoma-related mortality as the endpoint.

The TCGA cohorts for both UM and cutaneous melanoma were analyzed with the interactive web server GEPIA2, splitting the population along the median for each gene. In these cohorts, survival was calculated with overall survival as the endpoint.

Results

The presence of melanin and the upregulation of TYRP1 correlate with tumorigenic potential of UM PDX samples and with a decrease in disease-free survival in UM patients.

When studying the metastatic colonization capacity of uveal melanoma in a zebrafish model, we noticed striking differences between tumor samples. We had generated spheroid cultures from primary UM, as recently described by Groenewoud et al 2021. After dissociation of spheroids, cells were stained with a red transient dye and engrafted intravenously into blood vessels of reporter zebrafish larvae (*tg(fli:eGFP)*) at 48 hours post fertilization (hpf). We measured the engraftment over time based on the fluorescent intensity and the size of the metastatic foci, within the engrafted zebrafish larvae at 1-, 4-, and 6-days post injection (dpi) (Figure 1B). Of the three engrafted PDX samples, the highly-pigmented sample spUm-LB046 showed significant ($p<0.001$) enhancement of tumor cell number (as measured by fluorescence integrated density) over time, with many tumor cells visible all over the body after 6 days. Tumor sample spUm-LB048 (containing only medium levels of melanin) induced a significant enhancement of fluorescent signal between 1 dpi and 4 dpi ($p<0.001$), with almost total abrogation of the signal at 6 dpi ($p<0.001$), while the non-melanated primary UM sample spUM-LB049 was completely cleared from the engrafted zebrafish host at 4 dpi. We considered the option that the differences were caused by different degrees of melanin. As UM tend to spread hematogenously, we verified our findings by assessing the relation between tumor pigmentation and patient survival in a series of enucleated UM (LUMC cohort n=64) (Figure 1C). We used transcriptomics data to assess the effect of the transcription of the terminal enzymatic stages of melanin biosynthesis (Leiden cohort, Figure 1D). Pigmentation levels assessed after enucleation of primary UM sub-divided the tumors into two groups: non- and lightly-pigmented versus medium- and highly-pigmented tumors. Survival analysis indicated that there is a significant increase in melanoma-related death in patients with medium- and highly-pigmented tumors compared to those with non- and lightly-pigmented UM ($p=0.006$). When comparing melanin biosynthetic genes with melanoma-related death, only the final biosynthetic step of melanin synthesis demonstrated a correlation with bad disease outcome (*TYRP1*, $p=0.01$) whereas both upstream tyrosinase (*TYR*) and dopachrome tautomerase (*DCT*) were not related to

melanoma-related death (*TYR*, p=0.52; *DCT*, p=0.15). Overall, these results suggest that there is a causal link between the level of melanin in UM cells and their metastatic potential.

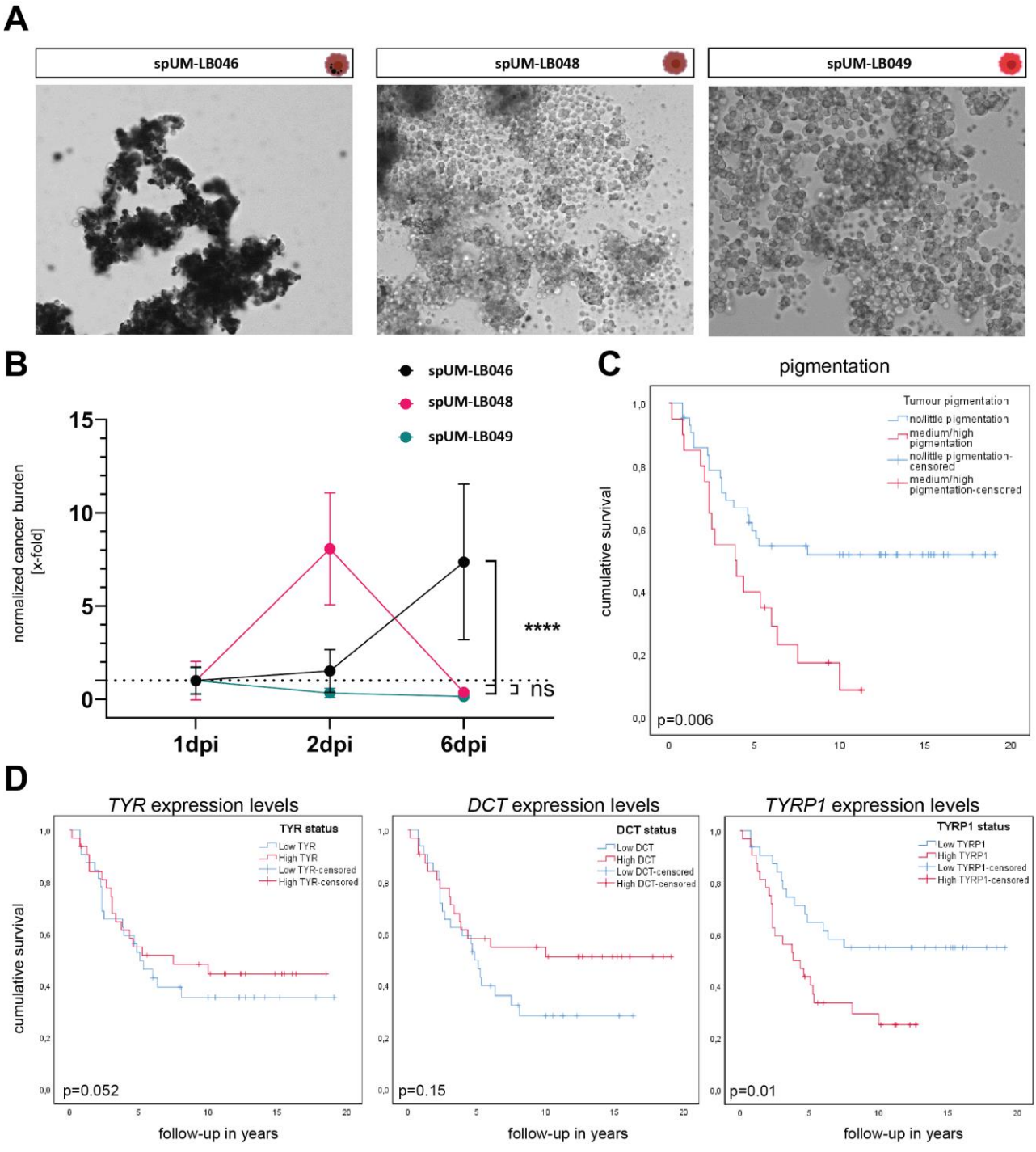

Figure 6 Melanin levels within primary UM cells correlate with survival *in vivo*. A) Three primary UM patient samples ranging from strongly melanated (spUm-LB046), intermediately melanated (spUm-LB048) and non-melanated (spUm-LB049). Melanin levels were derived from phase contrast images of spheroid cultures established from patient material, prior to engraftment. B) Three UM spheroid cultures were stained with red fluorescent lipid tracer (CMDiI) and then injected into zebrafish larvae and monitored for cancer cell engraftment on days 1, 4, and 6- post injection (dpi. C) Histological tumor pigmentation at the time of enucleation and their relation with survival of UM patients. Survival of patients with non and lightly-pigmented tumors (n= 43) was compared to survival in patients (n=20) medium- and highly-pigmented tumors based on pathological assessment. D) Assessment of the effect of individual melanin biosynthetic genes on UM survival. Expression of the most upstream located tyrosinase (TYR) and the downstream biosynthetic proteins dopachrome tautomerase (DCT, or alternatively TYRP2) and tyrosinase-related protein 1 (TYRP1), analyzed in a group of 64 patients; groups were determined according to the median mRNA expression only TYRP1 expression levels show a negative correlation with survival.

Chemical and genetic melanin depletion of highly-melanated CM melanoma cell line mugmel2 significantly reduces its metastatic potential.

After the primary assessment of the effect of melanin on metastatic dissemination of UM, we asked if this phenomenon could be extended to other melanomas. To determine this, we used a highly-melanated *RAS*-mutated CM cell line: mugmel2[31]. We first determined the presence of all stages of melanosome maturation in mugmel2 cells, using transmission electron microscopy (TEM) as shown in (Figure 2A). Melanosomes Type II, III and IV were readily visualized due to their intrinsic electron density, and are demarcated with yellow (▲ type II), blue (▲ type III) and red (▲ type IV) arrowheads, respectively. The eGFP-expressing mugmel2 cells were engrafted in zebrafish as described previously, with or without prior chemical depletion of melanin through 1-phenyl 2-thiourea (PTU). Intravenous injection of the melanin-depleted mugmel2 cells induced less metastatic colonization in *Casper* zebrafish at 6 dpi (Figure 2B) in comparison to non-depleted cells, and measured the effect of chemical melanin depletion on the total concentration of intracellular melanin *in vitro* (Figure 2D). We measured significant dose-dependent decreases of metastatic potential at 4 dpi and 6 dpi for two concentrations of PTU (125 and 500μM) when compared to treatment with equivalent volumes of vehicle control (DMSO) (Figure 2C). We showed a dose-dependent inhibition of intracellular melanin biosynthesis, when compared to vehicle control. The strongest inhibition, without deleterious effects on cell survival, was induced by 500 μM PTU (approximately 85%, $p<0.001$) and a dose-dependent

increase in melanin content between 500 μM and lower PTU concentrations ($p<0.05$) (Figure 2D). Concentrations of PTU >500 μM were deleterious to the proliferation and survival of the cells (results not shown).

Genetic interference with melanin biosynthesis through inhibition of tyrosine (*TYR)* expression by shRNA-mediated mRNA decay led to a significant inhibition of both melanin biosynthesis and intracellular melanin levels (Figure 2D)[20,32]. We used two individual shRNA constructs targeting *TYR.* This shRNA-mediated knock down of TYR in mugmel2 reduced the cells' metastatic capacity when compared to scrambled shRNA control concordantly (Figure 2E, $p<0.001$). To assess whether this decrease in metastatic capacity could be due to a decrease in overall migration, we measured cell migration *in vitro* using a wound healing assay. We observed no difference in the migratory potential when comparing PTU-treated cells with the vehicle control (Figure 2F, G). Using TEM, we determined whether PTU treatment induced loss of melanosomal structures in mugmel2 cells (Figure 2H). We observed a loss of type II, III and IV melanosomes upon treatment with both 500 and 250μM PTU (data for 250μM not shown). In summary, these data clearly suggest that the degree of melanation of mugmel2 correlates with its tumorigenic potential. The presence of all known stages of melanosomes indicates that cell line mugmel2 has retained its canonical melanogenic phenotype. The depletion of melanin from mugmel2 through either chemical or genetic means significantly alters its cellular tumorigenic capacity. This depletion does not significantly alter its migratory capacity suggesting that *in vitro* and *in vivo* functions of melanin inclusion are disjoined.

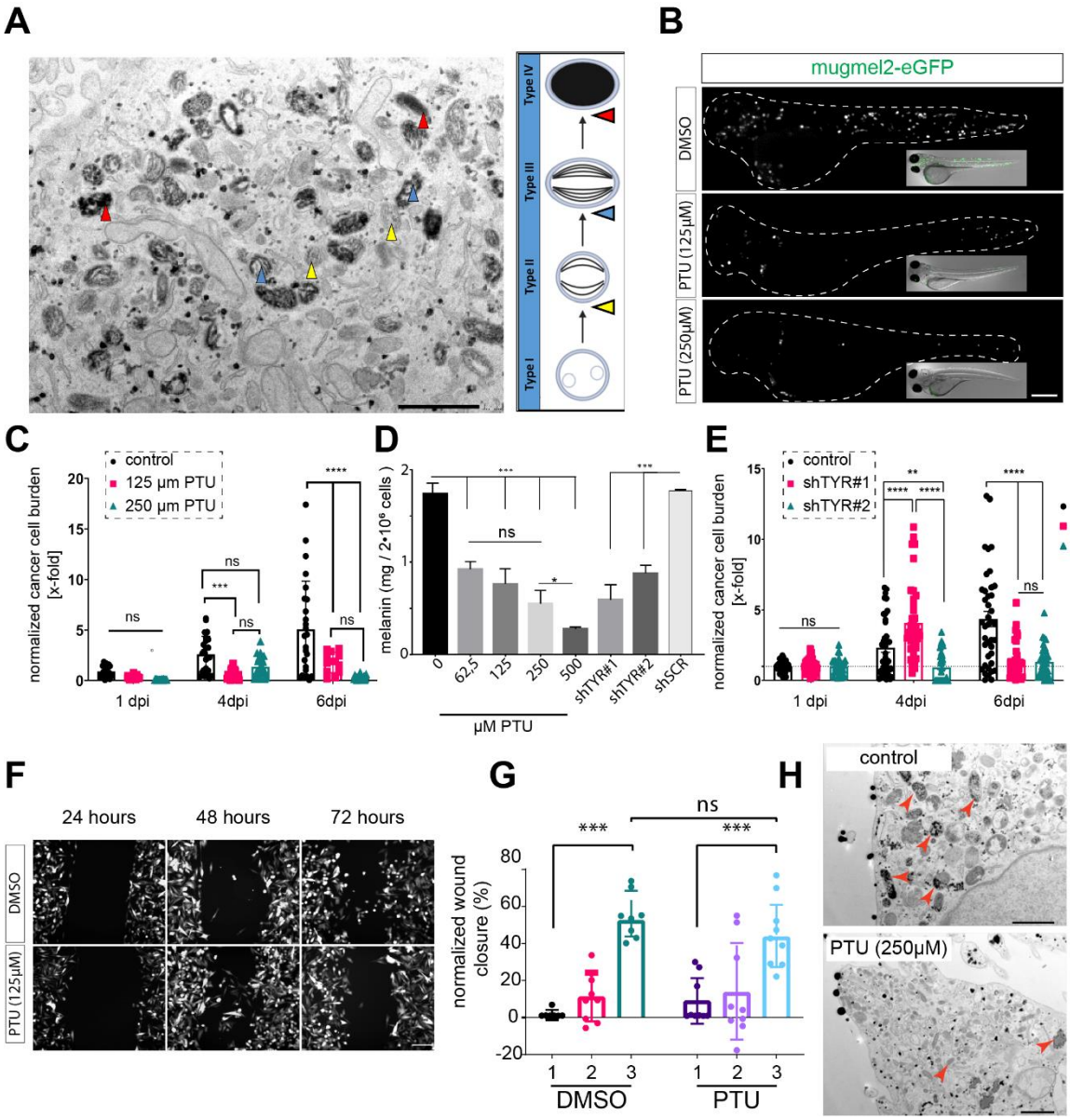

Figure 7 Melanin depletion of melanated melanoma cell lines decreases their tumorigenic potential. A) TEM assessment of melanosome maturation in mugmel2 cells: type II melanosomes are indicated by ▲, type III melanosomes by ▲ and type IV by ▲. Scale bars are 2 µm, and all images are representative images. B) Engraftment of melanotic melanoma cell line mugmel2 in non-pigmented CASPER zebrafish, confocal micrograph; cells were labeled with CMV:eGFP-blasticidin. Mugmel2 cells were treated with 1-phenyl 2-thiourea (PTU) *in vitro* prior to engraftment and its effect on cell intrinsic metastatic potential was compared to DMSO control C) PTU inhibition of mugmel2 melanation and its effect on the metastatic capacity of mugmel2 *in vivo*. Cells were depleted *in vitro* through PTU addition 2 weeks prior to hematogenous engraftment into CASPER zebrafish (n=2 * 20). Measurements were normalized to 1 day post injection (dpi), engraftment was monitored on 1, 4 and 6- dpi. D) Dose-dependent melanin depletion upon *in vitro* application of PTU to mugmel2 cells compared to solvent control and genetic depletion of TYR (lentiviral shRNA mediated knock down) compared to scrambled short hairpin control, as measured by spectrophotometer. E) Quantification of cancer cell engraftment

of zebrafish implanted with mugmel2-eGFP, containing shSCR, shTYR1#1 or shTYR1#2. Measurements were normalized to day 1 of each individual condition. F) Wound healing of mugmel2 cells treated with solvent control (DMSO) compared to PTU-mediated chemical depletion of melanin, shown as representative epifluorescent micrographs and in panel G) as quantification of wound area over time, normalized to wound area at t=0. H) TEM micrographs noting the chemical depletion of melanin and the subsequent reduction of visible melanosomes when compared to solvent control. The mean and the standard error of the mean were plotted (SEM), n=20*2. p<0.05=* p<0.01=** p<0.001=***.

Comparative analysis of pan-melanoma panel reveals a correlation between melanin levels, TYRP1 expression and tumorigenic capacity.

To further test our hypothesis that the presence of intracellular melanin plays a role in metastatic dissemination of different types of melanomas, we analyzed a matched panel of melanated and non-melanated melanoma cell lines (schematic representation in Figure 3A). The metastatic colonization in zebrafish was measured at 1, 4 and 6 dpi, comparing melanated and non-melanated cell lines derived from CoM (CRMM1, CRMM2), CM (SK-Mel28, PDX11917) and UM (XMM66 and OMM2.3). All tested cell lines were transduced with lentiviral tdTomato and data was analyzed after normalization of fluorescent intensity to 1 dpi (as described previously)[33]. For both CoM and CM, we noted a significantly enhanced metastatic colonization for the melanated cell line in the cell line pairs. Metastatic colonization did not seem exclusively linked to melanin content, CRMM1, p<0,001, as a melanated cell line and SK-Mel28, p<0,001 as a not visibly melanated cell line. PDX-derived CM cell line PDX11917 was found to be overtly melanated, both in culture and when pelleted during sub-cultivation, and showed only marginal proliferation in zebrafish, but was able to establish metastatic colonies at 6 dpi[34]. UM lines that were used in this panel were deemed to be non-metastatic and as expected failed to form any metastatic colonies, in a similar manner as reported by Groenewoud et al 2021. Subsequently, we determined if there were detectable melanosomes within the cell lines that made up our panel, to ensure that all our designated non-melanated cell lines indeed did not contain any melanosomes (Figure. 3D). Strikingly, not only CRMM1, PDX11917 but also SK-Mel28 showed active melanosome formation when observed using TEM. As an extension thereof and in line with the findings detailed in Figure 1, we asked if in this cell line panel, we could correlate *TYRP1* mRNA levels with their metastatic capacity (Figure 3E). We noted a significant increase of *TYRP1* expression in CRMM1,

PDX11917 and SK-Mel28 when compared to their non-melanated counter parts or when compared to the non-melanated cells within this panel ($p<0.001$). None of the non-melanated cell lines (CRMM2, XMM66, OMM2.3) showed detectable *TYRP1* mRNA.

Subsequently, we measured the effect of chemical inhibition of melanin biosynthesis on the metastatic colonization of highly-melanated PDX-derived CM cell line PDX11917 when compared to SkMel28, a cell line bearing only occult melanin. Here we demonstrated that PDX11917's metastatic capacity was significantly inhibited after chemical melanin depletion contrary to vehicle control, at 6 dpi ($p<0.01$). SkMel28 was not significantly inhibited by melanin depletion at 6 dpi, but instead displayed a significant delay in metastatic colonization at 4 dpi ($p<0.01$) when compared to DMSO control. SKMel28s tumorigenic capacity was eventually compensated by 6 dpi, and indicated no overall significant inhibition when compared to untreated control.

These observations suggest that the presence of melanin enhances a cell line's tumorigenic capacity and that TYRP1 levels are indicative of melanin biosynthesis, given that upstream activation is present. Strikingly, SkMel28 shows strong expression of TYRP1, but has only minimal melanosome formation and occult melanin, as visualized under TEM, under normal culture conditions. This further implies that the presence of melanin rather than solely the expression of TYRP1 is required for the enhancement of tumorigenic capacity.

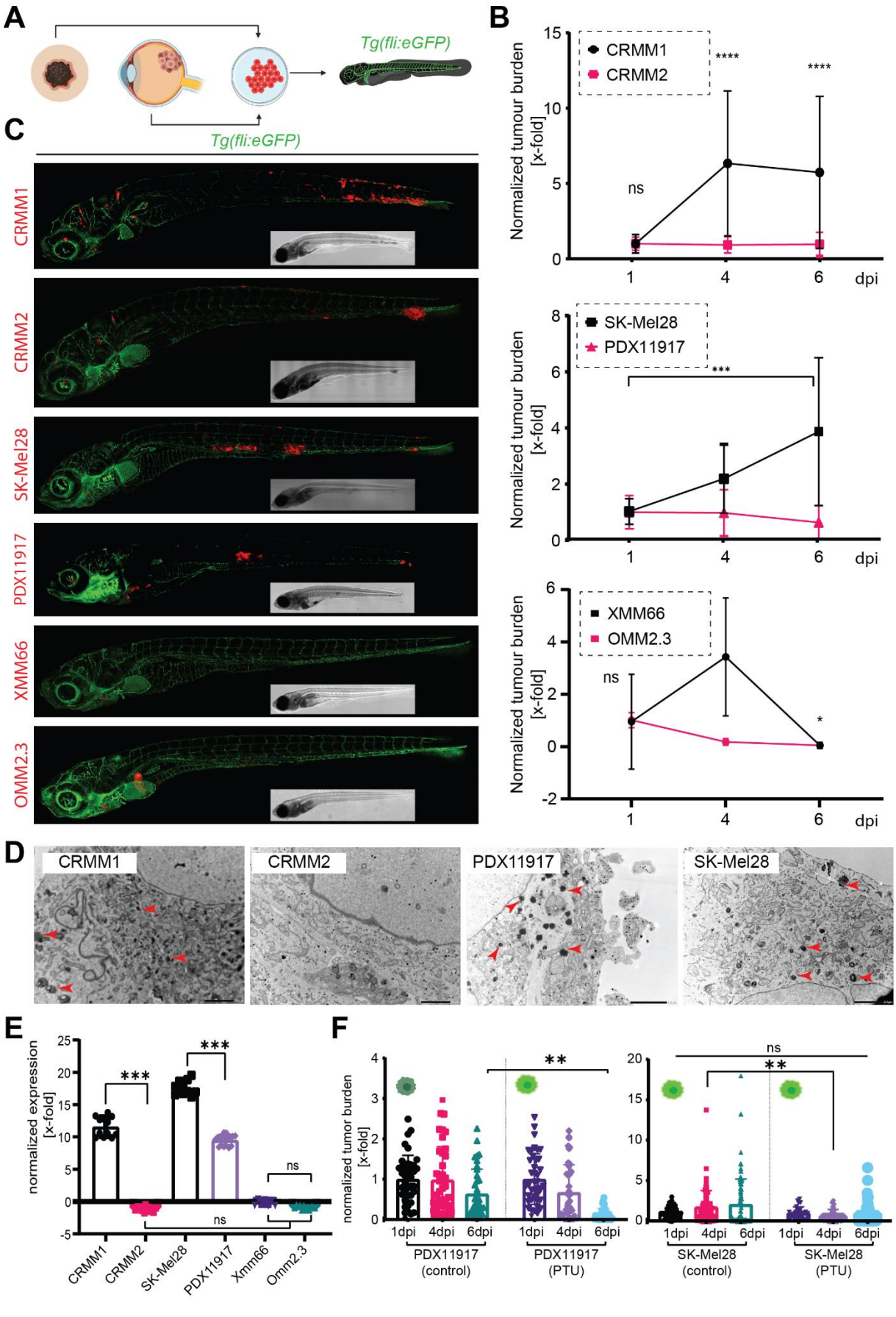
A
Tg(fli:eGFP)
Tg(fli:eGFP)
B
CRMM1
CRMM2
****
****
ns
Normalized tumour burden [x-fold]
dpi
SK-Mel28
PDX11917
***
XMM66
OMM2.3
ns
*
C
CRMM1
CRMM2
SK-Mel28
PDX11917
XMM66
OMM2.3
D
CRMM1
CRMM2
PDX11917
SK-Mel28
E
normalized expression [x-fold]
***
***
ns
ns
CRMM1
CRMM2
SK-Mel28
PDX11917
Xmm66
Omm2.3
F
normalized tumor burden [x-fold]
**
ns
**
1dpi 4dpi 6dpi
PDX11917 (control)
PDX11917 (PTU)
SK-Mel28 (control)
SK-Mel28 (PTU)

Figure 8 Engraftment of a (pan)melanoma panel in tg(fli:eGFP) zebrafish shows efficient engraftment of CM and CoM melanoma, whereas UM is readily cleared from zebrafish. A) Schematic representation of the experimental approach: CoM, CM and UM cell lines were injected in to Tg(fli:GFP) blood vessel reporter zebrafish through the duct of Cuvier at 48 hours post fertilization. Pairs of melanated and non- melanated cell lines were chosen for CoM and CM and two non-melanated cell lines for UM. B) Growth kinetics of the (pan)melanoma cell line panel, after hematogenous engraftment into zebrafish. For each experiment, 40 individuals were imaged, divided over two biological replicates. For all measurement, the integrated fluorescence density was plotted for 1, 4 and 6- dpi (all measurements were normalized to day 1 of the individual cell line). Measurements shown are the mean, error bars represent ± SEM. C) Confocal micrographs of representative phenotypes of the engrafted cell lines at 6 dpi D) Transmission electron micrographs of CoM and CM melanoma cell line pairs; (type IV melanosomes, indicated with ▲). Scale bars are 2 μm, all images are representative images. E) Quantitative PCR measurements of tyrosine related protein 1 (TYRP1), the enzyme responsible for the terminal biosynthetic conversion of tyrosine into melanin. F) Melanin depletion through PTU treatment of melanated and non-melanated cells. CM melanoma PDX-derived cell line PDX11917 and non-melanated melanoma cell line SK-Mel28 were depleted for 14 days prior to engraftment through injection into zebrafish. The mean and the standard error of the mean (SEM) were plotted, n=20*2. $p<0.05$=* $p<0.01$=** $p<0.001$=***.

Introduction of extraneous melanin re-instates UM metastatic potential.

We previously observed that UM cell lines are generally non-metastatic, non-melanated and do not express TYRP1. Many UM patients have a dark brown to black tumor at the time of enucleation, and we noticed that both a high level of pigmentation as well as a high TYRP1 expression correlate with poor survival (Figure 1C, D). Furthermore, the tested melanated primary samples (data for spUm-LB046 shown) were capable of establishing metastatic colonies in zebrafish (Figure1B).

To determine if introduction of extraneous melanin would be able to re-instate the metastatic potential of non-metastatic non-melanated UM cells, we established a co-culture system to allow *in vitro* transfer of melanin from donor melanated cells (mugmel2) to naïve UM cells (XMM66, OMM2.3) (Figure 4A, Supplementary Figure S1). We included a co-culture with vehicle (DMSO) in parallel to a melanin-depleted co-culture. Donor cells were pre-incubated with Mitomycin-C, a mitotic spindle poison, abrogating mitotic potential, while retaining overall cell viability; this allowed us to perform a protracted (72 hours) co-culture with the donor cells while blocking donor cell outgrowth. To determine how much melanin would be taken up, we measured the

intracellular melanin concentration in naïve UM cultures, UM cells co-cultured with melanated mugmel2 (mel+) and chemically melanin-depleted mugmel2 (mel-) cells. We noted a significant melanin enhancement in melanated co-cultures, for both UM cell lines compared to both naïve (2 to 3-fold) and melanin-depleted co-cultures (8 to 10-fold approximately) (Figure 4B). Using TEM, we verified the successful transfer of intracellular melanin from highly-melanated melanoma cell line mugmel2 (mugmel2 mel+) to XMM66 cells (Figure 4C). In naïve XMM66 cells, melanosomes were completely absent, whereas large melanosomal structures were observed in the co-cultures with melanated cells. In contrast, in the melanin-depleted co-culture, only a few small electron dense vesicles and some empty vesicles were observed (Figure 4C), indicating functional transfer of melanin from melanated CM donor cells to naïve non-melanated UM cells. Subsequently, we asked if the transferred intracellular melanin could play a protective role after UM cell injection into the bloodstream of zebrafish. We therefore injected these sets of co-cultured cells Xmm66 and OMM2.3 labeled with red fluorescent, co-cultured with green mugmel2mel+ and mugmel2mel- cells, into zebrafish and scored the metastatic burden at 6 dpi. In melanated co-cultures, both UM cell lines gained a significant enhancement in metastatic colonization in contrast to the melanin-depleted co-cultures (Figure 4D, E). Importantly these results proves that melanin inclusion into UM cells rescues their survival in circulation leading to metastatic dissemination.

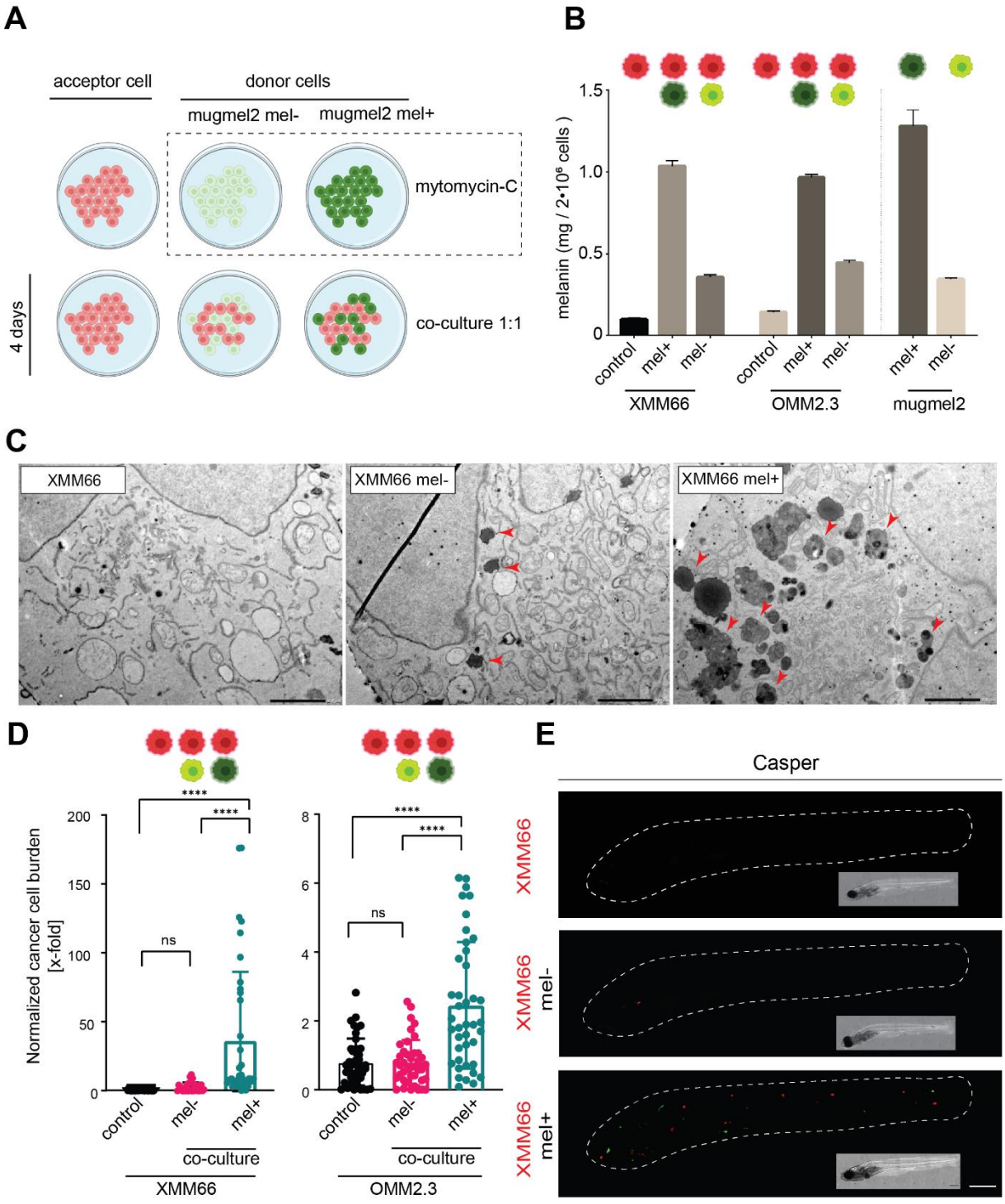

Figure 9 In vitro melanin transfer from donor (mugmel2) cells into recipient UM cells rescues their metastatic potential *in vivo*. A) Schematic representation of melanin transfer co-culture model. Recipient (red, UM cells) and donor cells (green, mugmel2, mugmel2 mel+, pre-treated with DMSO and mugmel2 mel- melanin depleted through pre-treatment with PTU) were cultured separately. Prior to co-culture, donor cells were pre-treated with mitomycin-C (100µg/mL) for 3 hours. Cells were mixed in a 1:1 ratio of acceptor cell combined with mel+ or mel- mugmel cells. After 4 days of co-culture, cells are harvested and either engrafted into zebrafish or used for *in vitro* analyses. B) Spectrophotometric analysis of uptaken melanin in UM cells, calculating mg / 2* 10^6 cells. Two individual experiments, 3

biological repeats. C) Representative transmission electron micrograph indicates the internalized melanosomes in UM cells donated from mugmel2 mel+ cells (type IV melanosomes, indicated with ▲). Scale bar represents 2 µm. D) End point measurement (6 dpi) of zebrafish (n=2 x 20) engrafted with naïve cells (control), UM cells co-cultured with melanin-depleted donor cells (mel-) and co-cultured with melanated donor cells (mel+). E) Representative fluorescent micrographs of co-cultured UM cell line XMM66, show the naïve XMM66 cells (red), XMM66 cells co-cultured with green melanin-depleted (mel-) and melanin-proficient (mel+) mugmel2 donor cells. Some mugmel2 cells (green) remain in circulation, do not form metastatic colonies but increase survival of UM cells as indicated in D.

Melanin protects against ferroptosis *in vivo*.

Successful metastatic colonization is a rare occurrence in most cancers and can be described by a stochastic process where random chance aligns with the metastatic cells intrinsic properties to allow a minute subset of cancer cells to form a metastatic colony in a suitable niche. Recent discoveries have highlighted the importance of reactive oxygen species (ROS) and more specifically ferroptosis in the curbing of metastatic dissemination in CM[7,35]. Since melanin has long been known to act as a ROS scavenger[18,19], we hypothesized that melanin might scavenge ROS while cells are in the circulation, thus prolonging circulating tumour cell (CTC) survival and thereby enhancing their chance of finding a suitable niche. The presence of melanin would thereby enhance a tumor's metastatic capacity. To address this hypothesis, we first tested the effect of melanin depletion on ROS induction *in vitro,* measured by CellRox fluorescent assay. CellRox utilizes a dye that becomes highly fluorescent after ROS-mediated oxidation. We measured a significant enhancement in the level of induced ROS in melanin-depleted mugmel2 cells visualized by CellRox: melanin depletion by pre-treatment with PTU led to increased ROS production following a challenge with ROS inducers Menadione, Paraquat and H_2O_2 (Figure 5A, B)., Moreover, the imaging clearly shows that at the time of analysis most of the melanin-depleted cells have been killed by the ROS inducers while the melanated control (DMSO pre-treated) cells were still adherent to the culture plate. These results suggest that melanin-depleted cells are more sensitive to ROS induction.

Due to the recent publications linking ferroptosis to the curbing of metastatic dissemination[7], we reasoned that ferroptosis might be the leading cause of ROS-mediated cell death. These findings are supported by our previous observation, where melanin retained in cells protects them during metastatic dissemination. To assess the

specific growth inhibitory effect of known ferroptosis-inducers erastin and RSL3, we performed a WST1-based proliferation assay on both melanin proficient and deficient mugmel2 cells (Figure 5C). Strikingly, we noted that mugmel2 (derived from an NRAS-driven cutaneous melanoma) was, in normal culture conditions, refractory to the entire concentration range of either erastin or RSL3 (2-fold dilution series, 10 to 0,039 µM, data not shown). To more accurately mimic the biological situation *in vivo,* we subsequently repeated the experiment with lowered glutamine and fetal bovine serum concentrations. We found that in these *in vitro* conditions, only melanin-depleted mugmel2 was significantly sensitized to both erastin (approximate growth inhibition 70-80%, 10-0.625 µM, $p<0.001$) and RSL3 (approximate growth inhibition 60-80%, 10-1,25 µM, $p<0.001$ and 0.625 at $p<0.05$). In contrast, the melanin-proficient mugmel2 remained refractory to erastin and were only susceptible to the highest concentrations of RSL3 (10 and 5 µM, $p<0.001$). Finally, we determined if the growth inhibitory effect of ferroptosis would translate to an *in vivo* situation. To this end, we injected intravenously zebrafish larvae with our previously described set of melanoma cells (UM, CM and CoM), at 48 hpf and treated the engrafted larvae from 1 dpi with 5 µM erastin and 10 µM RSL (Figure 5D). We subsequently measured the tumor burden at 6 dpi and normalized the tumor burden to the vehicle control (DMSO). We noted that CoM cell lines CRMM1 and CRMM2 and CM cell line SK-Mel28 showed a significant ($p<0.001$) reduction of tumor burden when treated with erastin. Mugmel2 was insensitive to this treatment. RSL3 did not reduce tumor burden in any of the tested cell lines, although it did induce a clear, yet non-significant reduction in tumor burden using cell lines CRMM1 and SK-Mel28. Subsequently, we assessed the efficacy of ferroptosis induction in mugmel2 after melanin depletion, *in vivo*, through both genetic and chemical means, reasoning that through melanin depletion we could sensitize this refractory cell line to ferroptosis-mediated cell death. We engrafted zebrafish larvae as previously described (Figure 5D) with mugmel2 depleted from melanin through chemical and genetic means and treated the engrafted larvae from 1 dpi with 5 µM erastin and 10 µM RSL (Figure 5E). We determined the tumor burden, normalized to vehicle control (DMSO) at 6 dpi. There is no significant sensitization to erastin, most likely due to its strong inhibitor capacity on the melanated sample as well. Strikingly RSL3, acting through GPX4, strongly reduced the tumor burden in chemically as well as genetically-melanin depleted populations, indicative of resistance to canonical ferroptosis mediated by melanin.

In conclusion, these data suggest that melanin protects melanoma cells in circulation, functionally mitigating intracellular ROS and protecting circulating cancer cells from ferroptotic cell death, indirectly enhancing tumorigenic capacity.

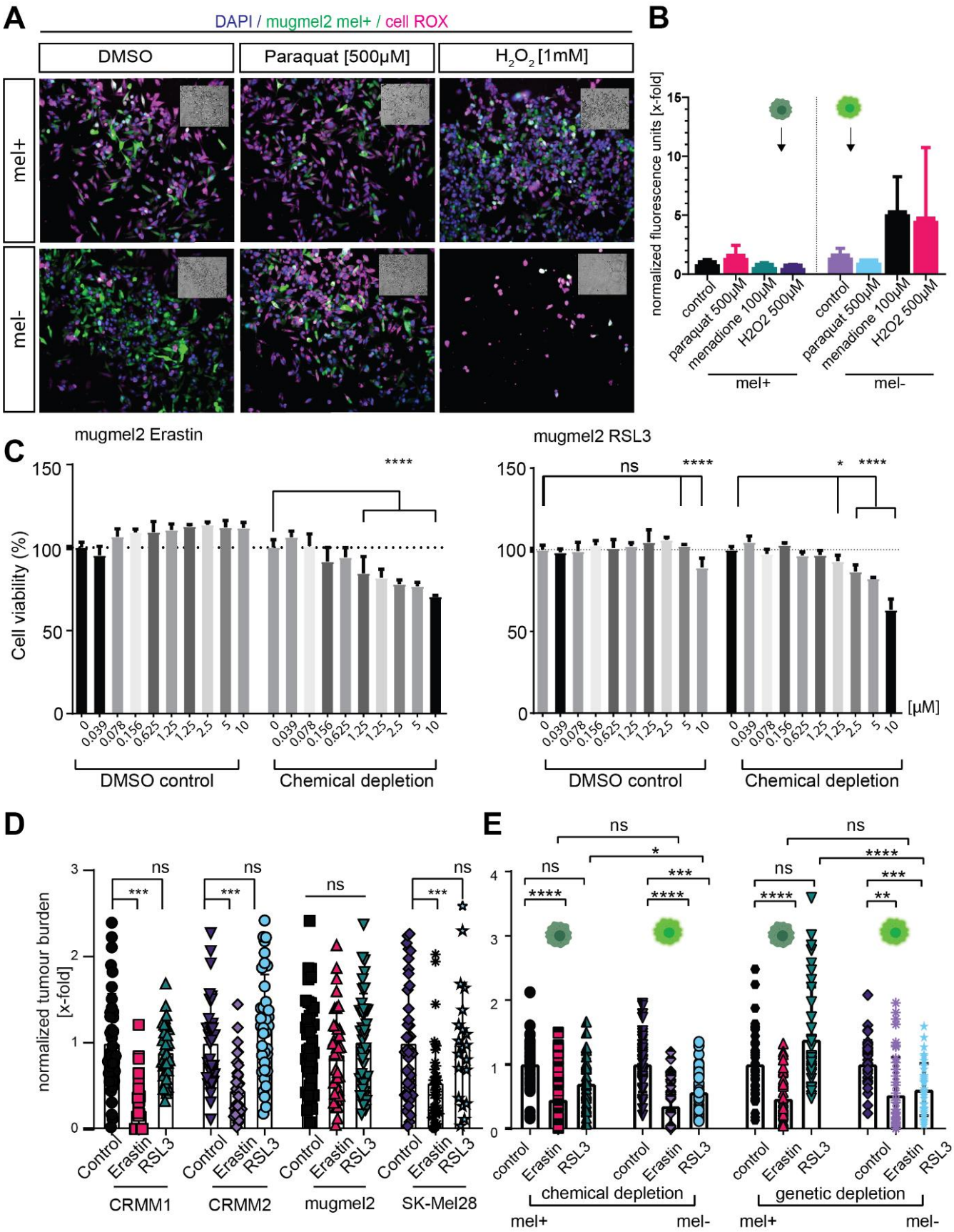
A
DAPI / mugmel2 mel+ / cell ROX
DMSO
Paraquat [500µM]
H2O2 [1mM]
mel+
mel-
B
normalized fluorescence units [x-fold]
control
paraquat 500µM
menadione 100µM
H2O2 500µM
mel+
mel-
C
mugmel2 Erastin
mugmel2 RSL3
Cell viability (%)
[µM]
DMSO control
Chemical depletion
D
normalized tumour burden [x-fold]
Control
Erastin
RSL3
CRMM1
CRMM2
mugmel2
SK-Mel28
E
chemical depletion
genetic depletion
mel+
mel-

Figure 10 ROS and ferroptosis is quenched by intracellular melanin, erastin induces ferroptosis at sufficient levels to overcome cellular ROS defenses. A) CellRox fluorescent ROS measurement of mugmel2 cells with (mel-) and without melanin (mel+) depletion through PTU pre-treatment, as described previously (i.e. in Figure 2D). All wells were seeded with $5{,}0*10^4$ cells per well and treated with ROS inducers for 60 min and imaged after fixation. Paraquat, menadione and H_2O_2 were used to induce non-specific intracellular ROS. Nuclei are stained with 4,6-diamidino-2-phenylindole (DAPI), cells are stained with cytoplasmic GFP (shown as green), CellRox deep red (shown as magenta). B) Quantification of CellRox signal, through epifluorescent imaging and subsequent processing. All measurements were normalized for the number of remaining cells using the number of nuclei ($DAPI^+$) and only CellRox signal within the GFP-positive cells were measured; measurements were repeated twice with 3 biological repeats. C) Represents *in vitro* proliferation (WST1) assay to assess the growth inhibitory effects of ferroptosis inducers erastin and RSL3 on mel+ and mel- mugmel2 cells. D) Ferroptosis induction in ZF xenograft models *in vivo* obtained by engraftment of a melanoma panel with CoM (CRMM1 and CRMM2) and CM cell lines (SK-Mel28 and mugmel2). Ferroptosis inducers erastin and RSL3 were added to the previously determined maximum tolerated dose (MTD) (results not shown, manuscript in writing, erastin 5 µM and RSL3, 10 µM) to the eggwater of engrafted larvae at 3 dpi. The water containing the compounds was exchanged every other day. At 6 dpi, the cancer cell burden was measured and subsequently normalized to the vehicle control group (of each individual condition). E) *In vivo* ferroptosis induction as described in D in larvae engrafted with naïve mel+ and depleted (mel-) mugmel2 cells after chemical (PTU) and genetical (shTYR#2) melanin depletion prior-engraftment. Melanin depletion by chemical and genetics means sensitized melanoma cell lines to RSL3 whereas erastin mainly seems to circumvent or overpower ferroptosis resistance mediated by melanin.

Translational value and future implementation of pro-ferroptotic strategies for the treatment of melanomas.

These findings led us to search for both elevations in GPX4 levels or alterations in melanin biosynthesis in CM and UM patient survival data (Figure 6). We compared TCGA datasets, analyzing the effect of melanin biosynthetic genes on overall survival (Figure 6A). We subsequently focused on the effect of melanin biosynthetic genes on overall survival of CM patients in a group of 458 patients and were able to demonstrate a strong effect of melanin biosynthetic molecules. All melanin biosynthetic pathway genes assessed in this manner correlated negatively with patient overall survival (Figure 6 B, *MITF*, p=0.022; *TYR*, p=0.03; *DCT*, p=0.038; *TYRP1* p=0.0019).

For UM, using the Leiden data set, a high expression level of GPX4 strongly correlated with a reduction in overall survival, whereas melanin biosynthetic activity as assessed by mRNA levels of TYRP1 revealed an even stronger negative relation with survival of primary UM patients (Figure 1D). Mitochondrial voltage-gated anion channel

(VDAC) is another target for the induction of ferroptosis, and one of the erastin targets. We assessed the relation between VDAC levels and survival of CM and UM patients and showed that high VDAC1 expression was significantly correlated with a reduced overall survival time for both melanomas (Figure 6C). No transcriptomics data was available to us for CoM melanoma at the time of writing. Taking together the experimental data linking melanin to ferroptosis resistance, ferroptosis susceptibility and the transcriptional data presented in this manuscript, we generated a model (Figure 6D). We propose that in the cancer cell, melanin forms a physical depot with ROS-absorptive properties. This functions to protect cancer cells in the circulation from ROS and more specifically, ferroptosis. Cells are thus protected from slow increases in ferroptotic stimuli, as indicated through the intrinsic resistance of strongly-melanated cells to GPX4 inhibition (RSL3) mediated-ferroptotic cell death. Sharp increases in ferroptotic ROS through inhibition of VDAC function through treatment with erastin overwhelm the anti-ferroptotic function of melanin.

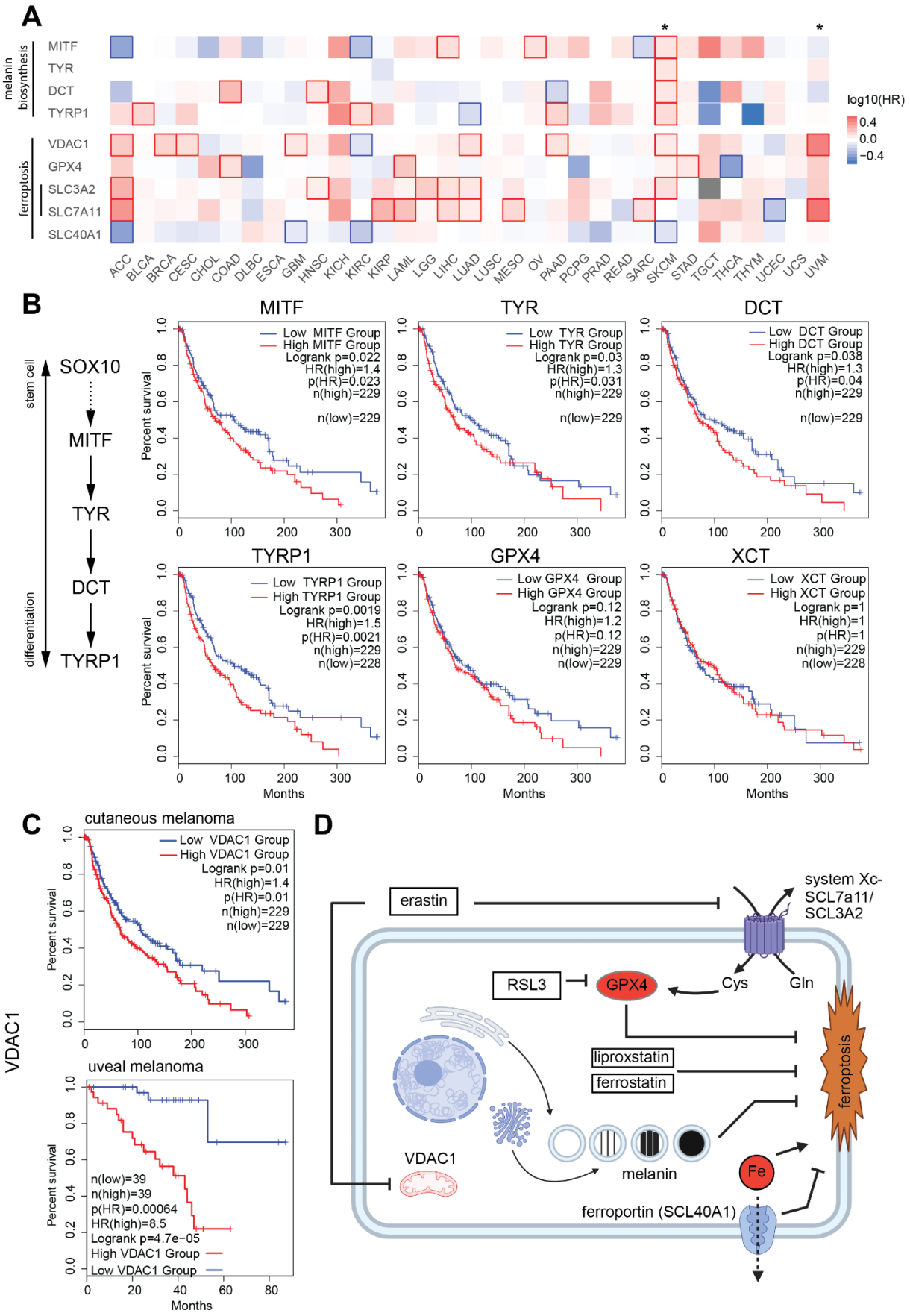
A
melanin biosynthesis
MITF
TYR
DCT
TYRP1
ferroptosis
VDAC1
GPX4
SLC3A2
SLC7A11
SLC40A1
log10(HR)
0.4
0.0
−0.4
ACC BLCA BRCA CESC CHOL COAD DLBC ESCA GBM HNSC KICH KIRC KIRP LAML LGG LIHC LUAD LUSC MESO OV PAAD PCPG PRAD READ SARC SKCM STAD TGCT THCA THYM UCEC UCS UVM
B
stem cell
SOX10
MITF
TYR
DCT
TYRP1
differentiation
MITF
Low MITF Group
High MITF Group
Logrank p=0.022
HR(high)=1.4
p(HR)=0.023
n(high)=229
n(low)=229
TYR
Low TYR Group
High TYR Group
Logrank p=0.03
HR(high)=1.3
p(HR)=0.031
n(high)=229
n(low)=229
DCT
Low DCT Group
High DCT Group
Logrank p=0.038
HR(high)=1.3
p(HR)=0.04
n(high)=229
n(low)=229
TYRP1
Low TYRP1 Group
High TYRP1 Group
Logrank p=0.0019
HR(high)=1.5
p(HR)=0.0021
n(high)=229
n(low)=228
GPX4
Low GPX4 Group
High GPX4 Group
Logrank p=0.12
HR(high)=1.2
p(HR)=0.12
n(high)=229
n(low)=229
XCT
Low XCT Group
High XCT Group
Logrank p=1
HR(high)=1
p(HR)=1
n(high)=229
n(low)=228
Percent survival
Months
C
VDAC1
cutaneous melanoma
Low VDAC1 Group
High VDAC1 Group
Logrank p=0.01
HR(high)=1.4
p(HR)=0.01
n(high)=229
n(low)=229
uveal melanoma
n(low)=39
n(high)=39
p(HR)=0.00064
HR(high)=8.5
Logrank p=4.7e−05
High VDAC1 Group
Low VDAC1 Group
Percent survival
Months
D
erastin
system Xc-
SCL7a11/
SCL3A2
RSL3
GPX4
Cys
Gln
liproxstatin
ferrostatin
ferroptosis
VDAC1
melanin
Fe
ferroportin (SCL40A1)

Figure 6 **Analysis of transcriptional activity of melanin biosynthesis in CM melanoma patient material (TCGA, accessed through GEPIA).** A) Survival map of all available TCGA cancer data sets, comparing the effect of melanin biosynthesis genes on melanoma-related survival (CM melanoma (SKCM) and UM (UVM) are noted with an asterisk, additional abbreviations can be found in supplementary figure S3), significant effect on survival is denoted with a red bounding box. In CM melanoma (n= 458), a significant negative correlation with disease free survival for all known melanin biosynthetic genes can be noted (MITF, TYR, DCT, TYRP1) whereas in UM (n=78), only TYR and TYRP1 show no significant correlation to overall survival. Similar comparative analysis of the TCGA, plotting the correlation of disease-free survival for the known anti-ferroptotic mechanisms, system Xc- (SCL7A11 and SCL3A2), ferroportin (SCL40A1), GPX4 and mitochondrial VDAC1 show that there is a significant effect of SCL3A2 on survival in CM (p=0.00022, data not shown) and SCL7A11 in UM (p=0.00014, data not shown). Moreover, both CM and UM display a significant reduction in overall survival for patients with a high expression of VDAC1. B) comparative analysis of the effect of melanin biosynthetic gene expression on disease free survival in CM melanoma patients (TCGA data). All known major melanin biosynthetic genes negatively correlate with overall survival (MITF, p=0.022; TYR, p=0.03; DCT, p=0.038; TYRP1 p=0.0019). Analysis of ferroptosis detoxifying enzymes GPX4 and XCT (synonymous with SCL7A11) shows that only GPX4 correlates negatively with overall survival. Expression of SOX10 did not yield any correlation with disease free survival (p=0.19, data not shown). TCGA SKCM cohort size = 458, all values are split along the median for each gene. C) erastin (one of the main and most potent inducers of ferroptosis) is thought to act through the perturbation of VDAC function, releasing reactive oxygen into the cytoplasm from mitochondria. Analysis of the effect of VDAC1 on CM and UM disease free survival, indicate that VDAC1 expression significantly influences survival (CM, p=0.01; UM, p=0.00064). D) model of the proposed mechanisms of melanin-mediated ROS resistance in melanoma cells.

Discussion

Melanomas are often strongly pigmented in patients. The prevalence of melanoma pigmentation underlines not only the cellular lineage they derive from, but also the presence of selection pressure forcing the expression of melanin-related genes. Cells derived from pigmented melanomas generally lose their melanin biosynthetic capacity and increase their migratory capacity *in vitro*[22]. Next to clinical correlations that associate either melanin or melanin-related gene signatures with a bad disease outcome, the true functional role of melanin in melanoma development remains unclear and contradictory[21,36].

We engrafted spheroids derived from primary UMs tissues in zebrafish and observed that there was a relation between the presence of melanin in the primary UM samples (clinically scored for melanotic level in a +, +/- and – scale) and prolonged circulation and tumorigenic potential in zebrafish after engraftment. This experiment indicated that there is a significant difference in tumorigenic potential of heavily-melanated patient samples when compared to both intermediate and lightly-melanated samples. Interestingly, UM cell lines OMM2.3 and XMM66, originally derived from metastatic UM, had lost all melanogenic capacity *in vitro*, and were readily cleared from the engrafted host after systemic injection (within 16 hours post injection). This observation and the short timeframe, wherein near complete attrition of CTCs is attained, is in line with a possible induction of ROS-mediated cell death[8]. Strikingly, we observed strong tumorigenic capacity when engrafting low passage spXMM66 cells, derived from a pigmented patient-derived xenograft tissue (PDX), while an immortalized cell line from the same patient XMM66 proved to be non-tumorigenic. In addition, our analysis of a clinical UM cohort confirmed a strong association between high tumor pigmentation, high expression of *TYRP1*, the terminal melanin biosynthetic, and high UM-related death in patients (LUMC cohort n=64).

Following this observation, we reasoned that this phenomenon might hold true for other melanoma sub-types. We concordantly observed that there has been a nearly complete loss of melanin biosynthesis in most melanoma cell lines, presumably through negative selection (or general lack of selection pressure) by successive *in vitro* cultures without selection pressure.

To assess this, we acquired the aberrant CM cell line mugmel2, an NRAS-driven and heavily-melanated melanoma cell line[31]. We assessed the formation of melanosomes using TEM and measured melanin levels using a spectrophotometric method described by Friedmann et al[18]. Both chemical and genetic inhibition of melanin biosynthesis, by treatment with 1-Phenyl-2-thiourea (PTU) or *TYR1* shRNA interference, reduced melanin levels and decreased metastatic dissemination in zebrafish xenografts.

We assembled a set of UM, CM and CoM melanoma cell lines and were able to generate a set of paired melanated and non-melanated CM and CoM cell lines. We repeated the chemical depletion of melanin in the CoM melanoma set and found that also within this set there is a significant reduction of tumorigenic potential upon depletion of melanin, suggesting that melanin has a canonical pro-tumorigenic function in all melanomas. Strikingly, our findings validate the work from Pinner et al 2009, where they state that low melanation correlates with high migratory capacity of CM cells *in vivo*, but that melanated cells do generate more distant metastases[22].

To assess the mechanistic effect of melanin levels on the metastatic behavior of UM cell lines we developed a co-culture system to transfer melanin from mugmel2 donor cells into UM acceptor cells. Through this system, we introduced exogenous melanin to UM cells, for subsequent assessment of metastatic capacity. Other methods to re-instate melanin biosynthesis were unsuccessful (treatment with a-MSH, forskolin or lentiviral over-expression of melanin biosynthetic genes *DCT*, *TYR* and *TYRP1*, results not shown). Spectrophotometric measurement of the uptake of melanin and visualization of melanosomes through TEM confirmed that UM cells readily take up melanin from external donors. Co-cultures of both melanin biosynthesis proficient and deficient donor cells were generated and we measured a significant enhancement of detected melanin in co-culture with melanin proficient donors when compared to melanin deficient donors or untreated control cells. Both OMM2.3 and XMM66 co-cultured with melanin-proficient cells showed a significant enhancement in tumorigenic potential when compared to either co-culture with melanin deficient or untreated cells. These findings indicate that UM cells are capable of up taking melanosomal melanin, at least *in vitro,* and underscore one of the possible functions of melanin in the distant metastasis of UM.

Taking together our observations with recently published experimental proof that circulating melanoma cells are largely killed through reactive oxygen[7,35], we hypothesized that ROS-based cell death might be the underlying mechanism driving UM attrition in circulation[7]. In line with this hypothesis, melanin inclusion within UM cells might thus help prevent *in vivo* cell death of circulating UM cells. More recently there has been experimental proof that circulating tumor cells are killed specifically by an iron-dependent non-apoptotic cell death mechanism known as ferroptosis[35].

Using our model, we tested if melanoma cells were responsive to the induction of ferroptosis during their time in circulation in the zebrafish model. We started out by challenging duplicate sets of melanated and non-melanated melanoma cells we used previously and demonstrated a clear correlation between the levels of melanation and the response to the induction of ferroptosis with inhibitors of GPX4 ((1S,3R)-RSL3; alternatively named RSL3) and system Xc- (erastin)[23,25,27,37]. Ferroptosis induction by erastin occurs through perturbation of system Xc- and mitochondrial voltage-dependent anion channels[26,37]. The *in vivo* induction of ferroptosis with erastin proved to be highly effective, reducing tumor burden independent of melanin inclusion for cell line SK-Mel28, which showed low level melanation under TEM. Additionally, erastin proved sufficiently potent to induce ferroptosis in strongly-melanated mugmel2 cells. Although there was a trend indicative of sensitization of SK-Mel28 cells to erastin by melanin depletion, this was presumably negated by the strong effects of erastin on the mel+ population.

Furthermore, we showed that there was a melanin-dependent sensitivity to ferroptosis induction, when melanin-depleted mugmel2 cells were compared with melanated mugmel2 cells. Ferroptosis was induced either directly through the inhibition of GPX4 or indirectly by blocking the glutamate antiporter function of the system Xc- (erastin) and concordant perturbation of VDAC function. We found that mugmel2, derived from an NRAS-driven CM, is largely refractory to ferroptosis induction *in vitro* under conventional conditions, whereas these cells can be sensitized through depletion of glutamine (a co-factor for GPX4 function). The ferroptosis refractory nature of this RAS-driven cell line is contra-dogmatic, as both RSL3 (RAS specific lethal 3) and erastin have been selected through a RAS hyperactivation specific *in vitro* synthetic lethal screen[37]. Therefore, we reason that chemical depletion of melanin sensitizes mugmel2 cells to ferroptosis. This highlights the functional relationship between the

presence of melanin and ferroptosis resistance, *in vitro*. Only ferroptosis induction through GPX4 inhibition induced a significant difference between melanated and non-melanated mugmel2 cells, indicating that non-melanated cells are more susceptible to canonical ferroptosis induction through inhibition of GPX4.

These findings led us to search for both elevations in GPX4 levels or alterations in melanin-biosynthesis genes (*MITF, TYR, DCT, TYRP1*) in patient survival data, where we found that a high expression of GPX4 in CM significantly correlated with decreased overall survival. A high tumor expression of all melanin biosynthetic genes was correlated with increased death in CM patients. Strikingly, there were only insignificant reductions when correlating ferroptosis mediators *GPX4* and *SCL7A11* to overall survival of CM patients, on a whole tumor level. This however does not exclude the presence of inter-tumoral differences.

For UM we found that a higher GPX4 expression strongly correlated with shorter survival, whereas melanin biosynthetic activity when assessed as a measure of mRNA levels of TYRP1 showed an even stronger negative relation with survival of primary UM patients. No transcriptomics data was available to us for CoM melanoma at the time of writing.

VDAC1, one of the putative targets of erastin, showed a significant negative correlation relation with patient survival for both CM and UM. This finding is in line with the strong inhibitory effect of erastin and explains erastin's strong inhibitory capacity on circulating cancer cells irrespective of intracellular melanin levels. Our findings are in line with Nawarak et al 2008, who show that arbutin, a known skin whitening agent and inhibitor of TYR, works by enhancing VDAC1 protein levels in A375 melanoma cells[38].

Taken together, our findings establish a functional link between intracellular melanin levels in melanoma cells irrespective of their tissue of origin. Cells containing melanin survive longer in the circulation of zebrafish during experimental micro-metastasis formation and hence display an enhanced capacity to establish micro-metastatic colonies. In line with the elegant experiments performed by Pinner et al in 2017[22], melanin content lowers (albeit in our hands not significantly so) the migration capacity of melanated cells (endogenously or exogenously melanated). Here our findings prove

that metastatic dissemination and metastatic initiation is effectively enhanced by the presence of intracellular melanin.

The biological function of melanin as a ROS quencher is widely accepted[13,14,19]. Furthermore, there are several studies that correlate melanin concentrations, either through direct measurements of melanin levels or through the detection of blood borne mRNA in CM patients, with a worse prognosis[21,36]. Paradoxically, there are experimental studies showing a converse role of melanin, inhibiting small scale metastasis in animal models[21,22]. Taken together, we reason that our findings bridge the gap between the observed phenomenon in patients and the discrepancy in experimental animal models by showing that melanated melanoma cells have a survival advantage *in vivo* in the blood circulation and are more resistant to ferroptosis. Furthermore, we show, using available patient survival data (TCGA and LUMC cohort for UM), that CM, UM patients have a worse prognosis when melanin biosynthesis is upregulated, notably the expression of terminal melanin biosynthetic enzyme TYRP1. VDAC1 was identified as another gene associated with a negative disease outcome and is a potential target for future therapy.

Acknowledgements:

We kindly thank Emilie Vinolo for the managerial assistance provided during this UMcure2020 project.

This work has received funding from the European Union's Horizon 2020 research and innovation program under grant agreement No 667787 (UM Cure 2020 project, www.umcure2020.org).

We kindly thank Prof. R. Hoeben and M. Rabelink (Department of Cell Biology, LUMC) for providing shRNA (lentiviral) vectors (TRC library, Sigma-Aldrich)

All graphics (excluding scientific data) were generated using Biorender.com

The results shown here are in whole or part based upon data generated by the TCGA Research Network: https://www.cancer.gov/tcga accessed through gepia(2)

AG Conceived, performed, analyzed all experiments and interpreted all the data (unless otherwise stated), wrote the manuscript.

MCG performed the UM patient pigment data analysis, and provided feedback on the manuscript.

JY performed *in vitro* proliferation assays, read the manuscript.

GEML performed all the TEM sample prep and data acquisition, read the manuscript.

MJJ supplied materials and reviewed the manuscript.

BES-J provided funding, supervised the project and reviewed the manuscript.

References

1. Mehlen, P. & Puisieux, A. Metastasis: A question of life or death. *Nature Reviews Cancer* vol. 6 449–458 (2006).

2. Bayraktar, S. & Glück, S. Molecularly targeted therapies for metastatic triple-negative breast cancer. *Breast Cancer Res. Treat.* **138**, 21–35 (2013).

3. Balch, C. M. *et al.* Final version of 2009 AJCC melanoma staging and classification. *J. Clin. Oncol.* **27**, 6199–6206 (2009).

4. Chiang, A. C. & Massagué, J. Molecular Basis of Metastasis. *N. Engl. J. Med.* **359**, 2814–2823 (2008).

5. Weiss, L. Metastatic Inefficiency. *Adv. Cancer Res.* **54**, 159–211 (1990).

6. Luzzi, K. J. *et al.* Multistep Nature of Metastatic Inefficiency : Dormancy of Solitary Cells after Successful Extravasation and Limited Survival of Early Micrometastases. *Am. J. Pathol.* **153**, 865 (1998).

7. Piskounova, E. *et al.* Oxidative stress inhibits distant metastasis by human melanoma cells. *Nature* **527**, 186–191 (2015).

8. Chandra, J., Samali, A. & Orrenius, S. Triggering and modulation of apoptosis by oxidative stress. *Free Radic. Biol. Med.* **29**, 323–333 (2000).

9. NC, J. & D, G. Role of melanin in melanocyte dysregulation of reactive oxygen species. *Biomed Res. Int.* **2013**, (2013).

10. Yang, H. *et al.* The role of cellular reactive oxygen species in cancer chemotherapy. *J. Exp. Clin. Cancer Res. 2018 371* **37**, 1–10 (2018).

11. Kumari, S., Badana, A. K., G, M. M., G, S. & Malla, R. Reactive Oxygen Species: A Key Constituent in Cancer Survival. *Biomark. Insights* **13**, (2018).

12. Liou, G.-Y. & Storz, P. Reactive oxygen species in cancer. *Free Radic. Res.* **44**, 479–496 (2010).

13. Brenner, M. & Hearing, V. J. The Protective Role of Melanin Against UV Damage in Human Skin. *Photochem. Photobiol.* **84**, 539 (2008).

14. GJ, F. *et al.* Mechanisms of photoaging and chronological skin aging. *Arch. Dermatol.* **138**, 1462–1470 (2002).

15. Noonan, F. P. *et al.* Melanoma induction by ultraviolet A but not ultraviolet B radiation requires melanin pigment. *Nat. Commun. 2012 31* **3**, 1–10 (2012).

16. Cichorek, M., Wachulska, M., Stasiewicz, A. & Tymińska, A. Skin melanocytes: biology and development. *Adv. Dermatology Allergol. Dermatologii I Alergol.* **30**, 30 (2013).

17. Li, M., Knapp, S. K. & Iden, S. Mechanisms of melanocyte polarity and differentiation: What can we learn from other neuroectoderm-derived lineages? *Curr. Opin. Cell Biol.* **67**, 99–108 (2020).

18. Friedmann, P. S. & Gilchrest, B. A. Ultraviolet radiation directly induces pigment production by cultured human melanocytes. *J. Cell. Physiol.* **133**, 88–94 (1987).

19. Denat, L., Kadekaro, A. L., Marrot, L., Leachman, S. A. & Abdel-Malek, Z. A. Melanocytes as instigators and victims of oxidative stress. *Journal of Investigative Dermatology* vol. 134 1512–1518 (2014).

20. Whittaker, J. R. An analysis of melanogenesis in differentiating pigment cells of ascidian embryos. *Dev. Biol.* **14**, 1–39 (1966).

21. Sarna, M., Krzykawska-Serda, M., Jakubowska, M., Zadlo, A. & Urbanska, K. Melanin presence inhibits melanoma cell spread in mice in a unique mechanical fashion. *Sci. Rep.* **9**, 1–9 (2019).

22. Pinner, S. *et al.* Intravital imaging reveals transient changes in pigment production and Brn2 expression during metastatic melanoma dissemination. *Cancer Res.* **69**, 7969–7977 (2009).

23. Yang, W. S. *et al.* Regulation of ferroptotic cancer cell death by GPX4. *Cell* **156**, 317–331 (2014).

24. Imai, H., Matsuoka, M., Kumagai, T., Sakamoto, T. & Koumura, T. Lipid peroxidation-dependent cell death regulated by GPx4 and ferroptosis. in *Current Topics in Microbiology and Immunology* vol. 403 143–170 (Springer Verlag, 2017).

25. Yang, W. S. *et al.* Peroxidation of polyunsaturated fatty acids by lipoxygenases drives ferroptosis. *Proc. Natl. Acad. Sci. U. S. A.* **113**, E4966–E4975 (2016).

26. Yagoda, N. *et al.* RAS-RAF-MEK-dependent oxidative cell death involving voltage-dependent anion channels. *Nature* **447**, 864–868 (2007).

27. Dolma, S., Lessnick, S. L., Hahn, W. C. & Stockwell, B. R. Identification of genotype-selective antitumor agents using synthetic lethal chemical screening in engineered human tumor cells. *Cancer Cell* **3**, 285–296 (2003).

28. Riegman, M. *et al.* Ferroptosis occurs through an osmotic mechanism and propagates independently of cell rupture. *Nat. Cell Biol. 2020 229* **22**, 1042–1048 (2020).

29. Yan, B. *et al.* Membrane Damage during Ferroptosis Is Caused by Oxidation of Phospholipids Catalyzed by the Oxidoreductases POR and CYB5R1. *Mol. Cell* **81**, 355-369.e10 (2021).

30. Xie, Y. *et al.* Ferroptosis: Process and function. *Cell Death and Differentiation* vol. 23 369–379 (2016).

31. Rinner, B. *et al.* MUG-Mel2, a novel highly pigmented and well characterized NRAS mutated human melanoma cell line. *Sci. Rep.* **7**, (2017).

32. Hosoi, J., Abe, E., Suda, T. & Kuroki2, T. Regulation of Melanin Synthesis of B16 Mouse Melanoma Cells by 1a,25- Dihydroxyvitamin D3 and Retinoic Acid1. *CANCER Res.* **45**, 1474–1478 (1985).

33. Heitzer, E. *et al.* Human melanoma brain metastases cell line MUG-Mel1, isolated clones and their detailed characterization. *Sci. Rep.* **9**, 4096 (2019).

34. Kemper, K. *et al.* BRAFV600E Kinase Domain Duplication Identified in Therapy-Refractory Melanoma Patient-Derived Xenografts. *Cell Rep.* **16**, 263–277 (2016).

35. JM, U. *et al.* Lymph protects metastasizing melanoma cells from ferroptosis. *Nature* **585**, 113–118 (2020).

36. Brozyna, A. A., Józwicki, W., Roszkowski, K., Filipiak, J. & Slominski, A. T. Melanin content in melanoma metastases affects the outcome of radiotherapy. *Oncotarget* **7**, 17844–17853 (2016).

37. Yang, W. S. & Stockwell, B. R. Synthetic Lethal Screening Identifies Compounds Activating Iron-Dependent, Nonapoptotic Cell Death in Oncogenic-RAS-Harboring Cancer Cells. *Chem. Biol.* **15**, 234–245 (2008).

38. J, N. *et al.* Proteomics analysis of A375 human malignant melanoma cells in response to arbutin treatment. *Biochim. Biophys. Acta* **1794**, 159–167 (2009).

39. Lange, M. J. de *et al.* Heterogeneity revealed by integrated genomic analysis uncovers a molecular switch in malignant uveal melanoma. *Oncotarget* **6**, 37824–37835 (2015).

40. Robertson, A. G. *et al.* Integrative Analysis Identifies Four Molecular and Clinical Subsets in Uveal Melanoma. *Cancer Cell* **32**, 204-220.e15 (2017).

41. Weinstein, J. N. *et al.* The cancer genome atlas pan-cancer analysis project. *Nature Genetics* vol. 45 1113–1120 (2013).

42. Tang, Z. *et al.* GEPIA: A web server for cancer and normal gene expression profiling and interactive analyses. *Nucleic Acids Res.* **45**, W98–W102 (2017).

43. G, N., H, W., D, von der H. & G, A. Establishment of two cell lines derived from conjunctival melanomas. *Exp. Eye Res.* **81**, 361–362 (2005).

44. Chen, P. W. *et al.* Expression of MAGE genes in ocular melanoma during progression from primary to metastatic disease. *Clin. Exp. Metastasis* **15**, 509–518 (1997).

45. Amirouchene-Angelozzi, N. *et al.* Establishment of novel cell lines recapitulating the genetic landscape of uveal melanoma and preclinical validation of mTOR as a therapeutic target. *Mol. Oncol.* **8**, 1508–1520 (2014).

46. Ortho- and Ectopic Zebrafish Xeno-Engraftment of Ocular Melanoma to Recapitulate Primary Tumor and Experimental Metastasis Development | Protocol.

https://www.jove.com/de/t/62356/ortho-ectopic-zebrafish-xeno-engraftment-ocular-melanoma-to.

47. Karlsson, J., Von Hofsten, J. & Olsson, P. E. Generating transparent zebrafish: A refined method to improve detection of gene expression during embryonic development. *Mar. Biotechnol.* **3**, 522–527 (2001).

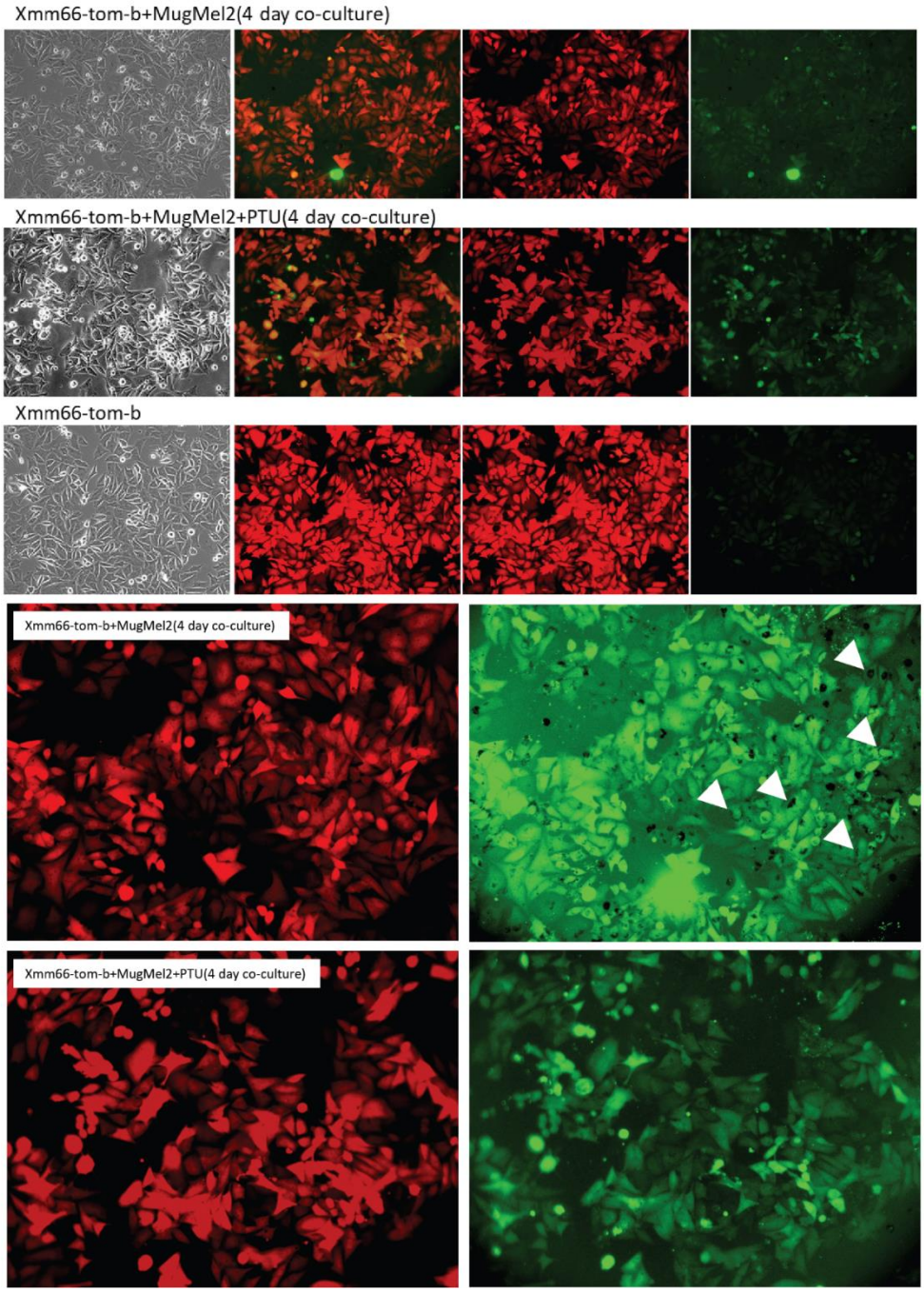

Supplementary figure S1 Co-culture of human CM melanoma cells mugmel2 and human UM cells XMM66. Example of co-cultured UM cell line XMM66 (acceptor) with melanin proficient (mugmel2 mel+) and melanin deficient (mugmel2 mel-) donor cells after mitomycin-C treatment, and control XMM66 cells. Melanin granules are present and visible in XMM66 after 4 days of co-culture (noted by the white arrowheads).

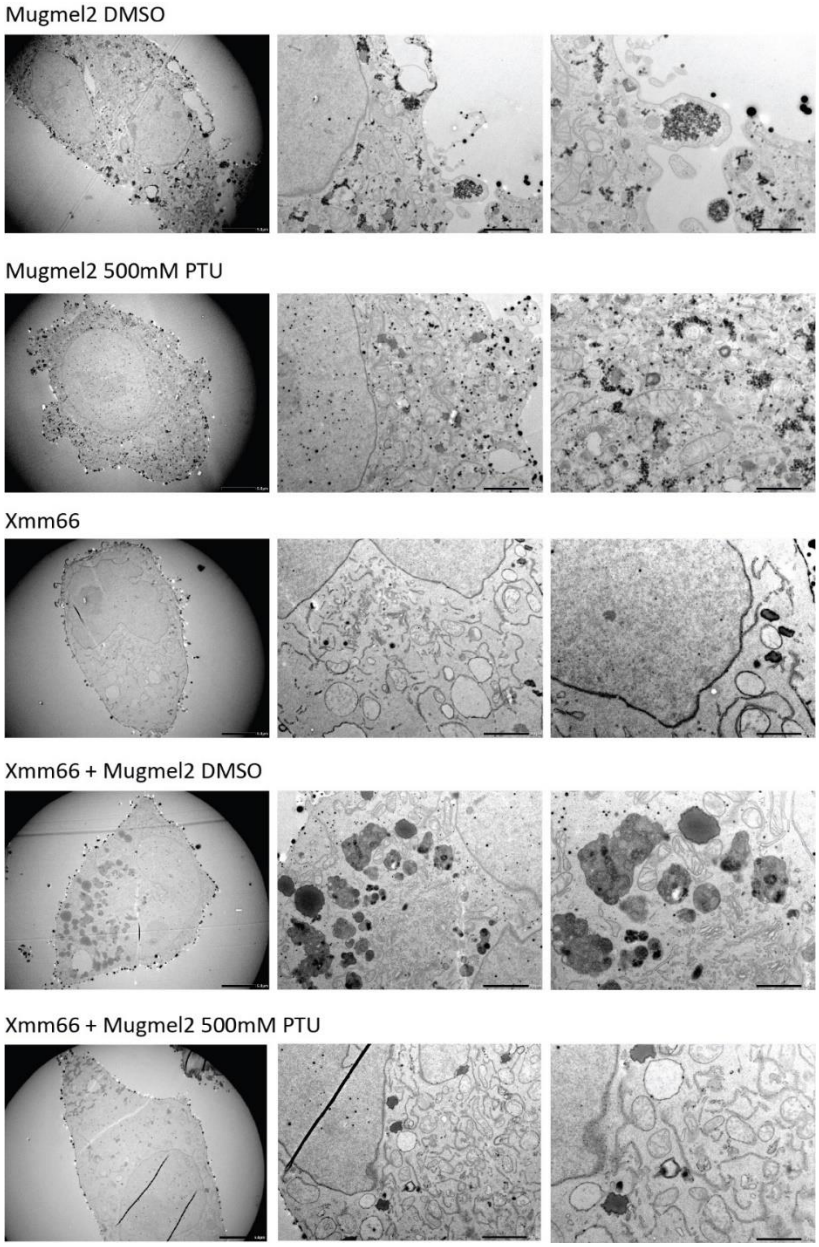

Supplementary figure S2 Transmission electron micrographs (TEM) of mugmel2 and XMM66 both with or without melanin. Mugmel2 without and with chemical melanin depletion. XMM66 naïve, melanin (mugmel2 mel+) proficient co-culture and melanin deficient (mel-) co-culture. Scalebar depicts 2µM.

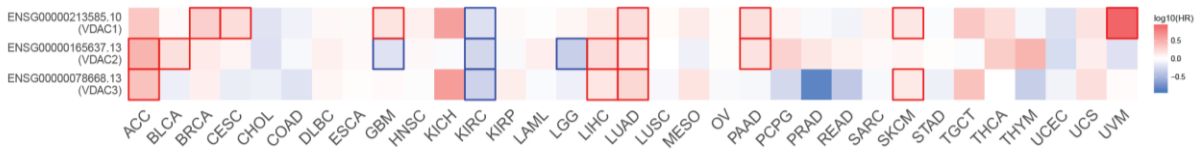

Supplementary figure S3 TCGA wide survival analysis of VDAC 1-3. Comparative analysis of all TCGA datasets for VDAC1-3. Red bounding boxes indicate a significant negative correlation between gene expression and survival. VDAC1 expression correlates with a decreased overall survival in breast, cervical squamous cell carcinoma and endocervical adenocarcinoma, glioblastoma multiforme, lung-, pancreatic adenocarcinoma, skin cutaneous and uveal melanoma (21.2% of all TCGA data sets).

TCGA abbreviations: Adrenocortical carcinoma (ACCA), Bladder Urothelial Carcinoma (BLCA), Breast invasive carcinoma (BRCA), Cervical squamous cell carcinoma and endocervical adenocarcinoma (CESC) Cholangio carcinoma (CHOL), Colon adenocarcinoma (COAD), Lymphoid Neoplasm Diffuse Large B-cell Lymphoma (DLBC), Esophageal carcinoma (ESCA), Glioblastoma multiforme (GBM), Head and Neck squamous cell carcinoma (HNSC), Kidney Chromophobe (KICH), Kidney renal clear cell carcinoma (KIRC), Kidney renal papillary cell carcinoma (KIRP) Acute Myeloid Leukemia (LAML) Brain Lower Grade Glioma (LGG), Liver hepatocellular carcinoma (LIHC), Lung adenocarcinoma (LUAD), Lung squamous cell carcinoma (LUSC), Mesothelioma (MESO), Ovarian serous cystadenocarcinoma (OVO), Pancreatic adenocarcinoma (PAAD), Pheochromocytoma and Paraganglioma (PCPG), Prostate adenocarcinoma (PRAD), Rectum adenocarcinoma (READ), Sarcoma (SARC), Skin Cutaneous Melanoma (SKCM), Stomach adenocarcinoma (STAD), Testicular Germ Cell Tumors(TGCT), Thyroid carcinoma (THCA), Thymoma (THYM), Uterine Corpus Endometrial Carcinoma (UCEC), Uterine Carcinosarcoma (UCSU), Uveal Melanoma (UVM).

Chapter 6:

XePhIR: The zebrafish Xenograft Phenotype Interactive Repository

XePhIR: The zebrafish Xenograft Phenotype Interactive Repository

Groenewoud A.*[1†2], Forn-Cuní G. [1†], Engel F.B. [2,3], Snaar-Jagalska B. E. [1]

* Corresponding author

† Both authors contributed equally

1) Institute of Biology Leiden, Animal Sciences, Leiden University, Einsteinweg 55, 2333 CC Leiden, The Netherlands.
2) Experimental Renal and Cardiovascular Research, Department of Nephropathology, Institute of Pathology, Friedrich-Alexander-Universität Erlangen-Nürnberg (FAU), Erlangen, 91054, Germany.
3) Comprehensive Cancer Center Erlangen-EMN (CCC ER-EMN), Erlangen, Germany

*arwin.groenewoud@uk-erlangen.de, current address: Schwabach anlage 12, 91054, Bayern, Germany

Database, Volume 2022, 2022, baac028, https://doi.org/10.1093/database/baac028

Published: 28 April 2022

Abstract

Zebrafish xenografts are an established model in cancer biology, with a steadily rising number of models and users. However, as of yet, there is no platform dedicated to standardizing protocols and sharing data regarding zebrafish xenograft phenotypes. Here, we present the Xenograft Phenotype Interactive Repository (XePhIR, www.xephir.org) as an independent data sharing platform to deposit, share and repurpose zebrafish xenograft data. Deposition of data and publication with XePhIR will be done after the acceptation of the original publication. This will enhance the reach of the original research article, enhance visibility, and does not interfere with publication or copyrights of the original article. With XePhIR, we strive to fulfill these objectives and reason that this resource will enhance reproducibility and showcase the appeal and applicability of the zebrafish xenograft model.

Introduction and purpose

Since the transplantation of human metastatic melanoma cells into zebrafish blastula-stage embryos (*Danio rerio*) by Lee et al. in 2005[1], the popularity of the zebrafish to model human cancer has been on a steady rise (Figure 1): scientists all over the world incorporate zebrafish as a model for cancer compound screening and utilize the zebrafish xenograft model to address basic questions in tumor biology and metastasis[2,3,4].

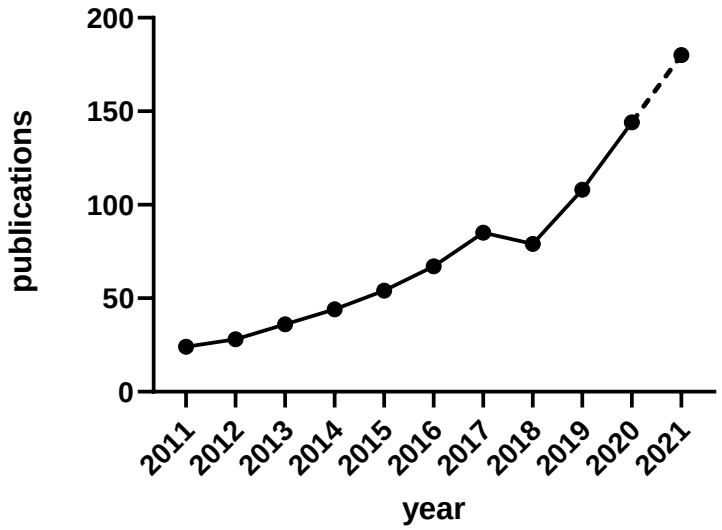

Figure 1 Increasing popularity of the zebrafish xenograft model. Over the course of the last 10 years the popularity of zebrafish xenograft models has been steadily increasing.

In 2016, we have published the first description of a zebrafish patient-derived xenograft[5]. One of the main issues we noted since then was a general lack of

conformity among different laboratories working with zebrafish xenograft models (i.e., cell types, growth medium, cancer cell processing prior to engraftment, staining of cells, injection site and time). Recently, several highly translational studies using both stable cell lines and patient-derived xenografts have further supported the overall value of the zebrafish as a cancer model[6–8]. One of the main difficulties in evaluating and comparing data obtained with the zebrafish xenograft model as well as interlaboratory adoption is the lack of standardized protocols. Detailed protocols are needed due to the variable nature and needs of each cancer line, which may result in invalid engraftment phenotypes or incorrect data interpretation.

Considering the increasing interest and number of zebrafish-based studies in the cancer field and the ever-growing need for transparent and reproducible science, we have created a platform where zebrafish xenograft phenotypes can be showcased, in an open access database. This platform will help to exchange experience inside the zebrafish community as well increase visibility and appreciation for this useful cancer model by wider audience. The need for a platform of this kind is also evidenced by the recent initiative by Targen et al. 2020, who created a zebrafish xenograft metadata repository[9]. However, zebrafish research is often driven by image-based quantification analyses. Therefore, we believe that a visual data repository is a more fitting representation of the underlying data and furthers the goal of enhancing the reproducibility of zebrafish assays. We want to enable external users to quickly choose the cell lines and zebrafish models for their assay of choice, such as dissemination, orthotopic/ ectopic engraftment, angiogenesis, etc. (Figure 2). Alternatively, this platform will facilitate the comparison of phenotypes, cell lines and zebrafish models between labs to enhance the overall reproducibility of zebrafish models around the world. In addition, our approach enables easy outreach to users unfamiliar with the zebrafish xenograft model.

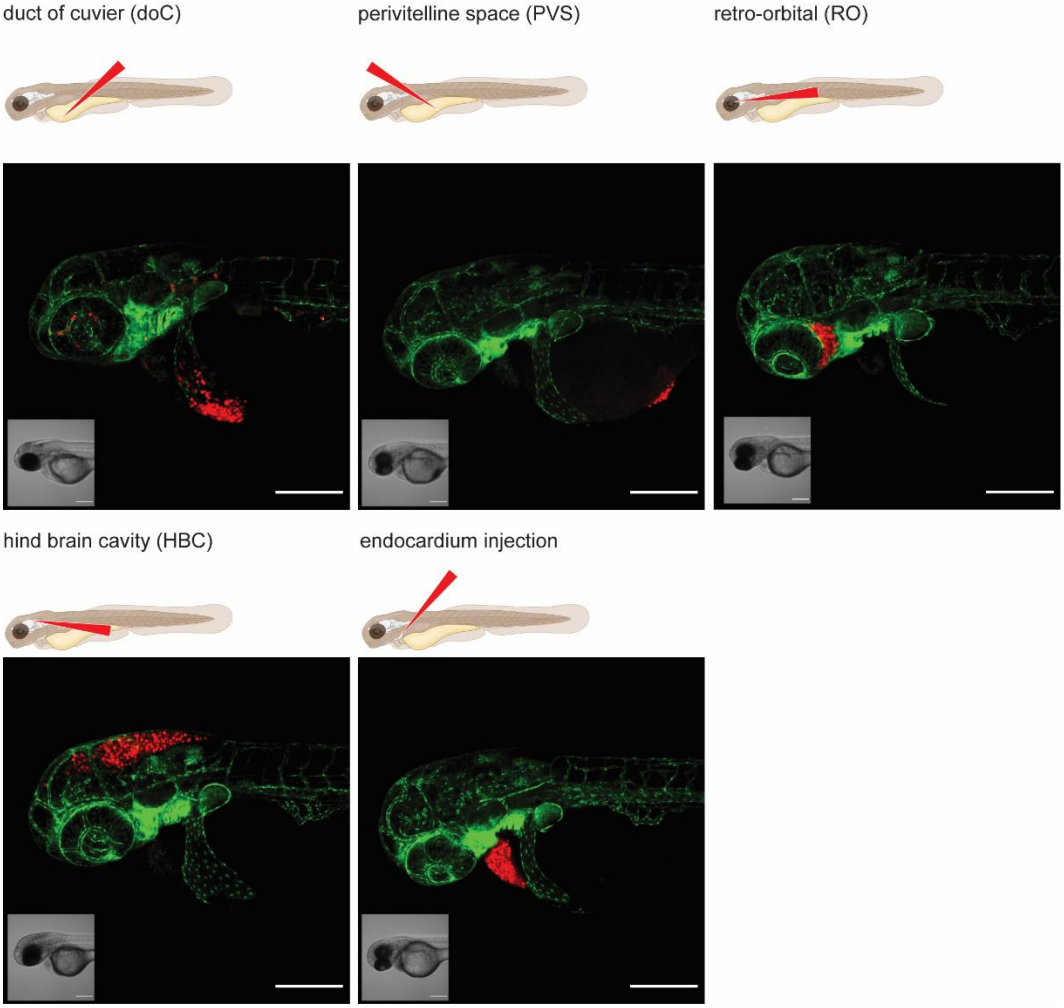

Figure 11 Graphical representation of common injection sites of the zebrafish xenograft model. Injection through the duct of Cuvier, a common route of injection to generate hematogenously disseminated cancer, also described as an experimental micro metastatic model.[10,11] Perivitelline space injection, originally described as a model for the generation and assessment of angiogenesis, more recently developed as a model for the generation of primary-like tumors.[6] Retro-orbital engraftment, used for the generation of orthotopic primary-like tumors derived from eye tumors, allows for the development of distant metastases.[12] Hind brain cavity injection models, used for the generation of orthotopic brain cancer models and for the generation of brain metastasis models.[13]

Since most zebrafish assays are image-based, there is an untapped host of data, outlining the zebrafish phenotypes generated during the conventional course of the experiments. We therefore propose to use one representative image per timepoint for submission to XePhIR. Citations to the original research will be included to allow and stimulate the citation of the originator of the model to further enhance visibility.

Comprehensive xenograft metadata and phenotype

To enhance the outreach potential of XePhiR, we will include a description of the cancer cells and explanation of the general experiment (a summary of the goal of the experiment and the outcome <150 words). To facilitate comparison and exchange

between laboratories, we will include a comprehensive list of all metadata required to repeat the experiment (cell types, culture conditions, injection space, etc. as specified in Table 1) as well as phenotypes to check if well engrafted. Among the metadata, there are for example American Type Cell Culture (ATCC) and/or Expasy (Cellosaurus) identifiers for the engrafted cells, Addgene identifier for reporter constructs used, chemical tracer used (specified, by supplier and catalog number), and zebrafish line as by ZFIN identifier.

Table 1. metadata sheet for data submission to Xephir

Cell line				
Name	Origin	Cellosaurus ID	Medium	Confluence (%)
MDA-mb231	ATCC	CVCL_0062	DMEM-F12	75-90%

Dissociation			
Reagent	Time (min)	Tracer	Construct ID†
Trypsin-EDT	3-5 min	dsRED	Addgene106171

Zebrafish	
Reporter (ZFIN identifier)	synonym
ZDB-TGCONSTRCT-070117-94	Tg(fli1:GFP)

Injection			
Concentration/mL (10^6)	Timepoint (hpf)	Location	Amount (cells/inj.)
250	48	DoC	250-350

Phenotype			
Negative selection		Imaging	
Time (dpi)	Type‡	Timepoints (dpi)	Microscope
1	CA/YS	1,4,6	Leica MZ16FA

Source data
Publication Ref (DOI)
10.3390/ijms17081375

†Addgene ID or other stable ID
‡ CE(cardiac edema), YS (yolk sac injection/leakage), UD (unwanted dissemination) MF (malformation)

Database contents

Since most zebrafish xenograft experiments are image-based, we have chosen for a graphic driven database. Here, users can upload one data set per timepoint of the performed zebrafish experiment (Fiji/bioformats compatible raw data only)[14]. The visual data will be supplemented with a comprehensive set of metadata as described previously (representation of the final website user interface in Figure 3).

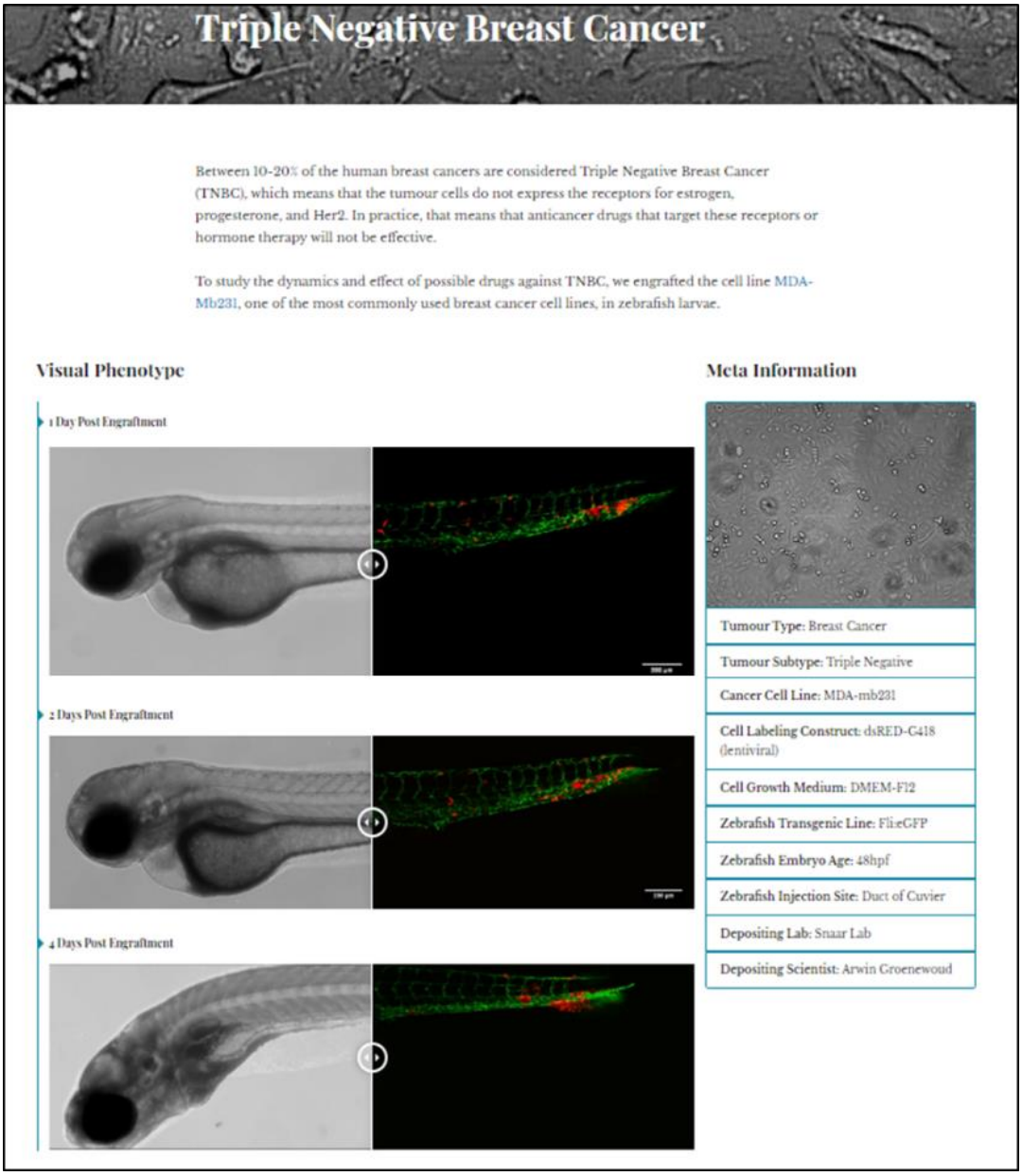

Figure 3 Triple negative breast cancer sample data as deposited. Image-based analysis data is used to generate a graph for the original publication and is subsequently uploaded to XePHIR (either directly or indirectly). Subsequently the available metadata is entered during submission (filling in the available data in the submission template). All metadata will be displayed next to the images that have been uploaded, when uploaded via Zenodo a digital object identifier will be provided to allow easy access to the original dataset.

Standardized protocols

As to further enhance the ease of interpretation of protocols and to support the worldwide repeatability of zebrafish xenograft experimentation, we have provided standardized engraftment protocols. These protocols are dynamic and can be adapted through drop down menus to encompass all conventional injection sites (duct of Cuvier, perivitelline space, retro-orbital, and hind brain cavity), carrier solutions, cell densities, cell number, and time of injection (in hours post fertilization, hpf).

Submission guidelines and Intellectual Property

Our database is open for submission. The focus of the submissions will be placed on the dissemination of already published data, to ensure that there will be no conflicts of interest between publishers and researchers. Next to the dissemination of previously published work, we will also provide a platform for unpublished data. Given that this could lead to a possible conflict of interest during later publication in a journal, this can only be done at the users informed request. If needed, uploaded data will be time-gated prior to publication, where the items will be released to the public after publication of the original manuscript.

To submit data to XePHIR, data has to be placed under a selection of creative commons licenses, namely the choice between the BY-NC-ND, BY-NC-SA and BY-SA licenses (more information at creativecommons.org). All CC licenses chosen disallow respective commercial use. Through CC licensing we can facilitate the use of the deposited material for future use in for instance grant applications. To do so, data can be uploaded either directly to XePHIR.org or via Zenodo[15] as a whole dataset, thus automatically placing it under CC license and generating a digital object identifier (DOI) allowing the referencing of the data (Figure 4).

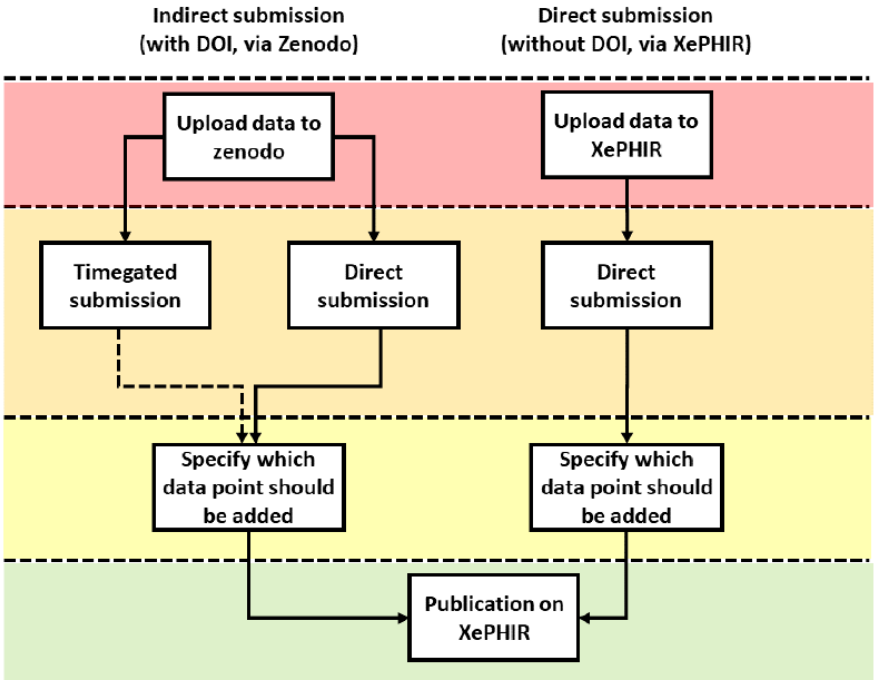

Figure 4 Methods of data submission to XePHIR. Indirect submission through Zenodo, allowing uploading of whole data sets (after acceptation of publication) will allow for enhanced transparency and re-usability of data and will provide the user with a DOI enabling citation of the data set. Uploading to Zenodo will automatically place the data under a creative commons license (CC). Direct submission to XePHIR will not provide the user with a DOI and will require the user to place the data under a CC license.

Careful selection of the representative data submitted to XePhIR will ensure a representative measure of the phenotype depicted and will thus enhance global reproducibility and minimize bias when selecting cancer cell lines for future experiments (Figure 5).

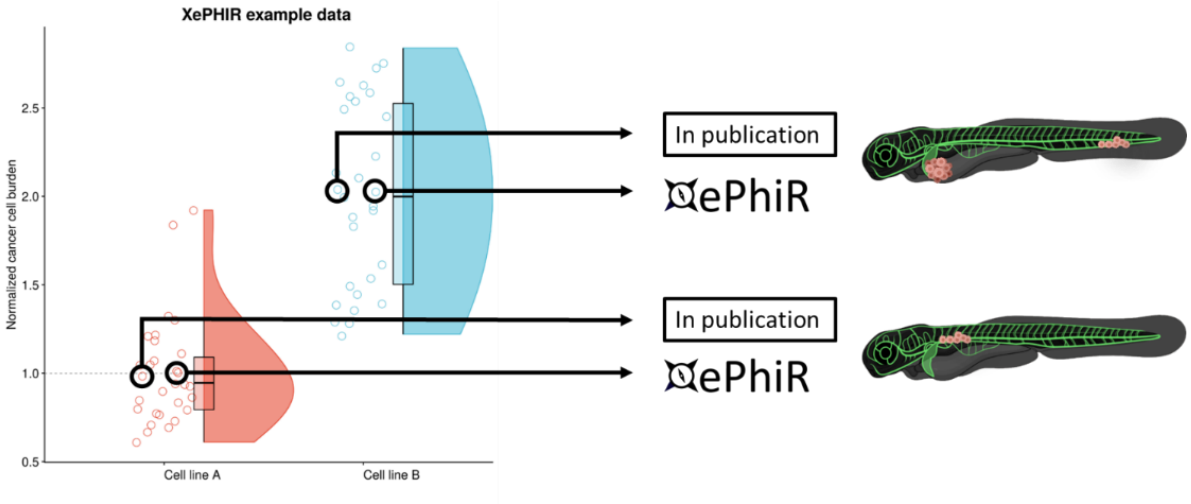

Figure 5 Data is derived from redundant image-based analysis. Image-based analysis data is used to generate a graph and is subsequently used for the publication of the original paper, where one sample individual is used in the original manuscript. Another representative individual is submitted to XePHIR either directly, or indirectly through deposition of the underlying dataset in Zenodo and subsequent publication of the representative image in XePhIR.

As the guidelines for the ethic use of animals vary between different countries, we will ask all depositors to sign a waiver stating that the generation of all data deposited has been generated in accordance with local animal ethical guidelines. We do not condone and take no responsibility for the unethical use of animals.

Conclusion

With XePHIR we represent for the first time, a visual, user-driven zebrafish xenograft database which provides 1-page summaries with the most important information of a cancer study utilizing zebrafish (Figure 5), collating all required data to reproduce the experiments, referring to the original paper. Through XePHIR we will enhance the visibility of individual research groups and the zebrafish xenograft models they generate and use. Using a two-pronged data submission approach, we will be able to generate data for future comparative analysis between groups, models or cell lines, further enhancing the reproducibility of zebrafish xenograft models worldwide. Data submission through Zenodo would further enhance the data re-use capacity and allows for the referencing of individual (un)published data sets using the Zenodo generated DOI.

Financial support: AG has received funding from the European Union's Horizon 2020 research and innovation program under grant agreement No 667787 (UM Cure 2020 project, www.umcure2020.org, Felix B. Engel by the Wilhelm Sander-Stiftung (2019.143.1 to FBE)

References:

1. Lee, L. M. J., Seftor, E. A., Bonde, G., Cornell, R. A. & Hendrix, M. J. C. The fate of human malignant melanoma cells transplanted into zebrafish embryos: Assessment of migration and cell division in the absence of tumor formation. *Dev. Dyn.* **233**, 1560–1570 (2005).

2. White, R., Rose, K. & Zon, L. Zebrafish cancer: the state of the art and the path forward. *Nat. Rev. Cancer* **13**, 624–636 (2013).

3. White, R. M. *et al.* Transparent Adult Zebrafish as a Tool for *In vivo* Transplantation Analysis. *Cell Stem Cell* **2**, 183–189 (2008).

4. Fazio, M., Ablain, J., Chuan, Y., Langenau, D. M. & Zon, L. I. Zebrafish patient avatars in cancer biology and precision cancer therapy. *Nature Reviews Cancer* vol. 20 263–273 (2020).

5. Mercatali, L. *et al.* Development of a patient-derived xenograft (PDX) of breast cancer bone metastasis in a Zebrafish model. *Int. J. Mol. Sci.* **17**, (2016).

6. Fior, R. *et al.* Single-cell functional and chemosensitive profiling of combinatorial colorectal therapy in zebrafish xenografts. *Proc. Natl. Acad. Sci. U. S. A.* **114**, E8234–E8243 (2017).

7. Chen, L. *et al.* A NF-κB-Activin A signaling axis enhances prostate cancer metastasis. *Oncogene* **39**, 1634–1651 (2020).

8. Yan, C. *et al.* Visualizing Engrafted Human Cancer and Therapy Responses in Immunodeficient Zebrafish. *Cell* **177**, 1903-1914.e14 (2019).

9. Targen, S. *et al.* ZenoFishDb v1.1: A database for xenotransplantation studies in Zebrafish. *Zebrafish* **17**, 305–318 (2020).

10. Chen, L. *et al. A zebrafish xenograft model for studying human cancer stem cells in distant metastasis and therapy response*. vol. 138 471–496 (2017).

11. Tulotta, C., Groenewoud, A., Snaar-Jagalska, B. E. E. & Ottewell, P. *Animal models of breast cancer bone metastasis*. *Methods in Molecular Biology* vol. 1914 309–330 (Humana Press Inc., 2019).

12. Ortho- and Ectopic Zebrafish Xeno-Engraftment of Ocular Melanoma to Recapitulate Primary Tumor and Experimental Metastasis Development | Protocol. https://www.jove.com/de/t/62356/ortho-ectopic-zebrafish-xeno-engraftment-ocular-melanoma-to.

13. Welker, A. M. *et al.* Standardized orthotopic xenografts in zebrafish reveal glioma cell-line-specific characteristics and tumor cell heterogeneity. *Dis. Model. Mech.* **9**, 199–210 (2016).

14. Schindelin, J. *et al.* Fiji: an open-source platform for biological-image analysis. *Nat. Methods* **9**, 676–682 (2012).

15. European Organization For Nuclear Research and OpenAIRE. Zenodo. (2013).

Appendix

Chapter 7: Summary and general discussion

Cancer and melanomagenesis

Cancer is one of the leading causes of death worldwide: three out of ten disease-related deaths can be ascribed directly to the consequences of cancer[1]. Worryingly, the overall incidence of cancer is on a steady rise[1,2]. The vast majority of cancer patients do not die from a primary tumor, but instead from the metastatic spread of the disease[3]. After its dissemination from a primary tumor, cancer cells invade distant tissues and through a combination of invasion and subsequent growth perturb the functions of the organs harboring these metastatic colonies and underlying bodily functions[3–5].

One of the most common cancers found in man are melanomas. Melanomas are cancers that canonically derive from melanocytes in the skin and in the eye leading to formation of skin and ocular melanoma, respectively. Melanocytes (with the exception of uveal melanocytes) are generally thought to be transformed through subsequent mutational events induced by UV damage. The causal event driving initial oncogenic transformation of uveal melanocytes remains unknown. The predisposing factors to melanoma development are a fair skin, the inability to tan, and light eye color. The general incidence of melanoma increases with age and most patients are of Caucasian skin type. The outlook for patients with metastatic melanoma is grim, despite that, there have been considerable advances in the treatment of cutaneous melanoma (CM), including anti PD1, PDL1 immunotherapy, oncolytic virotherapy, and targeted therapy[6–8]. Ocular melanoma, such as uveal melanoma (UM) and conjunctival melanoma (CoM), are less common than cutaneous melanoma, but more lethal. This is caused by the limited availability of treatment options for these types of ocular melanoma therefore new therapeutic options are desperately needed.

Generation of ortho- and ectopic- zebrafish xenograft models for ocular melanoma.

Currently, the development of new treatments for ocular melanoma is hindered by the fact that there are few options to test potential new therapies *in vivo* prior to translation of new treatments to clinical trials. Moreover, ocular melanoma animal models generally use non-native injection sites (mainly ectopic) to mimic primary tumor formation.

In **Chapter 1**, we strove to overcome this issue through the generation of a standardized protocol for the establishment of orthotopic ocular melanoma model. This protocol generates experimental primary-like tumor through engraftment of fluorescent conjunctival melanoma cells into the retroorbital site of 48 hours post fertilization zebrafish larvae. In parallel, we created a standardized protocol to establish a disseminated, ectopic ocular melanoma model. By combining these two models, the effects of novel putative anti-cancer compounds can be assessed in an animal model at an unprecedented throughput level. We validated our methodology with the known effective therapeutic vemurafenib, which targets cancers with the BRAFV600E mutation, as found in the CoM line CRMM1. In conclusion, we established a standardized approach for the pre-clinical assessment of therapeutic efficiency in a zebrafish xenograft model with physiological and translational relevance that allows the efficacy analysis of a novel compound on a cancer cell line of interest in less than a month.

Assessment of zebrafish models for preclinical screening of conjunctival melanoma targeted therapeutics.

Although CoM is a rare subtype of ocular melanoma, its incidence worldwide is increasing. The current standard of care for primary tumors consists of surgical excision combined with secondary brachytherapy, topical chemotherapy and cryotherapy. However, CoM displays a high rate of recurrence, which associates with metastasis and overall poor prognosis. Genetically, CoM shares similar driver mutations with CM and the majority bear one of either mutually exclusive oncogenic BRAF of NRAS mutations. Currently, there are only few targeted therapies available for the treatment of CoM, namely focusing on the inhibition of oncogenic BRAF. Although there are mouse models available to study metastatic CoM, these models are limited in their applicability for drug development due to their high cost and extremely long experimental duration.

In **Chapter 2**, we developed a fluorescence-based zebrafish screening platform for the rapid *in vivo* assessment of targeted therapeutics for the treatment of CoM. To this end, we xenografted the blood vessel reporter transgenic zebrafish line Tg(*fli1*:EGFP) with conjunctival melanoma cell lines CRMM1, CRMM2 and CM2005.1 expressing lentiviral tdTomato. We investigated two commonly used sites of xenotransplantation: yolk sac engraftment, and hematogenous engraftment through the duct of Cuvier. In

addition, we developed a new orthotopic engraftment strategy, applying the newly developed method described in **Chapter 1**, that not only generates a localized primary tumor-like growth, but also enables distant metastasis at later stages.

We have validated the CoM zebrafish xenograft model using the BRAFV600E mutation specific inhibitor vemurafenib, which showed significant reduction in tumor volume for the BRAF-mutated CoM cell lines *CRMM1* and *CM2005.1*, while the NRAS mutated cell line *CRMM2* was refractory. We concluded that both retro-orbital and intravenous engraftment were suitable for the recapitulation of different stages of CoM development, where yolk sac engraftment did not yield any viable cells after implantation. We adapted the intravenous engraftment strategy of CoM for drug screening. With the generation of these models, we are the first to create and validate a CoM xenograft platform that allows for medium- to high-throughput screening of (targeted) therapies for CoM in an *in vivo* context.

Uveal melanoma zebrafish patient derived melanoma models, for the pre-clinical assessment of targeted therapy.

Despite causing up to approximately 90% of all Ocular Melanoma cases, UM is a relatively rare but deadly type of melanoma. From all patients diagnosed with UM, 50% form liver metastasis, with the liver being predominant site of metastatic dissemination for UM. After diagnosis of liver metastasis, the medium survival for UM patients is 3.9 months, independent of treatment. That is because there is currently no effective targeted therapy available for the treatment for metastatic UM. In addition, there are currently no tailored animal models that recapitulate hematogenous UM metastasis formation, and subcutaneously engrafted UM models do not spontaneously metastasize.

In **Chapter 3**, we address the issue of the limited availability of treatment options through the generation of zebrafish patient-derived xenograft (zfPDX) models for UM. We established the first reported hematogenous dissemination PDX model for UM, using the zebrafish models mentioned above. In addition, we generated a system for the cultivation of metastatic and primary UM tissue, to allow the establishment of distinct zebrafish engraftments from a single patient biopsy. During this process, we discovered that spheroid-derived, non-adherent UM samples are tumorigenic, while adherent cell lines are non-tumorigenic despite the same origin. We verified that this

phenomenon is reproducible in a set of novel adherent lines derived from tumorigenic spheroid line *spXmm66*. Upon engraftment, we confirmed that the engrafted adherent lines, independent of origin, were non-tumorigenic, whereas the spheroid line was tumorigenic. Forcing adherent lines into suspension did not provide any enhancement of tumorigenic capacity, while inhibition of ROCK signaling through ROCK inhibitor Y27632 stunted the reduction of tumorigenic capacity, possibly by ROCK mediated differentiation as reported by Maekwa et al 1999[9]. The spheroids derived from PDX derived metastatic UM tissues were used to generated a robust spheroid culture system that allowed the retention UM tumorigenic potential *in vivo*. Using these tumorigenic UM spheroid cultures, we established a zebrafish UM PDX model which was subsequently validated with previously published experimental drugs and drug combinations[10–13].

During the establishment of our zebrafish xenograft model for UM we observed the rapid clearance of circulating UM cells derived from adherent cell lines: engrafted, non-melanated, UM cells show complete clearance within 24 hours post-injection into the zebrafish host, as an exception to all other cell lines derived from other cancer types injected in our lab. We reasoned that the aforementioned attrition of circulating UM cells would be driven through a cell intrinsic mechanism, given its speed and totality. We asked if reactive oxygen species (ROS), and more specifically ferroptosis –a newly discovered mechanism of iron-dependent, ROS driven lipid oxidation-based necrosis– could be important for the observed cell death *in vivo*. We first showed that the expression of two major components, namely glutathione peroxidase 4 (GPX4) and solute carrier family 7 member 11/System Xc- (SCL7A11/XCT) involved in the maintenance and repair of ferroptosis-induced damage is inversely correlated with UM related survival. Clinical data was suggestive of a correlation between BRCA associated protein 1 (BAP1) loss, a major negative clinical prognosticator of bad disease outcome and GPX4 expression. We then assessed the efficacy of known inducers of ferroptosis in our zebrafish PDX model of metastatic UM. We leveraged the inherent advantages of our newly established model to rapidly generate patient-specific xenografts from primary UM biopsies, and used them for the assessment of ferroptosis susceptibility on a patient-to-patient basis. We induced ferroptosis through two independent pathways: via inhibition of GPX4 with RSL3, and with erastin, an inhibitor of system Xc- (SCL7A11 and SCL3A2) and mitochondrial voltage-dependent

anion channels. Both therapies significantly reduced the amount of UM cells with BAP1 loss when compared to the vehicle-treated control.

Taken together, we have provided insights in the mechanisms behind the metastatic potential of UM and, for the first time, *in vivo* preclinical evidence for the validity of ferroptosis-inducing therapy for the treatment of otherwise untreatable UM.

Modeling of metastatic melanomas in zebrafish models revealed ferroptosis as druggable pathway for clinical translation.

Melanomas are derived from melanocytes as cellular precursors and, therefore, have the intrinsic capacity to synthesize melanin. Melanin normally functions to protect the skin from free radicals generated through UV radiation[14,15] Melanin biosynthesis is driven in normal situations by the release of α-melanocyte stimulating hormone (αMSH) from the pituitary gland, where it reaches melanocytes after permeating the skin, activating the melanocortin receptors[16,17]. After binding and subsequent activation of the melanocortin receptors, Microphthalmia-associated transcription factor (MITF) translocates to the nucleus and drives expression of melanin biosynthesis via upregulating the gene expression of tyrosinase (TYR), Dopachrome tautomerase (DCT) and tyrosinase related protein 1 (TYRP1), among others[18,19].

The role of melanin in melanoma development and dissemination has been linked to a worsening of disease prognosis at an epidemiological level[20], and intracellular melanin levels have been linked to treatment resistance[21,22]. However, paradoxically, the role of melanin has also been linked to a lowered propensity to metastasize and a decrease of cellular migration[23,24].

Most melanoma cells readily produce melanin when extracted from patient tissue, but the vast majority of these cells lose melanogenic capacity *in vitro*. We have previously shown that UM lose their tumorigenic capacity when they adhere to a rigid cell culture substrate in the absence of ROCK inhibitor Y27632. In addition, in the case of *spXmm66*, we observed a co-occurrent loss of melanin in early passages. We therefore asked if the reintroduction of melanin in cells could protect UM cells in circulation, thus reinstating the lost metastatic capacity in most adherent UM cell lines. To this end we developed a co-culture system utilizing the heavily melanated cutaneous cell line MUG-Mel2 as a donor and the non-melanated UM cell lines XMM66 (adherent line derived from the same original donor as spheroid spXmm66)

and OMM2.3 as recipients. Through this coculture, we showed, for the first time, that UM cells can take in melanin from extraneous sources, and that, after melanin uptake, those cells survived significantly longer in circulation.

In **Chapter 4** we assess the observation that uveal melanoma cells derived from stable non-melanated cultures rapidly die in circulation after zebrafish xenotransplantation, as previously discussed in **Chapter 3**. In contrast we observed that, patient-derived samples, which are often intrinsically strongly melanated, survive for prolonged periods of time after hematogenous injection in zebrafish. We subsequently correlated pathological pigmentation levels at the time of enucleation with a significant reduction in disease-free survival in primary UM patients. This prompted us to ask whether the expression of melanin biosynthetic genes affect disease outcome in UM patients. Indeed, we could show that the high expression of the terminal melanin biosynthetic enzyme TYRp1 strongly correlated with a decrease in disease-free survival.

We then strove to generalize our findings to other types of melanomas. To this end, we engrafted the strongly melanated CM cell line MUG-Mel2[25] with or without prior melanin depletion. Interestingly, we found that either chemical and or genetic melanin depletion significantly reduces metastatic potential of these cells, without affecting cell viability or migratory capacity. In concordance, we demonstrated that the presence of melanin does correlate with metastatic potential in a set of tumorigenic CM and CoM cell lines.

In conclusion, we have shown that chemical perturbation of melanin biosynthesis reduces melanoma metastatic colonization in a zebrafish xenograft model across several melanoma lines and types. Moreover, we correlated TYRp1 levels with metastatic potential of melanoma lines in our zebrafish xenograft model.

Previously (**Chapter 3)**, we determined that ferroptosis was one of the main mechanisms leading to cell death of UM cells in circulation. Here, in **Chapter 4**, we demonstrated a concordant relation between the level of intracellular melanin and melanoma metastatic potential. We, therefore, hypothesized that ferroptosis might be causal to the attrition we observed in circulating UM, and melanin inhibits this process. We studied the effects of melanin on ROS, and more specifically, ferroptosis resistance of melanoma cells *in vitro*. To do so, we induced ferroptosis with RSL3 and erastin as characterized previously. We measured a significant sensitization to

ferroptosis induction in cells that were depleted of melanin prior to induction. We then validated our key findings using the zebrafish xenograft model, showing that this sensitization for ferroptosis induction through melanin-depletion also holds true in an *in vivo* context.

We further mined clinical patient data to demonstrate that most targets, if not all, of the compounds used to induce ferroptosis in our model (GPX4 for RSL3, and system Xc- components SCL7A11, SCL3A2 and VDACs for erastin), significantly negatively correlate with melanoma-specific survival in both primary CM and UM. Ultimately, we conclude that both ferroptosis resistance and melanin biosynthetic machinery are implicated in melanoma formation. These findings underscore the potential of ferroptosis-inducing strategies for the treatment of primary CM, UM, and possibly CoM patients in an adjuvant therapeutic setting.

Dissemination and standardization of zebrafish xenograft models

Since its advent in 2005, the zebrafish xenograft model is gaining in popularity[26]. Together with this rise in popularity, the need for standardization between labs also increases. Given that one of the hallmarks of the zebrafish model is its amenability to microscopic observation due to its translucent tissue architecture, many zebrafish xenograft experiments heavily utilize microscopic image-based analysis.

In **Chapter 5** we strove to combine the abundance of zebrafish micrographs and the need for both dissemination and standardization into a single web-based platform. We created the Xenograft Phenotype Interactive Repository (XePhIR). In doing so, we strive to integrate the present (superfluous) data and standardized protocols to create a visual, searchable database. Using linked, standardized metadata we aspire to help in the standardization and dissemination of our developed protocols and images in zebrafish community and beyond. XePhIR aims to advance usage of versatile zebrafish xenograft models against cancer.

Concluding remarks

This thesis describes the establishment of standardized protocols for the recapitulation of metastatic ocular melanoma in an experimental zebrafish model. Using this model, we generated platforms for the assessment of drug efficacy for both CoM and UM. We have discovered a possible reason for the loss of tumorigenic capacity of adherent UM cells, linking it to adherence, ROCK signaling and melanin loss. Utilizing a non-

adherent sphere culture system, we have been able to generate a tumorigenic PDX-derived UM animal model. This UM animal model was used for the preclinical development of ferroptosis-inducing strategies. In addition, we are the first to functionally link the presence of melanin in melanoma cells to its enhanced metastatic capacity. Ultimately, we combined all the generated protocols and knowledge to explore the function of melanin in the prevention of ferroptosis cell death in circulating melanoma cells (CM, CoM and UM). Finally, we developed a novel data sharing platform for the repurposing, standardization and enhanced dissemination of zebrafish xenograft data such as the one presented in this thesis.

References

1. Bray, F., Laversanne, M., Weiderpass, E. & Soerjomataram, I. The ever-increasing importance of cancer as a leading cause of premature death worldwide. *Cancer* **0**, 2021 (2021).

2. Sung, H. *et al.* Global Cancer Statistics 2020: GLOBOCAN Estimates of Incidence and Mortality Worldwide for 36 Cancers in 185 Countries. *CA. Cancer J. Clin.* **71**, 209–249 (2021).

3. Chambers, A. F., Groom, A. C. & MacDonald, I. C. Dissemination and growth of cancer cells in metastatic sites. *Nat. Rev. Cancer* **2**, 563–572 (2002).

4. Luzzi, K. J. *et al.* Multistep Nature of Metastatic Inefficiency : Dormancy of Solitary Cells after Successful Extravasation and Limited Survival of Early Micrometastases. *Am. J. Pathol.* **153**, 865 (1998).

5. Gupta, G. P. & Massagué, J. Cancer Metastasis: Building a Framework. *Cell* vol. 127 679–695 (2006).

6. Gkiala, A. & Palioura, S. Conjunctival Melanoma: Update on Genetics, Epigenetics and Targeted Molecular and Immune-Based Therapies. *Clin. Ophthalmol.* **14**, 3137 (2020).

7. Everts, B. & van der Poel, H. G. Replication-selective oncolytic viruses in the treatment of cancer. *Cancer Gene Ther.* **12**, 141–61 (2005).

8. Michielin, O. *et al.* ESMO consensus conference recommendations on the management of locoregional melanoma: under the auspices of the ESMO Guidelines Committee. *Ann. Oncol.* **31**, 1449–1461 (2020).

9. Maekawa, M. *et al.* Signaling from Rho to the actin cytoskeleton through protein kinases ROCK and LIM-kinase. *Science (80-.).* **285**, 895–898 (1999).

10. Decaudin, D. *et al.* Preclinical evaluation of drug combinations identifies co-inhibition of Bcl-2/XL/W and MDM2 as a potential therapy in uveal melanoma. *Eur. J. Cancer* **126**, 93–103 (2020).

11. Amirouchene-Angelozzi, N. *et al.* Establishment of novel cell lines recapitulating the genetic landscape of uveal melanoma and preclinical validation of mTOR as a therapeutic target. *Mol. Oncol.* **8**, 1508–1520 (2014).

12. Heijkants, R. *et al.* Combined inhibition of CDK and HDAC as a promising therapeutic strategy for both cutaneous and uveal metastatic melanoma. *Oncotarget* **9**, 6174–6187 (2018).

13. Carita, G. *et al.* Dual inhibition of protein kinase C and p53-MDM2 or PKC and mTORC1 are novel efficient therapeutic approaches for uveal melanoma. *Oncotarget* **7**, 33542–33556 (2016).

14. Noonan, F. P. *et al.* Melanoma induction by ultraviolet A but not ultraviolet B radiation requires melanin pigment. *Nat. Commun. 2012 31* **3**, 1–10 (2012).

15. Brenner, M. & Hearing, V. J. The Protective Role of Melanin Against UV Damage in Human

Skin. *Photochem. Photobiol.* **84**, 539 (2008).

16. Friedmann, P. S. & Gilchrest, B. A. Ultraviolet radiation directly induces pigment production by cultured human melanocytes. *J. Cell. Physiol.* **133**, 88–94 (1987).

17. Whittaker, J. R. An analysis of melanogenesis in differentiating pigment cells of ascidian embryos. *Dev. Biol.* **14**, 1–39 (1966).

18. Hosoi, J., Abe, E., Suda, T. & Kuroki2, T. Regulation of Melanin Synthesis of B16 Mouse Melanoma Cells by 1a,25- Dihydroxyvitamin D3 and Retinoic Acid1. *CANCER Res.* **45**, 1474–1478 (1985).

19. Maranduca, M. A. *et al.* Synthesis and physiological implications of melanic pigments. *Oncol. Lett.* **17**, 4183 (2019).

20. AA, B., W, J., JA, C. & AT, S. Melanogenesis affects overall and disease-free survival in patients with stage III and IV melanoma. *Hum. Pathol.* **44**, 2071–2074 (2013).

21. Kinnaert, E. *et al.* The Degree of Pigmentation Modulates the Radiosensitivity of Human Melanoma Cells. *Radiat. Res.* **Vol. 154**, 497–502 (2000).

22. Brożyna, A. A., VanMiddlesworth, L. & Slominski, A. T. Inhibition of melanogenesis as a radiation sensitizer for melanoma therapy. *Int. J. Cancer* **123**, 1448–1456 (2008).

23. Pinner, S. *et al.* Intravital imaging reveals transient changes in pigment production and Brn2 expression during metastatic melanoma dissemination. *Cancer Res.* **69**, 7969–7977 (2009).

24. Sarna, M., Krzykawska-Serda, M., Jakubowska, M., Zadlo, A. & Urbanska, K. Melanin presence inhibits melanoma cell spread in mice in a unique mechanical fashion. *Sci. Rep.* **9**, 1–9 (2019).

25. Rinner, B. *et al.* MUG-Mel2, a novel highly pigmented and well characterized NRAS mutated human melanoma cell line. *Sci. Rep.* **7**, (2017).

26. Lee, L. M. J., Seftor, E. A., Bonde, G., Cornell, R. A. & Hendrix, M. J. C. The fate of human malignant melanoma cells transplanted into zebrafish embryos: Assessment of migration and cell division in the absence of tumor formation. *Dev. Dyn.* **233**, 1560–1570 (2005).

Nederlandse samenvatting

Etiologie van kanker

Kanker is een complexe, cellulaire ziekte. Kanker ontstaat als een cel in het lichaam door middel van een reeks mutaties, ontsnapt uit de gecontroleerde cyclus van celdeling en celdood. Twee mutaties kunnen genoeg zijn om zowel geprogrammeerde celdood als ongeremde celdeling te bevorderen. Elke normale cel heeft oncogenen en tumorsuppressorgenen. Oncogenen (bijvoorbeeld onderdelen van de RAS-RAF-MEK-ERK signaaltransductie route) zijn genen die ervoor zorgen dat celdeling versneld wordt. Een tumorsupppressorgen (bijvoorbeeld P53 eiwit) doet het omgekeerde en kan het vermeerderen van cellen stilleggen. Het uitschakelen van de functie van deze genen heeft daarom een pro-tumor-werking. Een kankercel is een ontspoorde cel met gemuteerde oncogenen en/of tumorsuppressorgenen die veel meer, sneller en ongecontroleerd zal delen en niet reageert op controlemechanismen die normaliter invloed hebben op gezonde cellen. Kanker ontstaat na een opstapeling van meerdere fouten en mutaties, door middel van bijvoorbeeld mutaties in het eiwit P53, aangevuld met een mutatie die verantwoordelijk is voor het versneld en ongeremd delen van de cellen (bijvoorbeeld door een activerende mutatie in een RAS- of RAF-eiwit als onderdeel van de RAS-RAF-MEK-ERK signaaltransductieroute). De tumor die hieruit gevormd wordt is een evolutionaire microkosmos waarin een continue strijd is tussen verschillende populaties cellen. Dit zorgt ervoor dat kankercellen zich aan een toenemende selectiedruk aanpassen, wat uiteindelijk tot uitzaaiingen zal leiden.

Melanoomontwikkeling en cel van herkomst

Melanoom is een type kanker dat ontstaat uit melanocyten. Deze gepigmenteerde cellen functioneren in de huid als een producent van melanine, een pigment dat door middel van opname in keratinocyten de onderliggende huidcellen beschermt tegen ultraviolette straling (UV). Deze UV-straling zorgt in de huid voor DNA-schade door middel van de productie van intracellulaire reactieve zuurstof (ROS). Deze DNA-schade leidt tot een toename van DNA-mutaties en is direct gekoppeld aan een toename in huidkanker.

Cutane (huid) melanoom is de meest voorkomende vorm van melanoom, en komt het vaakst voor onder Kaukasische (blanke) populatie, en blauwe/groene ogen en een verhoogde kans op verbranden in de zon, zijn risicofactoren. Andere, zeldzamere vormen van melanomen zijn, onder andere melanoom van de conjunctiva en van de uvea. Deze vormen een zeldzamere subgroep van melanomen, en ontwikkelen zich in het oog. Conjunctivale melanomen delen veel karakteristieken van cutane melanomen (dezelfde aandrijvende mutaties i.e. RAS/RAF en worden gekenmerkt door een UV specifiek DNA-schadepatroon). Uveale melanoom ontwikkelt zich uit de melanocyten van de uvea (het *choroides*/vaatvlies, het *corpus cilliare*/straalvormig lichaam en de iris). Dit zeldzame melanoom-subtype heeft weinig overeenkomsten met andere melanomen. De aandrijvende mutaties zijn voornamelijk GNA_Q en GNA11[11], GTPases die een hyperactivatie van onder andere RAS bewerkstelligen. Bovendien zijn er geen duidelijke UV DNA-schadepatronen te herkennen en zijn deze tumoren, in tegenstelling tot huidmelanomen, niet sterk gemuteerd. In het geval van uveaal melanoom is er een duidelijke scheiding te maken tussen hoog- en laag-risicopatiënten. Hier is het gebrek aan expressie van BRCA associated protein 1 (BAP1) een zeer sterke indicator van een slechte prognose. Eveneens is het verlies van een kopie van chromosoom 3 (monosomie 3) een prognostische marker voor slecht ziekteverloop.

Metastase

Kankerpatiënten sterven voornamelijk (>90%) aan metastatische kanker (uitzaaiing) en niet aan de primaire tumor. Dit komt doordat metastatische kankercellen in staat zijn om op nieuwe locaties in het lichaam te nestelen en uit te groeien van enkele cellen tot nieuwe metastatische kolonies. Metastase vindt plaats door het infiltreren van bloed- of lymfevaten (intravasatie) om vervolgens uit deze vaten uit te treden. Deze nieuwe metastatische kolonies infiltreren de omringende weefsels en verstoren de functie van de organen, die geïnfiltreerd raken door de metastases.

Diermodellen in de ontwikkeling van anti-kanker en anti-metastatische behandelingen

Metastase is een uiterst complex en moeilijk bestudeerbaar proces. Het grootste gedeelte van de zogenaamde “metastatische cascade” vindt plaats buiten de observatiecapaciteiten van de geneeskunde, zowel binnen experimentele als klinische setting. Deze observatie en daarmee analyse wordt bemoeilijkt door het ontraceerbare

en willekeurige aspect van metastatische kankercellen. Naast een aantal mogelijke risico-organen, specifiek voor een bepaalde soort primaire tumor - voornamelijk bepaald door de aanwezige afferente bloedvaten van het aangedane orgaan - is de uiteindelijke metastatische locatie van de meeste tumoren niet te voorspellen. Dit gebrek aan informatie bemoeilijkt het ontwikkelen van behandelingen die zich focussen op bestrijding van metastatische kanker; het stadium waarvoor aanvullende behandelingen juist hard nodig zijn.

Diermodellen vormen hier een noodzakelijke brug tussen het klassieke *in vitro* laboratoriumonderzoek, welke slechts cel-intrinsieke afwijkingen of gedereguleerde cel-cel interacties aan kunnen tonen, en *in vivo* onderzoek, waarbij cel-cel interacties van een hogere complexiteit getest kunnen worden. Bij dit onderzoek worden muizen of, in deze thesis, de zebravislarf (*Danio Rerio*) gebruikt voor het nabootsen van de complexe metastatische cascade, met alle biologische, fysische interacties die een rol spelen in patiënten.

De zebravislarf, een snel ontwikkelende, *ex utero* bevruchte gewervelde met van nature doorzichtige weefsels, stelt ons in staat om niet alleen fluorescente kankercellen tot op het niveau van een enkele cel te volgen gedurende de metastase, maar laat ons ook snel en gemakkelijk nieuwe potentiële behandelingen testen in een levend organisme.

Ontwikkeling van ortho- en ectopische modellen voor oogmelanoom

Om metastatische tumoren te bestrijden moet de intrinsieke complexiteit van de ontwikkeling van metastase zo nauwkeurig mogelijk nagebootst worden. In de zebravis kan zowel het primaire stadium als het metastatische stadium van conjunctivale en uveale melanomen gerecapituleerd worden door het injecteren van kankercellen in de retro-orbitale ruimte (achter het oog) (**Hoofdstuk 2**). Deze methode van injectie maakt het mogelijk om een onderscheid te maken in de efficiëntie van experimentele behandeling, zowel op de primaire tumor als op de metastatische tumor (**Hoofdstuk 3**).

Reactieve zuurstof in metastase

Hoewel metastase ten grondslag ligt aan het verergeren van het ziektebeeld van patiënten, met uiteindelijk de dood tot gevolg, is het een bijzonder inefficiënt proces. Geschat is dat slechts 1-5% van alle uitzaaiende (disseminerende) kankercellen uiteindelijk een metastase vormt. Deze inefficiëntie verklaart het verschil tussen de vaak grote hoeveelheden disseminerende kankercellen en een kleine (maar alsnog vaak dodelijke) hoeveelheid metastasen. De sterfte van deze disseminerende kankercellen wordt veroorzaakt door een aantal factoren waaraan de cellen van de primaire tumor niet voldoende zijn aangepast. Een van de factoren die als externe selectiedruk functioneert, is reactieve zuurstof (ROS). Daarnaast speelt in het geval van metastaserende melanoomcellen (en andere RAS gedreven tumoren), ferroptose een specifieke rol. Ferroptose is een ijzerafhankelijk celdoodmechanisme, waarbij ROS de oxidatie van vetzuurmoleculen (het hoofdbestanddeel van het celmembraan) - aandrijft, met celdood tot gevolg.

Er zijn tot op heden geen diermodellen die de uitgezaaide vorm van uveaal melanoom recapituleren. Wanneer *in vitro* gecultiveerde cellen in de bloedsomloop van zebravissen geïnjecteerd worden, sterven deze cellen binnen 24 uur, in tegenstelling tot zowel cutane- als conjunctivale melanoomcellen. Wanneer primaire uveale melanoomcellen (opgezuiverd uit zowel muizen als patiënt gederiveerde xenografts (patient derived xenografts, PDX) geïnjecteerd worden, zijn deze in staat om langdurig te circuleren in de bloedsomloop van zebravissen en vormen na enkele dagen metastases. In vitro cultivatie van deze cellen in suspensiekweek stelt deze cellen in staat om hun tumorigene potentieel te behouden. Adherente kweek doet dit tumorigene potentieel teniet binnen enkele dagen. Het induceren van ferroptose door middel van inhibitie van hetzij glutathion peroxidase 4 (GPX4) of door de inhibitie van een van de componenten van systeem Xc- (SCL7A11) bleek in staat om metastaserende uveale melanoomcellen significant te reduceren (**Hoofdstuk 4**). Ten slotte waren wij in staat om te demonsteren dat GPX4 levels in uveaal melanoom correleren met een verhoogde expressie van *BAP1,* wat een indicator is voor een slechte prognose en een sterk verhoogde kans op metastase. In **Hoofstuk 4** poneren wij om deze reden dat een zebravismodel van uveaal melanoom kan functioneren als een hulpmiddel waarmee patiëntenmateriaal van primaire uveaal melanoom getest

kan worden op de ontvankelijkheid voor ferroptose-inducerende substanties, voordat deze patiënten een metastase gevormd hebben.

Melanine en reactieve zuurstof in (pan)melanoma

De meeste melanomen worden gekenmerkt door een hoge productie van melanine. Deze kleurstof wordt binnen in melanocyten - de cel die als voorloper van melanoom fungeert - geproduceerd. Deze kleurstof fungeert intracellulair als een reservoir van antioxidanten. Deze gaan de schadelijke werking van UV-straling tegen. In melanoomcellen zijn ROS gekoppeld aan een reductie in metastatisch potentieel. Hier zorgt de verhoging van ROS voor het doden van cellen die ontsnappen aan de primaire tumor, waardoor de totale efficiëntie van het metastatische proces sterk wordt teruggedrongen. Recente ontdekkingen hebben een verband gelegd tussen de verhoging van ijzer (Fe^{2+}) en ROS aangedreven celdood, met name ferroptose. Dit vrije ijzer, dat sterk verhoogd is zowel in bloed als in lymfe (de twee voornaamste routes van metastase), zorgt tijdens het proces van ferroptose voor een kettingreactie (met als eindproduct de oxidatie van de lipiden waaruit het celmembraan bestaat) welke celdood tot gevolg heeft. In **Hoofdstuk 5** tonen wij de mechanistische verbinding aan tussen melaninebiosynthese (productie van een antioxidant) en ferroptoseresistentie, en een pan melanoom-cellijnpanel (zowel huid- als oogmelanomen). Na de observatie dat alle ongepigmenteerde oogmelanoomcellijnen geïmplanteerd in zebravislarven binnen 24 uur sterven (**Hoofdstuk 4**), vonden wij een correlatie tussen pigmentatie en een langere tijd dat deze cellen in de bloedsomloop van zebravislarven overleven. Vervolgens toonden wij aan dat het verstoren van deze biosynthese (zowel op chemische als genetische wijze) het metastatische potentieel van deze kankercellen significant vermindert. Uiteindelijk waren wij in staat om te demonstreren dat ongepigmenteerde cellen niet alleen minder metastatisch vermogen hebben, maar dat deze ook ontvankelijk zijn voor behandeling door middel van chemische inductie van ferroptose.

Toegankelijkheid, disseminatie van onderzoeksmateriaal en herhaalbaarheid van wetenschappelijk onderzoek.

Zebravisonderzoek is dankzij de intrinsieke optische transparantie van de larven, vaak gebaseerd op analyse van afbeeldingen. Gedurende het uitvoeren van het onderzoek in deze dissertatie, zijn er vele honderden (zo niet duizenden) foto’s van

zebravislarven gemaakt die geïnjecteerd waren met een wijde selectie aan kankercellen van velerlei verschillende kankertypes. Wetenschappers over de hele wereld bezitten op deze manier een grote hoeveelheid materiaal dat onderdeel is van een onderzoek, maar niet volledig met de wetenschappelijke gemeenschap gedeeld wordt.

In wetenschappelijk onderzoek is herhaalbaarheid van een onderzoek, evenals het dissemineren en het vergroten van het maatschappelijk draagvlak, vaak een onbesproken en onderbenut onderdeel. Door middel van websites en data archieven, zoals besproken in **Hoofdstuk 6,** kunnen deze doelen gecombineerd worden. XePhiR.org fungeert hier als een verzamelpunt voor zebraviskankermodellen vanuit verschillende laboratoria van over de hele wereld en koppelt protocollen, ruwe data en meta data, om zo de toegangsdrempel tot individuele zebravis modellen te verlagen.

Concluderend, heeft het in dit proefschrift beschreven onderzoek geleid tot nieuwe inzichten in de vorming van metastase van verschillende melanoom subtypes. Op grond van de verkregen resultaten suggereren wij dat zowel het blokkeren van melanine biosynthese, als het induceren van ferroptose (of de combinatie van beide) als een potentiële nieuwe behandeling van verschillende types metastatische melanomen kan fungeren.

Chapter 8 List of publications

Original publications (*: shared first author)**:**

1. **Groenewoud A**, Forn-Cuní G, Engel F.B, Snaar-Jagalska B. E. XePhIR: The zebrafish Xenograft Phenotype Interactive Repository
2. **Groenewoud A**, Yin J, Snaar-Jagalska BE 'Ortho- and ectopic zebrafish xeno-engraftment of ocular melanoma to recapitulate primary tumor and experimental metastasis development. ***J Vis Exp.*** **2021**; (in press: https://www.jove.com/de/t/62356/ortho-ectopic-zebrafish-xeno-engraftment-ocular-melanoma-to)
3. Chen Q, Ramu V, Aydar Y, **Groenewoud A**, Zhou XQ, Jager MJ, Cole H, Cameron CG, McFarland SA, Bonnet S, Snaar-Jagalska BE. TLD1433 Photosensitizer Inhibits Conjunctival Melanoma Cells in Zebrafish Ectopic and Orthotopic Tumour Models. ***Cancers (Basel).*** **2020**; 12(3):587. doi: 10.3390/cancers12030587.
4. Chen L, De Menna M, **Groenewoud A**, Thalmann GN, Kruithof-de Julio M, Snaar-Jagalska BE. A NF-κB-Activin A signaling axis enhances prostate cancer metastasis. ***Oncogene*****. 2020**; 39(8):1634-1651. doi: 10.1038/s41388-019-1103-0.
5. Heitzer E*, **Groenewoud A***, Meditz K, Lohberger B, Liegl-Atzwanger B, Prokesch A, Kashofer K, Behrens D, Haybaeck J, Kolb-Lenz D, Koefeler H, Riedl S, Schaider H, Fischer C, Snaar-Jagalska BE, de'Jong D, Szuhai K, Zweytick D, Rinner B. Human melanoma brain metastases cell line MUG-Mel1, isolated clones and their detailed characterization. ***Sci Rep*****. 2019**; 9(1):4096. doi: 10.1038/s41598-019-40570-1.
6. Tulotta C, Groenewoud A, Snaar-Jagalska BE, Ottewell P. Animal Models of Breast Cancer Bone Metastasis. ***Methods Mol Biol*****. 2019**; 1914:309-330. doi: 10.1007/978-1-4939-8997-3_17.
7. van der Helm D, **Groenewoud A**, de Jonge-Muller ESM, Barnhoorn MC, Schoonderwoerd MJA, Coenraad MJ, Hawinkels LJAC, Snaar-Jagalska BE, van Hoek B, Verspaget HW. Mesenchymal stromal cells prevent progression of liver

fibrosis in a novel zebrafish embryo model. ***Sci Rep*. 2018**; 8(1):16005. doi: 10.1038/s41598-018-34351-5.

8. Paauwe M, Schoonderwoerd MJA, Helderman RFCP, Harryvan TJ, **Groenewoud A**, van Pelt GW, Bor R, Hemmer DM, Versteeg HH, Snaar-Jagalska BE, Theuer CP, Hardwick JCH, Sier CFM, Ten Dijke P, Hawinkels LJAC. Endoglin Expression on Cancer-Associated Fibroblasts Regulates Invasion and Stimulates Colorectal Cancer Metastasis. ***Clin Cancer Res*. 2018**; 24(24):6331-6344. doi: 10.1158/1078-0432.CCR-18-0329.

9. Cao J, Pontes KC, Heijkants RC, Brouwer NJ, **Groenewoud A**, Jordanova ES, Marinkovic M, van Duinen S, Teunisse AF, Verdijk RM, Snaar-Jagalska E, Jochemsen AG, Jager MJ. Overexpression of EZH2 in conjunctival melanoma offers a new therapeutic target. ***J Pathol*. 2018**; 245(4):433-444. doi: 10.1002/path.5094.

10. Pontes KCS, **Groenewoud A**, Cao J, Ataide LMS, Snaar-Jagalska E, Jager MJ. Evaluation of (fli:GFP) Casper Zebrafish Embryos as a Model for Human Conjunctival Melanoma. ***Invest Ophthalmol Vis Sci*. 2017**; 58(14):6065-6071. doi: 10.1167/iovs.17-22023.

11. Liverani C, La Manna F, **Groenewoud A**, Mercatali L, Van Der Pluijm G, Pieri F, Cavaliere D, De Vita A, Spadazzi C, Miserocchi G, Bongiovanni A, Recine F, Riva N, Amadori D, Tasciotti E, Snaar-Jagalska E, Ibrahim T. **CORRECTION**: Innovative approaches to establish and characterize primary cultures: an ex vivo 3D system and the zebrafish model. ***Biol Open*. 2017**; 6(2):309. doi: 10.1242/bio.023911.

12. Liverani C, La Manna F, **Groenewoud A**, Mercatali L, Van Der Pluijm G, Pieri F, Cavaliere D, De Vita A, Spadazzi C, Miserocchi G, Bongiovanni A, Recine F, Riva N, Amadori D, Tasciotti E, Snaar-Jagalska E, Ibrahim T. Innovative approaches to establish and characterize primary cultures: an ex vivo 3D system and the zebrafish model. ***Biol Open*. 2017**; 6(2):133-140. doi: 10.1242/bio.022483.

13. Mercatali L, La Manna F, **Groenewoud A**, Casadei R, Recine F, Miserocchi G, Pieri F, Liverani C, Bongiovanni A, Spadazzi C, de Vita A, van der Pluijm G, Giorgini A, Biagini R, Amadori D, Ibrahim T, Snaar-Jagalska E. Development of a Patient-Derived Xenograft (PDX) of Breast Cancer Bone Metastasis in a Zebrafish Model. ***Int J Mol Sci*. 2016**; 17(8):1375. doi: 10.3390/ijms17081375.

14. Tulotta C, He S, Chen L, **Groenewoud A**, van der Ent W, Meijer AH, Spaink HP, Snaar-Jagalska BE. Imaging of Human Cancer Cell Proliferation, Invasion, and Micrometastasis in a Zebrafish Xenogeneic Engraftment Model. ***Methods Mol Biol*. 2016**; 1451:155-69. doi: 10.1007/978-1-4939-3771-4_11.

15. Riaz M, Berns EM, Sieuwerts AM, Ruigrok-Ritstier K, de Weerd V, **Groenewoud A**, Uitterlinden AG, Look MP, Klijn JG, Sleijfer S, Foekens JA, Martens JW. Correlation of breast cancer susceptibility loci with patient characteristics, metastasis-free survival, and mRNA expression of the nearest genes. ***Breast Cancer Res Treat*. 2012** Jun;133(3):843-51. doi: 10.1007/s10549-011-1663-3.

Reviews and Editorials:

1. Chen L*, **Groenewoud A***, Tulotta C, Zoni E, Kruithof-de Julio M, van der Horst G, van der Pluijm G, Ewa Snaar-Jagalska B. A zebrafish xenograft model for studying human cancer stem cells in distant metastasis and therapy response. ***Methods Cell Biol*. 2017**; 138:471-496. doi: 10.1016/bs.mcb.2016.10.009.

2. van der Ent W, Veneman WJ, **Groenewoud A**, Chen L, Tulotta C, Hogendoorn PC, Spaink HP, Snaar-Jagalska BE. Automation of Technology for Cancer Research. ***Adv Exp Med Biol*. 2016**; 916:315-32. doi: 10.1007/978-3-319-30654-4_14.

3. Tulotta C, He S, van der Ent W, Chen L, **Groenewoud A**, Spaink HP, Snaar-Jagalska BE. Imaging Cancer Angiogenesis and Metastasis in a Zebrafish Embryo Model. ***Adv Exp Med Biol*. 2016**; 916:239-63. doi: 10.1007/978-3-319-30654-4_11.

Research monographs, chapters in collective volumes:

1. **Groenewoud A**, Mathijs Kint, B. Ewa Snaar-Jagalska , Anne-Marie Cleton-Jansen, PhD. Zebrafish models for studying bone tumors. ed. Heymann D. *Bone Cancer: Bone Sarcomas and Bone Metastases - From Bench to Bedside*. Academic Press Inc., San Diego, USA, **2021**. ISBN 978-0-12-821666-8, pp. (in press).

Submitted manuscripts:

1. Varela M, Flier A, Lamers G, van der Vaart M, **Groenewoud A**, Meijer AH. Gasdermin D pore formation in bacterial phagosomes 2 initiates macrophage pyroptosis.
2. **Arwin Groenewoud**, Jie Yin, Maria-Chiara Gelmi, Samar Alsafadi, Fariba Nemati, Didier Decaudin, Sergio Roman-Roman, Helen Kalirai, Sarah E. Coupland, Aart G. Jochemsen, Martine J. Jager, Ewa Snaar-Jagalska
   Patient-derived zebrafish xenograft models reveal ferroptosis as a fatal and druggable weakness in metastatic uveal melanoma

Chapter 9 Curriculum vitae

Arwin Groenewoud was born in Heerjansdam the Netherlands on April 2nd, 1988. In 2005 he completed Walburg college Zwijndrecht and started his studies as lower-level laboratory technician (MLO) at Zadkine, Rotterdam. As part of his MLO education, he performed an internship in the department of medical oncology, under the supervision of Anieta Sieuwerts, in the group of John Foekens on SNP profiling in breast cancer, finishing in 2009. Subsequently he continued with his BSc degree in biotechnology and medical research at Avans applied science university, Breda the Netherlands, where he performed two internships. The first in the department of molecular allergology of the Paul Ehrlich Institute, Langen, Germany under the supervision of Stefan Schülke in the group of Stephan Scheurer on TLR ligand-based allergy vaccines. His second internship was conducted in the department of experimental surgical oncology, in the Erasmus Medical Center in Rotterdam, the Netherlands. During this internship he worked on the development of cationic, temperature triggered release liposomes for the delivery of chemotherapeutics, under the supervision of Bilyana Dicheva in the group of Timo ten Hagen in the Erasmus Medical Center. He obtained his BSc with honors in 2012 and started a MSc program in molecular biology at Leiden University, where he performed and internship in the group of Ewa Snaar-Jagalska, working on modelling nascent breast cancer metastases in zebrafish, he finished his MSc in 2015. In the interim between his MSc and the start of his PhD he worked at Leiden University as a research and teaching assistant. He started his PhD in 2016, wherefrom the work outlined in this thesis was derived. In 2021 he moved to Germany to join the group of Prof Felix Engel, to continue his research on cancer using the zebrafish model.